OPTICAL MICROFIBER DEVICES BASED LASER AND SENSOR APPLICATIONS

MD. JAHID FARUKI

FACULTY OF SCIENCE
UNIVERSITY OF MALAYA
KUALA LUMPUR

2018

OPTICAL MICROFIBER DEVICES BASED LASER AND SENSOR APPLICATIONS

MD. JAHID FARUKI

DISSERTATION SUBMITTED IN FULFILMENT OF THE REQUIREMENTS FOR THE DEGREE OF MASTER OF SCIENCE

DEPARTMENT OF PHYSICS
FACULTY OF SCIENCE
UNIVERSITY OF MALAYA
KUALA LUMPUR

2018

UNIVERSITY OF MALAYA

ORIGINAL LITERARY WORK DECLARATION

Name of Candidate: **MD. JAHID FARUKI**

Matric No: **SGR150067**

Name of Degree: **MASTER OF SCIENCE**

Title of Project Paper/Research Report/Dissertation/Thesis ("this Work"):

OPTICAL MICROFIBER DEVICES BASED LASER AND SENSOR APPLICATIONS

Field of Study: **EXPERIMENTAL PHYSICS**

I do solemnly and sincerely declare that:

(1) I am the sole author/writer of this Work;
(2) This Work is original;
(3) Any use of any work in which copyright exists was done by way of fair dealing and for permitted purposes and any excerpt or extract from, or reference to or reproduction of any copyright work has been disclosed expressly and sufficiently and the title of the Work and its authorship have been acknowledged in this Work;
(4) I do not have any actual knowledge nor do I ought reasonably to know that the making of this work constitutes an infringement of any copyright work;
(5) I hereby assign all and every rights in the copyright to this Work to the University of Malaya ("UM"), who henceforth shall be owner of the copyright in this Work and that any reproduction or use in any form or by any means whatsoever is prohibited without the written consent of UM having been first had and obtained;
(6) I am fully aware that if in the course of making this Work I have infringed any copyright whether intentionally or otherwise, I may be subject to legal action or any other action as may be determined by UM.

Candidate's Signature Date:

Subscribed and solemnly declared before,

Witness's Signature Date:

Name:

Designation:

OPTICAL MICROFIBER DEVICES BASED LASER AND SENSOR APPLICATIONS

ABSTRACT

Optical microfiber has attracted many researchers attention due to many interesting properties such as strong evanescent fields, tight optical confinement, compact size and easy integration with the optical system. All these advantages can be used to develop various lasers and refractive index-based sensors. In this work, the microfiber has been fabricated using the flame brushing technique and it has been used in both laser and sensor applications. The microfiber has been used as a filter device to generate dual wavelength fiber laser by taking the advantage of the interference pattern and the unique arrangement of polarization controller (PC). The proposed microfiber device can generate highly stable and tunable dual wavelength with spacing between 0.40 nm to 3.32 nm (corresponding to frequency from 49.4 GHz to 409 GHz). The application of microfiber in pulse laser (Q-switched and mode-locked) generation is demonstrated where graphene coated microfiber device has been utilized as a saturable absorber device. A new Poly (N-vinyl Carbazole) - Polypyrrole/Graphene Oxide (PNVC-PPy/GO) nano-composite material has been deposited on a tapered part to fabricate microfiber based saturable absorber device, and a passively Q-switched fiber laser has been demonstrated with repetition rates from 25.2 kHz to 42.7 kHz. Meanwhile, microfiber based mode locked pulse generation is also demonstrated where pulse trains with a pulse width of 3.46 ps, a 3dB optical bandwidth of 11.82 nm and a repetition rate of 920 kHz are obtained. Moreover, this study has also investigated the mechanism of tuning the mode-locked pulses by stretching the microfiber. The mode-locked pulse is tuned over a span of 4.4 nm (from 1560.6 nm to 1556.2) by stretching the tapered fiber from 0 to 100 μm (strain). Furthermore, microfiber based devices such as dual tapered optical microfiber inline Mach-Zhender interferometer (OMI-MZI) and microfiber knot resonator (MKR) have been exploited in sensor

applications. An OMI-MZI has been used as a temperature sensor, and the sensitivity has been observed before and after the coating with PNVC-PPy/GO. The uncoated and PNVC-PPy/GO coated OMI-MZI exhibited a sensitivity of 30.4 pm/^{o}C and 37.1 pm/^{o}C, respectively. Thereafter, a refractive index based humidity sensor has also been demonstrated by using microfiber knot resonator (MKR) where uncoated MKR showed a sensitivity of 1.3 pm/%RH and TiO_2 nanoparticles coated MKR showed a sensitivity of 2.5 pm/%RH. Further, the results indicate that the optical microfiber is highly potential for various sensing and lasing applications.

Keywords: Optical Microfiber, Fiber Laser, Sensor, Pulse Laser, Optical Sensing.

LASER DAN APLIKASI SENSOR BERASASKAN PERANTI GENTIAN-MIKRO OPTIK

ABSTRAK

Gentian-mikro optik telah mendapat perhatian ramai penyelidik kerana sifat-sifatnya yang menarik, contohnya, medan *evanescent* yang kuat, kebolehan pengurungan-optik ketat, bersaiz padat, dan mudah untuk diintegrasikan dengan sistem optik lain. Kelebihan-kelebihan ini boleh digunakan untuk membangunkan pelbagai laser dan sensor berasaskan indeks pembiasan. Dalam kajian ini, teknik berusan-api digunakan dalam fabrikasi gentian-mikro dan digunakan dalam aplikasi laser dan sensor. Gentian-mikro ini boleh digunakan sebagai alat penapis optik untuk menjana dwi-laser gentian fiber dengan mengguna pakai spektrum interferns dan susunan unik pengawal polarisasi (PC). Cadangan peranti gentian-mikro tersebut berkebolehan untuk menjana dwi-laser dengan jarak 0.40 nm hingga 3.32 nm antara setiap panjang-gelombang (sepadan dengan frekuensi dari 49.4 GHz hingga 409 GHz). Aplikasi gentian-mikro dalam penjanaan denyutan (Q-switch dan mode-locked) turut didemonstrasikan, di mana, gentian-fiber bersalut *graphene* telah digunakan sebagai komponen penyerap boleh-tepu. Bahan nano-komposit baru, Poly (N-vinyl Carbazole) - Polypyrrole/Graphene Oxide (PNVC-PPy/GO) yang didepositkan ke atas bahagian tirus dalam fabrikasi peranti penyerap boleh-tepu gentian-mikro dan laser-gentian pasif Q-switch telah didemonstrasikan dengan kadar pengulangan dari 25.2 kHz hingga 42.7 kHz. Manakala, penjanaan denyut mode-locked berasaskan gentian-mikro turut didemonstrasikan di mana jajaran denyutan tersebut mempunyai lebar-denyut bernilai 3.46 ps, jalur lebar 3dB optikal sepanjang 11.82 nm dan kadar pengulangan sebanyak 920 kHz. Tambahan lagi, kajian ini turut menyelidik mekanisma penalaan denyutan mode-locked dengan meregang gentian-mikro. Denyutan mod-locked tersebut telah ditala dalam kadar sebanyak 4.4 nm (dari 1560.6 nm hingga 1556.2 nm) dengan meregang gentian-mikro dari 0 hingga 100 μm

(vegayan). Tambahan pula, peranti berasaskan gentian-mikro seperti interferometer Mach-Zehnder dwi-tirus berjajar (OMI-MZI) dan resonator tersimpul gentian-mikro (MKR) telah dieksploitkan dalam aplikasi sensor. OMI-MZI telah digunakan sebagai sensor suhu dan sensitivitnya telah diperhatikan sebelum dan selepas salutan PNVC-PPy/GO. OMI-MZI yang tidak bersalut dan bersalut PNVC-PPy/GO masing-masing mempunyai sensitiviti 30.4 pm/^{o}C and 37.1 pm/^{o}C. Selain itu, sensor berasaskan indeks pembiasan telah didemonstrasikan menggunakan resonator tersimpul gentian-mikro (MKR), dimana, MKR yang tidak bersalut menunjukkan sensitiviti sebanyak 1.3 pm/%RH manakala MKR bersalut nano-partikel TiO_2 menunjukkan sensitiviti 2.5 pm/%RH. Keputusan-keputusan tersebut telah menunjukkan bahawa gentian-mikro optik berpotensi tinggi untuk kegunaan dalam pelbagai aplikasi sensor dan laser.

Kata Kunci: Gentian-mikro Optik, Laser Gentian, Sensor, Laser Denyut, Pengesanan Optik.

ACKNOWLEDGEMENTS

Thanks to Almighty Allah for allowing me to complete my master project and thesis work successfully. I would like to grab this chance to express my gratitude to all the people associated who helped me with their kind assistance and support towards the completion of the current study.

First of all, I would like to thank my supervisor distinguished Professor Datuk Dr. Harith Ahmad, the director of Photonics Research Centre (PRC), for his kind guidance and support towards the project completion. I would like to thank him personally for allowing me to use many of the expensive optical equipments, and for having trust on my ability. Without his support, this number of journal publications won't be possible.

I would like to thank Dr. Mohd Zulhakimi Ab Razak for his kind assistance and guidance in the beginning of masters' study. He provided ample support and motivation towards my work. My writing skills have been developed greatly through his kind feedback and facilitation.

I would also offer my sincere thanks to Dr. Ali A. Jasim for his kind guidance in some of the experiments. He provided invaluable feedback on my manuscript and helped me in all the ways he could.

I would like to thank Dr. Saaidal Azzuhri, Dr. Tiu Zian Cheak, Dr. Afiq Ismail, and Dr. Rezaul Karim for their kind guidance and assistance. I'm thanking the examiners of my proposal defense and candidature defense who offered their kind feedbacks and helpful opinions towards the development of this work. I would like to thank all the colleagues and friends in PRC, especially Mr. Muwafaq Fadhil Jaddoa.

Last but not least, I would like to thank my family for standing beside me all the time and University of Malaya for their continuous support on my studies.

TABLE OF CONTENTS

LIST OF FIGURES

LIST OF TABLES

LIST OF SYMBOLS AND ABBREVIATIONS

AOMs	:	Acousto-optic modulators
ASE	:	Amplified spontaneous emission
CNT	:	Carbon nanotube
DBSA	:	Dodecylbenzene sulfonic acid
DIAL	:	Differential absorption lidars
DWFL	:	Dual wavelength fiber laser
EDF	:	Erbium doped fiber
EDFA	:	Erbium doped fiber amplifier
EOMs	:	Electro optic modulators
FBG	:	Fiber Bragg gratings
FBT	:	Flame-brushing technique
$FeCl_3$. 6 H_2O	:	Ferric chloride hexa hydrate
FESEM	:	Field-emission scanning electron microscopy
FSR	:	Free spectral range
FWHM	:	Full width at half maximum
GO	:	Graphene oxide
HOPG	:	Highly oriented pyrolitic graphite
HML	:	Harmonic mode-locked
ITU	:	International Telecommunication Union
kHz	:	kilohertz
LD	:	Laser diode
Lidar	:	Light Detection And Ranging
MCR	:	Microfiber coil resonator

MHz	:	Megahertz
MF	:	Microfiber
MFBT	:	Modified flame brushing technique
MKR	:	Microfiber knot resonator
MLR	:	Microfiber loop resonator
MNF	:	Micro and nano fiber
nGL	:	Number of graphene layer
NMP	:	N-Methyl-2-Pyrrolidone
NPR	:	Non-linear polarization
OFNM	:	Optical fiber nano-wire and micro-wire
OMF	:	Optical microfiber
OMI-MZI	:	Optical microfiber inline Mach-Zhender interferometer
OPM	:	Optical power meter
OMNF	:	Optical micro and nano fiber
OSA	:	Optical spectrum analyser
PC	:	Polarization controller
PDI	:	Polarization dependent isolator
PNVC-PPy/GO	:	Poly (N-vinyl Carbazole) - Polypyrrole/Graphene Oxide
Q-factor	:	Quality factor
RF	:	Radio frequency
RFSA	:	Radio frequency spectrum analyser
RH	:	Relative humidity
SA	:	Satuarble absorber
SLM	:	Single longitudinal mode
SMF	:	Single mode fiber

SMTD	:	Single mode taper-drawing
SNR	:	Signal to noise ratio
SPF	:	Side polished fiber
SPM	:	Self-phase modulation
TBP	:	Time-bandwidth product
TF	:	Tapered fiber
TiO_2	:	Titanium dioxide
TLS	:	Tunable laser source
WDM	:	Wavelength division multiplexer
XRD	:	X-ray diffraction
2D	:	2-dimensional
3D	:	3-dimensional

CHAPTER 1: INTRODUCTION

1.1 Optical Fiber Based Laser and Sensing Technology

Over the past three decades, optical fiber technology has brought remarkable advancement in the field of communication. The transmission capacity of the optical fiber has improved greatly in the late 1990s through a technological revolution when wavelength division multiplexing (WDM) technique was introduced in the optical communication system. Currently, optical fiber is able to carry the information over a rate of 1 Tb/s (Essiambre & Tkach, 2012; Gnauck *et al.*, 2008) over a long distance with a low attenuation. The increase in the transmission capacity is more than 10000 times if compared with the capacity of data transmission in the early stage in the 1970s which was only 100 Mb/s. The success of optical fiber in communication applications influences the researchers to engage in optical fiber based laser and sensing application focused research. In fact, the potential of optical fiber in other applications besides communications such as in various laser applications (Mary *et al.*, 2014; Szipocs *et al.*, 2016) and sensing applications (Lee, 2003; Li *et al.*, 2012) has been studied.

Increasingly, lasers play a dominant role not only in our everyday lives, but also have become pervasive in various industrial, medical, and sensing applications. Fiber lasers are the newest and fastest developing lasers among other types of lasers (Taccheo *et al.*, 2016) for many of its advantages such as reliability, efficiency, low fabrication cost, low power consumption, and flexibility. Fiber lasers are being used in manufacturing process, new materials processing, mass production of solar cell, health care, and as a light sources in bio-photonics, environment control and security related applications. Moreover, they are potential to be used in cancer diagnosis (Taccheo *et al.*, 2016), hyperspectral imaging, and optical metrology systems, for instance optical coherence tomography (OCT)

(Heisterkamp *et al.*, 2015), precision surface profilometry (Taudt *et al.*, 2016), or in the characterization of optical components (Ortac *et al.*, 2009).

On the other hand, fiber optic sensing technology has grown rapidly because of the great improvement or remarkable progress that continues to be made in industries. Optical fiber sensors offer many significant benefits such as immunity to electromagnetic interference, small and compact size, high sensitivity and easy deployment in multiplexed or distributed sensors (Lee, 2003). So far, a number of optical fiber based sensors have been proposed and demonstrated built on various technologies such as interferometers and low-coherent interferometers, fiber-optic gyroscopes, fiber gratings, Faraday rotation, and scattering/ reflection. Optical fiber sensors have been successfully employed in various applications such as bio-sensing in bio-sensing, displacement sensing, vibration sensing, chemical sensing, gas sensing, current sensing, strain sensing, temperature sensing, humidity sensing, viscosity sensing, pressure and acoustic sensing, electric and magnetic field measurements, and many more (Lee, 2003; Li *et al.*, 2012). Overall, optical fiber based lasers and sensors are believed to be very influential in forthcoming laser and sensor applications.

1.2 Microfiber devices based technology

Optical microfiber is perceived as an amalgamation of fiber-optics and nano-technology. With the rapid growth of nanotechnology, fiber optical devices and components are getting miniaturized. This advanced miniaturization makes them high-speed devices with ultra-low power consumption. Optical microfibers and nanofibers are considered as potential building blocks for miniaturized photonics device, components and integrated optical system (Wu & Tong, 2013). Optical microfiber technology is growing as an attractive platform for the exploration of fiber-optic technology, and has

received a lot of attentions from the optical scientists because of their interesting properties and usefulness in various applications. A microfiber/nanofiber with high refractive index difference n and with a diameter close to the wavelength of the propagating light offers many interesting properties such as tight optical confinement, strong evanescent field and small mass which makes it very potential to be used in compact optical devices and sensors (Wu & Tong, 2013). Optical microfibers and nanofibers have been employed in various optical areas such as nonlinear optics (e.g. supercontinuum generation), light emitting devices (e.g. graphene mode-locked laser), quantum and atomic optics (e.g. atom trap and waveguide), optical sensors (e.g. sensitive coating and evanescent field absorption/loss), microfiber gratings (e.g. Bragg grattings), micro cavities (e.g. loop/ring/knot cavity), plasmonics (e.g. plasmonic nanowire excitation) and in many other passive components (e.g. Mach-Zhender interferometer, optical coupler) (Wu & Tong, 2013).

Researchers have exploited the properties and the characteristics of optical microfiber using various laser techniques. Generation of dual and multi wavelength fiber laser, tunable fiber laser, and pulse fiber laser have been demonstrated using microfiber based laser cavity (Ahmad *et al.*, 2016b; Fang *et al.*, 2010; Harun *et al.*, 2010; Meng *et al.*, 2014; Wang *et al.*, 2012). Besides, microfibers have been greatly explored in sensing applications (Chen *et al.*, 2013). A number of microfiber sensors have been designed and employed to measure humidity, temperature, strain, acoustic wave vibration, current, solution concentration, gas element, displacement, acceleration, force, rotation, electrical and magnetic field (Arregui *et al.*, 2000; Chen *et al.*, 2013; Jaddoa *et al.*, 2016; Jasim *et al.*, 2012; Liao *et al.*, 2013; Lim *et al.*, 2011; Sulaiman *et al.*, 2013; Wu *et al.*, 2009; Wu *et al.*, 2011).

1.3 Research objectives

This research study focuses on the fabrication of the optical microfiber and microfiber based devices, and exploits the characteristics of microfiber based devices in various laser and sensing applications. The work begins with fabrication of microfiber from the single mode fiber (SMF) using the flame brushing technique. Importantly, this investigation demonstrates fabrication techniques for both adiabatic and non-adiabatic microfibers. Different types of microfiber structure and device have been fabricated such as microfiber interferometric device, microfiber based saturable absorber device, microfiber based inline Mach-Zehnder interferometer, microfiber knot resonator which have been employed in various laser and sensing applications. The objectives of the current study are described in the following points:

1. To fabricate adiabatic and non-adiabatic microfiber based devices.
2. To investigate the use of microfiber based devices in dual-wavelength and pulse fiber laser applications, to be specific in tunable dual wavelength fiber laser in 1.5 μm wavelength, in Q-switched pulse fiber laser using a new Graphene oxide based nanocomposite coated microfiber device, and in wide-bandwidth mode-locked pulse fiber laser using graphene coated adiabatic microfiber saturable absorber device
3. To develop and investigate the effect of nano particle coating on microfiber devices in order to improve the temperature and humidity sensing performances by comparing the sensing performance of the device before coating and after coating. Moreover, comparisons are to be made with previous study where applicable.

1.4 Overview of the thesis

This thesis presents the research works on microfibers, microfiber based devices and their applications. This study covers from the fabrication of microfiber to the utilization of microfiber in various laser and sensor applications. Chapter 1 provides a brief introduction about optical fiber based laser and sensing technology followed by a short overview about microfiber devices based technology for various photonics applications. Furthermore, this chapter addresses the objectives of the study, scope and significance of the study.

Chapter 2 provides a review of the related scientific literature in the study of microfiber based devices. The chapter describes theories of adiabaticity and the optimal shape of optical microfiber, the properties of optical microfiber, different types of fabrication process, applications of the microfiber based devices, and lastly the recent development in microfiber based laser and sensing applications. The theoretical background and recent literature review about microfiber based devices, namely microfiber based saturable absorber device, microfiber based inline Mach-Zehnder interferometer device and microfiber based knot resonator device are stated.

Chapter 3 describes the details of the methodology of this research work. The fabrication set-up and procedures to fabricate microfiber using the flame brushing technique are also described. Two types of microfiber based on the geometry which are adiabatic microfiber and non-adiabatic microfiber are described. Afterward, fabrication procedure of microfiber based devices (microfiber based saturable absorber device, microfiber based inline Mach-Zehnder interferometer device, and microfiber based knot resonator device) are presented.

Chapter 4 describes the laser applications of the fabricated microfiber based devices. Particularly, a dual wavelength fiber laser, a Q-switched and a Mode-locked pulse fiber

laser and a tunable mode-locked fiber laser are attained and demonstrated in this chapter. Firstly, a non-adiabatic microfiber has been employed in dual wavelength generation. Secondly, the microfiber has been coated with graphene nanoparticle SA and employed in Q-switched and mode locked pulse fiber laser generation. Lastly, a tuning mechanism has been developed by stretching and changing the interaction length of the microfiber. The details of device fabrication, and results and discussion are described in Chapter 4.

Chapter 5 describes the sensing applications of microfiber based devices. As demonstrated in the chapter, microfibers have been constantly exploited in a variety of sensing applications, including temperature and humidity. A microfiber based inline Mach-Zehnder interferometer device has been exposed to temperature variations. Subsequently, Poly(N-vinyl Carbazole)-Polypyrrole-graphene oxide (PNVC-PPy/GO) solution coated inline Mach-Zehnder interferometer device has been exposed to similar trend of temperature variations. The responses of the uncoated and coated microfiber devices with respect to temperature variations are described. Furthermore, this study also investigates the responses of microfiber based knot resonator device against humidity variations. It also reports the responses of the uncoated knot resonator and humidity sensitive titanium dioxide (TiO_2) nanoparticle coated knot resonator with respect to humidity variations are also described. The details of the sensor fabrication, coating method and sensor response are narrated in this chapter.

Chapter 6 concludes the current study. Suggestions for future works are also recommended in this chapter and finally, the thesis is wrapped up.

CHAPTER 2: LITERATURE REVIEW

2.1 Introduction

Optical microfiber is popularly fabricated from single mode fiber (SMF) where a portion of the SMF is tapered to few micrometer diameter (even nanometer) scale. The fabricated tapered fibers are called by numerous names such as microfiber (MF), optical microfiber (OMF), optical micro and nano fiber (OMNF), micro and nano fiber (MFN), optical fiber nano-wire and micro-wire (OFNM), sub-wavelength fiber, tapered fiber, and fiber taper (Brambilla, 2010). However, two names have been used the most throughout the thesis, which are the tapered fiber (TF) and the microfiber (MF). This chapter describes the theoretical background and the properties of the optical microfiber. Various techniques of microfiber fabrication are presented and the overview for every available technique are described. In the last part of the chapter, the applications of microfiber devices in various laser and sensor applications are described along with the recent progress achieved in these devices, and the chapter is concluded.

2.2 Optical Microfiber

Optical microfibers have been attracting significant research interests because of its many interesting and useful optical properties such as large evanescent fields, nonlinearity, configurability and robustness (Brambilla, 2010). Optical Microfibers are very thin, and the diameter is very close or even smaller than the wavelength of the guided light. A significant percentage of light propagates outside of the microfiber creating an evanescent field in the waist region. Since the core diameter of the fabricated microfiber is very small, and the refractive index difference of the fiber material (glass) with surroundings medium is very high; the light gets confined in the cladding-air interface strongly. Microfiber is highly potential to be used in many applications such as optical

communications, nonlinear optics, high Q resonators, sensors and lasers. By using the transition region of the tapered fiber and by controlling the adiabatic angle, many useful things can be designed such as broadband single mode filters and couplers (Brambilla, 2010; Brambilla *et al.*, 2009; Jung *et al.*, 2008, 2009a) , selective excitation of the fundamental mode in multimode fibers (Jung *et al.*, 2009b), comb like filters for tunable lasers.

2.2.1 Theory and shape of the Microfiber

The microfiber is successfully made by heating a chosen section of the single mode fiber and by pulling on both ends of the heated fiber. The structure of the microfiber consists of a tapered waist region and two conical transition regions. The conical regions are connected with the un-tapered single mode fiber. Through the taper transitions, the local fundamental mode from a core mode of the un-tapered fiber are transformed to a cladding mode in the waist region of the microfiber, and this principle is used in many its applications (Birks *et al.*, 1992). The shape of the transition regions plays an important role in maintaining low-loss transmission. The shape of the taper is also very important in some particular devices where the taper needs to be deformed controllably such as miniature devices (Caspar & Bachus, 1989), sensors (Bobb *et al.*, 1990) and couplers (Birks, 1989).

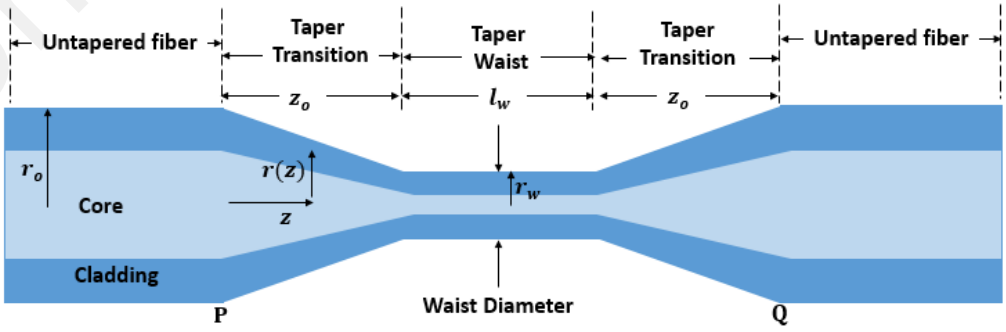

Figure 2.1: A schematic view of a microfiber.

Birks and Li presented a model for different types of tapered shape where both ends of the taper are assumed symmetric (Birks *et al.*, 1992). The system is designed to fabricate identical taper transition where the heat source heats the fiber, and both ends of the taper are being pulled with equal and opposite speeds. Figure 2.1 demonstrates the terminology that has been used to model the microfiber. $r_o$and $r_w$denotes the radius of the un-tapered fiber and tapered waist respectively. The length of the taper transition (transition region) and the taper waist are represented by $z_o$and l_w. $r(z)$ refers to a decreasing local radius function of the tapered transition region where z is the longitudinal coordinate. The z covers the whole transition region where $r(0) = r_o$and $r(z_o) = r_w$.

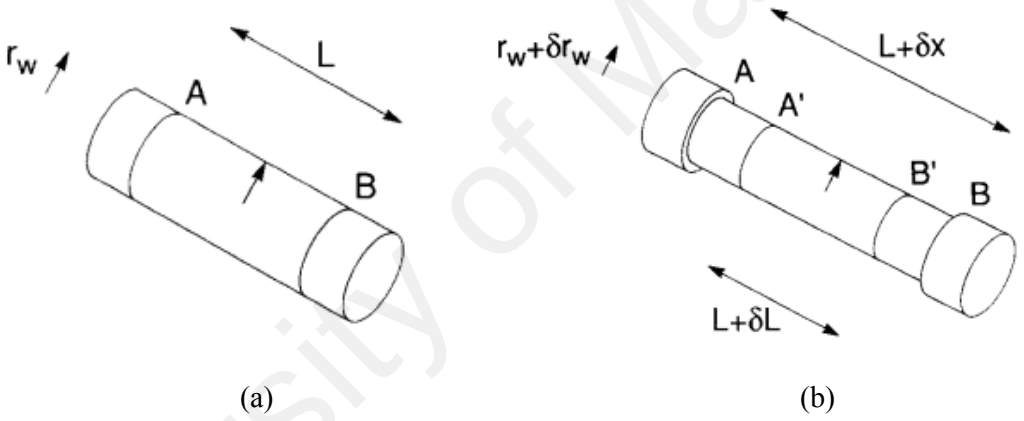

Figure 2.2: Graphical representation of tapering (a) at $t = 0$; (b) at $t = t + \delta t$ (Birks & Li, 1992).

According to this model, the heating zone of the fiber is assumed fixed. Figure 2.2(a) shows the schematic before tapering. The selected region (AB) is uniformly heated by the heat source, and all other regions of the fiber except the heating region are kept solid and cold. The fiber (referring to fiber materials hot glass) is always assumed to be soft enough that it can be pulled out, although some glass hold up well under melting, but can also be much more difficult to work.. The radius and length of the un-tapered fiber when the tapering starts $(t = 0)$, are denoted by r_w and L respectively. The tapering region is heated and pulled for a time, δt. Figure 2.2(b) depicts the shape after the pulling process

ends at time $t + \delta t$. The length of the fiber is increased to $L + \delta x$ (AB region) and the radius is reduced by δr_w. At a time during taper elongation (after some time of the process being started), the length AA′ and BB′ goes out of the heated region and forms the transition regions. The heating region now is A′ B′ and this will be further pulled and stretched.

The variation of L can be controlled by the heating element and is subjected to two constrains.

$$L \geq 0 \tag{2.1(a)}$$

$$\frac{dL}{dx} \leq 1 \tag{2.1(b)}$$

The instantaneous length of the taper waist at any time t is represented by

$$l_w(t) = L(t) \tag{2.2}$$

When the tapering process is complete, the final waist region is equal to the final hot zone length.

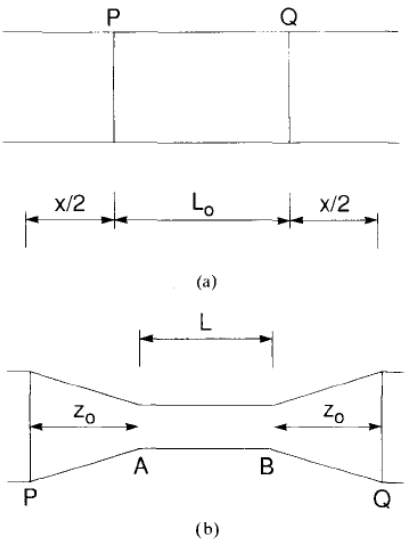

Figure 2.3: (a) The fiber at $t = 0$ when the tapering is initiated. The length L_o (section PQ) is heated. (b) The fiber at time t during tapering. The PQ section is stretched by distance x which is equal to $L + 2z_o$ (Birks, Timothy & Li, 1992).

The theory is based on the mass conservation law and the volume of the stretched fiber (at time $t + \delta t$) should be same as upstretched fiber (at time $t = 0$).

$$Volume\ before\ tapering = \ Volume\ after\ tapering$$

$$\pi r_w^2 L = \ \pi(r_w + \delta r_w)^2 (L + \delta x) \tag{2.3}$$

The radius of the waist region r_w can be expressed in terms of stretching distance x.

$$\frac{dr_w}{dx} = \quad \frac{r_w}{2L} \tag{2.4}$$

Figure 2.3 graphically represents the fabrication process. Comparing the total length of PQ before tapering (at $t = 0$) and after tapering (at $t = t + \delta t$)

$$2z_o + L = \frac{x}{2} + L_o + \frac{x}{2}$$

$$2z_o + L = L_o + x \tag{2.5}$$

According to the model, the local radius at any general point z along the taper transition is equal to the waist radius $r_w(x)$ when it is pulled out of the hot zone (the same radius when it was inside the hot zone). The extension $x(z)$ corresponding to the event is given by the distance law with $z_o = z$.

$$2z = x + L_o \quad L \tag{2.6}$$

Where x is the expression specifically the extension at which the point z is pulled out of the hot-zone.

The length of the taper waist is given by

$$l_w = L(x_o) \tag{2.7}$$

The variation of the waist radius r_w with x is obtained by integrating the volume law of equation (2.4), and the initial condition is assumed as $r_w(0) = r_o$.

$$\int_{r_o}^{r_w} \frac{dr_w'}{r_{w'}} = \frac{1}{2}\int_0^x \frac{dx'}{L(x')} \tag{2.8}$$

$$r_w(x) = r_o \exp\left(\frac{1}{2}\int_0^x \frac{\mathrm{dx}'}{\mathrm{L(x')}}\right) \tag{2.9}$$

The shape of the microfiber and the taper profile are depended on the heating-zone. The taper profiles for the constant hot-zone and linear hot zone variation are described in the subsequent sections.

Constant Hot-zone:

When the heating zone is constant,

$$L(x) = L_o \tag{2.10}$$

The taper profile function can be derived from equation 2.9 and expressed by

$$r_w(x) = r_o e^{-x/2L_o} \tag{2.11}$$

$$r(z) = r_o e^{-z/L_o} \tag{2.12}$$

This taper profile is a decaying exponential function. Narrower taper waist can be achieved based on this profile by using small hot zone length and drawing the taper for longer elongation. Figure 2.4 depicts an exponential decay profile fabricated using constant hot zone of 10 mm as demonstrated by Lim (Lim *et al.*, 2012).

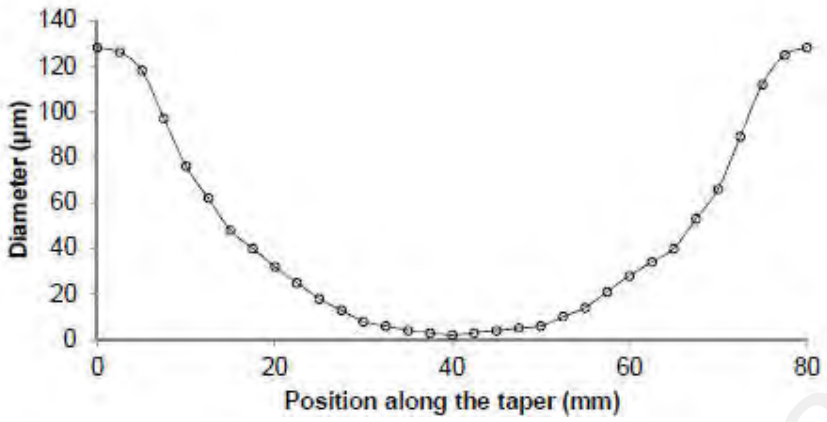

Figure 2.4: Decay exponential profile tapered fiber with fabricated using 10 mm constant hot zone ($L_o = 10\ mm$) (Lim *et al.*, 2012).

Linear Hot-zone variation:

If the hot-zone length changes linearly with time during taper extension.

$$L(x) = L_o + \alpha x \tag{2.13}$$

α is the constant ranges between -1 to +1. The change in relative hot-zone and taper extension depends on it.

The variation of the waist radius r_w derived from Equation (2.9)

$$r_w(x) = r_o \exp\left(\frac{1}{2}\int_0^x \frac{dx'}{L_o + \alpha x'}\right)$$

$$\text{So, } r_w(x) = r_o\left(1 + \frac{\alpha x}{L_o}\right)^{-1/2\alpha} \tag{2.14}$$

From the distance law (Equation 2.6)

$$z(x) = \frac{1}{2}(1 - \alpha)x \tag{2.15}$$

Thus, $$x = \frac{2z}{1-\alpha}$$

Thus the taper profile can be written as

$$r(z) = r_o \left[1 + \frac{2\alpha z}{(1-\alpha)L_o}\right]^{-1/2\alpha} \tag{2.16}$$

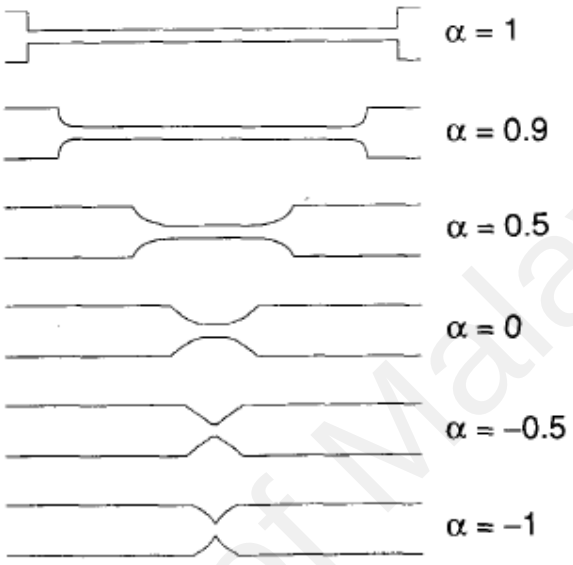

Figure 2.5: Calculated taper shape for various α value varying hot zone $L(x) = L_o + \alpha x$ (Birks & Li, 1992).

Specific Cases:

- When $\alpha = 0.5$, the hot zone is compressed by at a rate by half of the elongation. So the tapered profile can be written as

$$r(z) = r_o \left(1 \quad \frac{2z}{3L_o}\right) \tag{2.17}$$

Linear taper profile can be achieved using $\alpha = 0.5$ which has longer transition region but smaller waist region at the center of the tapered fiber. However, the waist region can be shifted from the center to one side of the tapered fiber by doing simple manipulation as depicted in Figure 2.6 (Lim *et al.*, 2012). This profile has many applications in chirped fiber Bragg gratings (CFBG) and optical tweezing.

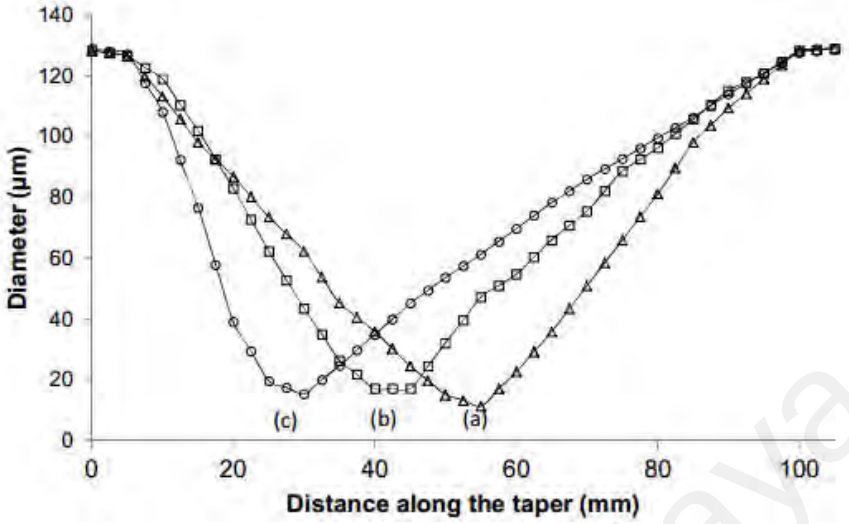

Figure 2.6: Linear taper profile ($\alpha = 0.5$) at different position; (a) smallest waist in the center, (b) and (c) taper waists are shifted (Lim *et al.*, 2012).

- When $\alpha = 0.5$, the taper transition region gets a reciprocal curve. This setting can fabricate short transition length taper.
- For $\alpha = 1.0$, the taper has no transition length and an abrupt junction is seen between tapered and untapered fiber.

Figure 2.5 shows few taper shapes with the range of $1 \leq \alpha \leq 1$where all the values are calculated based on the same value of r_o and L_o, and r_w is assumed as $\frac{r_o}{4}$. Linearly varying hot-zone (as per Equation 2.13) is used. The maximum waist length extension is measured as 16 L_o for $\alpha = 1$, whereas the minimum is measured as L_o for $\alpha = 0$ (Birks, Timothy & Li, 1992).

2.3 Properties of Optical Microfiber

There are many interesting properties of the microfiber, which are very useful in many applications. Some of the properties are low propagation loss, high non-linearity, and large evanescent field.

2.3.1 Propagation Loss

Propagation loss in microfibers is affected by many factors such as surface imperfections, cracks and impurities trapped around the microfiber (Kovalenko *et al.*, 2008; Zhai & Tong, 2007). The propagation loss increases as the radius decreases due to surface roughness and non-uniformity of the tapering shape. Figure 2.7 shows the propagation loss of different diameter microfibers manufactured using various available techniques (Brambilla, 2010). However, the mentioned loss is time dependent and high temperature treatment can recover the induced loss (Brambilla *et al.*, 2006). Smaller sized optical microfiber and nano fiber (OMNF) can degrade very fast in the air due to crack formation at the surface when the water gets absorbed. Embedding and coating the microfiber with low index materials such as Teflon or polymer are proposed to prevent easy degradation (Lim *et al.*, 2012; Vienne *et al.*, 2007; Xu & Brambilla, 2007).

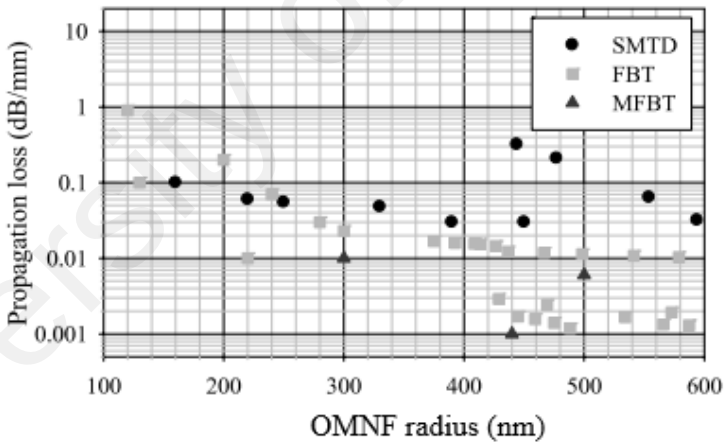

Figure 2.7: The transmission loss of optical micro and nano fiber fabricated using various method such as single mode taper-drawing (SMTD), Flame-brushing technique (FBT) and modified flame brushing technique (MFBT) (Brambilla, 2010).

2.3.2 Non-Linearity

The microfiber shows high non-linearity due to its strong modal confinement region. The non-linearity (γ) reaches maximum when the beam waist (ω) is at its minimum (Brambilla, 2010). The non-linearity is described by,

$$\gamma = \frac{2\pi n_2}{A_{eff}\lambda} \tag{2.18}$$

Where n_2 and A_{eff} refers to materials non-linear refractive index and beam effective area respectively.

$$A_{eff} = \frac{\pi\omega^2}{4} \tag{2.19}$$

$$\text{So, } \gamma = \frac{8n_2}{\lambda\omega^2} \tag{2.20}$$

Optical microfiber shows a non-linearity of $70 \times 10^{-3}\, W^{-1}m^{-1}$ whereas standard telecommunication single mode fiber demonstrates a non-linearity of $10^{-3}\, W^{-1}m^{-1}$ only. It implies that optical micro and nano fiber exhibits 70 times higher non-linearity than standard telecommunication fiber. More highly non-linear behavior can be achieved using liquid core OMNF (Xu *et al.*, 2008). Xu *et al.* demonstrated that Carbon disulfide and Toluene filled OFNM exhibits a non-linearity of $3.25\, W^{-1}m^{-1}$ and $70 \times 10^{-3}\, W^{-1}m^{-1}$ respectively at 1550 nm wavelength (Xu *et al.*, 2008). Highly non-linear microfiber have applications in optical communication and non-linear optics.

2.3.3 Large Evanescent Wave

If V<<2, the mode is guided weakly and most of the power propagates outside of the core creating large evanescent field (V number refers to a normalized frequency parameter, which determines the number of modes propagating in the step index fiber). The fraction of power propagating inside the microfiber core (η) can be expressed from the Poynting component which propagates in S_z direction (Tong *et al.*, 2004).

$$\eta = \frac{\int_{in} S_z\, dA}{\int_{in} S_z\, dA + \int_{out} S_z\, dA} = \frac{\int_0^r S_z\, dA}{\int_0^r S_z\, dA + \int_r^\infty S_z\, dA} \tag{2.21}$$

$\int_{in} S_z \, dA$ and $\int_{out} S_z \, dA$ refers to the cross section (inside) and outside of the OMNF respectively. Two parameters, e.g. refractive index and radius of the OMNF are important for mode confinement, thus mode confinement is easier to express in terms of the dependence on V (Brambilla, 2010). Figure 2.8 shows the portion of light that propagates inside the core with respect to V. For V=1, $\eta = 0.06$ which describes that about 94% of the light propagating outside of the OMNF boundary creating evanescent field.

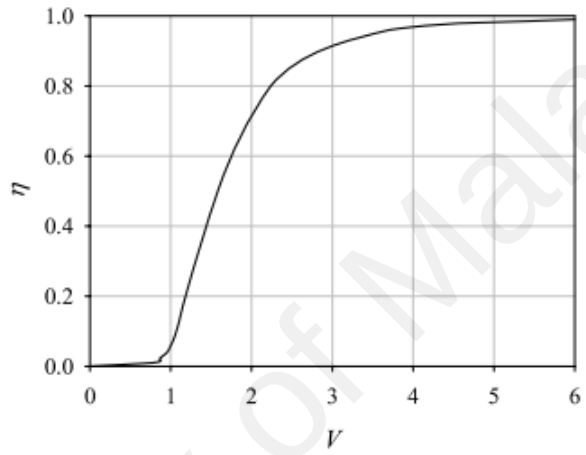

Figure 2.8: V number vs. light propagation inside the core (Brambilla, 2010).

The ratio of the light propagation wavelength and the radius of the OMNF (λ/r) has an influential impact on how wide the evanescent field spreads (how much area the evanescent field covers). Evanescent field intensity increases for any increase of (λ/r) and refractive index of the surroundings(n_{surr}).

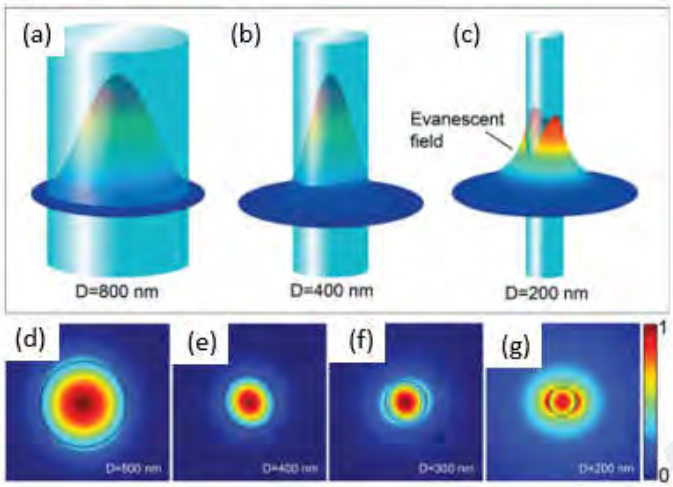

Figure 2.9: Z-direction Poynting vectors of silica MNFs at 633-nm wavelength; 3D view: diameters of (a) 800 nm, (b) 400 nm, and (c) 200 nm; 2D view: (d) 800 nm, (e) 400 nm, (f) 300 nm, and (g) 200 nm (Wu & Tong, 2013).

The power distribution (Z-direction Poynting vectors) of silica OMNF of diameter of 800 nm, 400 nm, and 200 nm are illustrated in Figure 2.9, both in 2D and 3D view. It can be evidently seen that a major portion of light remains confined in 800 nm diameter OMNF, whereas a major portion of light (more than 90%) is guided outside the fiber in 200 nm diameter OMNF creating a large evanescent field.

2.3.4 Mode propagation

In micro and nano-fiber, there is a difference between the refractive index of the core and the refractive index of the cladding, and the effective index consistently decreases along the down-taper transition region. Consequently, the taper modes propagate and can be guided and confined by the cladding-air interface. The approximations used in the derivation of the linearly polarized modes in conventional optical fiber don't apply to OMNF due to large refractive index difference in the cladding-air interface. The exact solution of Maxwell's equation for the hybrid modes HE_{vm} and EH_{vm} provides the eigenvalue equation (Brambilla, 2010; Grubsky & Savchenko, 2005; Tong *et al.*, 2004):

$$\left[\frac{J_v'(U)}{U\,J_v(U)}+\frac{K_v'(U)}{W\,K_v(U)}\right]\left[\frac{J_v'(U)}{U\,J_v(U)}+\left(\frac{n_{sur}}{n_{clad}}\right)^2\frac{K_v'(U)}{W\,K_v(U)}\right]=v^2\left(\frac{1}{U^2}+\frac{1}{W_2}\right)\left[\frac{1}{U^2}+\left(\frac{n_{sur}}{n_{clad}}\right)^2\frac{1}{W_2}\right] \quad (2.22)$$

J_v is the vth-order Bessel function of the first kind, K_v is the vth-order modified Bessel function of the second kind. n_{clad} and n_{sur} are referring to the refractive index of the cladding and the surrounding medium. The parameters U and W are defined as a function of the light propagation constant in vacuum (k_o) and in the optical OMNF (β).

$$U = r\sqrt{k_o^2 n_{clad}^2 - \beta^2} \quad (2.23)$$

$$W = r\sqrt{\beta^2 - k_o^2 n_{sur}^2} \quad (2.24)$$

The V number can be described by

$$V = \sqrt{U^2+W^2} = \frac{2\pi}{\lambda} r\,NA \quad (2.25)$$

In Equation 2.25, r refers to the radius of the OMNF, NA refers to numerical aperture and λ is the wavelength of the light propagating through OMNF.

The eigenvalue equation can be replaced as per equation below for $TE_{0m}$and TM_{0m} modes.

$$\left[\frac{J_1(U)}{U\,J_o(U)}+\frac{K_1(W)}{W\,K_o(W)}\right]=0 \quad (2.26)$$

$$\left[\frac{n_1^2 J_1(U)}{U\,J_o(U)}+\frac{n_2^2 K_1(W)}{W\,K_o(W)}\right]=0 \quad (2.27)$$

OMNF experiences single mode guidance when $V < 2.405$. For $V << 1$, a large portion of evanescent field will propagate outside of the OFNM. However, OMNF doesn't have degenerate modes for $V > 2.405$ which is unlikely to optical fiber.

2.4 Fabrication Techniques

To date, various techniques have been developed to fabricate microfibers. The available fabrication techniques can be broadly categorized into two themes, which are bottom up and top-down methods (Brambilla *et al.*, 2009). In bottom-up approach, the structure is formed from the smaller building blocks by stacking the atoms with each other, whereas in the top down approach, the structure is formulated into smaller size from a bigger piece of the same structure manually or through self-structuring process. The most widely used bottom-up techniques include the vapor-liquid-solid process (Westwater *et al.*, 1997), sol-gel methods (Miao *et al.*, 2002) and physical vapor deposition (Zhang *et al.*, 2000). On the other hand, top down method includes direct drawing from bulk materials (Tong *et al.*, 2006), and fiber pulling such as flame bushing technique (Brambilla *et al.*, 2006; Tong *et al.*, 2003). Bottom up methods have some drawbacks such as irregular profile and surface roughness which make it difficult to fabricate low loss fiber (Brambilla *et al.*, 2009). Top down method is considered much easier to taper the fiber. Top down methods reduce the macroscopic sample to micro scale and longer micro and nano-fiber can be achieved (Brambilla, 2010). There are few top down techniques available to produce microfiber, such as self-modulated taper-drawing, the flame-brushing technique, modified flame brushing technique and direct drawing from the bulk (Brambilla, 2010).

2.4.1 Self-modulated taper-drawing

In this technique, the SMF is tapered to a several micrometer diameter using conventional flame-brushing technique and the tapered is divided into two halves (Brambilla, 2010; Tong *et al.*, 2005). Later, one half of the taper is wrapped on a heated sapphire rod and the diameter is reduced into sub-micrometer diameter. Extremely smaller diameter tapered fiber can be fabricated using this technique. However, this process is considered complex and causes high loss (Brambilla, 2010). Figure 2.10 depicts

the fabrication set-up as proposed by Tong *et al.* (Tong *et al.*, 2005). A visible red light source (He-Ne laser) has been launched into the fiber to observe the tapering process. Besides that, a translational 3 dimension stage is used to adjust the taper angle during pulling.

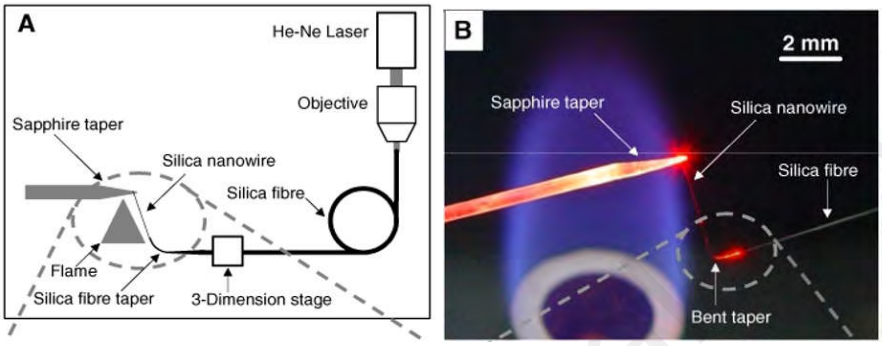

Figure 2.10: (A) self-modulated taper-drawing fabrication diagram adopted from (Tong *et al.*, 2005), and (B) Real image of nanowire fabrication assisted with a bent taper for self-modulation.

2.4.2 The flame-brushing technique

Initially, the flame brushing technique has been developed for the fabrication of fiber taper and couplers (Bilodeau *et al.*, 1988; Birks & Li, 1992). The process involves heating and pulling a certain region. Figure 2.11 shows the schematic of the flame-brushing technique. A translation torch is used to heat the desired tapered region and the SMF is being pulled to taper to micrometer/nanometer scale (Brambilla *et al.*, 2006; Jasim *et al.*, 2012). The flame of the torch is generated by burning butane and oxygen mixture. This technique can provide longer tapered fiber with relatively low loss compared with other techniques. The tapered shape can be highly controlled by optimizing the fiber stretching step and flame movement. A 30 nm radius and 110 mm long OMNF has been achieved by Brambilla *et al.* which signifies the potentiality of flame brushing technique (Brambilla *et al.*, 2006). However, the heat, flame quality and gas pressure, and pulling speed are needed to maintain optimally during tapering process. Microfiber might break - if the heat

is not high enough to soften the fiber, or if the heat is too hot that the fiber might melt before being pulled which will result in uneven distribution eventually, or if the pulling speed is too high compared to the ratio of fiber softening.

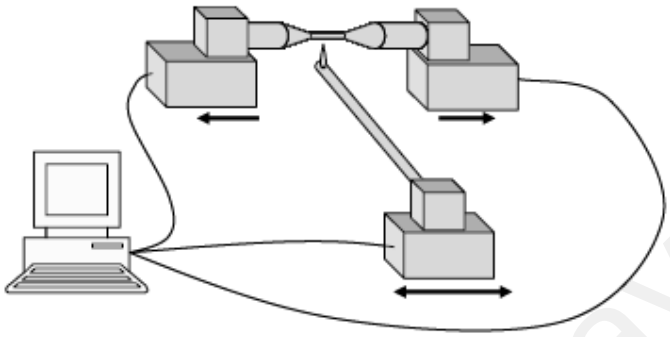

Figure 2.11: Schematic diagram of the flame-brushing technique. The flame continuously heats the selected region of the fiber and a computer controlled program pulls the fiber from both ends (Brambilla *et al.*, 2006).

2.4.3 The modified flame-brushing technique

The modified flame-brushing technique is derived from the flame brushing technique except that, it replaces the flame with a micro-heater (Brambilla *et al.*, 2005; Ding *et al.*, 2010) or CO_2 laser (Sumetsky *et al.*, 2010) instead of oxygen-butane flame.

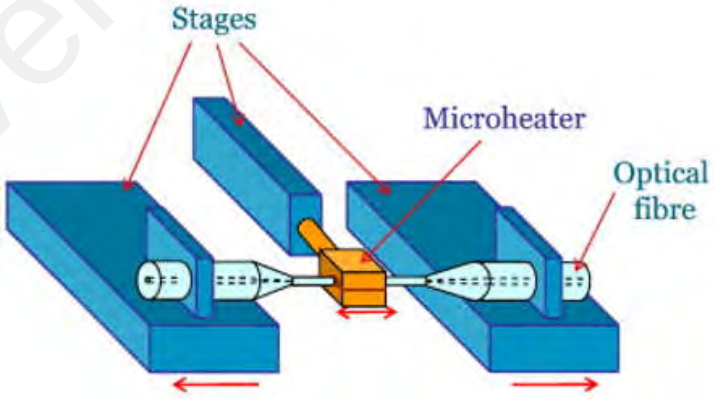

Figure 2.12: Schematic diagram of the modified flame brushing technique using micro-heater (Rodenburg *et al.*, 2011).

Micro-heater is a resistive element, and its temperature can be increased/decreased by controlling the current flow. The micro-heater offers excellent temperature control with high reliability and stability. It can heat up the selective region equally so that the better quality tapering can be obtained. The stripped part of the fiber is placed inside the micro-heater, which is typically a centimeter sized thermoelectric oven (Ding *et al.*, 2010) (Figure 2.12). Typical micro-heater can produce temperature within the range of 200 °C to 1700 °C which is good enough to soften the fiber (Brambilla *et al.*, 2005). Ding *et al.* achieved a 800 nm ultra-low loss tapered fiber with an average of 94% transmission by maintaining a temperature of 1160 °C in the micro-heater (Ding *et al.*, 2010).

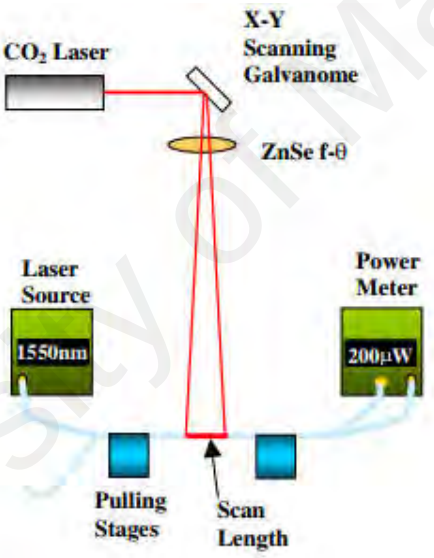

Figure 2.13: Schematic of a fiber tapering stage with CO_2 laser (McAtamney *et al.*, 2005).

In another approach, a combination of sapphire tube and CO_2 laser beam is used to control the temperature (Brambilla, 2010). Here, the temperature can be controlled by changing the degree of focus of the laser beam on to the sapphire tube. McAtamney *et al.* proposed a fiber tapering set-up where they have used CO_2 laser, X-Y scanning galvanome mirror and ZnSe f-θ lens to focus the laser on the fiber as shown in Figure 2.13 (McAtamney *et al.*, 2005). The controlled laser beam is generated, scanned through

the mirror and focused to the desired length of the fiber through the lens. Since the laser is coherent and easily controllable, the desired beam diameter of the microfiber can be fabricated using proper laser beam power and heat spot size of the laser beam. It has been reported by Sumetsky *et.al*. that a certain threshold diameter tapered fiber can be fabricated by heating the fiber with a certain power of the laser beam (Sumetsky *et al.*, 2010). This type of effect has never been reported using the flame brushing technique.

This modified technique using micro-heater and CO_2 laser adds flexibility to the flame brushing technique since processing temperature can be changed easily. This technique covers a wide range which can be used to fabricate micro/nano fiber from a wide range of glasses which have a low softening temperature. This method produces quality nano wire with very low OH content which are three orders magnitude smaller than conventional flame brushing technique. However, the experimental set-up cost is higher than flame brushing technique.

2.4.4 Direct drawing from the bulk

This particular technique has been proposed by Tong *et al.* (Tong *et al.*, 2006) with the purpose of microfiber and nanofiber fabrication. The mechanism can manufacture starting from bulk glasses using sapphire fibers with diameter ranging from 400 μm to 700 μm. Figure 2.14 depicts the process involved in direct drawing from the bulk method. A heat source is used to heat up the sapphire fiber to a certain temperature, which is sufficient to melt the fiber. Then, the fiber is immersed into the glass where the local melting happens. After that the glass is withdrawn and some part of the melt glass left on the fiber. Another sapphire fiber which is approximately 400 μm in diameter is brought into contact with the glass coated sapphire end. The heat source is reduced or removed allowing the melt to obtain a proper temperature (which is 800 K-1000 K for phosphate glass). The second

sapphire fiber is withdrawn with the melt at a slow speed (0.1-2 m/s) until the wire breaks. A microfiber with a considerable length can be obtained using this technique, and the nano/microfiber can be drawn from a very small quantity which can be up to the mass of 1 mg. However, this technique is flexible and cheap, but the uniformity and the diameter of the tapered fiber is difficult to control.

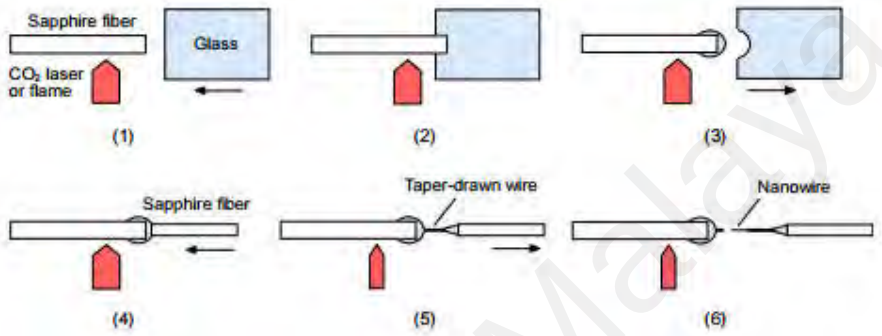

Figure 2.14: Schematic diagram illustrating the direct draw of nanowires from bulk glasses. (1) A glass is moved towards a sapphire fiber heated by a CO_2 laser or flame, (2) The fiber end is immersed into the glass through local melting, (3) A portion of molten glass is left on the end of the fiber when the glass is withdrawn, (4) A second sapphire fiber is brought into contact with the molten-glass-coated end of the first sapphire fiber, (5) The heating power is reduced and the second sapphire fiber is withdrawn, and (6) A nanowire is formed at the freestanding side of the taper drawn wire (Tong *et al.*, 2006).

2.5 Applications of Microfiber based devices

Optical microfiber devices mainly exploit three properties, which are- transition region properties, confinement and evanescent field effect (Brambilla, 2010). By controlling the tapering angle of the transition region, the mode guidance can be changed from the core to the cladding. Mode filter, comb like filter for tunable laser (Li & Bao, 2008), mode conversion, interferometric sensor (Zhu *et al.*, 2009), and selective excitation of the fundamental mode in multimode fiber (Jung *et al.*, 2009b) have been demonstrated based on microfiber based devices which utilizes the property transition regions. The mode confinement in the waist region of the microfiber device can be used in nonlinear optics and particle trapping such as supercontinuum generation, high harmonic generation,

optical trapping and tip nanosensors. The evanescent field of the microfiber devices can be used for nonlinear converters, particle manipulation and sensing applications (Brambilla, 2010).

2.5.1 Recent Progress in Microfiber based laser and sensor applications

Microfiber devices demonstrate similar characteristics as lithographic planar waveguides, and many photonics devices can be fabricated from the microfibers. The microfiber based devices can be used as building blocks for the larger and more complex photonic circuits (Lim *et al.*, 2012). Till date, many microfiber based devices have been reported such microfiber knot resonator (MKR) (Yu *et al.*, 2016), microfiber loop resonator (MLR) (Zheng *et al.*, 2013), microfiber coil resonator (MCR) (Sumetsky, M, 2008), optical microfiber inline Mach-Zehnder interferometer (OMI-MZI) (Ahmad *et al.*, 2015b; Lim *et al.*, 2012). Microfiber based devices have been explored in many laser and sensing applications. Microfiber based devices have been utilized in many laser applications, for instance, in applications of dual wavelength fiber laser (Harun *et al.*, 2010), multi wavelength fiber laser (Meng *et al.*, 2014), Q-switched pulse laser (Wang, J. *et al.*, 2012), mode-locked pulse laser (Wang *et al.*, 2012) and tunable laser (Ahmad *et al.*, 2016b; Fang *et al.*, 2010) generation. On the other hand, microfiber based sensors have been greatly exposed in many sensing applications such as humidity (Wu *et al.*, 2011), temperature (Wu *et al.*, 2009), strain (Arregui *et al.*, 2000; Liao *et al.*, 2013), acoustic wave vibration (Sulaiman *et al.*, 2013), current (Jasim *et al.*, 2012; Lim *et al.*, 2011), and solution concentration measurement (Jaddoa *et al.*, 2016).

In this study, the microfiber based devices have been utilized in various laser and sensor applications. Mainly 3 kinds of microfiber device has been fabricated and used in this study, which are: Microfiber based saturable absorber device, Optical Microfiber

Inline Mach-Zehnder interferometer (OMI-MZI), and Optical Microfiber Knot Resonator (MKR).

2.5.1.1 Microfiber based saturable absorber device

Saturable absorber (SA) is an intensity dependent optical component in which the absorption and the optical loss decreases at high optical intensities. When a medium consists of absorbing dopant ions and a strong optical intensity hits the medium, a depletion in the ground state of these dopant ion occurs, and saturable absorption may happen. The main applications of the saturable absorber are Q-switched pulse fiber laser and mode-locked pulse fiber laser.

By inserting saturable absorber inside the laser cavity, pulse fiber laser can be fabricated. This technique is known as passive pulse generation technique. For Q-switched pulse laser fabrication, passive technique is preferred since it offers advantages like compact geometry and simpler set-up compared to active techniques such as acousto-optic modulators, electro-optic modulators. On the other hand, even though, besides saturable absorber technique, many other passive techniques are available which utilize the advantages of nonlinear effects occurring in the fiber to generate mode-locked pulse fiber laser, such as nonlinear polarization technique, nonlinear amplification loop mirror (Sobon, 2015), satuarble absorber is considered as the most effective approach to fabricate pulse since fine-tuning of the polarization state is not required in this approach (Luo *et al.*, 2013).

The discovery of graphene and its highly desirable optical characteristics quickly saw the rapid development of saturable absorbers (SAs), mostly because of the compact size, low fabrication and operation cost and easy integration into current optical technologies (Luo *et al.*, 2010; Popa *et al.*, 2010a; Wang *et al.*, 2012; Zhang *et al.*, 2012). Many other 2-dimensional (2D) and 3-dimensional (3D) materials have been analysed and their

potential for use as an SA explored. The saturable absorber components are fabricated using various nano-materials such as Graphene (Bao *et al.*, 2011; Hasan *et al.*, 2009a; Sobon *et al.*, 2013; Wang *et al.*, 2012), MoS_2 (Luo *et al.*, 2014; Zhang *et al.*, 2014), $MoSe_2$ (Ahmad *et al.*, 2016), WS_2 (Janisch *et al.*, 2014) , Carbon nanotube (CNT) (Ahmad *et al.*, 2015a; Zhou *et al.*, 2010), Sb_2Te_3 (Boguslawski *et al.*, 2015), Bi_2Se_3 (Zhao *et al.*, 2012a; Zhao *et al.*, 2012b), Bi_2Te_3 (Lee *et al.*, 2015; Lee *et al.*, 2014), Black phosphorus (Chen *et al.*, 2015; Sotor *et al.*, 2015), and Gold nanospheres (Fan *et al.*, 2014).

The saturable absorber device/component using the nanomaterial can be fabricated in two ways which are – the sandwich method, and the coating method, as demonstrated in Figure 2.15. In the sandwich method, the SA nano-material is deposited in the fiber ferrule on the connector (similar as inserting the thin film), allowing light to penetrate the SA directly to fabricate pulse. On the other hand, in coating method, the SA nano-material is deposited on the microfiber waist region as a coating where the evanescent field is utilized to create the interaction between the SA and the light to fabricate pulse.

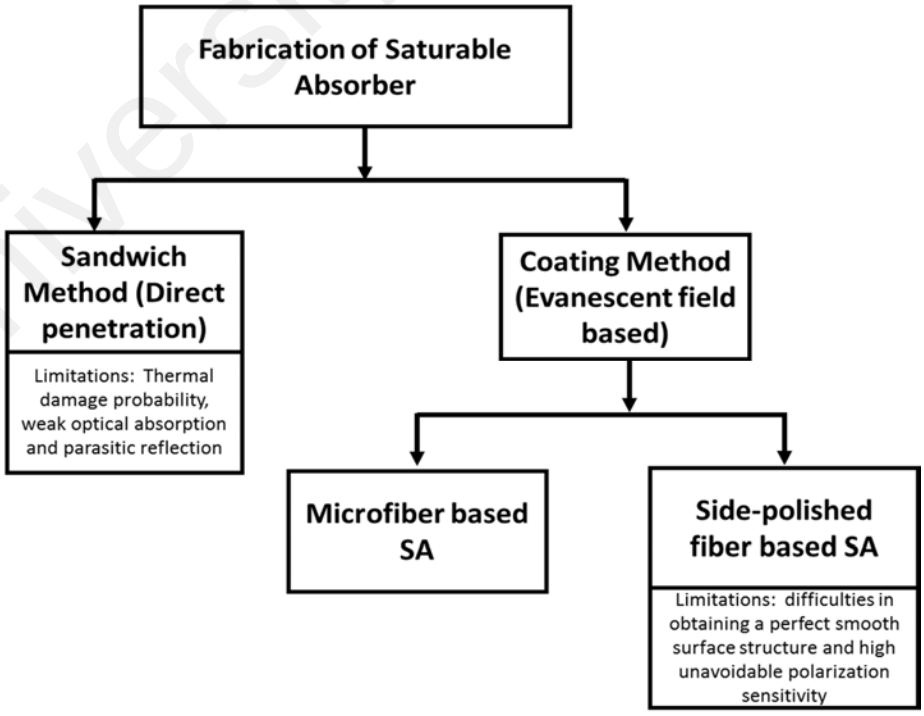

Figure 2.15: Types of SA based on fabrication method.

The issues associated with the sandwich method based SA are - thermal damage probability, weak optical absorption and parasitic reflection (He *et al.*, 2012b; Park *et al.*, 2015; Wang *et al.*, 2012). Thermal damage might occur when light passes directly through the SA layers which might be a barrier to ensure safe and robust SA application. On the other hand, it exhibits a weak optical absorption, since nonlinear interaction length is limited. Moreover, parasitic reflection may inside the fiber ferrule may affect the laser performance. Evanescent field based SA fabricated using coating method, such as SA coated microfibers and side polish fibers is considered as an alternative approach of pulse fabrication which tackles the issues associated with the sandwich method. SA coated microfibers and side-polished fibers require only a small portion of light to interact with a thin layer of SA in the waist region, thus allowing for a faster cooldown and reducing the probability of thermal damage in high optical power applications (Wang *et al.*, 2012). Unfortunately, there are some drawbacks to the use of side-polished fiber based SAs, such as difficulties in obtaining a perfect smooth surface structure and high unavoidable polarization sensitivity because of the asymmetric structure (Wang *et al.*, 2012). Thus, a microfiber based SA seems as a better choice which can generate pulse employing evanescent field interaction.

Table 2.1: Previously reported microfiber based SA device.

Waist diameter of the microfiber	Coated SA Materials	Output	Results	Authors (Ref)
3.2 μm	Graphene	Q-switched and Mode-Locked	*For Q-Switched :* Repetition rate: 10.36 kHz to 41.8 kHz; Average Output power: 1.13 mW, pulse energy: up to 28.7 nJ, Pulse duration: 3.89 μs *For Mode-Locked:* FWHM: 0.2 nm, Repetition Rate: 3.33 MHz Pulse Width: 15.7 ps Cavity Length: 62 m, Signal to Noise ratio (SNR): 50.7 dB	Wang *et al.*, 2012
3.5 μm	Graphene	Multi-wavelength Dissipative soliton	Repetition Rate: 551.5 kHz Pulse duration: 74.6 ps SNR: 62.5 dB	Luo *et al.*, 2012
6 μm	Reduced graphene oxide	Mode-Locked	Repetition Rate:7.47 MHz SNR: 70 dB Pulse width: 26 ps	He *et al.*, 2012b
6 μm	Graphene	Mode-Locked	3 dB Bandwidth: 4.3 nm Pulse Width: 679 fs Repetition rate: 5.48 MHz Cavity length: 38.01 m (by calculation)	Zhu *et al.*, 2013
6 μm	Carbon nanotubes (CNTs)	Mode-Locked	3-dB bandwidth: 3.7 nm Repetition rate: 1.54 MHz Pulse width: 1.61 ps	Kashiwagi & Yamashita, 2009
11 μm	MoS_2	Mode-Locked	3-dB Bandwidth: 2.47 nm Repetition rate: 6.77 MHz Pulse width: 3 ps	Liu *et al.*, 2014

Table 2.1, continued.

Waist diameter of the microfiber	Coated SA Materials	Output	Results	Authors (Ref)
12 μm	Topological insulator (TI) Bi_2Te_3	Mode-Locked	3 dB bandwidth: 0.95 nm Repetition Rate: 4.88 MHz Pulse width: 1.22 ps	Luo *et al.*, 2013
12 μm	Graphene	Mode-Locked	Repetition Rate :26.7 MHz Pulse duration: 26 ps 3 dB bandwidth: 0.4 nm SNR: 70 dB	He *et al.*, 2012a

In this study, a microfiber based saturable absorber device is fabricated by coating it graphene oxide (GO) and used for pulse fiber laser generation. The microfiber based saturable absorber device uses the evanescent field, and interacts with the 2D materials (e.g. graphene oxide) coated in the waist region to fabricate pulse train. There is a close relationship between the diameter of the microfiber and intensity of evanescent field. The diameter of the microfiber is inversely proportional to the evanescent field intensity. The lower the taper diameter, the stronger the evanescent field intensity. When the evanescent field is strong, it can penetrate to the coated SA layer (graphene oxide), and produce pulses. On contrary, the lower the taper diameter, the higher the fragility. Lower diameter microfiber is highly susceptible to break. The experimental method of coating involves deposition process, and microfiber can break easily when immersed inside the graphene oxide solution. Thus, an optimum balance between the two issues is required to attain. In fact, different waist diameter microfibers have been employed in pulse fiber laser generation, where the diameter varies in range between 3-12 μm as described in Table 2.1 (He *et al.*, 2012b; Liu *et al.*, 2014; Wang *et al.*, 2012). The results achieved in previous study are summarized in Table 2.1, where the coated materials, the output of the laser (Q-

Switched/ Mode-Locked) and output pulse characterization parameters are described in brief. As mentioned earlier that the lower diameter microfiber has stronger the evanescent field, but it is highly susceptible to break. In this study, the waist diameter of the microfiber has been optimized to a certain range, which complies with sufficient evanescent field interaction and optimal taper strength. It has been figured out from several practical experiments conducted in the lab that 8-11 μm (8 μm, 9 μm , 10 μm and 11 μm) waist diameter microfiber are the best in providing sufficient evanescent field and optimum taper strength, and in this study, microfibers within the diameter range of 8-11 μm have been employed. The details of the microfiber based saturable absorber device fabrication, particularly the deposition mechanism of nano-materials on the microfiber and characterization (Raman spectrum, and modulation depth) are described in Section 3.4.1.

Two major applications of the SA devices are the generation of Q-Switched pulse and the generation of Mode-Locked pulse. The literature review about Q-Switched pulse laser and Mode-Locked pulse laser are described below.

(a) ***Q-switched Pulse Laser***

In the last decade, Q-switched pulse fiber laser generation has attracted increasing attention due to its unique potential to be used in a wide range of applications such as telecommunication, micro mechanical machining, supercontinuum generation, range finding, metal cutting, material processing, environmental sensing, medicine and long-pulse nonlinear experiments (Chen *et al.*, 2010; Dong *et al.*, 2010; Huang *et al.*, 2008; Kuznetsov & Babin, 2010; Popa *et al.*, 2010a; Zhang *et al.*, 2012). Q-switching is the modulation of quality factor (Q-factor) which can be defined as the ratio of energy stored in the active medium and energy lost per oscillation cycle (Svelto & Hanna, 1976). Initially, the lasing of Q-switch mechanism is prevented by the low Q-factor; and after

achieving high Q-factor, the stored energy is released in a pulse form. The time needed to refill the energy extracted between two consecutive pulses is dependent on the gain medium life. The lasing in 1.5 micro-meter wavelength range, usually depends on the Erbium Doped Fibers (EDFs) as gain medium, and the lifetime of EDFs is in microsecond (ms), thus the repetition rate of the Q-switched laser in 1. 5 μm is usually in kilohertz (kHz) range (Popa *et al.*, 2010a; Svelto & Hanna, 1976). The generation of Q-switched pulses in the 1.5 micron region is of particular interest, as it falls within the main telecommunications bandwidth.

There are two primary techniques to fabricate Q-switched pulse fiber laser, which are active Q-switching technique and passive Q-switching technique. A number of reports are available which use the active techniques such as the use of as acousto-optic modulators (AOMs) or electro optic modulators (EOMs) (Bouyge *et al.*, 2008; Kir'yanov *et al.*, 2013; Villegas *et al.*, 2011) , and by physically oscillating a microsphere in front of the propagating beam to produce pulses (Kieu & Mansuripur, 2006a). Even though active technique offers substantial control over many characteristics of the pulses, it has many drawbacks such as bulky size, complexity and high cost. On the other hand, passive Q-switching technique in which saturable absorber (SA) is used to fabricate pulse offers many advantages such as compact geometry and simpler set-up (Popa *et al.*, 2010a). Thus, the passive Q-switching method is mostly preferred than the active method (Popa *et al.*, 2010a). Although passive Q-switching provides less control over the characteristics of the output pulse, this drawback is outweighed by the advantages of passive Q-switching technique, primarily its compact geometry and simple set-up, as well as typically lower cost (Popa *et al.*, 2010a).

Different types of SA components have been used to generate Q-switched pulse laser such as Graphene (Luo *et al.*, 2010; Popa *et al.*, 2010a; Wang *et al.*, 2012; Zhang *et al.*,

2012), Carbon nano tube (CNT) (Ahmad *et al.*, 2015a; Zhou *et al.*, 2010), MoS_2 (Luo *et al.*, 2014), $MoSe_2$ (Ahmad *et al.*, 2016), Gold-nanosphere (Fan *et al.*, 2014), Black phosphorus (Chen *et al.*, 2015), Transition metal dichalcogenides and Topological insulators such as MoS_2 (Luo *et al.*, 2014), $MoSe_2$ (Ahmad *et al.*, 2016), Bi_2Se_3 (Ahmad *et al.*, 2015c; Zhao *et al.*, 2012a; Zhao *et al.*, 2012b) and Bi_2Te_3 (Lee *et al.*, 2015; Lee *et al.*, 2014). Among all the materials, graphene is considered the thinnest materials in the world, and it has attracted remarkable research interest in material science and opto-photonics research (Bai *et al.*, 2015; Chen *et al.*, 2012; Terrones *et al.*, 2011). The first SA based on graphene has been demonstrated by Bao *et al.* (Bao *et al.*, 2009), and since then graphene has been seen as a promising SA component in pulse laser generation (Fan *et al.*, 2014; Luo *et al.*, 2014; Luo *et al.*, 2010; Sun *et al.*, 2010a; Wang *et al.*, 2012; Zhou *et al.*, 2010). Broadband saturable absorption occurs in graphene, since the structure of the graphene allows frequency independent optical inter-band transitions and large absorption of incident light implying lower saturation (Bao *et al.*, 2009; Sun *et al.*, 2010a; Zhang *et al.*, 2012). Due to the its two-dimensional structure, graphene is expected to display higher damage threshold (Zhang *et al.*, 2009b). Moreover, Graphene based SA demonstrates ultrashort recovery time, and the modulation depth can be controlled (Zhang *et al.*, 2012). Regardless of all benefits, like most 2D and 3D materials, fabrication of graphene based SAs for photonic applications is found challenging. Simple method such as thermophoresis (Ahmad *et al.*, 2012; Martinez *et al.*, 2010) has managed to generate some results, however, it shows poor repeatability and consistency which stands as a barrier for practical applications. Other methods such as vapor deposition (Huang *et al.*, 2012) demonstrates substantial results and offers considerable consistency and repeatability, but the fabrication process is considered complex and fabrication cost is high. Therefore a new technique has been proposed in order to overcome the limitations, which is to incorporate new functional materials into polymers or advanced liquid crystals

(Dalton *et al.*, 1995; Hasan *et al.*, 2009b). Because of cost effectiveness and flexibility in manufacturing, new functional materials incorporating polymers/advanced liquid crystal with nanostructure such as graphene/carbon nanotubes are suitable for many kinds of applications such as integrated optical systems, miniaturised optical components and waveguides (Dalton *et al.*, 1995; Hasan *et al.*, 2009b). Many organic species and polymers can be bonded covalently onto the surface or the edge of the graphene nanostructure (Bai *et al.*, 2015). Photonics polymers (nanotubes/graphene derivatives with the polymer materials) bring a new window for light guidance and modulation due to the functionalities of the nanostructure (Hasan *et al.*, 2009b). These photonic polymers offer a new window for the development of pulsed optical devices, mainly because of their low-cost and simple fabrication procedure, as well as the reliability and consistent output they provide (Hasan *et al.*, 2009b; Ma *et al.*, 2002). Moreover, in these photonic polymers, oxide based derivatives of 2-D and 3-D materials can be dispersed homogenously within the aqueous solutions, and therefore, efficient SA can be fabricated.

(b) ***Mode-Locked Pulse Laser***

Ultrafast and ultra-short mode-locked pulses are vital elements in numerous applications such as micromachining, surgery, terahertz wave generation, optical imaging and supercontinuum generation (Sobon, 2015), in particular for communications applications in the C-band (Mahdi *et al.*, 2000). The longitudinal modes in the resonator must be synchronized in order to generate ultrafast pulses. Ultrafast mode-locked pulsed laser can be passively generated in two methods: i) by integrating a saturable absorber (SA) in the cavity, and ii) by taking the advantages of nonlinear effects occurring in the fiber (e.g. non liner polarization rotation technique, nonlinear amplification loop mirror) (Sobon, 2015). Since fine tuning of the polarization state is not required, using SA inside the cavity is believed to be a more efficient way than other techniques (Luo *et al.*, 2013). Numerous SAs have been employed for ultrafast mode-locked pulse generation, such as

Graphene (Bao *et al.*, 2011; Chang *et al.*, 2010; Hasan *et al.*, 2009a; Popa *et al.*, 2010b; Sobon *et al.*, 2012b; Sobon *et al.*, 2013; Sun *et al.*, 2010a; Wang *et al.*, 2012; Zhang *et al.*, 2009a; Zhao *et al.*, 2010), MoS_2 (Zhang *et al.*, 2014), WS_2 (Janisch *et al.*, 2014) , CNT (Hasan *et al.*, 2009a), Topological insulator (Boguslawski *et al.*, 2015) and Black phosphorus (Sotor *et al.*, 2015). Among all these SAs, graphene due to its remarkable electrical and electronic properties including outstanding nonlinear optical response (Avouris & Freitag, 2014; Bao & Loh, 2012; Bonaccorso *et al.*, 2010; Sobon, 2015) has attracted the attention of many optical researchers. There are many affirmative features of graphene, such as large Kerr nonlinearity, ultrafast carrier dynamics, easy integration with optical system, having ultrafast recovery time (200 fs), very low saturable absorption threshold, and wide operating range (due to its point band gap structure) including telecom band (Park *et al.*, 2015; Song *et al.*, 2010) . All these positive factors of graphene influence the scientists to employ it in wavelength dependent nonlinear signal generation (Hendry *et al.*, 2010) and broadband nonlinear saturable absorption for mode locking (Park *et al.*, 2015).

Bao *et al.* (Bao *et al.*, 2009) first demonstrated the mode locking fiber laser using multilayer graphene. Afterward, many works have been reported with various alike designs (Bao *et al.*, 2011; Chang *et al.*, 2010; Hasan *et al.*, 2009a; Popa *et al.*, 2010b; Sobon *et al.*, 2012b; Sobon *et al.*, 2013; Sun *et al.*, 2010a; Wang *et al.*, 2012; Zhang *et al.*, 2009a; Zhao *et al.*, 2010). Most of the SAs were fabricated using the sandwiching technique by putting either layered graphene (Bao *et al.*, 2011; Bao *et al.*, 2009; Chang *et al.*, 2010; Sobon *et al.*, 2012b; Sobon *et al.*, 2013; Zhao *et al.*, 2010) or graphene flake-polymer composite (Hasan *et al.*, 2009a; Popa *et al.*, 2010b; Sobon, 2015; Sun *et al.*, 2010a; Wang *et al.*, 2012; Zhang *et al.*, 2009a) onto the fiber ferrule inside the connectors. The very first mode-locked fiber laser employing evanescent field interactions with graphene SA (coating method) was demonstrated by Song *et al.* (Song *et al.*, 2010), where

pulse train with a repetition rate of 6.99 MHz was attained in a cavity length of 28 m. In this case (Song *et al.*, 2010), the interaction of a side polished fiber (SPF) and graphene suspension was exploited to fabricate mode-locked pulses. In another work, Nam Hun *et al.* reported an efficient mode-locked fiber laser, where the interaction of SPF and uniform monolayer graphene was used and a repetition rate of 37.72 MHz was achieved in cavity length of 5.49 m (Park *et al.*, 2015).

However, only a limited number of works have been found in the literature focused on coating method fabricated microfiber based SA device that employs the evanescent interaction of microfiber and graphene solution to generate mode-locked pulse fiber laser (He *et al.*, 2012b; Wang *et al.*, 2012; Zhu *et al.*, 2013). This limitation opens an opportunity to carry on further investigation in this field which could demonstrate substantial and valuable results. Wang *et al.* demonstrated a mode-locked pulse fiber laser utilizing the evanescent field interaction of reduced graphene oxide coated microfiber based SA device, in which a repetition rate of 3.33 MHz was measured in a cavity length of 62 m (Wang *et al.*, 2012). In the report of (Wang *et al.*, 2012), the attained pulses' 3 dB bandwidth was narrow and pulse-width was broad, which is undesirable. In a different work, a passive harmonic mode-locked (HML) pulse fiber laser was also attained using a microfiber-based graphene SA device (Zhu *et al.*, 2013), where a fundamental repetition rate of 5.46 MHz and HML operation up to the 101st were recorded in a cavity length of 38 m. It is noteworthy that also in the study of (Zhu *et al.*, 2013), the spectral bandwidth was found narrow, signifying broad pulse width. Furthermore, He *et al.* demonstrated a mode-locked pulse fiber laser using microfiber based reduced graphene coated SA device (He *et al.*, 2012b), where narrow spectral properties and wide pulse width were reported too. It can be seen that almost all the reported works based on microfiber based graphene SA have faced the issue of narrow spectral bandwidth (3 dB bandwidth). But for practical applications, pulses with broad spectral bandwidth and narrow pulse-width are preferred.

Wang *et al.* claimed the multimode interference occurring in microfiber's waist region as the cause for narrow spectral bandwidth of the pulse (Wang *et al.*, 2012). In this study, mode-locked pulses with longer spectral bandwidth and shorter pulse width are targeted, and adiabatic microfiber based SA device has been fabricated and used in to attain the desired pulses. It is described in details in Section 4.3.2.

2.5.1.2 Optical Microfiber Inline Mach-Zehnder interferometer (OMI-MZI)

Optical microfiber inline Mach-Zehnder interferometer (OMI-MZI) offers many remarkable advantages such as small size, fast response, immunity to electromagnetic environment, and durability against harsh environment (Li & Tong, 2008). Due to its compactness, simple fabrication process and response capability to wide variety of measurands; OMI-MZI device has attracted considerable attention among other promising photonic devices. All these advantages have attracted the researchers to develop OMI-MZI based sensors for various scientific and industrial applications. OMI-MZI device has been employed in a wide a range of application such as refractometer (Allsop *et al.*, 2002), refractive index sensor (Tian *et al.*, 2008a), temperature sensor (Lu *et al.*, 2009; Nguyen *et al.*, 2008), strain sensor (Liao *et al.*, 2013). Basically, in OMI-MZI device based sensor, the interference of the light is utilized for sensing purposes. In conventional way of OMI-MZI device fabrication, two microfibers are integrated by jointing them together. A relative phase difference occurs when the light passes the path between the microfibers as a result of path-length difference, and therefore, the interference is created (Jasim *et al.*, 2012). In another way of OMI-MZI fabrication, two tapered regions are created in a microfiber to fabricate the interferometer region. Due to core-cladding coupling modes in the OMI-MZI interferometer region, a relative phase difference is induced, and interference is occurred (Jasim *et al.*, 2013). In this section, the theoretical background and fabrication of OMI-MZI are described.

(a) ***Theoretical Background of OMI-MZI***

Figure 2.16 depicts the graphical representation of an OMI-MZI. When the light is inserted in the OMI-MZI, it is divided into guided and unguided mode at the first taper of the interference region. The guided mode continues travelling through the core, whereas the unguided mode passes through the cladding-air. Both core and cladding-air modes recouple at the second taper region of the interferometer, and create the interference. The working principle of OMI-MZI can be explained as the interference of dual optical beams and its intensity transmission spectrum is given as

$$I = I_1 + I_2 + 2\sqrt{I_1 I_2}\cos(\phi) \tag{2.28}$$

Where I denotes the interference signal, I_1 and I_2 refers to light intensity inside the core and cladding-air respectively; and ϕ refers to the phase difference of the core and cladding-air modes.

The phase difference ϕ can be expressed as

$$\phi = \frac{2\pi(n_{eff})L_{eff}}{\lambda} \tag{2.29}$$

Where, n_{eff} refers to the difference of the effective refractive index of the core and the m-th order cladding (n_{core}^{eff} $n_{clad,m}^{eff}$), L_{eff} refers to the effective interferometer length and λ is the input wavelength.

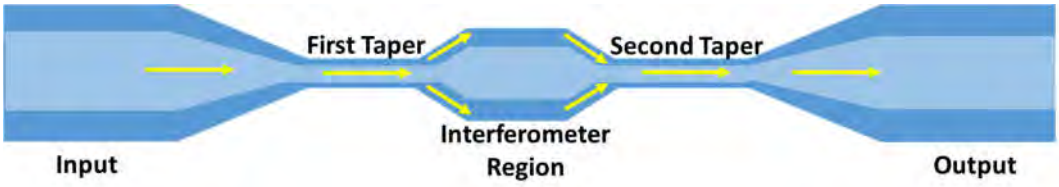

Figure 2.16: Graphical representation of an OMI-MZI.

It can be seen from Equation 2.29, the phase difference between the modes of the OMI-MZI is dependent on the variation of the effective refractive index and the effective interferometer length. Any change occurs in the effective refractive index or in the effective interferometer length, or in both the effective refractive index and the effective interferometer length, the phase difference between the modes get varied. Minimum interference (the intensity dip, $I = I_{min}$) appears, if the phase difference between the modes satisfied with the condition $\phi = (2k + 1)\pi$, where k is an integer (Liao *et al.*, 2013). By placing this condition in Equation 2.29, the k-th order attenuation peak wavelength can be expressed as,

$$\lambda_v = \frac{2(n_c{}^{eff} - n_{cl,m}{}^{eff})\, L_{eff}}{(2k+1)} \tag{2.30}$$

The effective refractive index of the cladding modes $n_{clad,m}^{eff}$ is more sensitive to the surrounding medium compared to the effective refractive index of the core mode n_{core}^{eff} (Li *et al.*, 2012; Smietana *et al.*, 2012; Yang *et al.*, 2011). It is perceived that the refractive index of the core n_{core}^{eff} hardly gets disturbed, and the refractive index of cladding modes $n_{clad,m}^{eff}$ gets highly influenced by the surrounding medium's refractive index. The relationship of $n_{cl,m}{}^{eff}$ with respect to λ_v can be described as (Jasim *et al.*, 2014):

$$\frac{d\lambda_v}{dn_{cl,m}{}^{eff}} = \frac{2\pi L_{eff}}{(2k+1)\pi} = \frac{\lambda_v}{(n_{cl,m}{}^{eff} - n_c{}^{eff})} \tag{2.31}$$

(b) ***OMI-MZI as a temperature Sensor***

This section describes how the temperature influences the transmission spectrum of the OMI-MZI. When the temperature of the surrounding medium of the OMI-MZI is increased, the effective refractive index of the cladding modes $n_{cl,m}{}^{eff}$ and the core modes $n_c{}^{eff}$ gets affected, and the interferometer length L_{eff} gets expanded (Lu *et al.*, 2009). This increment or decrement (in the refractive index and interferometer length)

occurs owing to the changes in thermo-optic coefficient and thermal expansion effects. The changes in the wavelength of the *k*-th order attenuation peak (λ_v) as a result of heat can be described as (Jasim *et al.*, 2013; Li & Ding, 2013),

$$\lambda_v = \lambda_v\left(\frac{\Delta n_{eff}}{n_{eff}} + \frac{\Delta L_{eff}}{L_{eff}}\right)_{\Delta T}$$

$$\lambda_v/_{\Delta T} = \lambda_v/_{n_{eff}}\left(\frac{\partial n_{eff}}{\partial n_{core}}\alpha_{core} + \frac{\partial n_{eff}}{\partial n_{cl}}\alpha_{cl}\right) + \lambda_v\beta_{core}\left(\frac{\partial n_{eff}}{\partial d}\frac{d}{n_{eff}} + 1\right) \quad (2.32)$$

Where, *d* refers to the diameter of the microfiber, α_{core} and α_{cl} denotes the thermo-optic coefficient of the core and the surrounding medium respectively, while β_{core} signifies the thermal expansion coefficient of the microfiber in both the radial and length.

Thus, any change in the temperature causes the λ_v to change, resulting changes in the transmission spectrum.

2.5.1.3 Optical Microfiber Knot Resonator (MKR)

Microfiber knot resonator (MKR) was the first optical microfiber based resonator to be experimentally demonstrated (Jiang *et al.*, 2006; Tong *et al.*, 2003), as stated in (Brambilla, 2010). Among the loop like shape resonators such as knot resonator, ring resonator and coil resonator, MKR offers the finest structure in terms of strength and robustness. The coupling region of the MKR is created by twisting the microfiber. Thus, it does not depend only on van der Waals attraction force to retain the coupling region, unlike ring and coil resonator. Since the coupling is stable, it offers a stable resonance condition. Moreover, the loop diameter of the MKR can be easily fine-tuned by pulling both ends of the microfiber, and it is possible to make very small diameter loop which is tough to perform in the ring and the coil resonator as loop could easily get opened.

The microfiber knot resonator (MKR) has a wide range of possible sensing applications, such as humidity (Wu *et al.*, 2011), temperature (Wu *et al.*, 2009; Zeng *et al.*, 2009), acoustic wave vibration (Sulaiman *et al.*, 2013), current (Lim *et al.*, 2011), and solution-concentration sensing (Yu *et al.*, 2014). Light travelling inside the loop of the knot resonator in an approximately circular shape creates an evanescent field at the outer surface that can be used for very effective sensing purposes. It offers many advantages (Wu *et al.*, 2011) - such as high resonance quality-factor (Q-factor), low-loss, and a faster and more reliable response, in terms of resonance wavelength shifting and transmitted output power variation. The MKR is very sensitive to the variation occurs in the fiber's refractive index (Wu *et al.*, 2011). When the refractive index in the sensing region (the tapered region of the knot) varies, it changes the resonance wavelength (Wu *et al.*, 2011) and the transmitted intensity of the light (Zhang *et al.*, 2008; Zheng *et al.*, 2013). Using this behavior many sensing application devices can be designed. In this study, the MKR device has been utilized for relative humidity measurements. The details of the work are described in Chapter 5. The following sub-section describes the theoretical background of MKR.

(a) ***Theoretical background of MKR***

Figure 2.17 displays the schematic of the microfiber knot resonator. The theory of MKR has been developed by merging the theory of ring resonator (Stokes *et al.*, 1982) and the theory of directional coupler (Schwelb, 2004; Stokes *et al.*, 1982). The Output field E_3 and E_4 are dependent on input light E_1 and are expressed as (Ren *et al.*, 2016)

$$E_3 = \frac{\sqrt{(1-r)(1-k)}}{1-j\sqrt{k(1-r)}\exp(j\beta L)} E_1 \tag{2.33}$$

$$E_4 = \frac{j\sqrt{k(1-r)}+(1-r)exp(j\beta L)}{1-j\sqrt{k(1-r)}\,exp\,(j\beta L)} E_1 = TE_1 \tag{2.34}$$

In Equation 2.33 and 2.34, r refers to the coupling loss coefficient, k is the coupling coefficient, β indicates the propagation constant, L denotes the circumference of the ring-like resonator (circular shape) and T denotes the amplitude transmission coefficient.

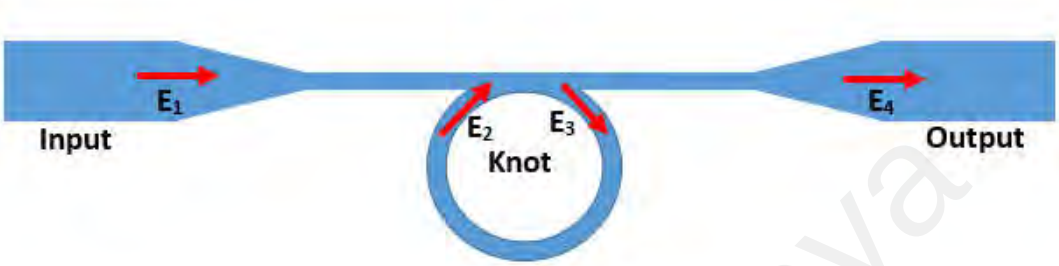

Figure 2.17: Schematic of the MKR.

The transmission of light through the MKR can be predicted by solving the coupled-mode equations. The free spectral range (FSR) can be expressed as per reference (Wu *et al.*, 2011):

$$FSR \approx \frac{\lambda^2}{N_g \pi D} \approx \frac{\lambda^2}{N_g L} \approx \frac{\lambda^2}{n_{eff} L} \tag{2.35}$$

where λ refers to the operating wavelength, N_g denotes the group index of the mode propagating in the microfiber, n_{eff} is the effective refractive index of the microfiber, and L represents the loop length of the MKR. From Equation 2.35, it can be seen that the resonance wavelength will shift if any change occurs in the refractive index or loop length. Changes in the resonance wavelength are given by (Wu *et al.*, 2011)

$$\frac{\lambda}{\lambda} = \frac{n}{n} + \frac{L}{L} \tag{2.36}$$

where n and L represent the changes of effective index and the loop length, respectively.

(b) ***MKR as Humidity Sensor***

This study focuses on the specific area of humidity sensing. Humidity is a measure of water vapor that appears in the gaseous form – in air, pure gases or gaseous mixtures. Humidity is considered a crucial factor in numerous industrial and environmental control processing conditions (Kulwicki, 1991; Traversa, 1995). From domestic use to use in various industrial sectors, humidity plays a vital role in various applications, e.g. in integrated semiconductor chip production, as well as in the agricultural, automotive, chemical and medical sectors (Chen & Lu, 2005; Wu *et al.*, 2011). The correct level of humidity is required to maintain in food processing, pharmaceutical processing, wafer processing, industrial microwave ovens, respiratory equipment, air conditioning - and many other sectors, in order to avoid defective manufacture.

Two different types of widely used humidity measurements are found in expressing the level of humidity, which are - relative humidity (RH) and absolute humidity. Relative humidity (RH) is usually expressed in terms of percentage (%) and it is a temperature dependent function. It indicates the ratio of the partial pressure of water vapor present to the saturation vapor pressure of any gas, at a stated temperature. RH is easier to understand and higher humidity range can be expressed in terms of percentage making it easier to compare (Chen & Lu, 2005). Therefore, RH expression is preferred in expressing the humidity conditions. In this study, the experimental humidity conditions are expressed in terms of RH.

Till date, a number of microfiber resonator based humidity sensors have been reported in the form of knots, rings and loops (Ahmad *et al.*, 2016a; Wang *et al.*, 2011; Wu *et al.*, 2011; Zheng *et al.*, 2013). A comparative study had been carried out by Wu *et al.* (Wu, *et al.*, 2011) where the humidity responses of silica based MKR and polymer based MKR had been observed and compared. A sensitivity of 1.2 pm/%RH was recorded over a range

from 20% to 60% RH using the silica-based MKRs, whereas a sensitivity of 8.8pm/%RH was measured over a range from 17% to 90% RH using polymer-based MKRs (Wu *et al.*, 2011). In a different work (Wang *et al.*, 2011), a wide range (5% to 71%) of relative humidity measurement had been reported employing a polyacrylamide micro-ring and a sensitivity of 490 pm/%RH was attained. Afterward, a humidity sensor based on a microfiber loop resonator (MLR) had been demonstrated by (Zheng *et al.*, 2013) where a sensitivity of 1.8 pm/%RH was reported. The authors of study (Wu *et al.*, 2011) and study (Wang *et al.*, 2011) have considered only one parameter to measure the sensitivity which is the resonance wavelength shifting. On the other hand, authors of study (Zheng *et al.*, 2013) have conducted their investigation by considering two other additional performance parameters (optical power level and extinction-ratio) besides resonance wavelength shifting.

The refractive index of a material medium is dependent on its structure and composition. According to the Lorentz-Lorenz formula, the refractive index can be illustrated by Equation 2.37, as described in reference (Wu *et al.*, 2011):

$$n = \left(\frac{3M + 8\pi N_A \gamma \rho}{3M - 4\pi N_A \gamma \rho}\right)^{\frac{1}{2}} \tag{2.37}$$

where n, M, N_A, γ, and ρ refer to the refractive index of the medium, the molecular weight of the medium, the Avogadro constant, the polarization index of the medium, and the density of the medium, respectively. All parameters are assumed to have constant values, with the exception of the medium density, ρ. If a medium gets expanded after absorption of the water molecules, it causes the values of ρ and n to decrease (Wu *et al.*, 2011). On the contrary, if the medium gets shrunk after absorption of the water molecules by filling the interstitial gaps in the medium; it causes both the values of ρ and n to increase (Wu *et al.*, 2011).

The transmission spectrum of the MKR can be forecasted by solving the coupled-mode equations. The free spectral range (FSR) can be expressed as per reference (Wu *et al.*, 2011):

$$FSR \approx \frac{\lambda^2}{N_g \pi D} \approx \frac{\lambda^2}{N_g L} \approx \frac{\lambda^2}{n_{eff} L} \tag{2.38}$$

where λ, N_g, n_{eff}, and L represent the operating wavelength, the group index of the mode propagating in the microfiber, the effective index of the microfiber, and the loop length of the MKR respectively. It can be understood from Equation (2.38) that the resonance wavelength will shift when any change occurs in the refractive index or in the loop length. Changes in the resonance wavelength are expressed by (Wu *et al.*, 2011)

$$\frac{\lambda}{\lambda} = \frac{n}{n} + \frac{L}{L} \tag{2.39}$$

where n and L represent the changes of the effective refractive index and the loop length, respectively.

In this investigation, the loop diameter of the MKR which has been employed in humidity sensing is very small (2.5 mm) and therefore it is presumed that the change of the normalized length (L/L) is much smaller than the change of the normalized index (n/n). The length of the MKR remains approximately constant, and consequently makes (L/L) negligible (Wu *et al.*, 2011). Principally, the resonance wavelength changes owing to the changes in the refractive index. The details of the study is described in Section 5.3.

2.6 Summary

A brief overview of optical microfiber is presented in this chapter. The background theory and the shape of the microfiber are described in Section 2.2. Various useful properties of the microfiber such as non-linearity, large evanescent field, mode

propagation and mechanical strength are described in Section 2.3. Thereafter, in Section 2.4, different types of top-down microfiber fabrication techniques are discussed, namely-self-modulated taper-drawing, the flame-brushing technique, the modified flame brushing technique, and direct drawing from the bulk. The application and recent progress of microfiber devices in laser and sensing applications are presented in Section 2.5, where background theory and literature review about microfiber based saturable absorber device (along with their applications in Q-Switched and Mode-Locked pulse generation), OMI-MZI device, and MKR device are described.

CHAPTER 3: MICROFIBER FABRICATION METHODOLOGY

3.1 Introduction

In this chapter, microfiber fabrication process using the flame brushing technique is presented. The fabrication of the microfiber is a vital step of the current study; since the microfiber has been fabricated initially, and lately the fabricated microfiber has been used to make microfiber based devices for various lasing and sensing applications. During the fabrication process, single mode fiber (SMF) is heated by a flame, and is pulled using a motorized stage to continuously reduce the diameter of the fiber into micrometer range. Based on the geometry, microfiber is classified into two categories, and the transmission characteristics of both the adiabatic and non-adiabatic microfiber have been described in this chapter. The last section of the chapter covers the fabrication process of various microfiber based devices that have been studied in current research, such as microfiber based saturable absorber device, Optical microfiber Mach-Zehnder interferometer (OMI-MZI) device, microfiber knot resonator (MKR) device using in-house systematic fabrication system.

3.2 Fabrication of microfiber using flame brushing technique

Flame brushing technique (Bilodeau *et al.*, 1988; Birks & Li, 1992; Brambilla, 2010; Razak *et al.*, 2015) is one of the easiest technique and commonly used for microfiber fabrication. It offers great advantages such as control of flame movement, control of fiber pulling speed and length, and control heating temperature, etc. The dimension and shape of the microfiber can be maintained with an acceptable accuracy, and it is possible to fabricate similar characteristics microfiber (reproducible). This technique allows to fabricate biconical microfiber, and both ends of the microfiber are connected with single mode fiber (SMF) which enables easy integration with the optical system. Moreover, the

experimental set-up of flame brushing technique is easily available and cheap in terms of cost. In this study, a homemade microfiber fabrication stage has been used to fabricate the microfiber. The homemade microfiber fabrication machine can fabricate low loss adiabatic tapered, and the tapered diameter can be controlled.

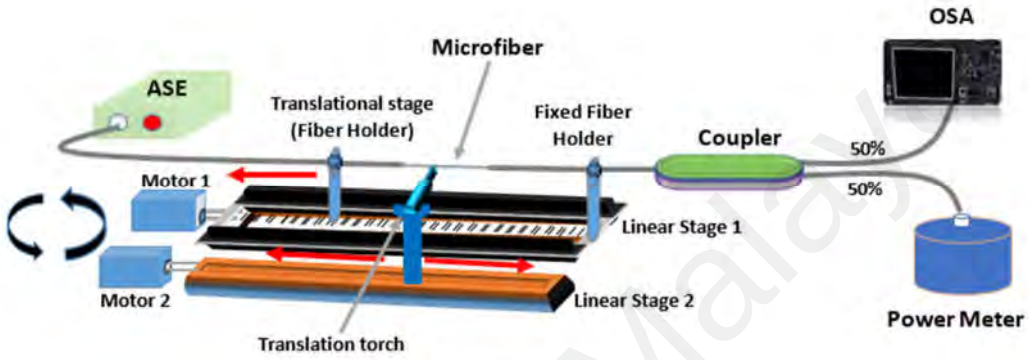

(a)

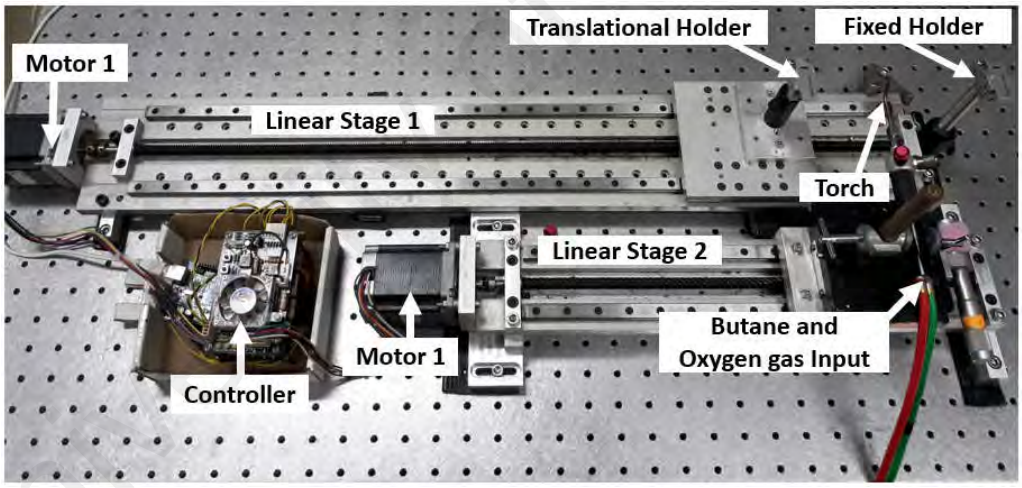

(b)

Figure 3.1: Microfiber fabrication stage: (a) Schematic Diagram, and (b) Real image.

3.2.1 Set-up and Fabrication process

Figure 3.1(a) depicts the schematic diagram and Figure 3.1(b) represents the real image of the microfiber fabrication stage. The set-up consists of two fiber holders, moveable torch (flame), two stepper motors (motor 1 and 2), two linear stages (linear stage 1 and 2) and an Arduino-based motor controller. One fiber holder is fixed, and other fiber holder

is translational which is used to pull the fiber during the tapering process. The translational holder is connected with the linear stage 1 and the stepper motor 1. The motor can be controlled to pull the fiber as per the needs. On the other hand, stepper motor 2 is connected to linear stage 2, and a torch is attached to linear stage 2.

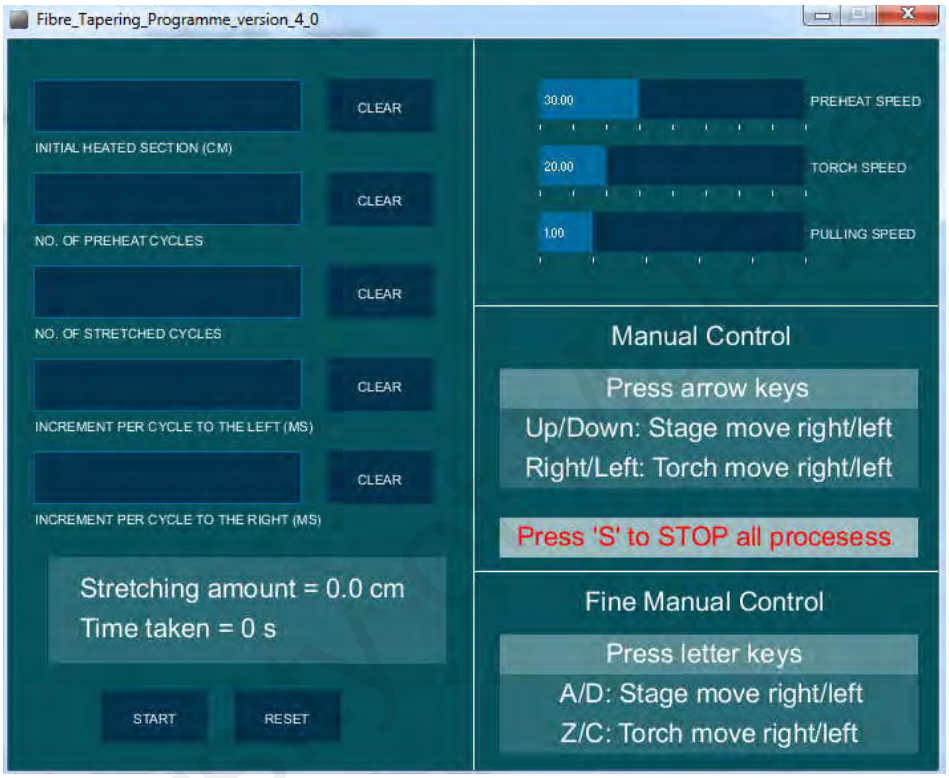

Figure 3.2: The user interface of the microfiber fabrication set-up.

The homemade microfiber fabrication stage has a user interface, where the users are required to input a few parameters, e.g., initial heated section, number of preheat cycles, number of stretched cycles, increment per cycle to the left, increment per cycle to the right, preheat speed, torch speed, and pulling speed. The user interface is displayed in Figure 3.2. Initial heated section refers to the initial length that the user wants to taper (e.g. 10 cm, 15 cm etc), and the flame brushes the desired section as per the user input. Number of preheat cycles refers to how many times the user wants the flame to brush the initial heated section (e.g. 20 times, 30 times etc). Number of stretched cycles belongs to

how many times the user wants the motor to stretches the fiber (e.g. 120 cycles, 150 cycles etc). Moreover, the interface shows the stretching amount and the time required to complete the process, based on the calculation of the input parameters. It is worthy to mention that the diameter of the microfiber (before fabrication) is predicted using volume conservation law (Taper simulator software is used), and later, the diameter is validated by microscopic image. The interface of the microfiber diameter estimation tool is shown in Figure 3.3.

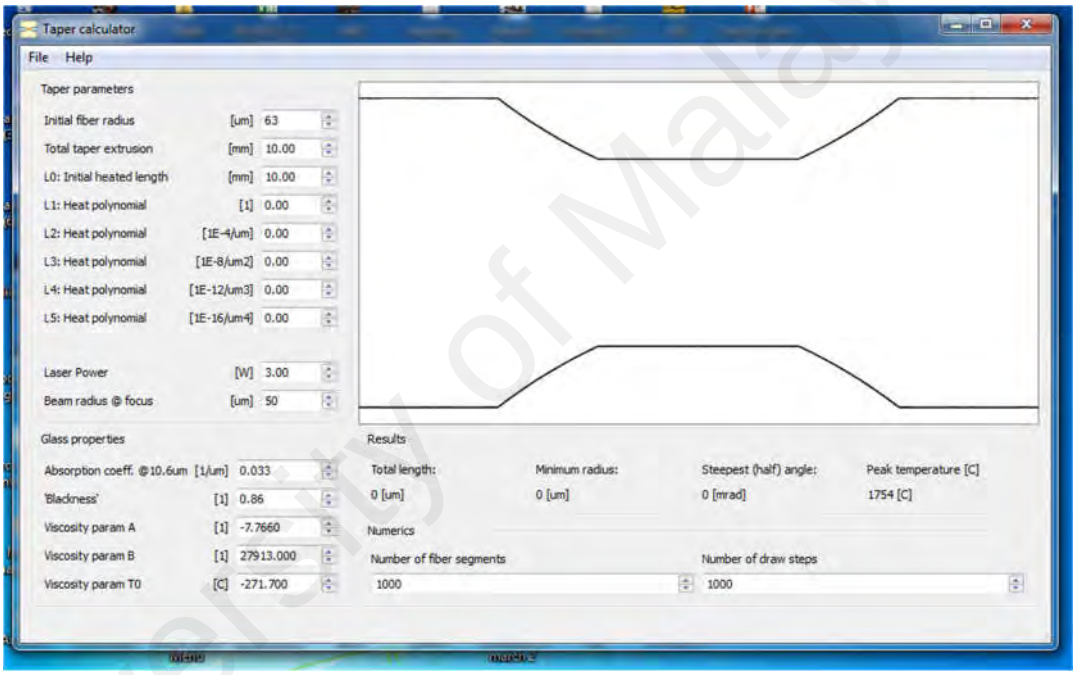

Figure 3.3: Interface of microfiber diameter estimation tool.

The motors that are connected to the linear stages, have a resolution of 1.8°/step. The travel range of the linear stage is 30 cm so that longer taper can be produced. The linear stage that pulls the fiber has a relatively low velocity compared to the linear stage that carries the flame. The fiber pulling stage moves slowly, so that smooth and low loss microfiber can be fabricated. On the other hand, the linear stage carrying the flame runs at higher speed since it has to provide uniform heat in the tapering region to fabricate high quality tapering. The designed program allows the user to select the pulling speed of the

translational stage on a scale of '1' to '5' referring to the minimum speed of '0.02 mm/s' to the maximum speed of '0.083 mm/s' respectively. On the other hand, the user can select the speed of the heating torch on a scale of '10' to '80' referring to the speed of '0.64 mm/s' (minimum) and '4.8 mm/s' (maximum) respectively. The speed of the translational pulling stage and torch speed should be optimized in order to fabricate low-loss high quality microfiber. If the flame mounted stage runs back and forth too fast, it might cause vibration in the stage and distort the microfiber structure. All the parameters especially the speed of the stage that carries the torch (preheat speed and normal heating speed), and the speed of the stage that pulls the fiber have been optimized to fabricate good quality microfiber. In this study, a moderate speed of '1.22'-'1.74' mm/s (referring to the scale of '20' and '30') has been used in the stage that carries the torch (linear stage 2). On the other hand, a linear speed of '0.028'-'0.045' mm/s (referring to the scale of '1' and '2') has been used in the translational stage that pulls the fiber (linear stage 1). In case of preheat cycle, the speed of the linear stage carrying torch has been set at 1.74 mm/s (referring to the scale of '30'). It is worthy to mention that the selected speed rate of the fiber pulling stage and the speed rate of the torch stage in the preheat cycle and pulling cycle are realized by trial and error basis. Fiber tapering process has been carried on multiple times using various combination of speed for both stages, and the mentioned speed ranges are found optimum to fabricate symmetric shaped low loss microfiber.

The flame of the torch is produced by burning a mixture of butane and oxygen gas which are separately taken from 2 different inlets, butane and oxygen cylinders. The pressure of both cylinders is maintained at ~5 psi in order to maintain adequately strong gas flow at the torch input. Both the Butane gas and Oxygen gas have been mixed in the torch chamber, and the mixed gas is supplied to ~1mm sized pin-point flame through a single orifice at the torch tip. The diameter of the tip torch also influences the flame. Stable flame can be achieved with less gas pressure by using smaller diameter torch tip.

In this study, a 0.2 mm core diameter torch tip has been used which is suitable for fiber tapering. The pressure of the gas mixture is controlled by adjusting the gauge valves to achieve a stable flame. The temperature of the flame is closely related to flame pressure. Usually the tapering rig employs around 1400-1700 °C temperature, which is close to the melting point of the silica. However, the silica fiber gets soft at 1100-1200 °C temperature, which is good enough to pull the fiber by stretching (Ding *et al.*, 2010). The flame temperature can be controlled by controlling the pressure of the oxygen gas that is supplied to the torch. It is worthy to mention that high pressure flame could bend the fiber and can cause additional insertion loss. Moreover, the fiber might break due to huge gas pressure and fast convection air flow. Thus, the pressure of the oxygen gas should be optimized and convection air flow from the flame should be maintained at a low level.

Before the fabrication process begins, the coating is stripped out from the SMF (as per desired length) and is cleaned using isopropyl alcohol. The SMF is then placed in the homemade linear fabrication stage. An amplified spontaneous emission (ASE) source is used as the feed during the tapering process - and the transmitted power output is divided equally using a 50:50 fiber-coupler. One of the output ports of the coupler is attached to an optical power meter (OPM) and the other port is attached to an optical spectrum analyser (OSA). The ASE source is used to characterize the filtering and transmission characteristics of the fabricated microfiber. The ASE source is launched into the fiber before, during and after the tapering process. The output spectrum of the ASE varies depending on the shape of the microfiber, since the shape of the microfiber affects the light propagation by modulating the light. The characteristics of the microfiber can be understood by monitoring the output ASE spectrum before and after the tapering. On the other hand, the OPM is used to measure insertion loss due to tapering. OPM logs the average output power before the tapering, during the tapering and after the tapering. However, the output spectrum of the microfiber fluctuates during the tapering process,

since the heating and pulling causes oscillation in the tapered region affecting the mode propagation of the light. Therefore the average output power also fluctuates during the fabrication process. Figure 3.4 shows the average transmitted output power data recorded through the OPM during the fabrication of a 2.1 μm diameter microfiber. The time spend refers to the time spend (in second) after the microfiber fabrication process has been initiated. It can be seen that the output power of the microfiber fluctuates during the fabrication and becomes stable at the once the process is completed.

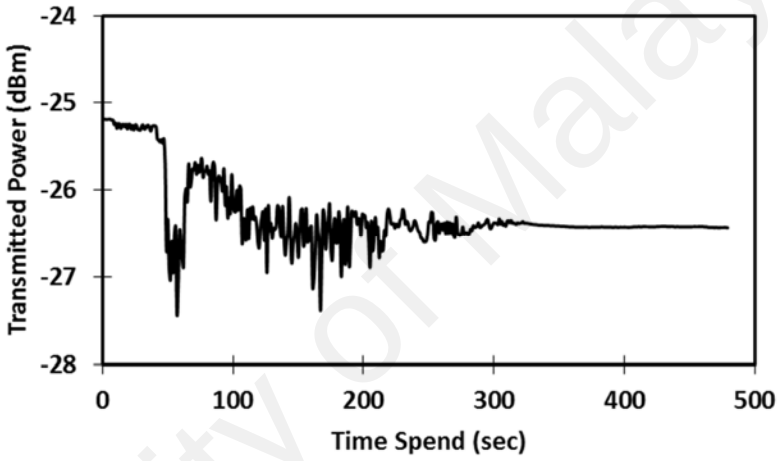

Figure 3.4: Transmitted power data measured using an OPM during the tapering process.

Primarily, the structure of the microfiber can be categorized into stripped untapered fiber region, transition regions and waist region, as described in Chapter 2. Figure 3.5 displays different parts of a fabricated microfiber, which are - the SMF upon the coating has been removed (stripped untapered fiber), part of the transition region, and the waist region.

Figure 3.5: View of the fabricated microfiber (i) stripped untapered fiber, (ii) part of the transition region, and (iii) waist region.

The microfiber based devices are highly dependent on the types, shape, and quality of the microfiber. Depending on the filtering effect and insertion loss, the microfiber can be categorized into two categories: adiabatic microfiber and non-adiabatic microfiber. Adiabatic microfiber usually has low insertion loss, and non-adiabatic microfiber has a bit higher insertion loss due to tapering process. In adiabatic microfiber, most of the power remains in the fundamental modes and doesn't couple to higher order modes when the light propagates through the microfiber. Thus, it gives minimal tapering loss. On the other hand, in non-adiabatic tapered fiber, the fundamental mode couples to the higher order mode and it gives higher insertion loss. This has been illustrated in detail in the following section.

3.3 Geometry of the Microfiber

The geometry of the microfiber plays a significant role in the transmission and filtering characteristics of the microfiber, especially the transition region vitally contributes to the mode propagation. If the diameter reduction rate is not sufficiently small, and there is an abrupt change in the tapering angle and slope, it causes mode interference between fundamental mode and higher order modes. Besides, the insertion loss is also affected by the geometry of the microfiber. In this section, both the adiabatic and the non-adiabatic types of microfiber are described.

3.3.1 Adiabatic Microfiber

Adiabaticity is one of the most desired criteria in quality microfiber fabrication. Typically in adiabatic microfiber, the fundamental mode remains the most dominating mode, and it doesn't couple to higher order modes. The shape and the length of the microfiber plays an important role in this circumstance. The local length of the microfiber has to be designed as much larger than the coupling length between two modes. In other words, it can be said that, the relative local change of the tapered radius has to be necessarily small (Lacroix *et al.*, 1988), so that the power exchange between fundamental mode and closest higher order modes can be prevented (Lim *et al.*, 2012).

Certain criterion have to be fulfilled in order fabricate an adiabatic microfiber. Birks and Li have developed (Birks & Li, 1992) the mathematical formulation about the adiabatic criterion of the microfiber. The shape of the optimal adiabatic microfiber can be calculated from Equation 2.3 and 2.4 (Section 2.2).

$$\left|\frac{dr}{dz}\right| \leq \frac{r(\beta_1 - \beta_2)}{2\pi} \tag{3.1}$$

Where β_1 and β_2 refers to the local propagation constant of the fundamental mode (LP_{01}) and the second local mode (LP_{02}) respectively. It is worthy to mention that the second local mode is most likely to be lost.

A factor (f) is introduced in Equation (3.1) to balance between taper length and diameter reduction rate to make microfiber eligible to be used in practical implementation.

$$\frac{dr}{dz} = \frac{f\, r\, [\beta_1(r) - \beta_2(r)]}{2\pi} \tag{3.2}$$

The value of f varies between 0 to 1.The local waveguide at any point along z is dependent on the cladding radius r. And the values of β_1 and β_2 are calculated

numerically as a function of r. The optimal profile can be attained using $f = 1$. When $f = 0.5$ is used, the length of the transition region gets doubled.

If the diameter reduction rate of the tapered fiber can be maintained sufficiently small, adiabatic characteristics can be achieved, which means the tapered fiber has to be sufficiently long to minimize the mode coupling. Two transition regions of the tapered fiber should be equal conical shape. Moreover, the surface roughness needed to be maintained at a low level, and any bending should be avoided. Any bending occurs in the transition region can cause interference between light modes and induce insertion loss, which could break the adiabaticity of the microfiber.

Figure 3.6(a) and Figure 3.6(b) shows the transmitted spectra of the microfiber measured using the OSA, before and after the tapering process, for the microfiber of waist diameter of 2.1 μm and 11 μm, respectively. The shape of the adiabatic microfiber is shown in Figure 3.7, where Figure 3.7(a) and Figure 3.7(b) shows the real images of the microfiber of waist region of 2.1 μm and 11 μm, respectively. However, to achieve a perfect adiabatic microfiber, one needs to be familiar with the fabrication technique. Many parameters should be optimized such as the distance of the flame from the fiber, initial heating region, pulling speed, no of heating cycle. It is worth to mention that adiabatic microfiber fabrication needed to be achieved in trial and error basis. Not every microfiber will be adiabatic.

In this study, adiabatic microfiber has been used in the fabrication of microfiber based saturable absorber devices in the application of pulse fiber laser. The details of the work are described in Chapter 4.

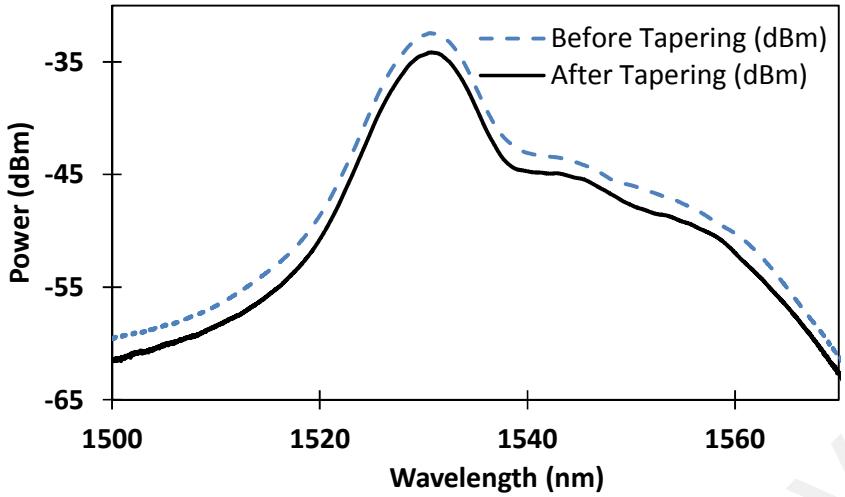

(a)

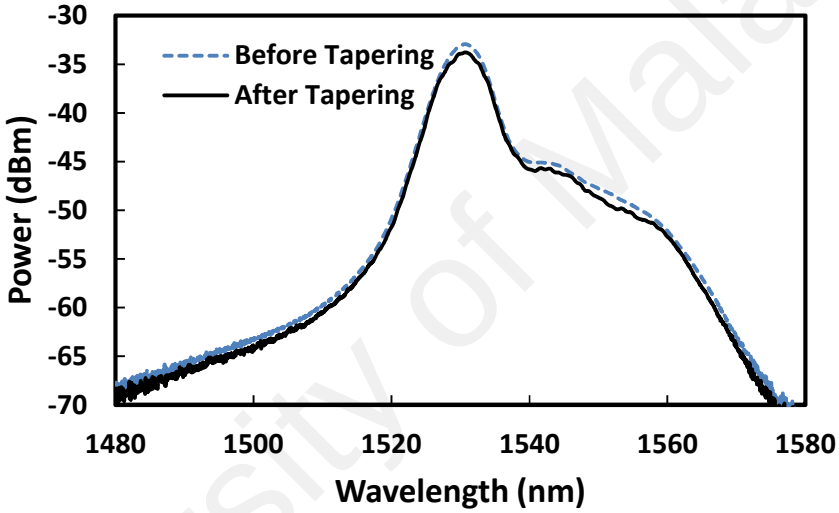

(b)

Figure 3.6: Characterization of adiabatic microfiber using an ASE source. Measured output spectrum before tapering and after tapering: (a) For a microfiber of waist diameter of 2.1 µm, and (b) For a microfiber of waist diameter of 11 µm.

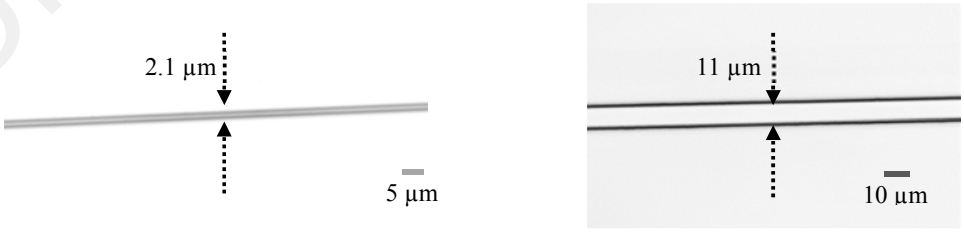

(a) (b)

Figure 3.7: Waist region of an adiabatic microfiber. (a) 2.1 µm, and (b) 11 µm.

3.3.2 Non-adiabatic microfiber

If there is any sudden change in the tapered region in terms of tapering angle and slope, it can be called as abrupt (non-adiabatic) microfiber. If fabricated microfiber doesn't satisfy the conditions of adiabatic microfiber, it is called as non-adiabatic microfiber. In this case, the fundamental modes couples with higher order modes and creates interference.

The interference occurs when the fundamental mode conjoins with some part of power from the higher order modes that survive in propagating through the tapered region. Basically, the interference is created by the coupling of the fundamental mode HE_{11} and nearest higher order mode HE_{12}, and irregular fringes are formed in the transmission spectrum as can be seen in Figure 3.8(a). The transmission spectrum is achieved through a 10 µm waist diameter non-adiabatic microfiber. The microscopic image of the waist region is shown in Figure 3.8(b).

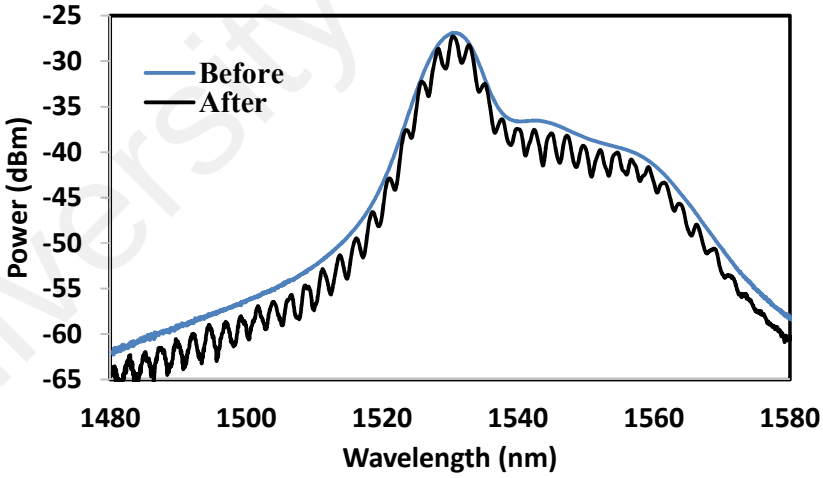

(a)

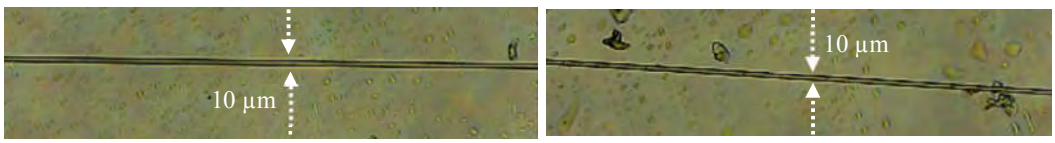

(b)

Figure 3.8: (a) ASE transmission spectrum of a non-adiabatic microfiber (before tapering and after tapering), and (b) Image of the non-adiabatic microfiber of waist region of 10 µm.

The non-adiabatic microfiber works as a modal interferometer and its transmission spectrum is given as

$$I = I_1 + I_2 + 2\sqrt{I_1 I_2}\cos(\phi) \tag{3.3}$$

Where I denotes the interference signal, I_1 and I_2 refers to light intensity inside the core and cladding respectively; and ϕ refers to the phase difference of the core and cladding.

The phase difference ϕ can be expressed as

$$\phi = \frac{2\pi(n_{eff})L}{\lambda} \tag{3.4}$$

where n_{eff} refers to the difference of the effective refractive index of the core and the cladding (n_{core}^{eff} n_{clad}^{eff}), L refers to interaction length and λ is the input wavelength.

The fringe spacing between two peaks of the interference can be presented as

$$\lambda = \frac{\lambda_0^2}{n_{eff}L} \tag{3.5}$$

Many microfiber devices can be designed using non-adiabatic interferometric device. In this study, a non-adiabatic microfiber interferometer device has been used to generate stable and tunable dual wavelength. The details of the work are described in Chapter 4.

3.4 Fabrication of microfiber based devices

Microfiber based device is an optical device which is fabricated using optical microfiber. In this thesis, microfiber based device refers to all the devices associated with microfiber. From microfiber based saturable absorber device to microfiber based sensor, everything can be called as microfiber based device provided that microfiber has been used in the experimental approach/design. Many photonic devices can be fabricated from microfibers which are conventionally fabricated lithographic planar waveguide (Lim *et al.*, 2012). Microfiber based devices are potential to be used in many applications in optical communications, lasers and sensors (Lim *et al.*, 2011). In this study, microfiber based saturable absorber device, microfiber based mach-zehnder interferometer device and microfiber knot resonator device has been utilized in various laser and sensor applications. The fabrication and characterization of microfiber based saturable absorber device, microfiber based Mach-Zehnder interferometer device and microfiber knot resonator device are described in Subsection 3.4.1, 3.4.2, and 3.4.3, respectively.

3.4.1 Fabrication of SA device and deposition mechanism

First of all, a microfiber of 11 μm waist diameter has been fabricated using the flame brushing technique following the technique as described in Section 3.2. The diameter of the microfiber is chosen based on the previous work (Liu *et al.*, 2014), in order to confirm sufficient evanescent field and satisfactory tapering strength (durability). Less than 2.5 dB insertion loss is recorded (in the 1.5 micron region) due to the tapering process. After fabrication, the microfiber is kept intact in between the holders of fabrication stage. Commercially available liquid Graphene Oxide has been obtained. The graphene oxide (GO) solution is dropped on a low indexed glass slide, and the glass slide is positioned on the top of a 2 dimensional (Y-Z) translational stage which can be moved in Y axis and Z axis. By adjusting and fine-tuning the axis micrometer of the translation stage, it is possible to reach microfiber's height as depicted in Figure 3.9. The glass slide is mounted

up to microfiber's height by adjusting the 2-dimensional translational stage to ensure that the waist diameter of the microfiber immersed entirely in the drop of the GO solution.

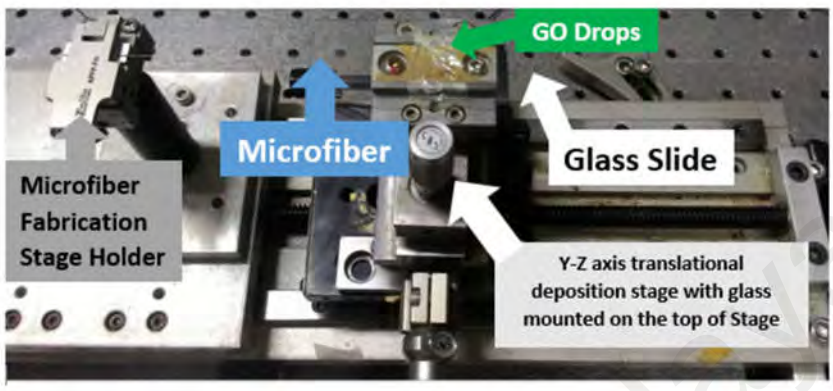

Figure 3.9: Microfiber immersed in GO (on glass slide).

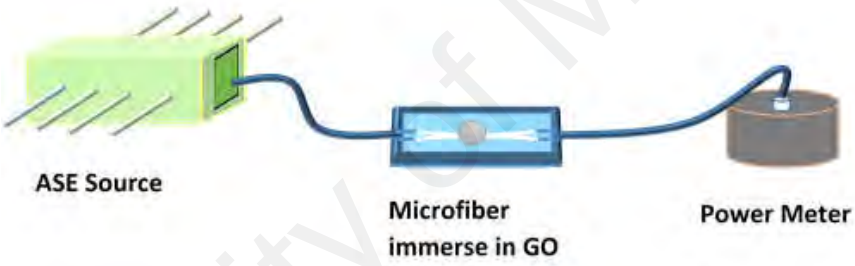

Figure 3.10: Schematic illustration of experimental set-up for graphene deposition.

The experimental set-up of the deposition is displayed in Figure 3.10. An amplified spontaneous emission (ASE) source with an output power of 13 dB is launched through the fabricated microfiber. When the ASE source is turned on, a strong evanescent field is created around the waist region of the microfiber which attracts the nano-sized particles of the GO and eventually a thin layer of GO is created surrounding the microfiber. Using an optical power meter (OPM), the deposition process has been monitored, in which the transmitted output power is logged during the time of deposition. The initially transmitted ASE power starts to decrease (transmission loss started to increase) after ASE source is turned on which indicating that the deposition process has been started and the GO nano-

particles are being attached to the microfiber. The decrease of the output power occurs because of the scattering and absorption induced by GO, analogous to the previously reported carbon nano-tube (CNT) deposition (Kashiwagi & Yamashita, 2009). It is worthy to mention that, the deposition time, amount of deposition, and deposition loss are closely related. The deposition loss can be seen as an indicator of materials deposition on the microfiber, whether the deposited material is sufficient enough or not to cause the saturable absorption to occur. High insertion loss due to deposition affects the efficiency of the laser cavity and decreases the pulse energy. On the other hand, very low insertion loss due to deposition indicates that only little amount of materials has been deposited on the microfiber which might not be enough to let the saturable absorption to occur. It is figured out from several experiments that around 6 dB loss in the deposition process ensures sufficient deposition of GO in the microfiber and can induce sufficient satuarble absorption to produce pulses. Several experiments have been conducted in the same cavity, and the laser efficiency and pulse energy are found to be decreased when the insertion loss due to deposition is measured more than 6 dB. In this study, deposition process is stopped after 15 minutes figuring out that the insertion loss of 6 dB due of the deposition process. The deposition is further confirmed by placing the microfiber based saturable absorber device under the microscope. A length of approximately 40 μm has been deposited as depicted in Figure 3.12. The possible mechanism behind the deposition can be explained by the swirl and convection caused by light injection and optical tweezer effect (Kashiwagi & Yamashita, 2009). Figure 3.11(a) and Figure 3.11(b) represent the possible mechanism of GO deposition, both schematically and experimentally, respectively. This phenomena has been presumed and is described according to the work of Ken Kashiwagi and Shinji Yamashita (Kashiwagi & Yamashita, 2009) who demonstrated the deposition of carbon nanotube (CNT) around the microfiber utilizing optical deposition technique. In this case (GO deposition onto the microfiber), when the

light is inserted from the air to the GO drop, swirl and convection effect occurred at the boundary of the microfiber. As a result, the GO nanoparticles get deposited around the microfiber. Using this phenomenon, area-selective deposition on the desire place is possible. One of the advantages of this deposition phenomenon is that it only takes place on the input boundary so that deposition can be done on the desired location conveniently. Besides, swirl and convection effect, another probable mechanism of optical deposition is optical tweezer effect. Using optical tweezer effect, micro and nano-sized objects can be trapped utilizing the optical intensity variation in the solution. The nano-sized particles of the solution can be seen as a point dipole. In electromagnetic field, the Lorentz force is employed onto the particle. In the case of optical power variance and heterogeneous electromagnetic field, the Lorentz force is stronger toward the direction of higher optical intensity compared to the lower optical intensity variation. Thus, the nanoparticles are tended to be trapped the most at the position where the Lorentz force is found maximum. The evanescent field of the microfiber has optical intensity variation, and there is a mode mismatch between the air-section and GO-section through which optical intensity variation can be generated by scattering. This variation might trap the GO nano-particles to be deposited onto the microfiber. However, optical tweezer force might not be able to trap bundled or entangled GO particles because evanescent field's optical intensity gradient is not steep. Thus, the deposition process is seen as a combination of dual mechanism (convection and swirl effect, and optical tweezer effect), where the swirl and the convection have carried the GO nanoparticles to the microfiber, and subsequently some part of the GO nanoparticles which are closely flowed to the microfiber due to swirl and convection effect are trapped through the optical tweezer effect (Kashiwagi & Yamashita, 2009).

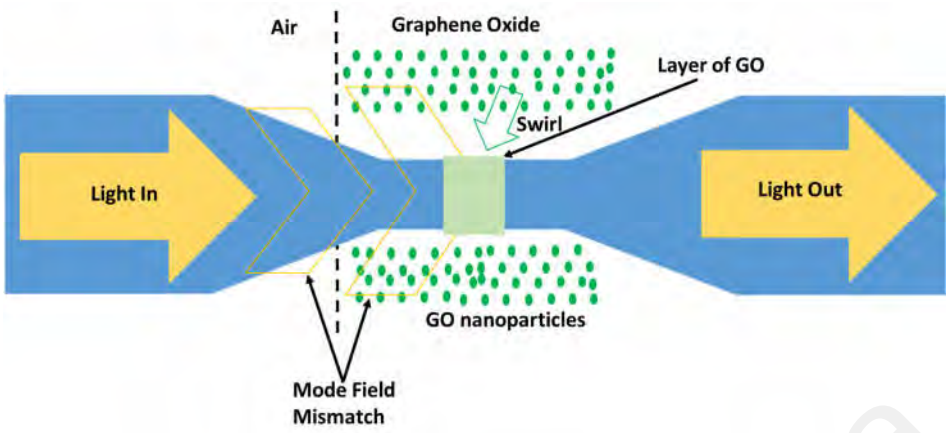

(a)

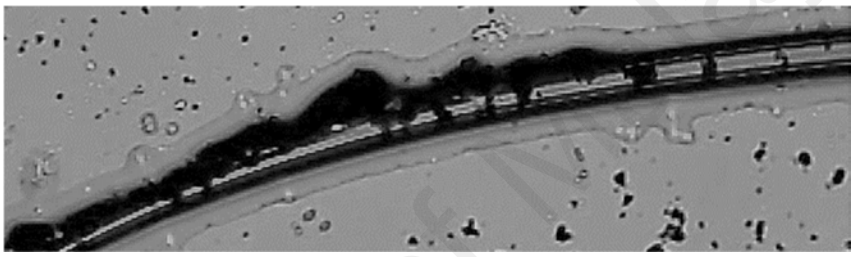

(b)

Figure 3.11: Optical deposition of the GO onto the microfiber: (a) Graphical representation, (b) experimental photo taken during the deposition process.

Figure 3.12: Optical microscopic image of graphene coated microfiber.

3.4.1.1 Characterization

Before the GO solution has been deposited in the microfiber, Raman spectroscopy was performed in order to characterize the GO sample. The Raman spectrum of the GO is presented in Figure 3.13. Three main peaks are detected from the characteristic curve. The peak D appears at 1353 cm^{-1} due to stretching of C-C bond from the doubly resonant disorder-induced mode. The G peak, a doubly degenerate phonon mode due to the first

order scattering of E_{2g} phonon of sp^2 C atoms (Ferrari & Robertson, 2000) is found at the Brillouin zone center (1605 cm^{-1}); and the 2D overtone peak is identified at 2715 cm^{-1} (Calizo *et al.*, 2007; Ferrari *et al.*, 2006; Kim *et al.*, 2009; Pimenta *et al.*, 2007). The GO sample indicates significant structural disorder by showing a prominent D peak which is caused by O-incorporation. The $2D_1$ band at 2691 cm^{-1} originates from two phonon double resonance Raman process, signifying that crystalline graphite materials are highly sensitive to number of graphene layers.

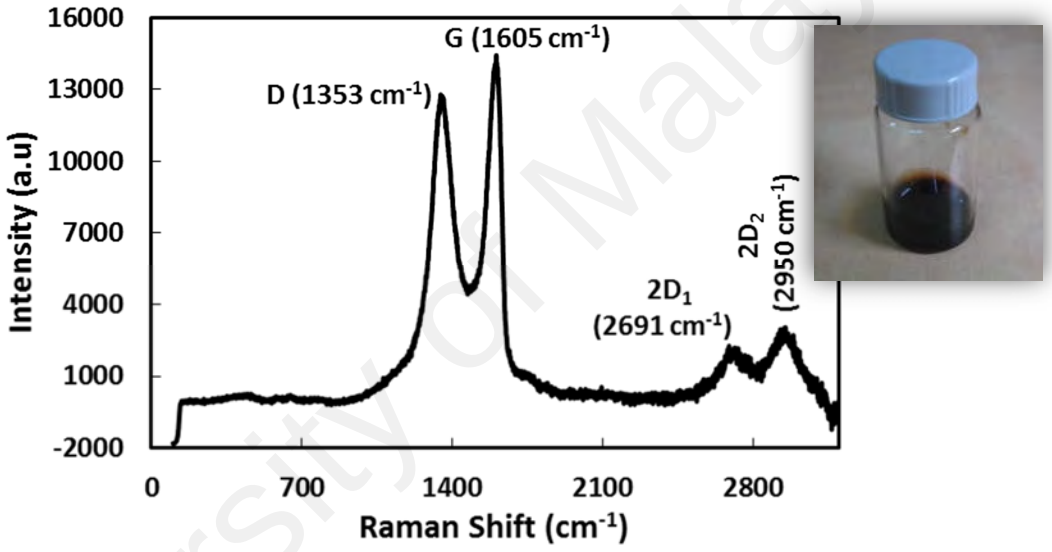

Figure 3.13: Raman spectrum of GO. Inset: A photo of GO solution used in this experiment (packaged in a glass bottle).

This study also investigates about various ways to determine the number layers of a graphene sample. One of the most popular methods to estimate the number of graphene layer is comparing the intensity of I_G and I_{2D} of the Raman Spectrum (Das *et al.*, 2008; Ferrari 2007; Graf *et al.*, 2007). The Raman spectrum is obtained for the particular material by performing Raman spectroscopy. The intensity of the peaks from the attained graph (in y-axis) are measured and compared in order to determine the number of Graphene layers. Anindya Das *et al.* have demonstrated that the number of Graphene can

be determined using the intensity ratio of G peak and 2D peak (Das *et al.*, 2008). Table 3.1 shows the estimation of graphene layers from the intensity ratio of G peak (I_G) and D peak (I_{2D}).

Table 3.1: Estimation of Graphene layer based on I_G and I_{2D}.

Ratio of the intensity G peak (I_G) and 2D peak (I_{2D})	**Estimated Number of Graphene layer**
I_G/I_{2D}=0.2	1
I_G/I_{2D}=0.4	2
I_G/I_{2D}=0.6	4
I_G/I_{2D}=1.3	23
I_G/I_{2D}=3.1	Bulk HOPG (highly oriented pyrolitic graphite)

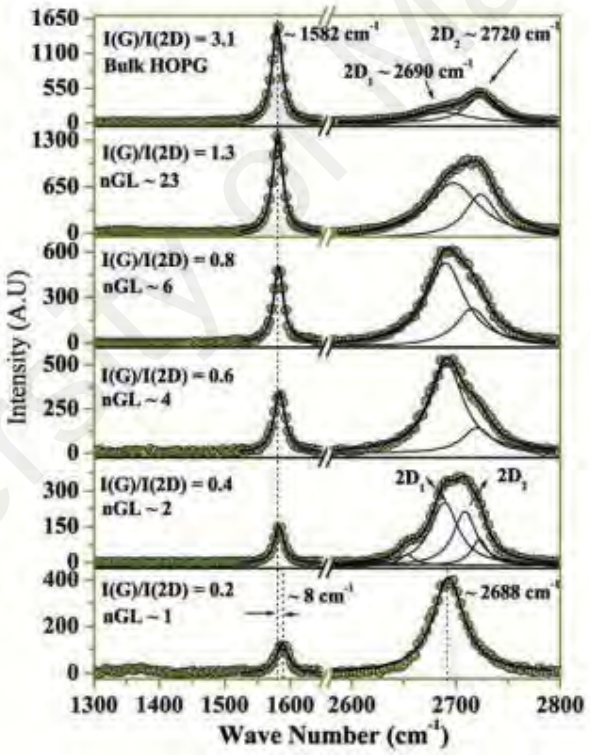

Figure 3.14: The Raman spectra of G and 2D mode for single, bi and few layers graphene (Das *et al.*, 2008). The open circles are raw data and the solid lines are the fitted Lorentzian functions. (nGL refers to the number of graphene layer).

Another interesting observation is that in bulk HOPG, $2D_1$ component is less intense than the $2D_2$ component; whereas, for the bilayer (number of graphene layer, nGL=2), both $2D_1$ peak and $2D_2$ peak have almost the same intensity; and furthermore increase in the number of layers leads to an increment of the intensity of the higher frequency, $2D_2$ component compared to the $2D_1$ component, as seen in Figure 3.14 (Das *et al.*, 2008). In bulk HOPG, there are two components of 2D mode, which are $2D_1$ and $2D_2$. The intensity ratio and the shape of the 2D mode changes substantially with the number of Graphene layers. Double resonance Raman scattering is seen as the cause for this. The electronic structure of the Graphene layers are invoked by the Double resonance scattering, and therefore, the 2D mode changes (Das *et al.*, 2008).

Similar observation has been reported by Graf *et al.* where the authors have demonstrated that the intensity of G peak increases, with the number of graphene layers (Graf *et al.*, 2007) as can be seen from Figure 3.15. A clear difference can be seen qualitatively from the Raman peak of G and D' (D' brings the similar meaning as $2D_1$), in different layers (the bulk layer to dual-layer and single layer). The intensity of G peak continuously decreases, when the number of graphene layer decreases. In single layer graphene the G peak is relatively low and D' peak is relatively high; whereas in bulk or multilayer graphene the G peak is relatively high and D' is relatively row as depicted in Figure 3.15.

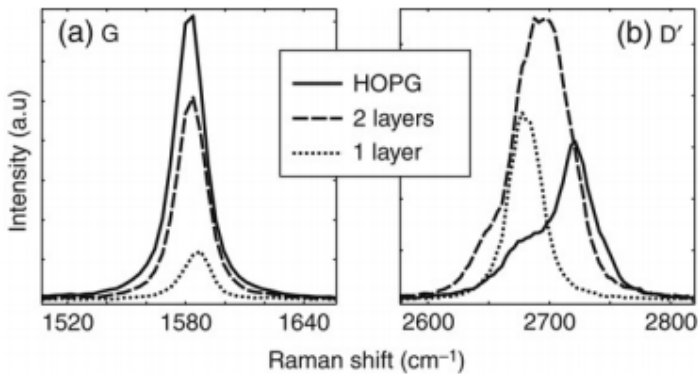

Figure 3.15: Raman spectra of the (a) G line, and (b) the D' line for HOPG (solid), double-layer (dashed) and single-layer (dotted) graphene. Peak amplitudes are scaled for clarity (Graf *et al.*, 2007).

The number of layers of the GO that has been used for coating the microfiber is calculated. In this study, the intensity of I_G and I_{2D} achieved from experimental Raman spectrum (Figure 3.13) is compared, and the ratio of I_G/I_{2D} is observed higher than 0.2, which indicates that multilayer graphene oxide has been formed in the sample (Das *et al.*, 2008; Graf *et al.*, 2007). On the other hand, $2D_1$ peak is found less intense than $2D_2$ peak, which indicates that multilayer bulk GO has been achieved (Das *et al.*, 2008). Without any further synthesis, this multilayer bulk GO has been used to coat the microfiber to fabricate microfiber based saturable absorber device. After the coating, the saturable absorption property (known as modulation depth) of the microfiber SA device has been obtained. The details of the process are described in the following section.

3.4.1.2 Modulation Depth

After the fabrication of microfiber based satuarble absorber device, its saturable absorption properties e.g. modulation depth is measured. Modulation depth is seen as an effective way to describe the saturable absorption properties of the SA. Modulation depth refers to the maximum variation in absorption (or reflectivity) that can be induced when light of a given wavelength be incident on the SA. In passively mode-locked pulse fiber lasers, modulation depth is considered an important design parameter since pulse shaping

and pulse duration is dependent on modulation depth. Strong pulse shaping can be achieved by using an SA with large modulation depth, which enables to attain short pulse duration and reliable self-starting mode-locked; however Q-switching instabilities can be occurred as well causing to the unstable pulse energy of the mode-locked laser.

A balanced twin-detector system is used to characterize the saturable absorption properties of the microfiber based saturable absorber device. The set-up of the balanced twin-detector system is depicted in Figure 3.16. An in-house made Erbium doped mode-locked fiber laser with a repetition rate of 27.76 MHz, pulse width of 0.74 ps, central wavelength of 1564.16 nm at 33 mW is used as a pulse seed. A low dispersion Erbium doped fiber amplifier (EDFA) is utilized in order to amplify the input laser. A 50 dB attenuator is utilized in the system in order to vary the input power, and the transmitted power is decreased from 50 dB to 0 dB in a step of 1 dB by adjusting the attenuator. A 50:50 coupler (3 dB coupler) is used to divide the light equally. As much as 50 percent of the light is transmitted through the microfiber based GO-SA to optical power meter 1, and other 50 percent of the light is transmitted directly to power meter 2, as reference. By gradually decreasing the attenuator, the output power with respect to the different input intensities is recorded by both power meters. The absorption of the microfiber based GO-SA device is measured by comparing the data achieved through power meter 1 and power meter 2.

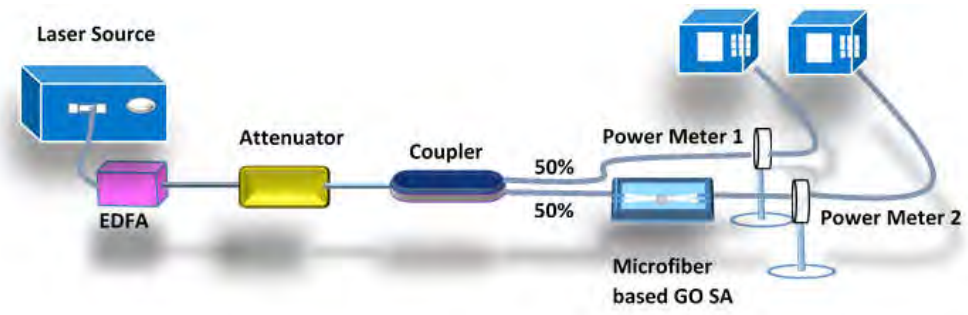

Figure 3.16: Experimental set-up for measuring saturable absorption property

The absorption as a function of increased light intensity is calculated using Equation (3.6), given by (Garmire, 2000; He *et al.*, 2012b)

$$\alpha(I) = \frac{\alpha_s}{1 + I/I_s} + \alpha_{ns} \tag{3.6}$$

Where α_s , α_{ns} , and I_s denotes the saturable absorption coefficient, non-saturable absorption coefficient, and saturation intensity respectively.

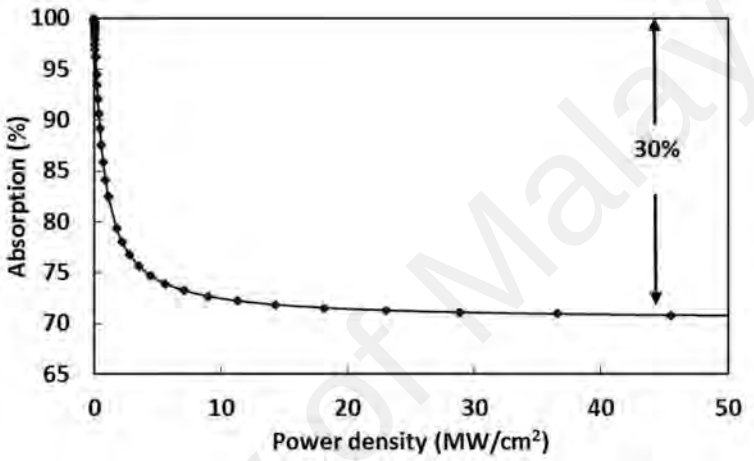

(a)

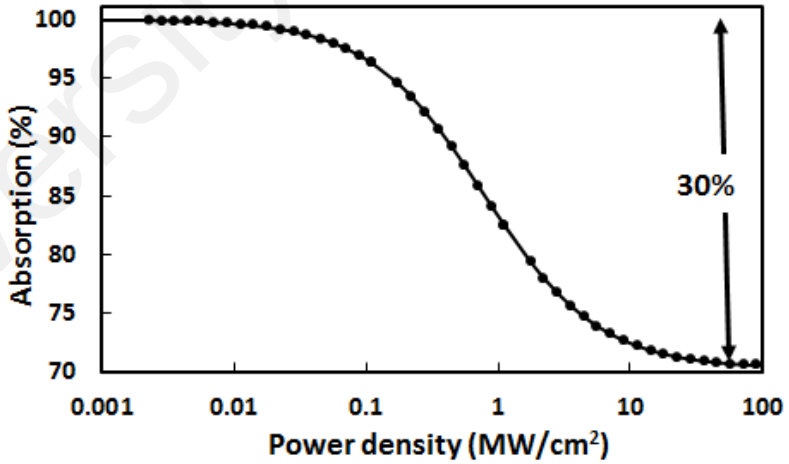

(b)

Figure 3.17: (a) Characterization of the saturable absorption property of Microfiber based GO SA device, and (b) Same graph as (a), but in this case x-axis is plotted in logarithmic scale with a base of 10 from 0.001 to 100.

The readings achieved experimentally from the power meters are plotted according to equation 3.6, and the absorption characteristics are depicted in Figure 3.17. The fabricated microfiber based-GO SA device demonstrates a saturation intensity of 0.7031 MW/cm^2 and 30% modulation depth. Meanwhile, non-saturable loss is recorded as 70%. Figure 3.17 (a) and 3.18 (b) are the same graph and are two just different ways to present saturable absorption property; (a) is plotted where x axis is linear and (b) is plotted where x axis is logarithmic scale with a base of 10 from 0.001 to 100.

3.4.2 Fabrication of OMI-MZI

A number of methods have been demonstrated to fabricate OMI-MZI such as forming abrupt taper fibers (Lu *et al.*, 2009; Tian *et al.*, 2008a), aligning core mismatch (Nguyen *et al.*, 2008), introducing micro-cavity in fiber core-cladding interface (Wang *et al.*, 2010), cascading two long-period grating (LPG), inducing two micro-bending through laser irradiation (Wei *et al.*, 2009). The authors in (Lu *et al.*, 2009; Tian *et al.*, 2008a) have made two fiber tapers in the single mode fiber using fusion splicer electric arc where a gap of few centimeter has been left as an interferometer region. Wei *et al.* (Wei *et al.*, 2009) used almost the same method as (Lu *et al.*, 2009; Tian *et al.*, 2008a) but used CO_2 laser irradiation to induce two micro-bends which enables the light to couple to lower order cladding mode from core mode and vice versa. Nguyen *et al.* demonstrated core mismatch method to fabricate OMI-MZI (Nguyen *et al.*, 2008) where multimode - single mode - multimode fiber configuration has been used to introduce interference pattern. The mode field mismatch at the single mode-multimode splicing point, and refractive index difference of the core and cladding modes in the multimode-single mode-multimode fiber structure induce the interference pattern. Wang *et al.* has designed an OMI-MZI structure where some part of the fiber in the core-cladding interface has been removed by a femtosecond laser machining (Wang *et al.*, 2010). In cascading LPG approach, the in-fiber OMI-MZI is formed using two long period gratings (LPG) with a fiber taper in

between (Ding *et al.*, 2005), as demonstrated by Ding *et al.* 2005, Fiber taper-based structured offers the advantage of simplicity and high repeatability among various types of OMI-MZI (Li *et al.*, 2011).

In this study, two fiber tapers with an in between interferometer region have been created to fabricate OMI-MZI and induce interference effect. First of all, a microfiber is fabricated from standard single mode fiber (SMF) by means of the flame brushing technique using the fabrication stage of Figure 3.1 (Section 3.2). The first taper is tapered down to a certain waist diameter (9 μm). After that, the torch is shifted to the transition region by adjusting the linear stage that carries the torch (linear stage 2), and a second taper is made (waist diameter of 15 μm). The distance between two tapers works as an interferometer region. The specification of the fabricated OMI-MZI is depicted in Figure 3.18. The total length of the OMI-MZI device is measured about 40 mm. An ASE source is used as a seed, and the transmission spectral response of the OMI-MZI is monitored through the OSA before and after the fabrication process. Figure 3.19 displays the output spectrum of the incident ASE into the IMMZI with ~4 dB of insertion loss. This loss mainly occurs because of non-uniform tapered sections.

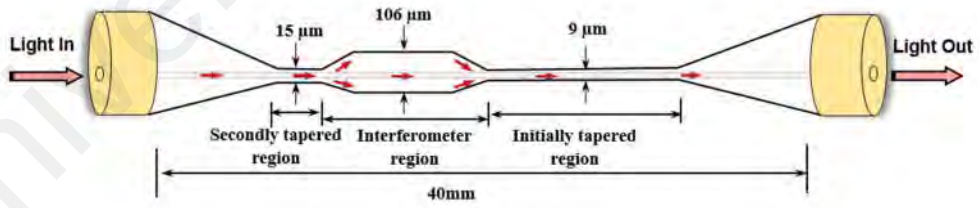

Figure 3.18: The schematic diagram of the proposed OMI-MZI.

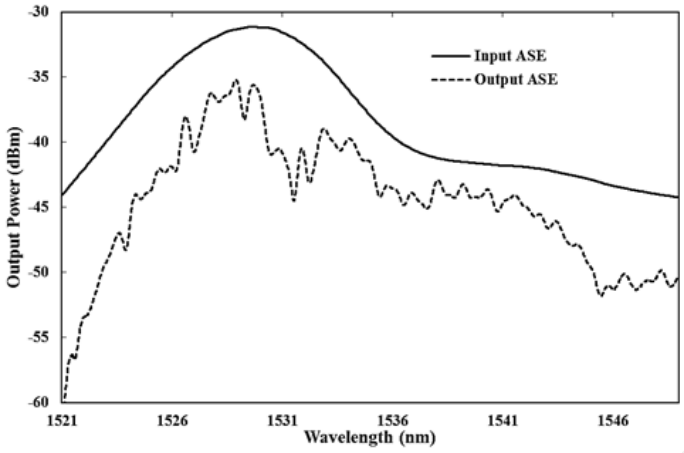

Figure 3.19: Output spectrum for the incident ASE before and after OMI-MZI fabrication.

3.4.3 Fabrication of MKR

Jiang *et al.* (Jiang *et al.*, 2006) has demonstrated the process of MKR fabrication in the year of 2006. Later in 2010, Lim *et al.*(Lim *et al.*, 2011) reported almost the similar mechanism as (Jiang *et al.*, 2006). The fabrication technique of MKR described in reference (Jiang *et al.*, 2006; Lim *et al.*, 2011) is shown in Figure 3.20. According to their technique (thereafter, will be called as method 1 of MKR fabrication), a long and uniform microfiber is first fabricated from the SMF using the flame brushing technique. Then, the microfiber is divided into 2 unequal parts. The long part is used to assemble the knot. By micro-manipulating the longer part of the microfiber, the knot is assembled. Initially, a relatively larger loop (about few millimeters in diameter, with the help of a Tweezer) has been fabricated by twisting the fiber and the loop has been tightened later. Later on, short part of the microfiber is coupled with the knot output through the use of evanescent coupling. The short part is used to collect the transmitted light coming out of the knot. However, it is worthy to mention that this method suffers from high insertion loss due to coupling.

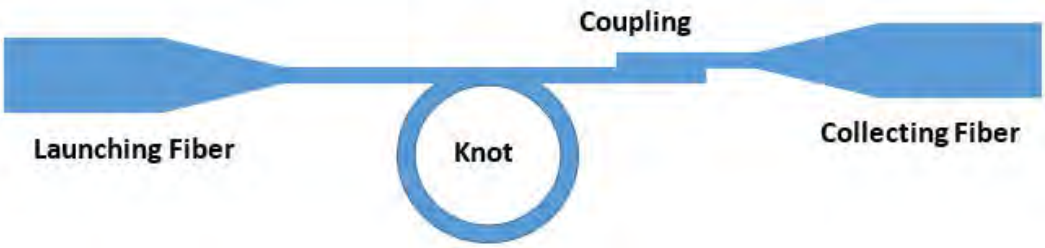

Figure 3.20: Fabrication of MKR using method 1.

Since the previously mentioned method to fabricate MKR (method 1) involves high insertion loss, a new technique of MKR fabrication has been proposed in this study (thereafter, will be called as method 2 of MKR fabrication). In method 2, the knot is fabricated without cutting the waist region of the microfiber. Firstly, a bigger diameter knot is made by twisting the normal 125 μm diameter SMF, and the whole knot is placed in the fabrication stage. Both ends of the knot is placed in the fiber holders and part of the knot is tapered up to the desired diameter. After the microfiber fabrication, both ends of the fiber is being pulled to make a desired diameter knot. This fabrication technique doesn't involve cutting and coupling and thus, it offers a robust and strong structure. Figure 3.21 shows the schematic of the MKR fabricated using method 2.

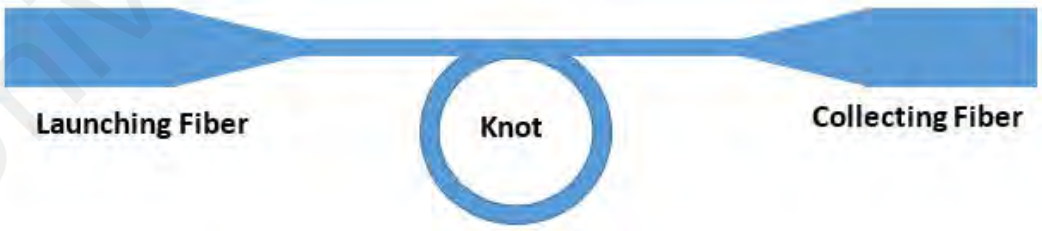

Figure 3.21: Schematic of MKR fabricated using method 2.

The diameter of the microfiber plays a crucial role in MKR fabrication. If the diameter of the microfiber is thick, it is hard to make a smaller diameter knot, and the fiber gets break easily. On the other hand, if the diameter of the microfiber is too thin, it get stucks

with itself easily, and it becomes tough to pull the fiber. A number of practical attempts have been taken in the laboratory in order to determine the optimum microfiber diameter for MKR fabrication, and the optimum diameter is found within the range of 2-3 μm. Moreover, the length of the microfiber also plays an important role in MKR fabrication. The microfiber is required to be long since it is being used to make the knot later on. The optimum length to fabricate MKR has also been estimated from several practical experiments. Typically, the total length of the microfiber should be around 8 cm with a waist length of 4 cm.

In this study, MKR has been fabricated using method 2. Initially, a microfiber of 3 μm diameter has been fabricated using the flame brushing technique and subsequently, an MKR with a loop diameter of 2.55 mm was fabricated. Figure 3.22 shows the transmission spectrum of a microfiber knot resonator fabricated with 3 μm diameter tapered fiber with a loop diameter of approximately 1.15 mm where a tunable laser source (TLS) is used as a seed.

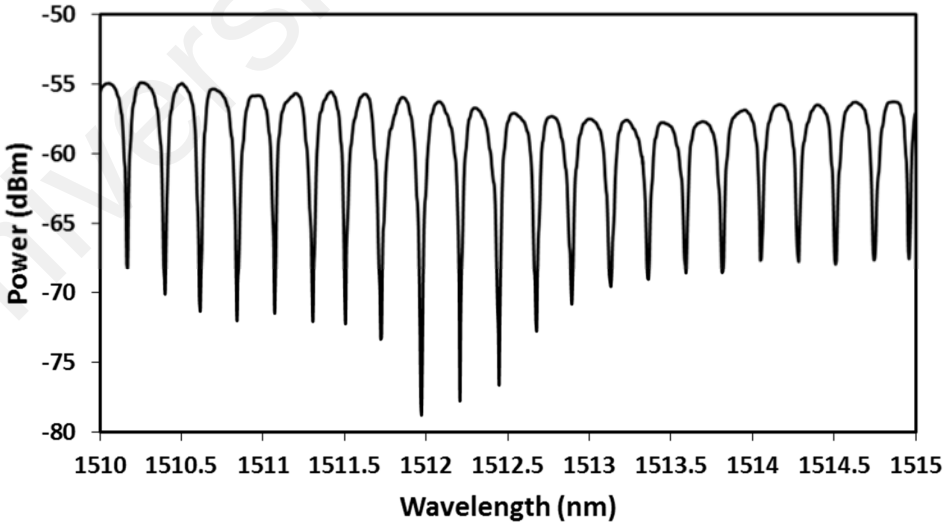

Figure 3.22: Transmission spectrum of an MKR.

3.5 Summary

In this chapter, the fabrication of microfiber and microfiber based devices is demonstrated. The fabrication set-up and process of the flame brushing technique that is used in this study to pull the fiber are illustrated in Section 3.2. The microfibers are categorized into 2 sorts, which are adiabatic microfiber and non-adiabatic microfiber; and both of the categories have been described in Section 3.3. In Section 3.4, different types of microfiber based devices, namely microfiber based SA device, OMI-MZI, and MKR are described. The fabrication of SA device, and its characterization using Raman spectroscopy, and balanced twin detector system are presented in Subsection 3.4.1. Thereafter, the fabrication process of the OMI-MZI device are described in Subsection 3.4.2. Subsequently, the fabrication process of the MKR device are presented in Subsection 3.4.3.

CHAPTER 4: MICROFIBER BASED LASER APPLICATIONS

4.1 Introduction

Laser devices have brought revolutionary changes in the technological landscape of the world in last twenty years and have extensively been utilized in various application devices such as CD players, laser pointers, computer chip etching, remote sensing, and many more (Walsh, 2010). In this chapter, the uses of the microfiber devices in various laser applications are demonstrated. The details of device fabrication and experimental set-up, and utilization of these microfiber devices in laser applications are described in the remaining part of the chapter. Both the adiabatic and the non-adiabatic microfiber devices have been fabricated and utilized in various laser applications. A non-adiabatic interferometric device has been utilized in the generation of stable and tunable dual wavelength fiber laser. It is described in Section 4.2. On the other hand, adiabatic microfibers have been used as saturable absorber devices by coating it with graphene oxide nano-materials in order to employ it in pulse fiber laser applications namely Q-switched pulse fiber laser and mode-locked fiber laser application. The Q-switched pulse fiber laser and mode-locked pulse fiber laser generation are described in Subsection 4.3.1 and Subsection 4.3.2, respectively.

4.2 Dual wavelength fiber laser (DWFL) generation

Dual wavelength fiber laser (DWFL) has grabbed significant research interest from the optical scientist due to its usage in numerous applications such as wavelength division multiplexing (WDM) (Yao *et al.*, 2006), microwave generation, high resolution spectroscopy, fiber sensing, distance measurements (Wang *et al.*, 1995), terahertz difference signal generation (Wang & Pan, 1995), frequency mixing (Pellandini *et al.*, 1997) , differential absorption lidars (DIALs) (Lidar refers to Light Detection And

Ranging) (Sharma *et al.*, 2004) and radio over fiber (ROF) (Ahmad *et al.*, 2013). DWFLs are very advantageous since it can produce perfectly synchronized two wavelength pulses using one laser (Sharma *et al.*, 2004). DWFL can be used to produce cost effective, light and compact, alignment hassle free, polarization independent, viable, highly efficient, and broadly tunable DIALs system which can be used for the purpose of gas tracing and monitoring (Sharma *et al.*, 2004). Besides, by utilizing the reaction of DWFL output with external crystal, terahertz radiation can be generated which can be used in new industrial process quality control and security monitoring (Ahmad *et al.*, 2009; Klehr *et al.*, 2008).

Till date, a limited number of works have been found in the literature focusing on the generation of dual wavelength using microfiber (Ahmad *et al.*, 2015b; Harun *et al.*, 2010; Tan *et al.*, 2013). A single longitudinal mode (SLM) dual wavelength erbium doped fiber (EDF) ring laser has been developed by Tan *et al.* (Tan *et al.*, 2013) where one superimposed fiber Bragg gratings (FBG) and a dual tapered optical microfiber inline Mach-Zehnder interferometer (OMI-MZI) have been utilized. In a different work, a dual wavelength EDF laser using a microfiber (Harun *et al.*, 2010) as a comb filter has been attained with an in-between spacing of 1.6 nm, SNR > 40 dB, operated in C-band region at 1557.0 nm and 1558.6 nm. However, the tunability of the DEFL is yet to be explored, and till date, no report has been found about the tunability of DWFL on 1.5 μm region. A dual wavelength SLM Ytterbium-doped fiber laser in 1 μm region has been reported using dual tapered optical microfiber inline Mach-Zehnder interferometer (OMI-MZI) by Ahmad *et al.* in (Ahmad *et al.*, 2015b) where the tunability of DWFL has been attained by utilizing the dual-tapered MZI and adjustment of cavity polarization state using a polarization controller (PC).

The current work is focused to develop tunable DWFL, and the work is aimed towards designing a simple but effective experimental set-up using microfiber devices. Figure 4.1

displays the experimental set-up of dual wavelength fiber laser generation using optical microfiber. A 980 nm laser diode (LD) is used as a pump with output power of 600 mW (Oclaro model LC96A74P-20R). A 980/1550 nm wavelength division multiplexing (WDM) is connected to the output of the LD. As a gain medium, a 3 m long Erbium doped fiber (EDF) is used in the cavity which is connected to the output port of the WDM. An isolator is applied in the cavity after the EDF in order to ensure unidirectional light circulation. An optical microfiber with a total length of 15 cm and a diameter of 2 µm has been inserted inside the cavity set-up. A polarization controller (PC) is included after the microfiber to regulate the polarization state of the cavity. A 95/5 coupler is coupled right after the PC, where 95% of the light keeps circulating in the cavity and the other 5% is extracted out of the cavity as the output and is monitored through an optical spectrum analyser (OSA) and an optical power meter (OPM).

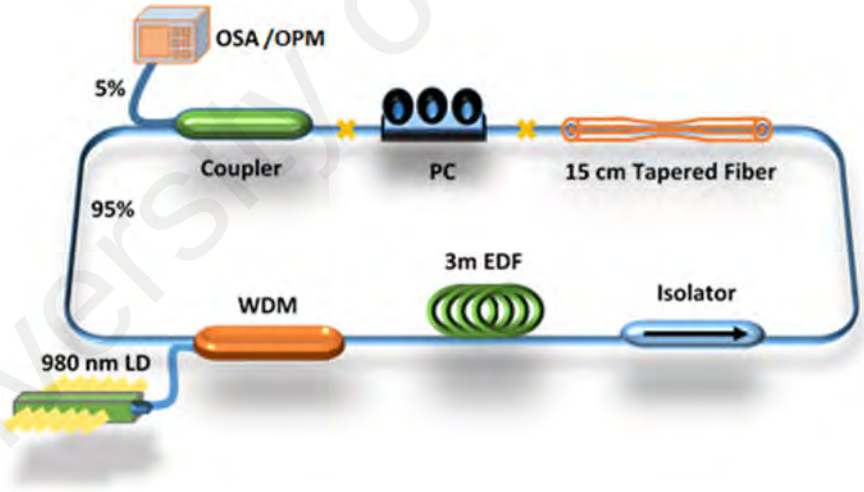

Figure 4.1: Schematic illustration of experimental setup for DWFL (with PC).

A microfiber is fabricated using the systematic flame brushing method by means of the fabrication stage. Firstly, the fiber coating of the SMF around 4 cm length is removed and is put in the fabrication stage. A microfiber of waist diameter of 2 µm and length of the 15 cm is achieved using the fabrication process described in Section 3.2. During the

fabrication process, an ASE source is used as a seed, and the transmission spectrum of the microfiber is monitored through an OSA. This study is aimed to utilize the inter-modal interference generated in the microfiber to achieve dual wavelength laser, and the inter-modal interference generated in the microfiber is monitored continuously. Many other modes get excited in the fiber besides fundamental mode, as an effect of tapering process. In the beginning, core mode or fundamental mode is the only mode propagating in the fiber and the effective refractive index of the core mode is in between the core index and cladding index (Harun *et al.*, 2010; Li & Bao, 2008). The effective refractive index of the core mode decreases continuously because the diameter of the core is being reduced during microfiber tapering process. The cladding modes are generated instead of the fundamental mode or core mode after the effective refractive index of the core mode reaches to cladding index (Harun *et al.*, 2010; Li & Bao, 2008). Due to the intermodal beating between these the cladding modes, spatial fringes can be observed in the transmission spectrum. Intermodal interference among these cladding modes generates the comb like transmission spectrum of the microfiber as can be seen in Figure 4.2. To generate interferences by exciting some higher order modes besides fundamental mode, the microfiber has to be fabricated non-adiabatically. Harun *et al.* reported that non-adiabatic microfiber with less than 5 μm diameter induces this intermodal interference (multi-beam) (Harun *et al.*, 2010). In this work, a microfiber with waist diameter of 2 μm has been fabricated to induce intermodal interference effect. However, it is worthy to mention that less than 5 μm diameter non-adiabatic microfiber can induce multi-modal and intermodal interference; and the diameter doesn't need to be exactly 2 μm. However, the diameter of the microfiber plays an important roles in attenuation or intersection loss. The attenuation rises as the diameter is reduced (Harun *et al.*, 2010; Li & Bao, 2008). In this investigation, less than 5 dB insertion loss is measured due to microfiber fabrication process. Figure 4.2 displays the transmission spectrum of the microfiber where non-

polarized ASE is used as a seed. The ASE transmission spectrum is measured before and after the fabrication of the microfiber. The blue dotted line represents the ASE spectrum of untapered normal SMF and the black line represents the ASE spectrum of microfiber. The ASE spectrum is recorded at 7 mW of input power where it is on the threshold level. A significant interference pattern is achieved. When microfiber is inserted in the designed cavity (Figure 4.1) and the loop is closed, it causes a narrow lasing on the optical spectrum. Typically, the lasing appears at a peak interference at a certain wavelength. The lasing peak can be shifted to another peak, or multiple peaks can be generated by adjusting polarization through the PC.

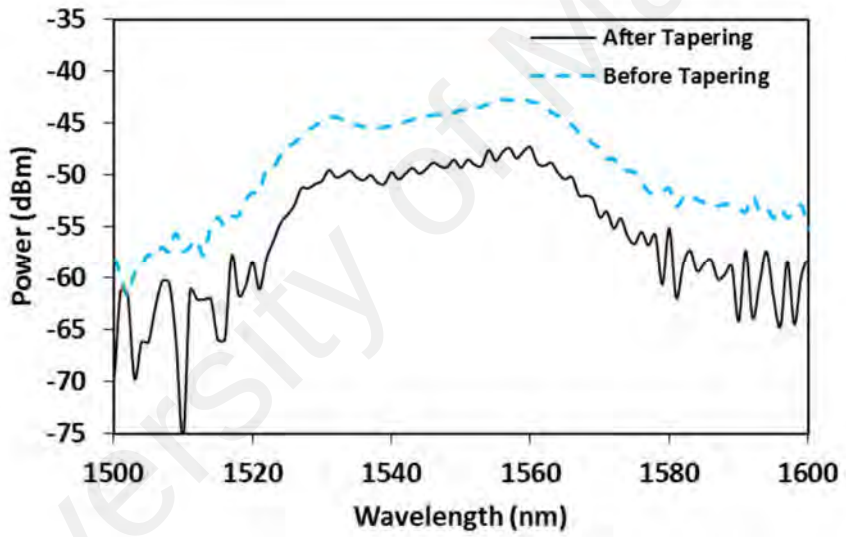

Figure 4.2: ASE spectrum of the tapered fiber (black) and non-tapered fiber (dotted).

The comb-like transmission spectrum generated by the fabricated microfiber can be explained as in (Ahmad *et al.*, 2015b). By taking the advantages of this interference pattern, the proposed cavity (Figure 4.1) can generate dual wavelength. Furthermore, the intermodal interference generated by the non-adiabatic microfiber suppresses the mode competition within the EDF, which is a result of homogenous broadening, and thus helps to stabilize the dual-wavelength (Harun *et al.*, 2010; Jasim *et al.*, 2015). The gain of the EDF medium is observed sufficient to compensate the insertion loss of the microfiber.

The EDF gain medium has amplified the propagating light inside the cavity, and a mode competition has occurred among the interference peaks of the transmission spectrum. The highest intensity peaks have demonstrated the most gain and become dominant in the loop ring (Harun *et al.*, 2010; Li & Bao, 2008). In this case, there are two peaks with almost similar intensity, and therefore, both peaks have gained higher energy from the EDF. These peaks has become dominant than others in the ring cavity, and dual wavelength has been generated.

At first, the experiment is performed without the insertion of the PC (Figure 4.1) with the aim of generating a stable dual wavelength using the interference of the microfiber. Consequently after attaining dual wavelength, the PC is included in the cavity, and dual wavelength is tuned by a unique arrangement of the PC. The output spectrum of the proposed cavity is shown in Figure 4.3 (without PC) and Figure 4.4 (with PC).

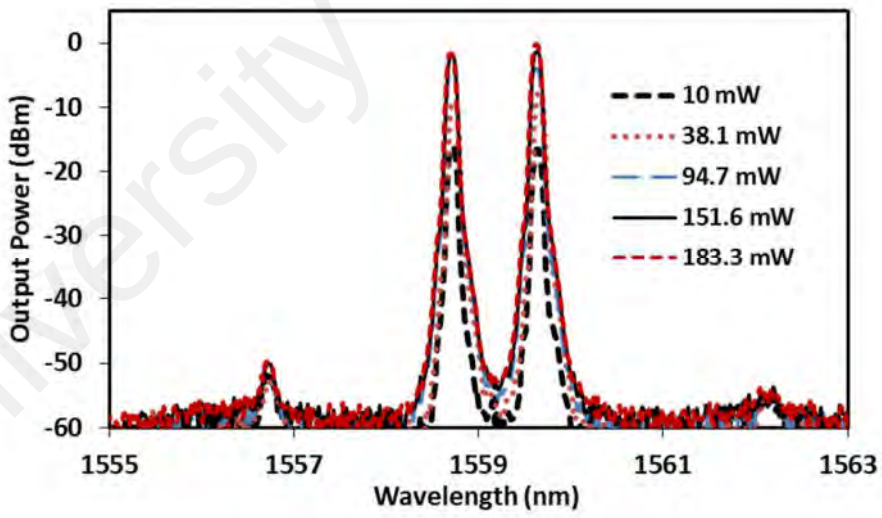

Figure 4.3: Dual wavelength using different pump power (without using PC).

Before including the PC in the cavity, it is evidently proved that the proposed cavity can produce a stable dual wavelength with different pump powers. When the pump power is increased, an increment in the peak power and side mode suppression ratio (SMSR) of DWFL is observed, but the increment has occurred at the identical wavelength. Figure 4.3

demonstrates the graphical result of the proposed dual wavelength cavity. The threshold power of the dual wavelength laser is recorded as 7.1 mW input pump power, and stable dual wavelength is achieved at 12.3 mW input pump power. The pump power is augmented gradually to measure the stability of the dual wavelength laser. The pump power is increased firstly to 38.1 mW, secondly 94.7 mW, thirdly to 151.6 mW, and lastly to 183.3 mW. Figure 4.3 illustrates the output dual wavelength laser (5%) measured through OSA. It is found that the lasing occurs at the same wavelength for the all mentioned pump powers.

Next, the PC is included in the cavity, as shown in Figure 4.1, in order to control the spacing between two wavelengths. The polarization state of the light propagation can be tuned by altering the PC orientation. The changes of polarization state in the cavity may induce different cavity loss and gain compensation in EDF (Desurvire *et al.*, 1991; Laming *et al.*, 1988; Mahdi *et al.*, 2000). When high loss is induced in the cavity due to PC tuning and polarization state alteration, the total cavity loss is increased; therefore, the net cavity gain profile tends to shift to shorter wavelength. The laser lases at the highest gain (at shorter wavelength) across the gain profile. Moreover, the microfiber induces particular interference peaks. Since interference peaks are dependent on polarization state, a slight adjustment of the PC causes the lasing to switch from one wavelength to another wavelength (Ahmad *et al.*, 2015b). The insertion loss for introducing the PC in the cavity is measured as 2 dB by comparing the attained spectrum with the inclusion of the PC and without the PC. The dual wavelength lasing output spectrum, recorded at 94.7 mW input power, is shown in Figure 4.4. By setting the pump power to 94.7 mW, the dual wavelength peaks are attained at 1558.77 nm and 1559.71 nm with a spacing of 0.94 nm. The output power is recorded as -5.9 dBm at 1558.77 nm and -6.4 dBm at 1559.71 nm. The SMSR is measured approximately 50 dB.

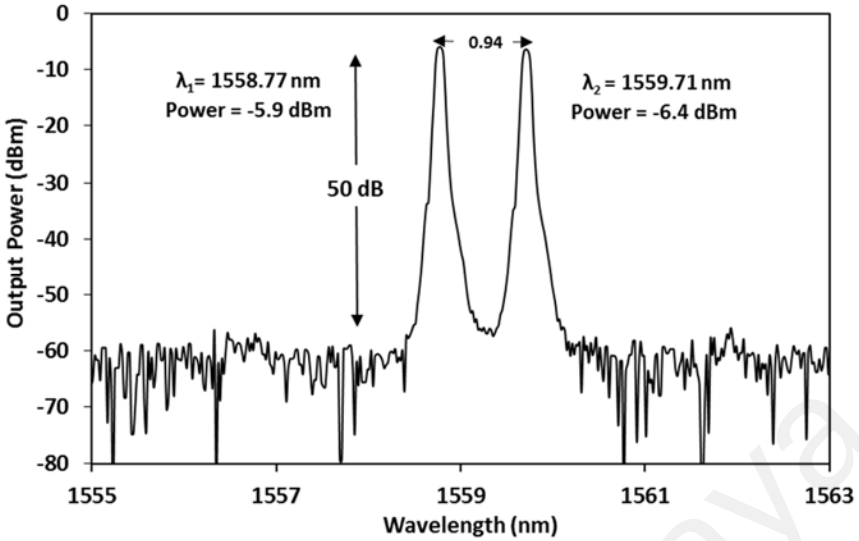

Figure 4.4: DWFL (with PC) at 94.7 mW input power ($\Delta\lambda$=0.94 nm).

The stability of the dual wavelength is measured over a time period of 60 minutes where the data are taken at every three minute interval. The system is observed stable at different input powers, and an acceptable peak difference and wavelength spacing between two lasing spectrums is recorded. The stability of dual wavelength for 60 minutes at 94.7 mW input power is shown in Figure 4.5(a).

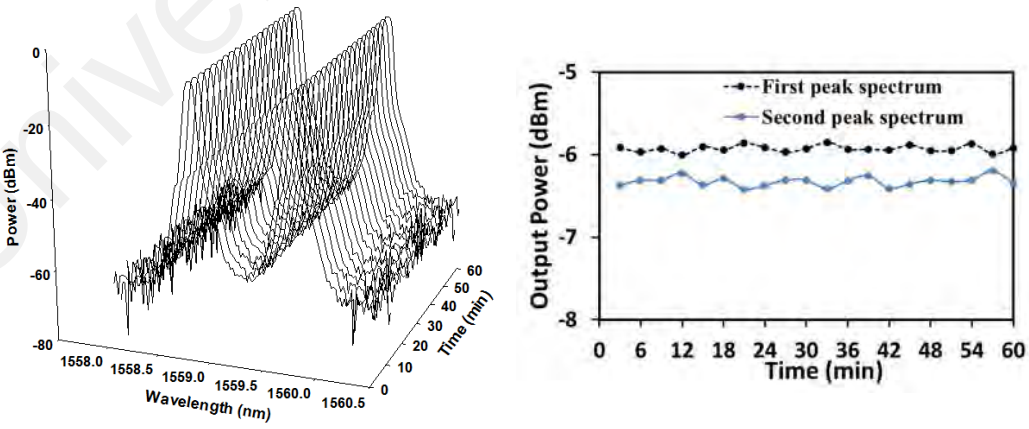

(a) (b)

Figure 4.5: (a) Dual wavelength output spectrum recorded at 94.7 mW power (20 readings for 60 minutes duration), and (b) Peak power fluctuation for λ_1 = 1558.77 nm and λ_2 = 1559.71 nm.

The power difference between two peaks of the dual wavelength, and the wavelength spacing between the two peaks have been measured. For the case of $\Delta\lambda$= 0.94 nm, the power difference between the dual peaks is observed in the range of 0.22 dB to 0.56 dB. A very minor shifting has been observed in the lasing wavelength where both peaks shifting (fluctuation) are observed only within the range of 0.02 nm. Figure 4.5(a) displays the stability of dual wavelength lasing, and Figure 4.5(b) displays the power fluctuation of the dual wavelength where the maximum fluctuation recorded is less than 0.2 dB. This fluctuation might have occurred due to the fluctuation of 980 nm pump power and temperature variant cavity loss (Harun *et al.*, 2010).

As mentioned earlier, by controlling the cavity polarization state through the PC, the dual wavelength can be shifted to other wavelengths. Six different sets of dual wavelength have been recorded with six different interspace between the wavelengths, which are 0.4 nm (corresponding a frequency of 49.9 GHz), 0.94 nm (corresponding to a frequency of 117 GHz), 1.10 nm (corresponding to the frequency of 137 GHz), 3.12 nm (corresponding to frequency of 390 GHz), and 3.32 nm (corresponding to frequency of 415 GHz). Figure 4.6 displays all six sets of DWFL. In the experiment, when the narrowest dual wavelength (0.4 nm) is generated by tuning the PC, no sideband is generated and therefore, it can be concluded that no four wave mixing (Ahmad *et al.*, 2010) is observed during the experiment.

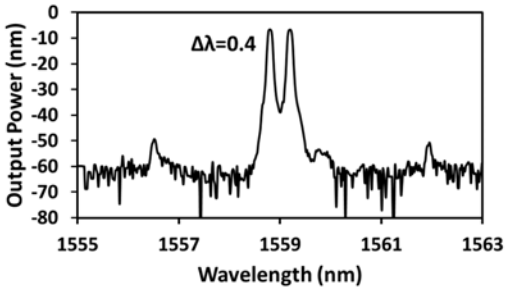

(a) $\Delta\lambda = 0.4$ at $\lambda_1 = 1558.79$ nm and $\lambda_2 = 1559.19$ nm (corresponding to frequency of 49.9 GHz)

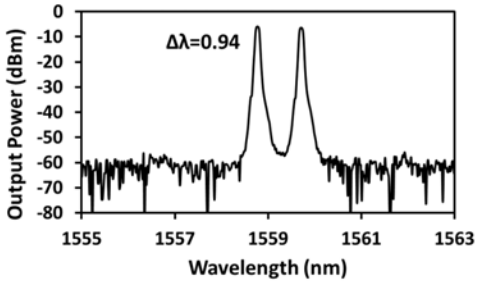

(b) $\Delta\lambda = 0.94$ at $\lambda_1 = 1558.77$ nm and $\lambda_2 = 1559.71$ nm (corresponding to frequency of 117 GHz)

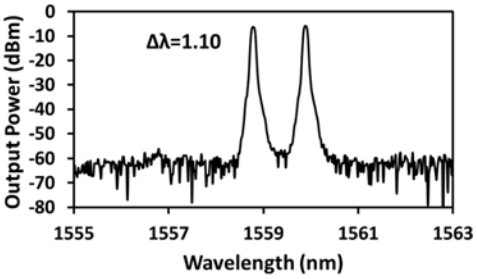

(c) $\Delta\lambda = 1.1$ at $\lambda_1 = 1558.79$ nm and $\lambda_2 = 1559.89$ nm (corresponding to frequency of 137 GHz)

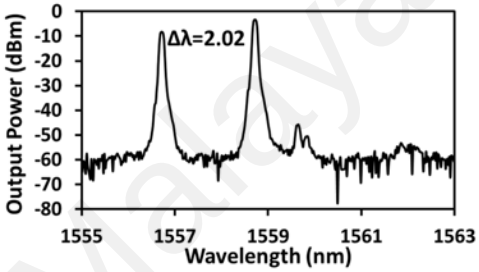

(d) $\Delta\lambda = 2.02$ at $\lambda_1 = 1556.71$ nm and $\lambda_2 = 1558.73$ nm (corresponding to frequency of 252 GHz)

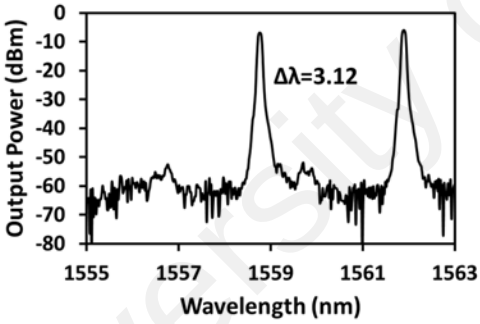

(e) $\Delta\lambda = 3.12$ at $\lambda_1 = 1558.77$ nm and $\lambda_2 = 1561.89$ nm (corresponding to a frequency of 390 GHz)

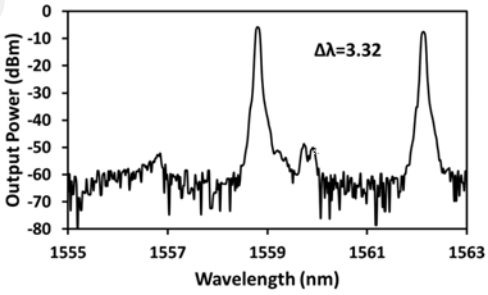

(f) $\Delta\lambda = 3.32$ at $\lambda_1 = 1558.81$ nm and $\lambda_2 = 1562.13$ nm (corresponding to frequency of 415 GHz)

Figure 4.6: Dual wavelength lasing spectrums with tunable spacing (with PC).

All six-sets of tunable dual wavelength have demonstrated high stability over the observation period of one hour. For every individual dual wavelength set, the stability is validated on every 3 minute interval, for example, that the stability of DWFL of 0.40 nm spacing is recorded for 60 minutes summing about 20 readings (similar procedure is followed for other five sets of dual wavelength with different spacing). The system has

exhibited acceptable power fluctuation and acceptable peak difference between two peak wavelengths. For demonstration purposes, the stability of the DWFL of 3.32 spacing (λ_1=1558.81 nm and λ_2= 1562.13 nm) is displayed in Figure 4.7(a). The peak difference between two wavelength peaks is detected in the range between 0.90 dB to 2.0 dB, and the wavelength spacing between them is recorded as 3.32 nm. Insignificant shifting has been observed in the lasing wavelength, and the shifting (fluctuation) is recorded within 0.02 nm range. Figure 4.7(b) presents the power fluctuation of the dual wavelength where the maximum fluctuation is recorded as less than 0.5 dB, which might occur from fluctuation of pump power and temperature variant cavity loss, as mentioned earlier.

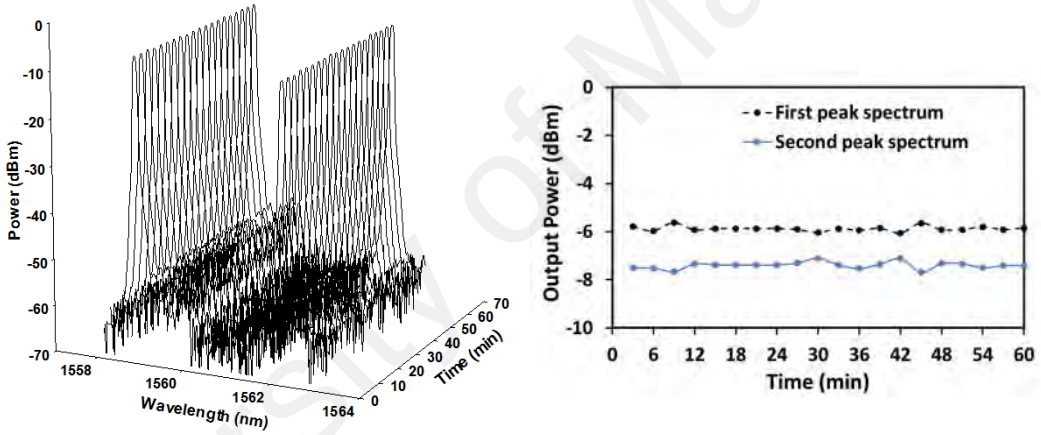

(a) (b)

Figure 4.7: DWFL λ_1 = 1558.81 nm and λ_2 = 1562.13 nm at 94.7 mW input power ($\Delta\lambda$ = 3.32 nm) (a) DWFL stability test (20 readings for 60 minutes duration), and (b) peak power fluctuation.

Development of high frequency sources from the beating of two optical signals can be one of the major applications of the proposed DWFL system. Ahmad *et al.* demonstrated that a closely spaced dual wavelength between 0.01 nm to 0.03 nm can generate a beating frequency between 1.4 GHz to 3.2 GHz (Yao *et al.*, 2006), while Yao *et al.* demonstrated a 3.389 GHz frequency beating signal with a dual wavelength spacing of 27 pm (Ahmad *et al.*, 2013). Additionally, the proposed system would also have significant applications

in the generation of microwave signals for communications and sensing applications, by exploiting the beating of two or more optical signals (Alavi *et al.*, 2016; Wang *et al.*, 2011). However, it is worthy to mention that in order to use DWFL in high frequency signal generation applications, the laser must satisfy single longitudinal mode (SLM) characteristic.

(a)

(b)

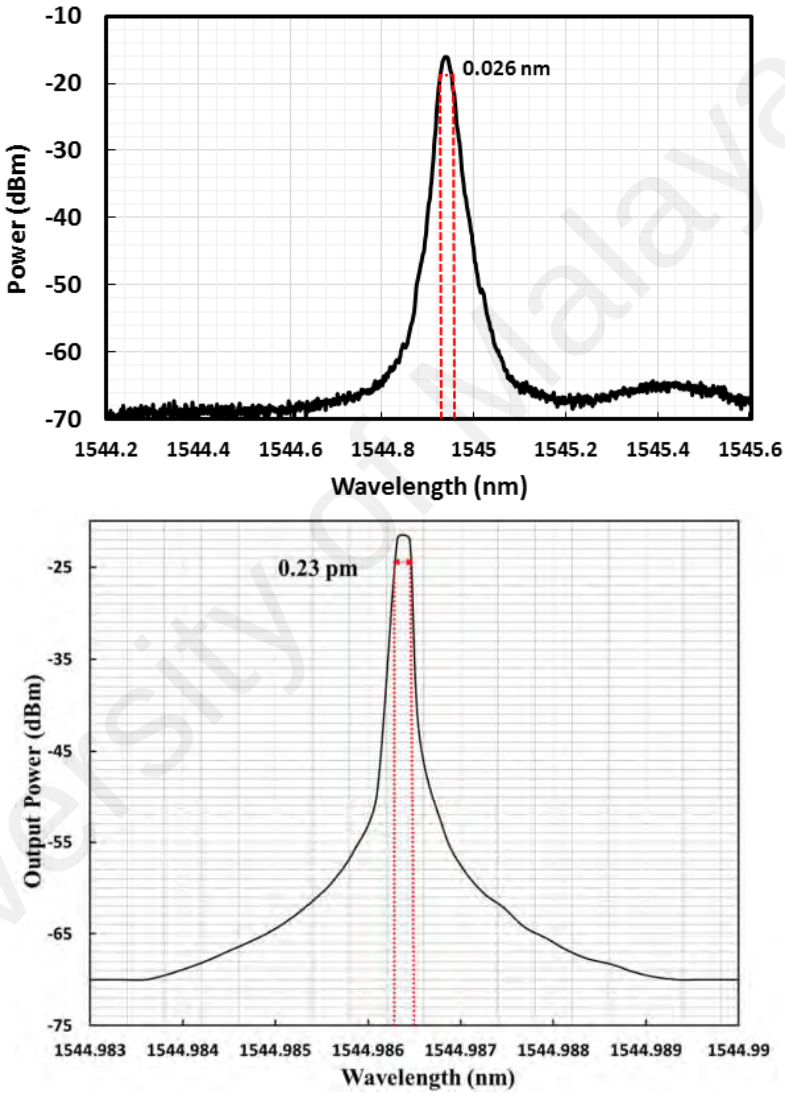

Figure 4.8: (a) Measurement of the 3 dB bandwidth of a single lasing wavelength at resolution 0.026 nm, using the Anritsu MS9740A OSA, and (b)Measurement of the 3 dB bandwidth of a single lasing wavelength at resolution 0.16 pm, using the Apex AP2051A OSA.

In order to investigate the single longitudinal mode operation of microfiber based DWFL, a similar specification's microfiber has been fabricated (because the previously fabricated microfiber broke in the middle of the experiment) and is inserted into the cavity. Single lasing output is measured through the Anritsu MS9740A optical spectrum analyser (OSA). The 3 dB bandwidth is measured as 0.026 nm (Figure 4.8(a)), which is not the actual 3 dB bandwidth value, rather it is the highest resolution that can be achieved using the utilized OSA (Anirtsu MS9740A model OSA). Therefore, in order to obtain more accurate reading, the laser output is measured using a high resolution OSA having a resolution of up to 0.16 pm (Apex AP2051A). The 3 dB bandwidth is measured as 0.23 pm with a central wavelength of 1544.986448 nm as shown in Figure 4.8(b). The linewidth of the laser is calculated as 29.6 MHz based on the 3 dB bandwidth obtained from high resolution OSA using the formula $v = (\frac{c}{\lambda^2})(\Delta\lambda)$, where v represents the frequency interval, $\Delta\lambda$ represents the 3 dB bandwidth, λ is the central wavelength, and c is the speed of the light. The computed linewidth confirms that the wavelength is operating in the single longitudinal mode regime.

Furthermore, the laser output is measured through Anritsu MS2683A radio frequency spectrum analyser (RFSA) as shown in Figure 4.9. No mode beating signal is observed in the range of 0 GHz to 7.88 GHz which further confirms the single longitudinal mode operation. It can be seen from Figure 4.9 that there are no spikes of peaks present in the spectrum, which indicating that the output is operating in the SLM regime. The mentioned technique is known as the standard method to investigate the SLM operation of the laser, it is undoubtedly proved the presented microfiber based DWFL is SLM in nature and can be used in high frequency generation applications. Further applications can also be realized by the proposed system, including various sensing applications such as high resolution spectroscopy and even the generation of terahertz signals, DIALs (Ahmad *et al.*, 2013; Ahmad *et al.*, 2009; Klehr *et al.*, 2008; Sharma *et al.*, 2004; Wang & Pan, 1995).

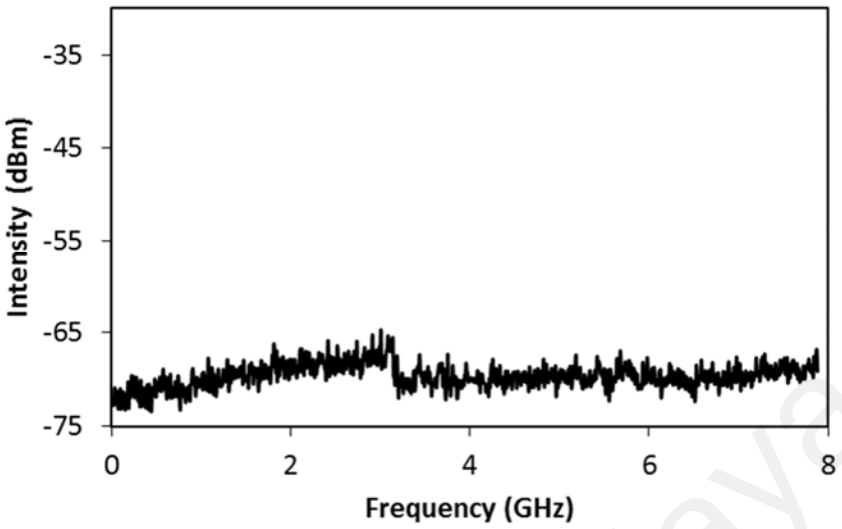

Figure 4.9: RFSA spectrum of the SLM wavelength output.

4.3 Fiber pulse laser generation

Microfiber is a potential candidate for pulse laser saturable absorber device fabrication since it offers many advantages over conventional method, such as thermal damage probability, weak optical absorption and parasitic reflection (He *et al.*, 2012b; Park *et al.*, 2015; Wang *et al.*, 2012) as mentioned in Section 3.4.1. A number of works have been reported in the literature, where microfiber based saturable absorber device has been fabricated and utilized for Q-switched and mode-locked pulse fiber laser generation (Fan *et al.*, 2014; He *et al.*, 2012b; Wang *et al.*, 2012; Zhu *et al.*, 2013). However, microfiber saturable absorber device based pulse generation, particularly mode-locked pulse generation has faced some critical issues. One of the issues is the occurrence of narrow spectral bandwidth. Wang *et al.* reported that multimode interference in the waist region of the microfiber causes narrow spectral bandwidth of the pulse (Wang *et al.*, 2012). But, for practical pulse laser applications, broader spectral bandwidth of the pulse is desired. This study aims to achieve a broader bandwidth pulse, and a special technique has been followed to attain the purpose. In this section, Q-switched and mode-locked pulse

generation using the microfiber saturable absorber device have been discussed. Moreover, a tuning mechanism to tune the mode-locked pulse spectrum is also described.

4.3.1 Q-switched fiber pulse laser Generation

Q-switching technique is a technique to generate strenuous short pulses from a laser cavity, where intracavity losses are controlled and Q-factor of the laser resonator is modulated in order to generate pulses (Paschotta, 2008c, 2008d, 2008e). In this technique, initially, high loss are maintained at the resonators. Since the lasing can't occur at that time, the gain medium is fed with energy because of the accumulation of energy supplied by the pumping mechanism. Suddenly, the losses are deceased by means of active or passive methods, therefore, a rapid increase in the power of the laser radiation is built up in the laser resonator. This process begins with noise from spontaneous emission, which is lately amplified to macroscopic level within hundreds to thousands of round trips.

The gain begins to be saturated as soon as the temporarily integrated intracavity power reaches gain medium's saturation energy level. After the gain matches as the same order with the remaining resonator loss (low), the peak of the pulse is achieved. Further depletion of the stored energy is occurred during the time where the power decays because of the existence of large intracavity power. In numerous cases, the energy extracted after the pulse maximum is akin to energy extracted before the pulse maximum.

The pulse duration attained with Q-switching typically observed in nanosecond range. The repetition rate of the pulse is normally in the range of one Kilohertz to one hundred Kilohertz, however, sometimes it can be higher.

Two techniques are available to switch the resonator loss and generate Q-switch pulse, which are active Q-switching technique and passive Q-switching technique. In active technique, active control element (e.g. acousto-optic or electro-optic modulator) is used

to modulate the losses, where the pulse is formed shortly after an electrical signal arrives. This work focuses on passive Q-switching technique. The mechanism of generating Q-switched pulse using passive technique is described as follows: saturable absorber is used to modulate the loss and generate Q-switched pulse, where the pulse is formed immediately after the energy stored in the gain medium reached a sufficient high level. The generation of Q-switched pulse is depicted in Figure 4.10. As can be seen from the figure, a short pulse is formed in a short after the gain exceeds the total losses of the resonator. Rapid increase in the power is observed after the saturation process initiated in the saturable absorber till the gain saturates to the level of resonator losses (in the figure the loss is about 10%). In order to avoid unnecessary energy losses, saturable absorber's recovery time is required to be longer than pulse duration. Pulse generation using passive Q-switching technique is cost effective and of simple design compared to active Q-switching technique since it doesn't require external modulator or triggering, therefore, suits for the applications that requires high repetition rates. The drawback of the passive Q-switching technique is that the pulse energy is usually lower.

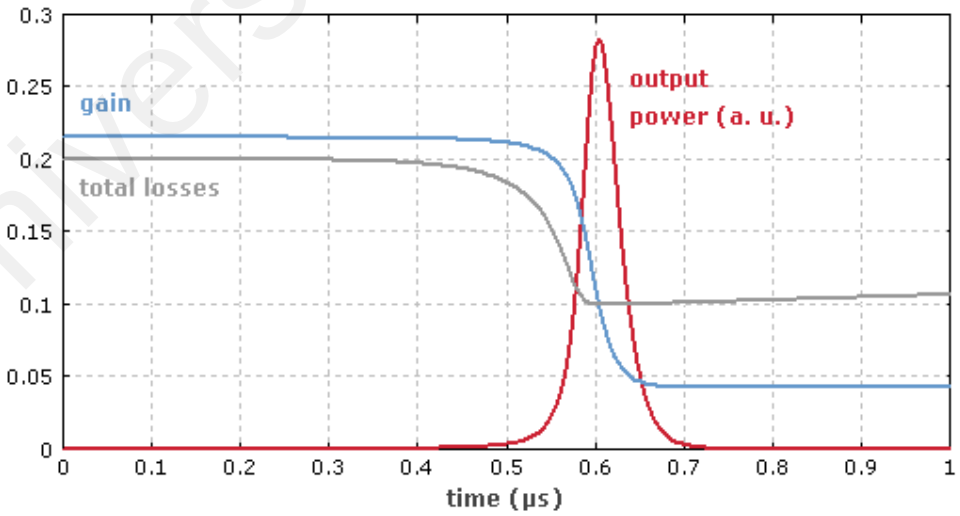

Figure 4.10: Temporal evaluation of gain and losses in passive Q-switching technique (Paschotta, 2008c).

This work investigates the potential of new photonic polymer, Poly (N-vinyl Carbazole) - Polypyrrole (PNVC-PPy) incorporated with graphene oxide (GO) based saturable absorber (SA). In SA fabrication, the Polypyrrole copolymer has been mixed with the GO, because it is rich with π-electron, it forms π-stacking with the graphene sheets in the nanocomposite and exhibits good thermal stability, electrical conductivity and stable dispensability (Gu *et al.*, 2010; Pernites *et al.*, 2011). The proposed Poly(N-vinyl Carbazole)-Polypyrrole-graphene oxide (PNVC-PPy/GO) solution is perceived to respond well as an SA. In this study, a microfiber based SA device has been fabricated by means of coating method where the microfiber has been coated with the PNVC-PPy-GO SA solution, and subsequently, the microfiber based SA device has been employed in Q-switched pulse generation. The details of the work are described in the following section.

4.3.1.1 Fabrication of PNVC-PPy/GO coated microfiber SA device

(a) ***Preparation of PNVC-PPy/GO Nanocomposite***

The PNVC-PPy/GO has been synthesized by in-situ chemical oxidative polymerization technique. In this process, Ferric chloride hexa hydrate ($FeCl_3$. 6 H_2O) is used as oxidant. Besides, anionic surfactant of dodecylbenzene sulfonic acid (DBSA) is used as a dopant and emulsifier to the PPy copolymer and GO, respectively. 1 mol of pyrrole, 15 mol of N-vinyl carbazole and 0.1 mol of DBSA are dissolved in acetonitrile separately (in beaker-1). 5 gm of GO (prepared using improved hammer method) is dissolved in the water (in beaker-2). Both of the solutions are mixed together and solicited (in beaker-3), and then $FeCl_3.6H_2O$ is added to the mixture dropwisely. The reaction mixture is processed through a continuous shaking process for 6 hours at 25 ^oC temperature. Thus, the PNVC-PPy/GO nanocomposite is obtained and it is washed with ethanol-water mixture. Finally the washing solvents are filtered, and the composite is obtained as residue which is dried in the vacuum for 24 hours at 80 ^oC temperature. After that PNVC-PPy/GO nanocomposite is dissolved in N-Methyl-2-Pyrrolidone (NMP) and

is used to coat the microfiber to fabricate microfiber based SA. The formation of the PPy-PNVC/GO nanocomposite has been confirmed by Raman spectroscopy. In Raman scans of pristine GO sheets, the D peak and G peak are found at 1352 cm^{-1} and 1560 cm^{-1} respectively (Sobon *et al.*, 2012a). However, the effective incorporation of GO in the PNVC-PPy/GO nanocomposite causes both the D and G peaks to shift, to 1360cm^{-1} and 1591 cm^{-1} as presented in Figure 4.11. Figure 4.12(a) represents the field emission scanning electron microscope (FESEM) of the graphene oxide, and Figure 4.12(b) shows the FESEM image of the PNVC-PPy/GO nanocomposite. Graphene oxide flakes have relatively large surface (with the edge of sheets typically measured about the size of micrometers), and its morphology resembles thin curtain. The surface morphology of the PNVC-PPy/GO nanocomposite resembles strongly folded curtain, which indicates the presence of the GO flakes in the nanocomposite as shown in Figure 4.12(b).

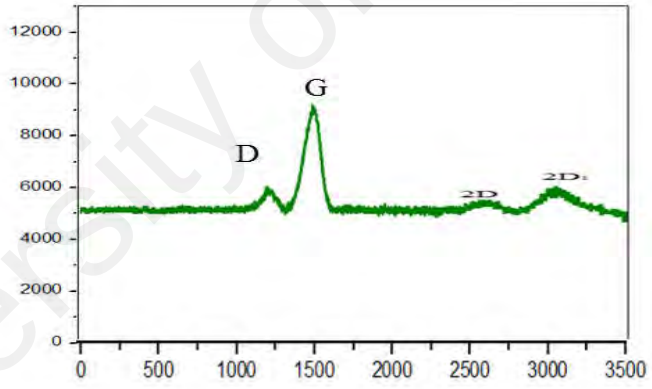

Figure 4.11: Raman spectrum of the PNVC-PPy/GO nanocomposite.

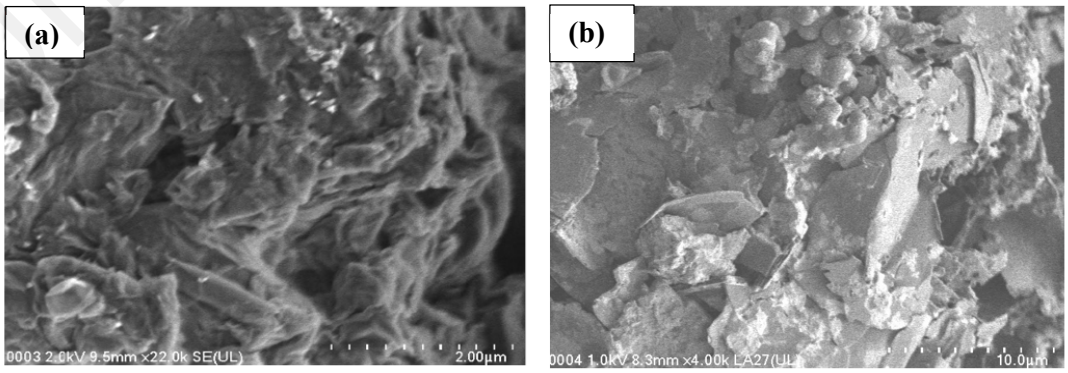

Figure 4.12: FESEM image (a) Graphene oxide, and (b) PNVC-PPy/GO nanocomposite.

(b) ***Fabrication of the Microfiber and the SA***

A microfiber has been fabricated using the systematic flame brushing method by means of the homemade fabrication stage. Firstly, the fiber coating of the SMF around 1 cm length is removed and is put in the fabrication stage. A microfiber of waist diameter of 8 μm and a length of 6.5 cm is achieved following the fabrication process described in Section 3.2.1. A homemade ASE source had is used as a seed source in microfiber characterization; and the output spectrum of the microfiber is measured using an OSA (Anritsu MS9740A) and an optical power meter (OPM) (Thorlabs PM100USB). Approximately 2 dB of insertion loss is measured due to tapering process.

As mentioned before, SA is a must and vital element for passive Q-switching pulse fabrication. The SA device/component using the nanomaterial can be fabricated in two ways, which are – the sandwich method, and the coating method (the details and the pros and cons of both methods can be found in Section 3.4.1). Obviously, microfiber based SA device fabricated by coating method seemed a better choice which can generate pulse employing evanescent field interaction, and in this study a microfiber based PNVC-PPy-GO SA device has been fabricated and utilized.

After microfiber fabrication, the PNVC-PPy-GO solution has been coated in the microfiber. Similar deposition method described in Section 3.4.1.1 is followed in deposition with the only exception that here PNVC-PPy-GO solution has been used instead of GO solution. For a quick overview, the deposition process is illustrated in Figure 4.13. The length of the fiber in which the PNVC-PPy/GO composite interacts with the incident light is estimated to be 3 mm. The deposition loss is measured as 4.7 dB. Figure 4.14 represents the microscopic image of the microfiber captured during PNVC-PPy/GO nanocomposite deposition process.

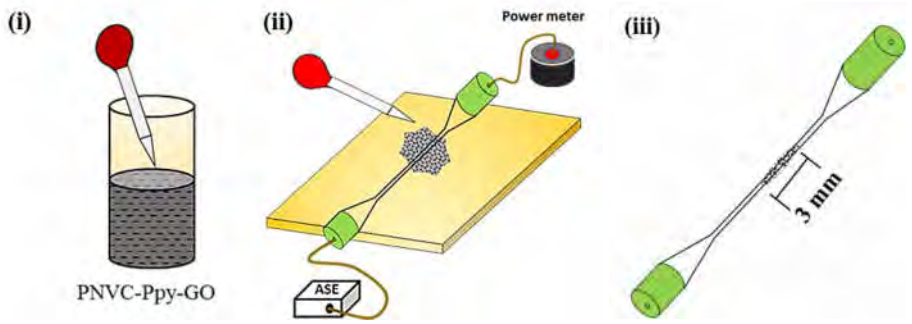

Figure 4.13: Deposition of the PNVC-PPy-GO composite onto the microfiber.

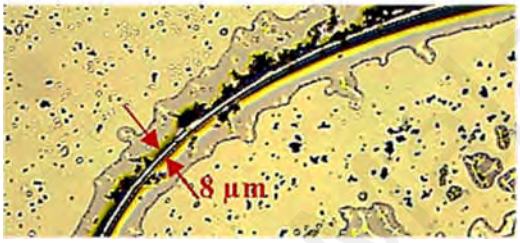

Figure 4.14: Image capture of the microfiber with deposited PNVC-PPy/GO nanoparticles.

4.3.1.2 Results and discussion

Figure 4.15 shows the experimental set-up of the laser cavity that is used to generate Q-switched pulses. The set-up consists of 980 nm laser diode (LD), 980/1550 nm wavelength division multiplexer (WDM), 3 meters of Erbium doped fiber (EDF) (Fibercore MetroGain M12-type), 1550 nm isolator, 95:5 coupler, polarization controller (PC), and microfiber based PNVC-PPy/GO SA device. The PC is used in the cavity to adjust the polarization state of the light propagation, and the isolator is used to confirm the unidirectional flow of light. The 95% port of the coupler is connected to the PC, and the light travels through the PC before entering the microfiber based SA. The interaction of the propagating signal at the SA generates the desired Q-switched pulse. 5% of the output signal is extracted out for further analysis and characterization of the generated pulses by means of OSA, oscilloscope and optical power meter (OPM). A YOKOGAWA

DLM2054 oscilloscope is used to monitor the pulse characteristics of the output signal, and a Thorlab DET01CFC InGaAs fiber optic photo detector with a bandwidth of 1.2 GHz is used when the signal is measured through the oscilloscope.

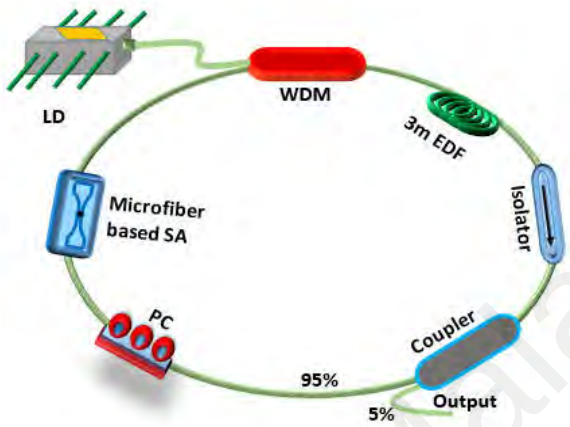

Figure 4.15: Experimental set-up of Q-switched pulse fabrication.

The threshold of Q-switching operation is observed at the pumping power of 10 mW. This low threshold indicates low saturable intensity of the fabricated SA component. However, stable Q-switched pulse train is observed at 12.8 mW pumping power. Figure 4.16(a) shows the oscilloscope trace of a single Q-switched pulse, while the inset of Figure 4.16(a) shows the pulse train as obtained from the oscilloscope. Figure 4.16(b) on the other hand displays the optical spectrum of the output pulses, as taken from the OSA. The repetition rate and the pulse width is recorded to be 25.2 kHz and 5.74 μs respectively, with the output power of 0.045 mW. The output spectrum of the pulse is analysed through OSA where it centred at 1559.07 nm, and the full width at half maximum (FWHM) is calculated as 0.02 nm.

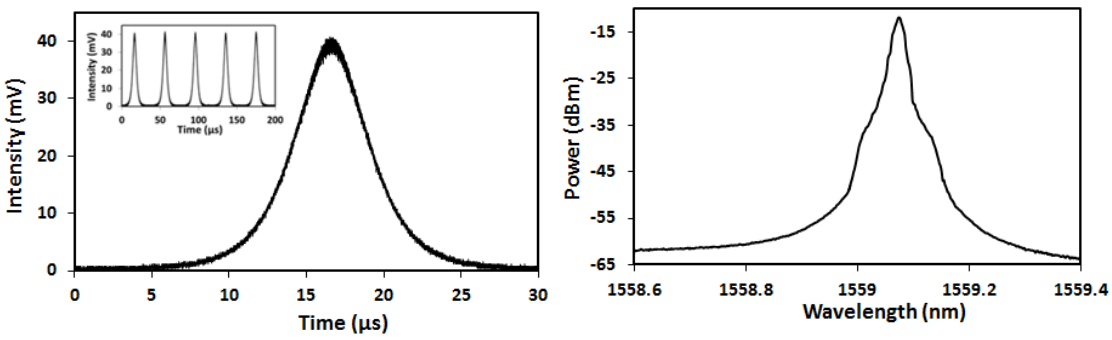

Figure 4.16: (a) Pulse envelope trace (inset: pulse train), and (b) Optical spectrum.

It is worthwhile to note that increasing the pump power will also result in the repetition rate increasing, as a result of saturation enhancement of the SA (Popa *et al.*, 2010a; Svelto & Hanna, 1976). It has also been observed that, when the pumping power increases, the pulse width decreases as per the behaviour of Q-switch pulse. Figure 4.17 describes the Q-switched pulse behavior in terms of repetition rate and pulse width with respect to the raising in pumping power. The repetition rate is increased from 25.2 kHz to 42.7 kHz and the pulse width is decreased from 5.74 µs to 2.48 µs, when the pumping power increased from 12.8 mW to 40 mW. It is worth to mention that the pulse width can be shortened further by optimizing of the Q-switched laser cavity in terms of cavity loss, cavity length and output coupling (Luo *et al.*, 2010).

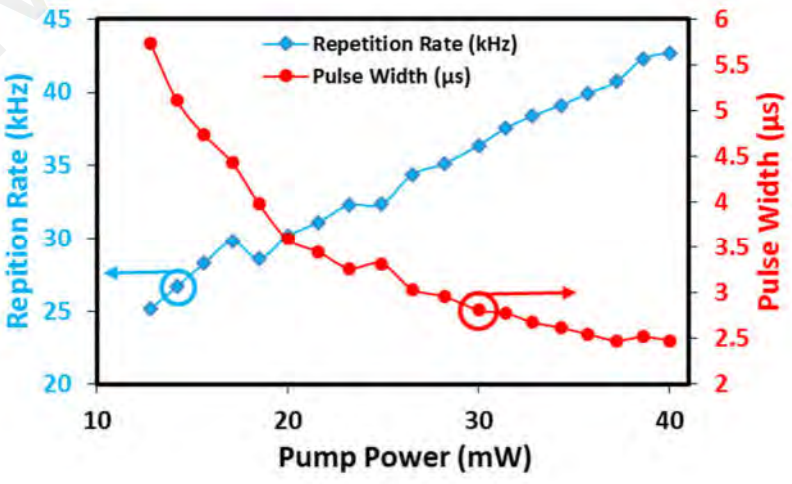

Figure 4.17: The repetition rate and pulse width behaviour with respect to pump power.

Figure 4.18 shows the Q-switched pulse trains obtained at different pump powers. The pulse trains are attained at pumping powers of 12.8 mW, 20.0 mW, 25.0 mW, 30.0 mW, 35.0 mW and 40.0 mW, with resulting repetition rates of 25.2 kHz, 30.2 kHz, 32.4 kHz, 35.1 kHz, 39.1 kHz and 42.7 kHz. The Q-switched pulses are found to be stable at all pump power, with no fluctuation in pulse width of pulse intensity observed.

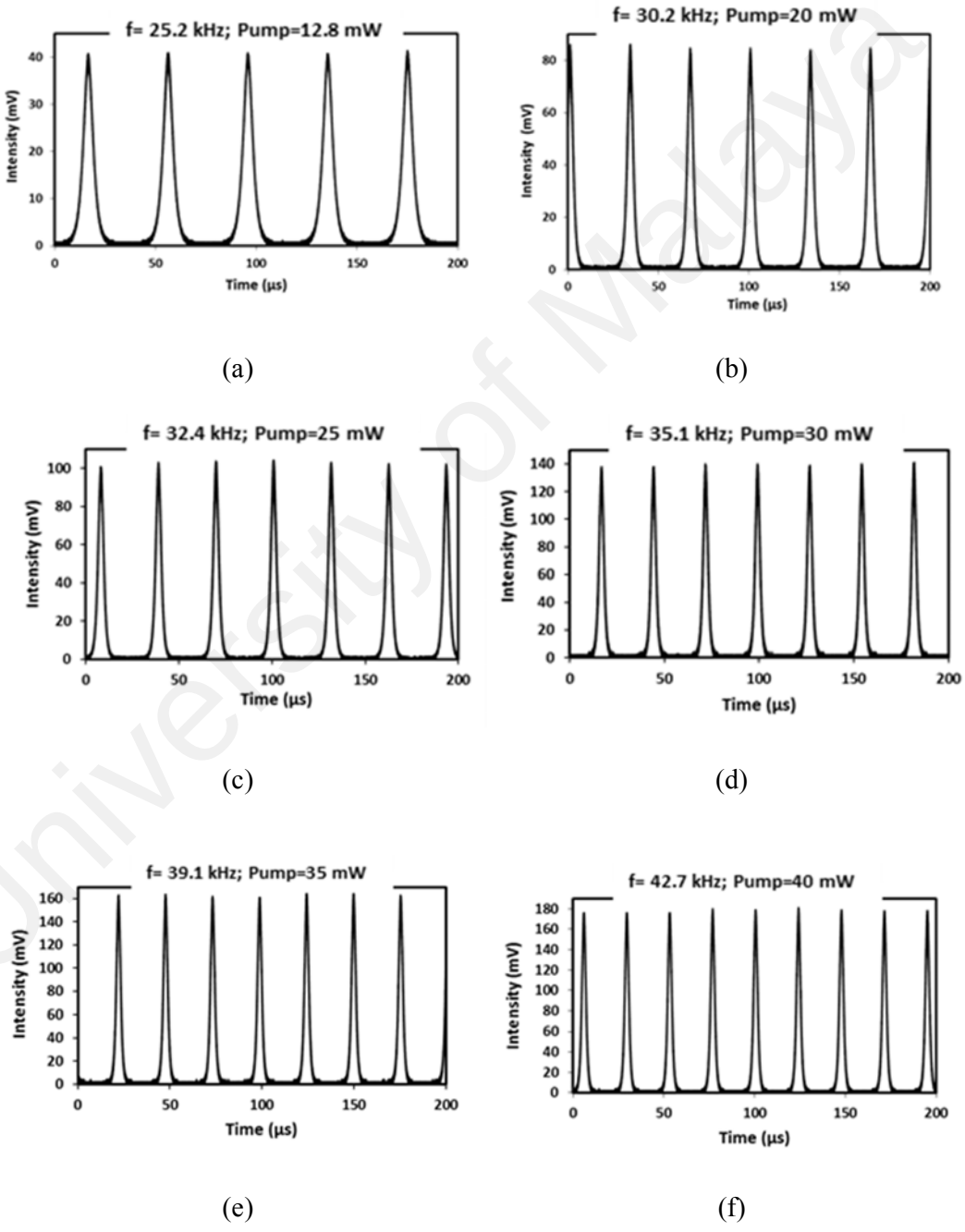

Figure 4.18: Pulse train of the Q-switched laser at different pumping powers, where (a) 12.8 mW, (b) 20 mW, (c) 25 mW, (d) 30 mW, (e) 35 mW, and (f) 40 mW.

Meanwhile, the average output power and pulse energy as a function to the pumping power are calculated and plotted in Figure 4.19. As it can see from Figure 4.19, the output power varies from 0.045 mW to 0.193 mW corresponding to the pumping power of 12.8 mW to 40 mW. The laser efficiency is calculated to be 0.54% with high linearity of 0.999. The pulse energy is calculated and it is found varying from 1.77 nJ to 4.43 nJ corresponding to the pumping power variation from 12.8 mW to 40 mW. The maximum single pulse energy is measured as 4.43 nJ at 40 mW pump power. It is worth to mention that by raising the pumping power more than 40 mW, the Q-switched pulse is disappeared. While this is initially assumed to be a consequence of the SA being damaged, however, reducing the pump power has resulted in Q-switched pulses being observed again. Hence, the hypothesis can be made that above a pump power of 40.0 mW, the SA becomes fully saturated, thus losing its ability to generate the Q-switched pulses.

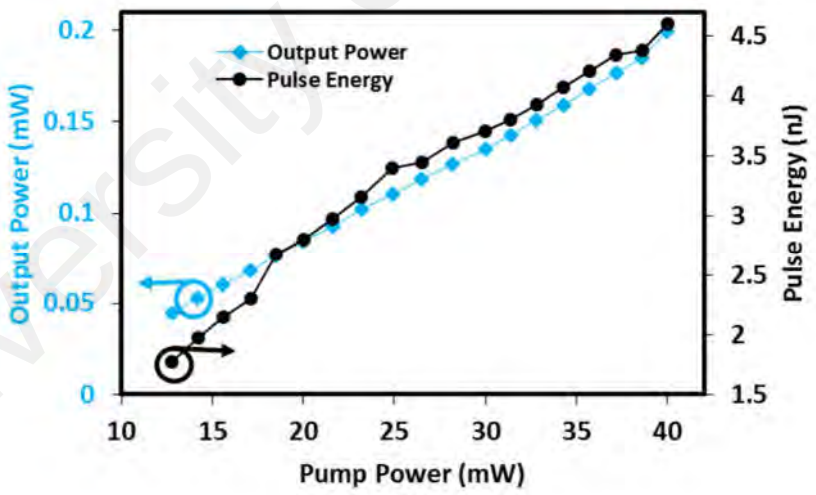

Figure 4.19: Average output power and pulse energy as a function of pump power.

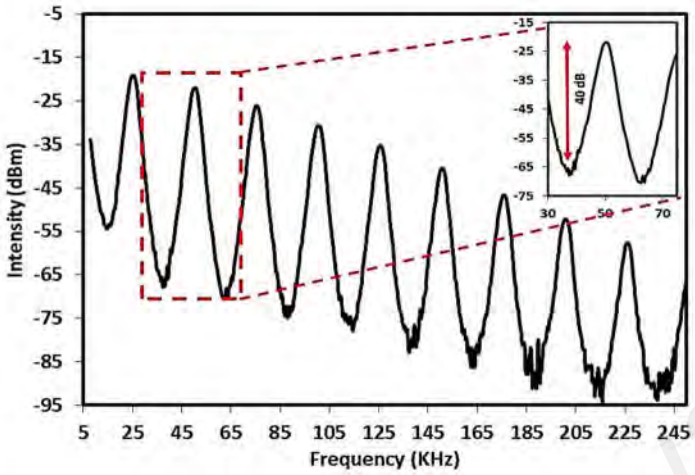

Figure 4.20: Radio frequency spectrum of the output pulse at 12.8 mW.

Figure 4.20 represents the radio frequency spectrum for the output pulse train that is measured at 12.8 mW of pumping power. An Anritsu MS2683A radio frequency spectrum analyzer (RFSA) is used to obtain the measurements at the resolution bandwidth of 3000 Hz. As can be seen from Figure 4.20, a fundamental frequency of 25.2 kHz is measured which agrees with the oscilloscope measurement as shown earlier in Figure 4.18(a). The peak to peak extinction ratio is also measured to be 40 dB, which confirming the stability of the pulse. Practically, such result indicates that the proposed SA component for Q-switched pulse laser generation retains the relative advantages of design simplicity and low cost of fabrication, while still being able to generate a high quality Q-switched pulses. Moreover, the proposed system could be used to generate Q-switched pulses for different applications at various fields such as in environmental, medical, industrial and telecommunication.

4.3.2 Mode-locked fiber pulse laser Generation

This current study intends to produce mode-locked pulse fiber laser with shorter pulse width and larger spectral bandwidth, and an effective approach has been taken in order to handle this issue. An adiabatic microfiber has been utilized to fabricate saturable absorber

device with the aim to minimize the multimode interference and comb filter effect, so that pulse with broader bandwidth and hence, shorter pulse-width can be achieved. A microfiber is fabricated by homemade fabrication stage, and subsequently, GO is deposited in the microfiber using optical coating deposition technique. The microfiber based GO SA device is introduced in the ring cavity to generate mode-locked pulses. The details of the work are described in the later part of the section.

4.3.2.1 Fabrication of SA

The microfiber is fabricated from single mode fiber (SMF) using the systematic flame brushing technique by means of the homemade fabrication stage. Approximately 4 cm length of the coating is stripped out from the SMF and then is placed in a homemade linear fabrication stage. A microfiber of waist diameter of 11 μm (figure 4.21) is achieved following the fabrication process described in Section 3.2. Less than 2.5 dB of the insertion loss is recorded in 1.5 μm region.

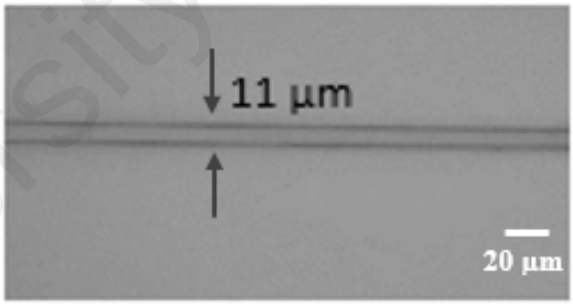

Figure 4.21: Microscopic image of the microfiber waist region after fabrication.

Before the experiment, the GO sample is characterized using Raman spectroscopy. The details of the characterization are discussed in Chapter 3 (Section 3.4.1.2). The GO solution was deposited in the microfiber waist region using the coating method, and the details of the deposition method are described earlier in Section 3.4.1.1. In the experiment, a total length of approximately 40 μm is deposited with the GO. A microscopic image, shown in Figure 4.22 indicates that the graphene is successfully deposited the microfiber.

After the deposition, the microfiber based GO SA is characterized using the balanced twin detector method as described in Section 3.4.1. The fabricated microfiber based-GO SA shows a saturation intensity of 0.7031 MW/cm^2 and 30% modulation depth. Meanwhile, non-saturable loss is recorded as 70%.

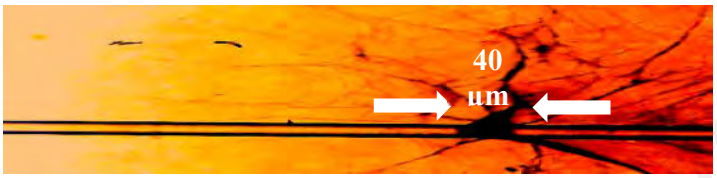

Figure 4.22: Optical microscopic image of graphene coated microfiber.

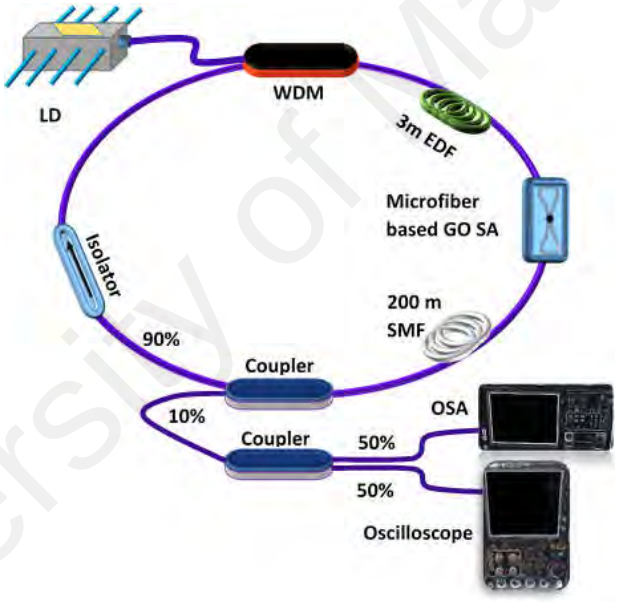

Figure 4.23: Schematic of mode locking fiber laser.

4.3.2.2 Results and Discussions

The proposed mode-locked fiber laser using microfiber based graphene SA is illustrated in Figure 4.23. The light is pumped from a Thorlabs CLD 1015 with an Oclaro LC96A74P 980 nm laser diode through a 980/1550 wavelength division multiplexer (WDM). As a gain medium, a 3 m Fibercore MetroGain M12-type Erbium doped fiber (EDF) is used. The microfiber based GO SA device is inserted next to the gain medium.

A 200 m Corning SMF (SMF-28) is introduced in the cavity to ensure anomalous net cavity dispersion for mode-locking operation. The total length of the cavity is measured as 226.45 m comprising 3 m EDF and 223.45 m SMF. The group velocity dispersion of the EDF and SMF-28 are $23.2\ ps^2/km$ and 18 ps/nm·km, respectively, as found in the specification provided by the manufacturer. The net cavity dispersion is estimated around $5.25\ ps^2$. The net Cavity Dispersion is calculated in 4 steps.

i. The dispersion value of the SMF is provided by the manufacturer in terms of $ps/nm.km$ unit. On the other hand, the dispersion value of the EDF is provided by the manufacturer in terms of group velocity dispersion (GVD) in ps^2/km unit, which is converted to dispersion in $ps/nm.km$ unit for calculation purposes.

$$GVD\ of\ t\ e\ EDF = \ 23.2\frac{ps^2}{km} = \ 23.2\frac{ps^2}{km} \times \frac{(10^{-12}s)^2}{(1ps)^2} \times \frac{1\ km}{1000\ m}$$

$$= \ 2.32\ \times 10^{-26}\ s^2/m$$

$$\downarrow By\ converting\ into\ dispersion\ (in\ ps/nm.km'unit) \quad ,$$

$$T\ \ e\ dispersion\ of\ t\ \ e\ EDF\ per\ km = 18.2\ ps/nm.km$$

ii. The total dispersion is calculated in terms of $ps/nm.km$ unit.

$$Total\ dispersion\ in\ t\ \ e\ cavity$$

$$= dispersion\ of\ t\ \ e\ 3\ m\ EDF + Dispersion\ of\ 223.45\ m\ SM\ F$$

$$= (3 \times 10^{-3}km) \times \left(18.2\frac{ps}{nm.km}\right) + (223.45 \times 10^{-3}km) \times (18\frac{ps}{nm.km})$$

$$= 4.0767\ ps/nm$$

$$So\ t\ \ e\ dispersion\ for\ 226.45\ m\ long\ cavity = 4.0767\ \ \frac{ps}{nm},$$

$$\therefore\ t\ \ e\ dispersion\ for\ 1\ m\ cavity = \frac{4.0767}{226.45}\frac{ps}{nm}$$

$$T\ \ e\ dispersion\ for\ 1000\ m\ long\ cavity = \frac{4.0767}{226.45}\frac{ps}{nm} \times 1000\ m$$

$$= 18.002\ ps/nm.km$$

$$\downarrow By\ converting\ into\ \frac{s^2}{m}unit, = \ \ 23.2 \times 10^{-27} s^2/m$$

iii. The total dispersion is converted from s^2/m to ps^2/m.

$$= 23.2\ \times 10^{-27}\frac{s^2}{m} \times \frac{(1ps)^2}{(10^{-12}s)^2} = \ \ 0.0232\ ps^2/m$$

It is notable that the dispersion value achieved in step iii ($0.0232\ ps^2/m$) is based on each meter cavity length. Thus, the dispersion value (ps^2/m) is multiplied with the total length (226.45 m) to calculate the total net cavity dispersion.

iv. $T\ \ e\ dispersion\ for\ t\ \ e\ w\ \ ole\ 226.45\ m = \ \ 0.0232\ \frac{ps^2}{m} \times 226.45\ m =$ $5.2536\ ps^2$

Group velocity of the propagated light in a transparent medium is dependent on the optical frequency or wavelength, and this phenomenon is known as group velocity dispersion (GVD) (Paschotta, 2008b). The derivative of the inverse group velocity with respect to angular frequency (or wavelength) is defined as group velocity dispersion.

$$GVD = \frac{\partial}{\partial\omega}\left(\frac{1}{v_g}\right) = \frac{\partial}{\partial\omega}\left(\frac{\partial k}{\partial\omega}\right) = \frac{\partial^2 k}{\partial\omega^2} \quad (4.1)$$

In Equation 4.1, k refers to frequency dependent wavenumber.

The group velocity dispersion basically refers to the group delay dispersion per unit length, which has the basic unit of s^2/m.

For the case of optical fiber, GVD is normally described as a derivative with respect to wavelength rather expressing it with respect to angular frequency. For the context of optical communication, the group velocity dispersion parameter (dispersion coefficient) D_λ can be described as,

$$D_\lambda = \frac{2\pi C}{\lambda^2} . GVD = \frac{2\pi C}{\lambda^2} . \frac{\partial^2 k}{\partial \omega^2} \quad (4.2)$$

The GVD of the optical fiber usually expressed in the unit of ps/(nm.km) which means picosecond(s) per nanometer change and kilometer distance propagation. For instance, typical dispersion value for telecom fiber is about 20 ps/nm.km at the wavelength of 1550 nm (corresponds to the value of -25509 fs^2/m).

It can be seen from the above two Equations (4.1 and 4.2), that GVD and D_λ have opposite sign which originates from the inverse relationship of wavelength and optical frequency. Shorter wavelength corresponds to higher optical frequency and vice versa. With an aim to avoid confusion, instead of using positive and negative dispersion, two terms are used such as normal dispersion and anomalous dispersion respectively for positive and negative group velocity dispersion. For the case of normal dispersion, the group velocity reduces if there is any increase of optical frequency. On the other hand, anomalous dispersion refers that the group velocity increases for the increase of optical frequency.

Dispersion plays an important influence in pulse's propagation. Dispersion causes the pulse's frequency components to propagate at different velocities. Normal dispersion causes positive chirp, whereas the anomalous dispersion causes negative chirp to the pulse (Paschotta, 2008a). Therefore, dispersion of the cavity is required to control cautiously.

In order to confirm the unidirectional flow of the light, an isolator is utilized in the cavity. A 90:10 coupler is used to tap out the mode-locked pulses, where 90 percent of the light is allowed to circulate inside the cavity. The 10 percent optical output is further divided equally through a 3 dB coupler which is measured through an optical spectrum analyser (YOKOGAWA, AQ6370C, spectral resolution 0.02 nm), an oscilloscope (YOKOGAWA, DLM2054, measuring capability of 2.5 GS/s), a radio frequency analyser (Anritsu MS2683A, operating range of 9 kHz-7.8 GHz), an auto correlator (Alnair Labs, HAC-200) and an optical power meter. A Thorlabs, D400FC InGaAs Fiber optic Photo detector with a bandwidth of 1GHz is used when the signal is measured through the oscilloscope and the RF analyser.

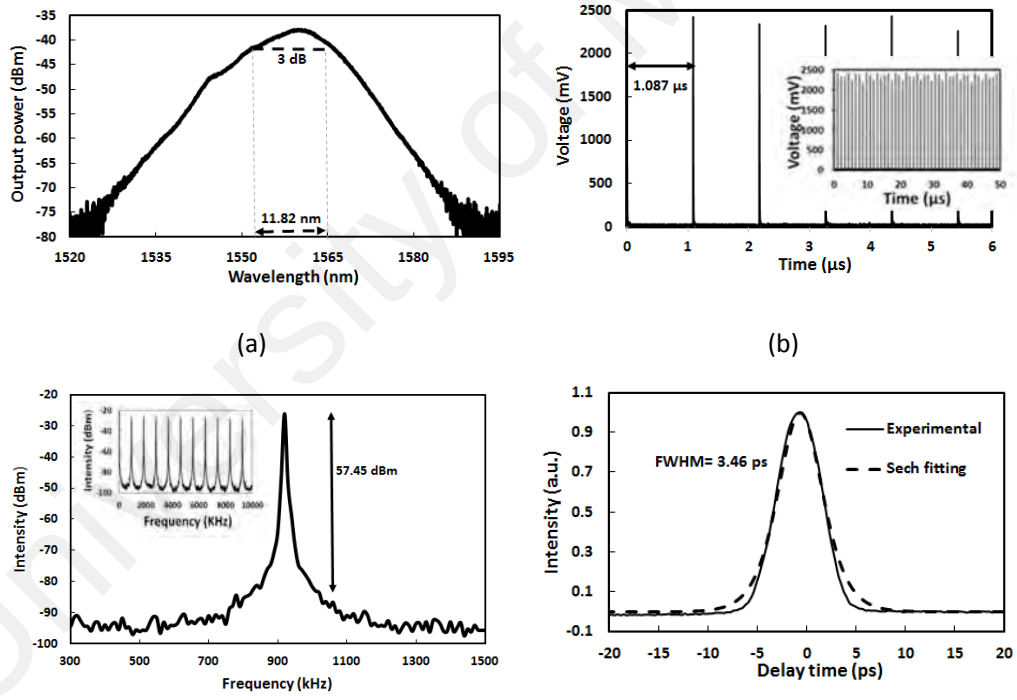

Figure 4.24: Characteristics of the mode-locked pulses (a) Output spectrum centered at 1560 nm with a 3 dB bandwidth of 11.82 nm (resolution 0.02 nm), (b) Output pulse train measured by the oscilloscope (1.087 µs), (c) Radio frequency optical spectrum (fundamental frequency of 920 kHz), Inset left: wideband spectrum 0 to 10 MHz, and (d) Intensity autocorrelation trace with a span of 40 ps (experimental data is presented in black color, whereas $sech^2$ fitting is presented in dotted line).

The Mode locking operation of the proposed pulsed laser set-up has initiated at 74 mW input power. A stable mode-locking operation is attained by increasing the pump power a little further to 97 mW. All subsequent results described in this section are recorded at the input pumping power of 188 mW in order to attain all the characteristics of mode locking operation.

The characteristics of the pulses' achieved using the microfiber based GO SA mode-locked pulse fiber laser cavity are summarized in Figure 4.24. The output of the 3 dB coupler is measured through the OSA to monitor the wavelength spectrum. The mode-locking operation is found to be operated in soliton regime, however, no Kelly sideband is found in the spectrum. This can be explicated that the dispersive waves is suppressed along the propagation in the cavity due to the dominant of soliton intensity (Tan, SJ *et al.*, 2015). Figure 4.24(a) illustrates the spectrum of the mode-locked pulse, indicating central wavelength of 1560 nm with the total spectral width of approximately 65 nm. A broader 3 dB bandwidth of 11.82 nm was achieved. However, in the previous reports (He *et al.*, 2012b; Wang *et al.*, 2012; Zhu *et al.*, 2013), narrow spectral bandwidth was reported, and the multimode interference occurring in the waist region was claimed as the reason for narrow spectral bandwidth of the lasing (Brambilla, 2010; Wang *et al.*, 2012). Multimode interference can be created when many higher order modes along with fundamental mode can be excited in the microfiber waist region. Multimode interference influences the microfiber to behave as comb-like filter, and therefore, it limits the lasing spectral bandwidth (Wang *et al.*, 2012). The reasons of multimode interference are- unsmooth transition and waist region, abrupt and non-adiabatic tapering, and micro-bending caused by the heat during the microfiber fabrication. However, multimode interference (higher order modes excitation and comb filter effect) can be minimized by careful and precise adiabatic microfiber fabrication. If the conical transition regions can be made as adiabatic, all guided modes can be continuously converted into guided cladding modes in down-

tapered region and can be coupled back at the up-taper region which is the fiber output. Thus, homogenous and smooth transition regions of the adiabatic microfiber can minimize the multimode interference and reduce the comb filter effect of the microfiber resulting broad spectral bandwidth. Furthermore, the smooth and adiabatic transition region also reduces the insertion loss of the microfiber, and therefore, can contribute to higher output power in pulse generation. In this study, the microfiber is fabricated adiabatically by monitoring the transmission spectrum continuously in the OSA during the tapering process to ensure minimum comb filter effect and so the multimode interference. By minimizing the multimode interference effect of the microfiber which implies that by using an adiabatic microfiber based GO SA, a broader 3 dB bandwidth has been achieved. The measured 3 dB spectral bandwidth is much broader than previously reported (He *et al.*, 2012b; Wang *et al.*, 2012; Zhu *et al.*, 2013). As can be seen from Figure 4.24(a), 3 dB spectral bandwidth of 11.82 nm is achieved; whereas reference (Zhu *et al.*, 2013) attained a 3 dB bandwidth of 4.1 nm, and reference (Wang *et al.*, 2012) reported a mere 0.2 nm. However, irregular scattering is originated due to inhomogeneous graphene deposition in microfiber, and it influenced the shape of spectrum in Figure 4.24(a) and causes not to form a perfect soliton like spectrum (Song *et al.*, 2010; Wang *et al.*, 2012).

The pulse train is measured and is presented in Figure 4.24(b). A pulse period of 1.087 μs is recorded- corresponding to the frequency of 920 kHz. The achieved frequency (repetition rate) is completely consistent with the cavity length of 226.45 m - and is validated using the formula $Frequency = \frac{c}{nL}$; where c is the speed of the light (3×10^8 m.s^{-1}), n signifies the refractive index of the medium which is 1.44, and *L* refers to the total cavity length which is 226.45 m. The output power is measured as 0.597 mW which means the efficiency of the proposed laser cavity is 0.3175%. The stability of the mode locked laser is investigated by performing radio frequency (RF) spectrum analysis.

Figure 4.24(c) describes the measured RF span where the fundamental frequency of 920 kHz is recorded which absolutely matches with the reading achieved through the oscilloscope. The left picture of Figure 4.24(c) displays the span up to 10 MHz and the right one shows the span up to 1200 kHz (300 kHz to 1500 kHz) with a resolution bandwidth of 10 MHz. A signal to noise ratio (SNR) of 57.45 dB is measured, and the achieved SNR is higher compared to reference (Wang *et al.*, 2012) where SNR of 50.7 dB was reported. All these data are the indication of the stable and reliable mode locking behaviour which is potential to be used in various practical applications such as supercontinuum generation, optoelectronics and optical communication. The stability test is performed for over an hour, and the mode locking pattern is recorded unchanged which signified the stability of the proposed laser. The auto correlation trace of the laser is demonstrated in Figure 4.24(d) where the full width at half maximum (FWHM) is measured as 3.46 ps, assuming a sech^2 pulse shape.

Even though the cavity length of this experiment is much longer than the previously reported works of 62 m in (Wang *et al.*, 2012) and ≈28 m in (He *et al.*, 2012b), a shorter pulse width is attained in this study as compared to both works (He *et al.*, 2012b; Wang *et al.*, 2012). A shorter pulse width of 3.46 ps is achieved at FWHM whereas reference (Wang *et al.*, 2012) reported 15.7 ps and reference (He *et al.*, 2012b) attained 26 ps. It is worthy to mention that typically smaller cavity length results a shorter pulse width. The longer the cavity length, the broader the pulse width. In this current study, even though the cavity length is long, a smaller pulse width is attained by exploiting the negative chirp effect in the microfiber (Adachi *et al.*, 2003; Türke *et al.*, 2006). This can be considered a significant achievement, and it demonstrates that microfiber based SA device can be an effective and efficient approach to fabricate shorter pulses, even in long cavity. The time-bandwidth product (TBP) of the pulses is calculated as 5.04 which signifies that the pulse has substantial chirp. This chirp can be triggered by the dispersion and self-phase

modulation (SPM) of the microfiber and the whole fiber system (He *et al.*, 2012b). The chirped mode locking pulses are compressed by the GO on the microfiber based SA in the cavity. The obtained TBP is considerable, and much larger TBP value had been reported (as high as 1557) in reference (Du *et al.*, 2014) where the authors attained highly chirped mode locking pulses using microfiber based MoS_2 SA device employing evanescent field.

Overall, the attained results demonstrate substantial improvements in comparison with the previously reported works. Since the proposed system exploits the evanescent field to generate mode-locked pulse and diminishes the possibility of SA burning, it can be undoubtedly said that the current study demonstrates the great potential of employing microfiber-based graphene SA for forthcoming ultrafast laser generation application.

4.3.3 Tunable mode-locked fiber pulse laser generation

Tunable ultrafast laser especially mode locked pulse laser is potential to be used in various applications (Wang *et al.*, 2008) such as spectroscopy (Shah, 2013), biomedical research (Letokhov, 1984), telecommunications (Keller, 2003; Mollenauer *et al.*, 2000; Ramaswami *et al.*, 2009) and scientific researches (Zhang *et al.*, 2010). Many methods have been proposed to achieve tunable fiber laser such as grating (Reekie *et al.*, 1986), fiber birefringence (Humphrey & Bowers, 1993), tunable filter (Huang *et al.*, 2014; Sun *et al.*, 2010b; Wang *et al.*, 2008; Woodward *et al.*, 2014). However, above mentioned techniques are considered complicated, possibly bulky and unable to tune consistently (Chen *et al.*, 2015). In addition, tuning range of the lasing is limited by the operating range of the tunable filter which is another constrain of the previously mentioned works (Huang *et al.*, 2014; Sun *et al.*, 2010b; Wang *et al.*, 2008; Woodward *et al.*, 2014). Therefore, alternative solution for tuneable fiber laser is desired to improve the current technology. Optical microfiber is a potential solution to achieve tunable fiber laser and has already

been used in tunable fiber laser applications (Chen *et al.*, 2015; Fang *et al.*, 2010; Kieu & Mansuripur, 2006b). Kieu *et al.* demonstrated that spectral response of the microfiber can be tuned by stretching the microfiber (Kieu & Mansuripur, 2006b). In the work of (Kieu & Mansuripur, 2006b), a tunable fiber laser was attained by changing microfiber's interaction length by means of stretching (Kieu & Mansuripur, 2006b). In another work demonstrated by Chen *et al.* 2015, a microfiber coupler was used to tune the Q-switched pulse laser's central operating wavelength by controlling the cavity loss (Chen *et al.*, 2015). Lately, Fang *et al.* demonstrated a wavelength tunable thulium-doped mode locked pulse laser (2 μm operating wavelength) where a microfiber based carbon nanotube satuarble absorber was used to fabricate mode-locked pulse and another microfiber was stretched for spectral tuning (Fang *et al.*, 2010). However, the tuning resolution reported in the reference (Chen *et al.*, 2015; Fang *et al.*, 2010; Kieu & Mansuripur, 2006b; Zhou *et al.*, 2010) is higher than 1 nm which making them incompatible and unsuitable for use in ITU (International Telecommunication Union) optical channels. Small scaled tuning resolution is desired in the optical communication channel switching throughout a certain range. In this work, a high resolution sub-nanometer scaled tuneable mode-locked fiber laser is proposed and demonstrated. The mode-locking operation is achieved using Non-linear polarization (NPR) technique, and a microfiber based novel tuning mechanism is included in the mode-locked cavity for tuning purpose. In the proposed tuning mechanism, the mode-locked pulses can be tuned in the sub-nanometer scale, below 1.0 nm. Moreover, the proposed technique is simple to fabricate and operate, and thus, highly cost effective in comparison to other tuning approaches such as the use of gratings (Reekie *et al.*, 1986), exploiting fiber birefringence (Humphrey & Bowers, 1993) or through the use of tunable filters (Huang *et al.*, 2014; Sun *et al.*, 2010b; Wang *et al.*, 2008; Woodward *et al.*, 2014).

4.3.3.1 Tuning Mechanism

The proposed tunable mode-locked pulse cavity set-up is depicted in Figure 4.25. A 980/1550 nm Wavelength division multiplexer (WDM) is used in the cavity, and the light is pumped from a 980 nm laser diode (LD) (Oclaro LC96A74P laser diode). A 0.5 m highly doped erbium doped fiber (Likkie EDF) is used as a gain medium. The output of the EDF is connected to a polarization dependent isolator (PDI), which is used to maintain the polarization state and to ensure unidirectional light propagation. The output of the PDI is connected to the tuning mechanism, which comprises of the microfiber mounted on the V-grooves of a Newport M-562 series XYZ linear stage. The system contains two XYZ linear stages and each stage has sub-micron scaled pulling-losing (tightening-unstretching) system. Two fiber holders are placed in each stage to hold the fiber tightly, and every holder has a "*V*" groove summing a total of 4 "*V*" grooves in four holders of both stages. The microfiber is placed between two stages and is held tightly by the holders. By adjusting the position of the stages (the holders), the microfiber interaction length can be stretched or un-stretched, resulting the tuning the wavelength of the mode-locked pulse. The real image of the tuning mechanism including the stages which is used to tune the mode-locked pulses circulating in the laser cavity is presented in Figure 4.26. The output from the tuning assembly is guided towards the polarization controller (PC) in order to regulate the polarization state of the light. Basically, the combination of the PDI and the PC acts as an artificial saturable absorber to induce mode-locking operation in the cavity. From the PC, the generated pulses continues circulating along the cavity, encountering a 90:10 coupler. 90% of the light is allowed to oscillate inside the laser cavity, and it is connected to the 1550 nm port of the WDM, thus completing the laser cavity. On the other hand, 10% light is tapped out and further divided into two equals portion using a 50:50 coupler, and is analysed using an optical spectrum analyser (OSA) (YOKOGAWA, AQ6370C, spectral resolution 0.02 nm), oscilloscope (YOKOGAWA,

DLM2054, 2.5 GS/s) , a radio frequency spectrum analyser (Anritsu, MS2683 A, 9 kHz-7.8 GHz), an auto-correlator (Alnair Labs, HAC-200) and an optical power meter. A high speed photo-detector (Thorlabs, D400FC InGaAs based, bandwidth 1 GHz) is used when the signal is measured using the oscilloscope and the radio frequency spectrum analyser. The total length of the cavity is estimated around 14.5 meters.

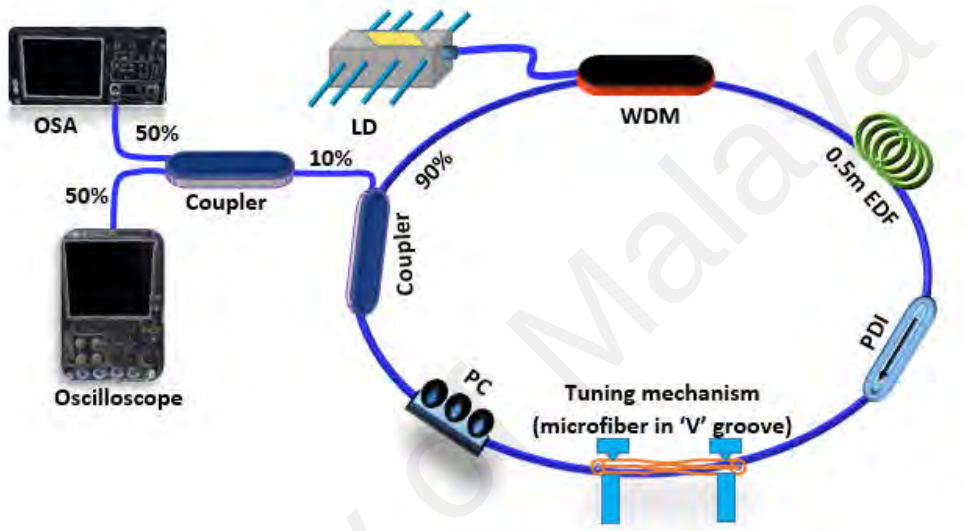

Figure 4.25: Experimental set-up for tunable mode-locked pulse generation using NPR technique and microfiber. Inset left: image of Pulling-losing mechanism enabled linear XYZ stage to stretch the tapered fiber.

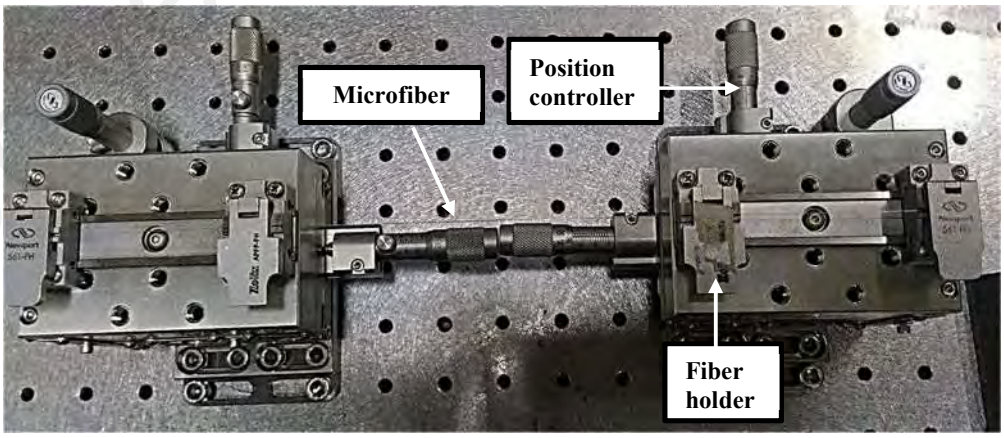

Figure 4.26: Pulling-losing mechanism enabled linear XYZ stage to stretch the microfiber.

The proposed cavity is capable to tune the mode-locked pulse spectrum by changing the spectral response of the microfiber. The microfiber that is utilized in the tuning stage to tune the mode-locked spectrum is fabricated using the flame-brushing technique by means of the homemade fabrication stage. A microfiber of waist diameter of 30 µm is fabricated by following the fabrication process described in Section 3.2. The transmission spectrum is monitored during the fabrication process, where a homemade amplified spontaneous emission (ASE) is used as the seed source. The transmission spectrum of the microfiber is measured through the OSA and the OPM simultaneously. Approximately 3.6 dB of insertion loss is recorded in 1.5 µm region. Figure 4.27 shows the microscopic image of the microfiber waist region, while Figure 4.28 shows the transmission spectrum of the microfiber before the tapering process is started, and also once it is completed.

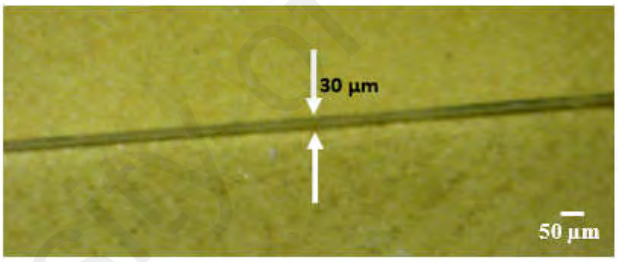

Figure 4.27: Waist region of the fabricated microfiber.

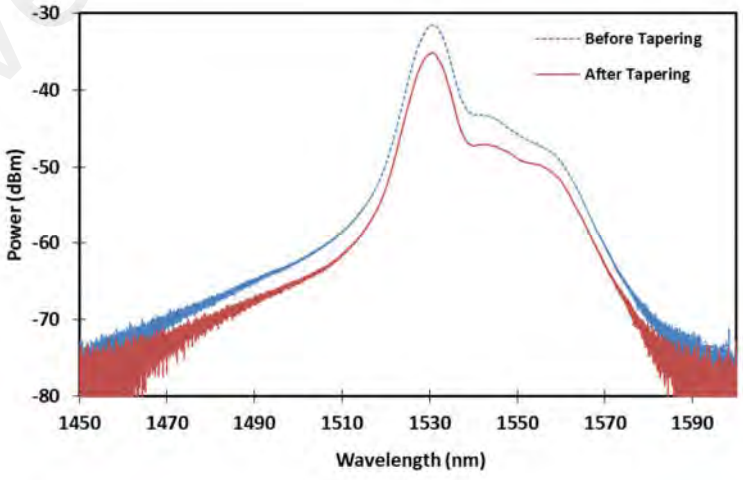

Figure 4.28: ASE spectrum before and after the tapering.

4.3.3.2 Results and Discussion

The threshold input power to fabricate mode-locked pulses is recorded as 60 mW. All the data presented in this work are measured at the pumping power of 130 mW. By tuning the PC, the linear polarized light is changed to elliptically polarized light. The polarized elliptical light gets divided into two orthogonal modes, and while propagating through the EDF, a different nonlinear phase shift occurs to the different orthogonal modes due to the Kerr effect of the fiber. The direction of elliptically polarized light rotates owing to the intensity variance. Rotation for the central part of the noise pulse has occurred in different degrees compared to leading and trailing edges. Mode-locking operation is attained as the light passes through the PDI. When the light propagates through the PDI, which functioned as a polarizer, the leading and the trailing edges get blocked, and only central part manages to propagate with low loss. After sufficient round trips in the ring cavity, mode-locked pulse is achieved (Tiu *et al.*, 2014). Figure 4.29 presents the characteristics of the mode-locked pulse attained through the proposed cavity.

The optical spectrum of the mode-locked cavity is demonstrated in Figure 4.29(a) as measured from the OSA at a resolution of 0.02 nm. The initial central wavelength of the spectrum is recorded at 1660.6 nm; where a full width at half maximum (FWHM) value of 4.04 nm and a spectral bandwidth of approximately 60 nm are measured. Kelly's side bands are observed in the spectrum, which indicates that the mode-locking operation is performed in the soliton regime. The pulse train is recorded using an oscilloscope along with a high speed photodetector. The pulse train is presented in Figure 4.29(b). The time period between two consecutive pulses is recorded about 70 ns signifying a repetition rate of 14.3 MHz, which corresponds to the fundamental repetition rate of the cavity. The stability of the mode-locked pulse is measured through radio frequency spectrum analyser (RFSA). A fundamental frequency of 14.3 MHz is observed as shown in Figure 4.29(c), which further confirms that the pulse fabrication happened at cavity's fundamental

frequency rate. A signal to noise ratio (SNR) of 41 dB is recorded from the RFSA which indicates the generation of stable mode-locked pulses. The pulse width of the pulse is further investigated using an auto-correlator, and a pulse width of 0.90 ps is measured assuming $sech^2$ curve fitting as presented in Figure 4.29(d). The output power is measured about 0.70 mW indicating the efficiency of the laser cavity about 0.53%.

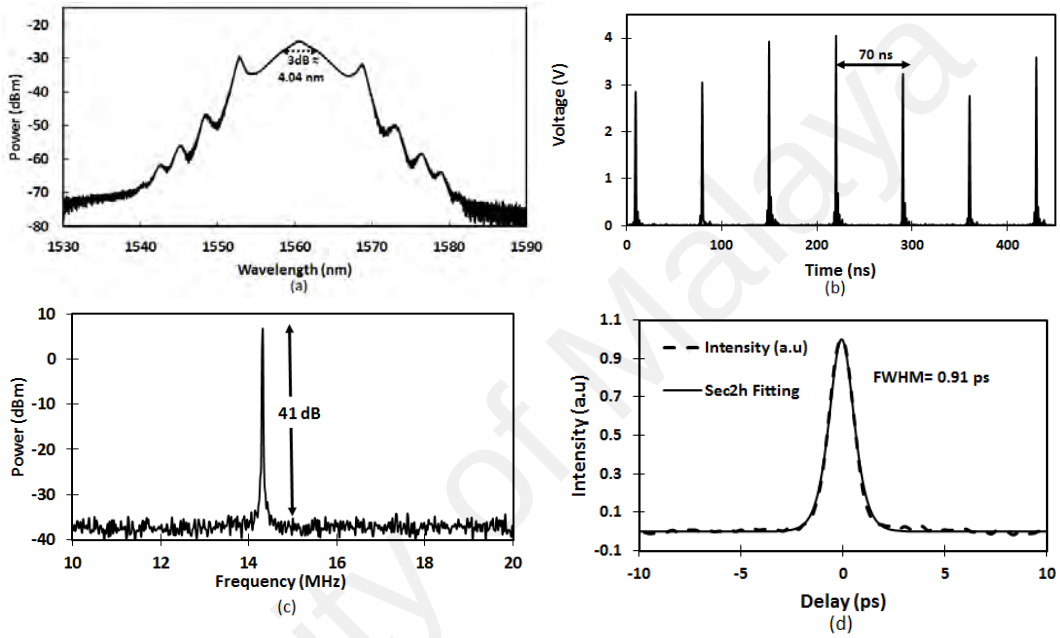

Figure 4.29: Mode-locked characteristic of the output pulses at a pump power of 130 mW, (a) the output spectrum, (b) the pulse train, (c) Radio frequency optical spectrum, and (d) the auto-correlator trace ($sech^2$ curve fitting).

Initially no stretch is implemented in the microfiber and the stretch has been continuously increased in increments of 10 µm. The microfiber has been exposed up to 100 µm of stretch. For the displacement of more than 100 µm, mode-locked spectrum has been found distorted. The central wavelength shifted to shorter wavelength by approximately 4.4 nm (from 1560.6 nm to 1556.2 nm), when 100 µm of stretch is imparted on the microfiber. The shifting of the mode-locked pulse against the imparted stretch is presented in Figure 4.30(a). The plot of the central wavelength shifting with respect to the imparted stretch is displayed in Figure 4.30(b). This phenomena of blue

shifting is related to the wavelength dependent gain of the EDF. Strain in the microfiber suppresses the core side of the fiber as well as increase the interaction length of microfiber and changes the effective refractive index of the microfiber; which generates additional loss. Therefore, the wavelength of the laser has shifted to shorter wavelength to achieve higher gain to compensate the additional loss occurred. This can be described by the phase difference of the light propagation as described by $\phi = \frac{2\pi(\ n_{eff})L}{\lambda}$ where n_{eff} refers to the difference of the effective refractive index of the core and the cladding, L refers to interaction length, and λ is the input wavelength. Any changes L or n_{eff} causes a relative phase change of the light propagation. By exploiting this behavior of the signal, the wavelength of the mode-locked pulse can now be tuned.

(a)

(b)

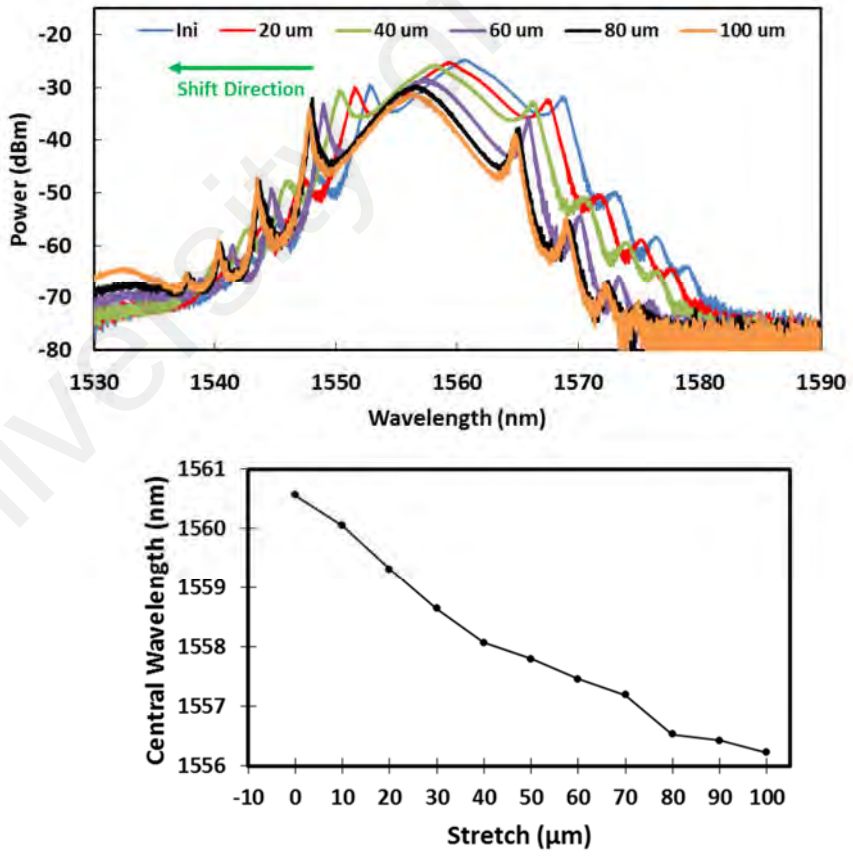

Figure 4.30: Tuning characteristics of mode-locked pulses obtained by imparting different stretch in the microfiber: (a) Spectra, and (b) plot of the central wavelength shifting.

Most importantly, the tuning process is observed as repeatable and reversible. The fabricated microfiber demonstrates a periodic spectral response which can be tuned by stretching and un-stretching. The tuning trend that has been observed in this experiment is consistent with previous reported works (Chen *et al.*, 2015; Kieu & Mansuripur, 2006b).

The behaviour of the pulse width due to the imparted strain is measured through the auto-correlator. No certain change pattern is observed during the experiment and pulse width varied from 0.87 ps to 0.95 ps. In this experiment, changes in the pulse width are observed random, and it varies in between 0.87 ps to 0.95 ps. This might be caused due to the strain imparted on microfiber causing different dispersion on the fiber, and therefore, the pulse width got affected. On the other hand, the output power has decreased because of the strain applied. The output power is decreased from -1.3 dBm to -1.9 dBm corresponding to the stretch of 0 µm to 100 µm. This reduction in output power is attributed to the increasing cavity losses, induced by the microfiber as it is stretched, as well as the shifting of the mode-locked wavelength towards the other gain region of the EDF. The changes in the pulse width and the output power with respect to the applied stretch in the microfiber is illustrated in Figure 4.31.

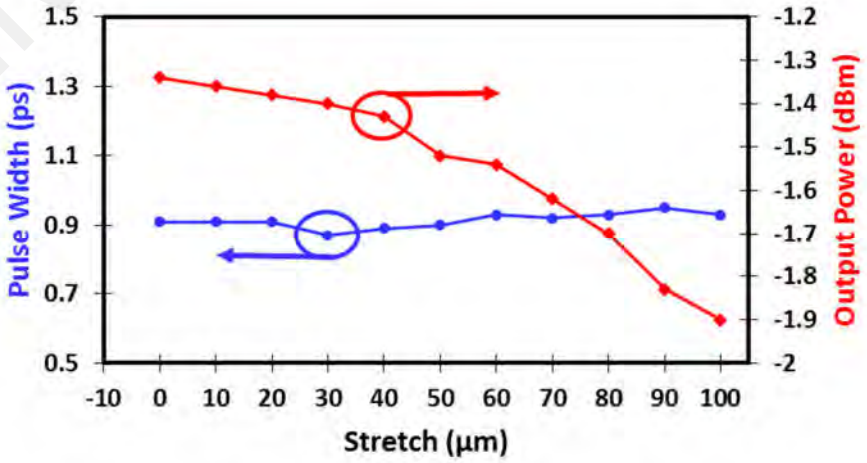

Figure 4.31: Pulse width (ps) and output power (dBm) of the mode-locked pulses against increasing microfiber lengths (stretch).

The overall behaviour of the pulse due to the stretch is investigated further by using the radio frequency spectrum analyser, however, no observable changes in the frequency spectrum of the pulse are observed. The measured signal to noise ratio varies within the range of 41 dB to 39 dB signifying the stability of the pulses. No change has been observed in the output of the laser both in terms of in the wavelength or power of the pulses, even after more than one hour of continuous operation which implies to the pulse stability.

In this work, the mode-locked spectrum central wavelength is tuned from 1560.6 nm to 1556.2 nm, and the achieved tuning range covers 6 different channels of ITU C-Band optical communication system (from channel C21 to channel C26). The proposed technique is able to perform small step tuning compared to the previous works (Chen *et al.*, 2015; Fang *et al.*, 2010; Kieu & Mansuripur, 2006b; Zhou *et al.*, 2010) , capable of maintaining the soliton in stable condition. Most importantly, the tuning process is repeatable and reversible. Thus, the system can be used in high speed communication conveniently and cost effectively (Buus & Murphy, 2006). Another potential application could be a displacement sensor. Moreover, the proposed system can also be used to design tunable lasers for various applications in biomedical and bio-imaging scientific research. This work will encourage further investigation of mechanical laser tuning process. However, material fatigue should be taken care properly due to the limitation of material elasticity.

4.4 Summary

In this chapter, various laser applications of microfiber based devices are described. A non-adiabatic microfiber interferometric device based dual wavelength fiber laser generation is demonstrated in Section 4.2. Subsequently, in Section 4.3, microfiber device based pulse generation, namely the Q-switched pulse generation and the mode-locked

pulse generation is depicted. Q-switched pulse generation is illustrated in Subsection 4.3.1, where the preparation of PNVC-PPy/GO nanocomposite, the fabrication of microfiber based SA device, and the characterization of obtained pulses are described. Mode-locked pulse generation is depicted in Subsection 4.3.2, where the fabrication of SA and the characterization of the attained mode-locked pulse are illustrated. Lastly, a tunable mode-locked fiber laser is described in Subsection 4.3.3, where microfiber based tuning mechanism is proposed and demonstrated.

CHAPTER 5: OPTICAL MICROFIBER BASED SENSORS

5.1 Introduction

Extraordinary optical and mechanical properties of the optical microfiber have been greatly exploited in optical sensing. Due to the small diameter of microfiber, the evanescent field in the surrounding of microfiber is large, and therefore, the microfiber devices are very sensitive to changes of the surrounding medium, particularly the refractive index of the medium (Cardenas-Sevilla *et al.*, 2012; Ding *et al.*, 2005; Jasim *et al.*, 2015; Jasim *et al.*, 2013; Kou *et al.*, 2010; Tian *et al.*, 2008b). So far, Microfiber based devices have been used in various refractometric sensing applications as micro-fluidic sensor, humidity sensor, bio-chemical sensor, gas sensor, temperature sensor, current sensor, displacement sensor, bend sensor, surface sensor, acceleration sensor, force sensor, rotation sensor, acoustic sensor, and electric field sensor (Chen *et al.*, 2013). In this study, microfiber based devices have been deployed in temperature and humidity sensing application. In particular, optical microfiber inline Mach-Zehnder interferometer (OMI-MZI) device has been utilized as a temperature sensor which is described in Section 5.2, and microfiber knot resonator (MKR) device has been used as a humidity sensor which is described in Section 5.3. In both cases, the sensitivity performance of the microfiber devices has been investigated before and after coating with nano-materials. In one case, the uncoated silica OMI-MZI device has been explored to a wide range of temperature changes. After that the OMI-MZI device has been coated with PNVC-PPY/GO nanoparticles, and explored to similar temperature changes as the uncoated one. The temperature sensitivity of OMI-MZI before and after the coating are compared. In the other case, the sensitivity of the uncoated MKR device against humidity variations has been measured and later on, the MKR device has been coated with humidity sensitive

TiO_2 nanoparticle. The effect of titanium dioxide (TiO_2) nanoparticle coating on the detection performance of microfiber knot resonator sensors for relative humidity measurement has been investigated. The details of the study are described in the following sections of the chapter.

5.2 OMI-MZI based Temperature Sensor

The OMI-MZI based sensor works based on the interference of different modes of the light that propagates through the OMI-MZI. The transmission spectrum of the OMI-MZI changes if any change occurs in the propagating modes of the OMI-MZI, e.g. change of the phase difference. The transmission spectrum of the OMI-MZI gets varied if any change in phase difference between the modes occurs by means of the changes in the effective refractive index or changes in the effective interferometer length, or changes in both refractive index and interferometer length. By utilizing and monitoring the shifting of the transmitted output spectrums, various types of refractive index based sensors can be designed. In this study, an OMI-MZI-based temperature sensor is designed and demonstrated.

5.2.1 Sensor Fabrication

In this experiment, an OMI-MZI is utilized as the sensing component. The OMI-MZI is fabricated as by means of flame brushing technique. Tapering is done in 2 places in the microfiber, and the in-between distance of the tapers has been used as the interferometer region. The details of the OMI-MZI fabrication and the specifications of the fabricated OMI-MZI are described in Section 3.4.2. The total length of the fabricated OMI-MZI is measured as 40 mm, and the diameter of the two tapers are measured as 9 μm and 15 μm whereas the diameter of the interferometer region is measured as 106 μm, as shown in Figure 5.1(a). The OMI-MZI transmission spectrum is characterized using OSA where a

homemade ASE source is used as the source. The transmission spectrum of the OMI-MZI along with the specifications are described in Figure 5.1(b).

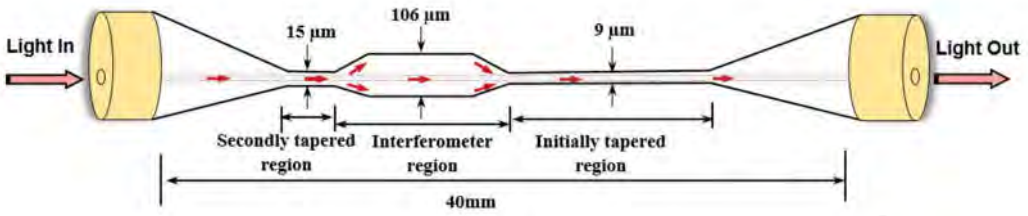

(a)

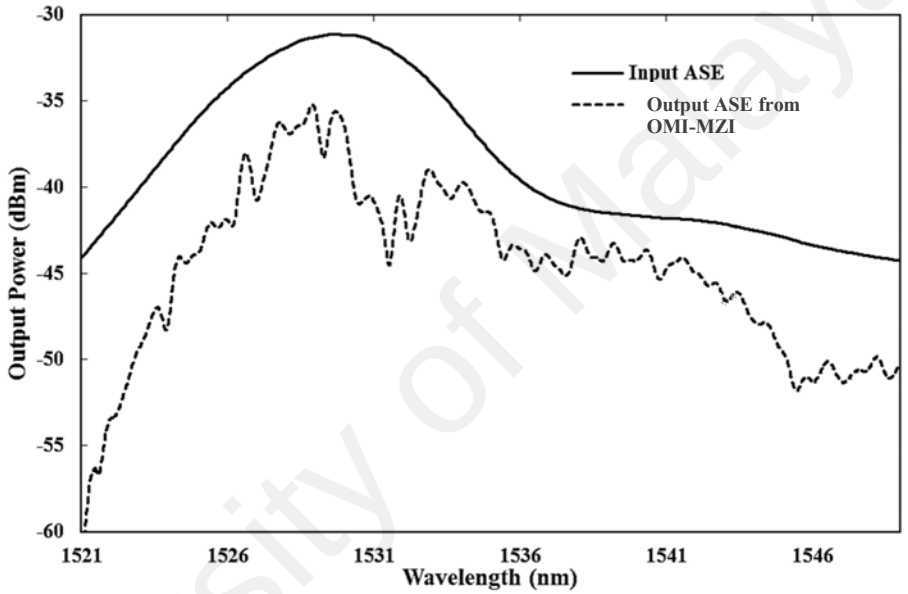

(b)

Figure 5.1: (a) Specification of the fabricated OMI-MZI, (b) Characterization of the OMI-MZI: Transmission spectrum for the incident ASE before and after fabrication.

5.2.2 Results and Discussions

The experimental set-up of the proposed temperature sensor is schematically diagrammed in Figure 5.2 using a hotplate as heating source. The OMI-MZI is placed on the top of the hotplate in such an arrangement that only the OMI-MZI is affected by the heat flow, particularly the dual tapered along with the interferometer region. An insulator box made from the wet carton is used to cover the hot plate so that the heat can be localized inside the box. A rectangular shaped hole is made in the rooftop of the box and the OMI-MZI

device is placed in the hole. The inset of Figure 5.2 displays a portion of the OMI-MZI that is placed in the box hole. The length of the hole is about 4 cm, close to the length of the OMI-MZI device. The settings led the heat to hit the OMI-MZI device directly. This arrangement has been taken in order to make the sensor as precise as possible. In this experiment, the temperature range varies from 26.4 °C to 90 °C. In this range, the wet carton is observed effective in shielding the heat. Once the wet carton got dry, it was taken out of the experimental set-up and water was applied cautiously in order to make it wet again using a watered-handkerchief. This design is observed okay to be used in low range temperature sensing. The OMI-MZI part is very sensitive to temperature change, and whole OMI-MZI was open to the heat (was placed on the hole) and there was no shield. Therefore, there was no or very minimum steam, and the steam was of insignificant impact in the measurement. A commercial thermocouple (FLUKE 714) is positioned just beside the OMI-MZI device as the reference to measure the real temperature and calibrate the sensor. A homemade broadband ASE source is used as a seed, and is connected to the input of the OMI-MZI. On the other hand, during the experiment, the output port of the OMI-MZI is connected to the OSA and OPM in order to monitor the spectral response and insertion loss.

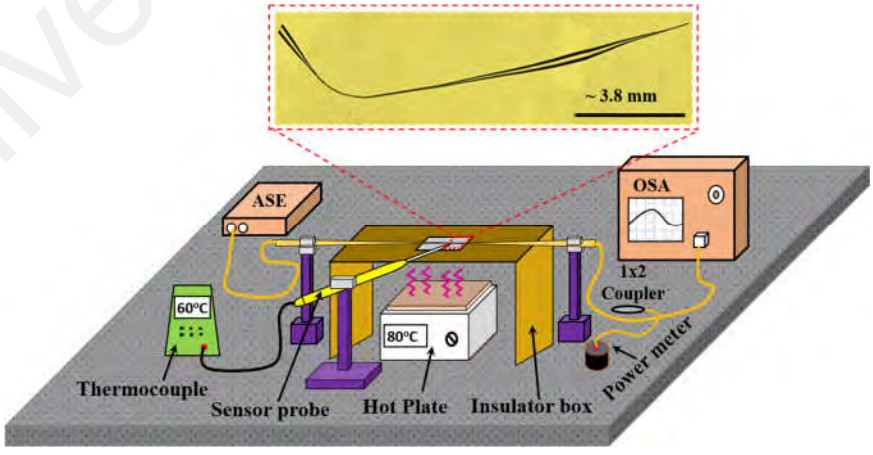

Figure 5.2: Schematic for temperature sensing.

The experiment is initiated at the standard room temperature (25 °C) and then, the temperature is increased sequentially. The heating mechanism works as follows- by increasing the temperature of the hotplate surface, the temperature of the insulator box gets increased which subsequently increases the temperature of the OMI-MZI and its surroundings. The wavelength of the k-th order attenuation peak λ_v shifts as a result of temperature increase in the OMI-MZI. The shifting of the wavelength occurs owing to the changes in the effective refractive index of the surroundings which causes the Δn_{eff} (the difference of the effective refractive index of the core and m-th order cladding-air modes, $n_{eff} = n_c^{eff} \quad n_{clm}^{eff}$), and the ΔL_{eff} (the changes in the interferometer length) to increase. The increase in Δn_{eff} and ΔL_{eff} comes from the thermo-optic and thermal expansion effects respectively as described in Equation 5.1. The increase can be explained based on the density of the air. When the temperature is increased, the air gets hot resulting a decrease in the air density and less refractive index. Therefore, effective refractive index of the cladding air $n_{clm}{}^{eff}$ decreases, and Δn_{eff} increases. Thus, the spectrum shifts to the longer wavelength (red shifting). Moreover, the increment of temperature reduces the evanescent field propagation resulting enhanced output power. The shifts of the OMI-MZI's interference fringe against varying temperatures are demonstrated in Figure 5.3. A red shifting trend can be easily observed from the spectrums displayed in Figure 5.3, as a consequence of increase of temperature. For instance, at the room temperature, the reference attenuation peak wavelength is recorded at 1532.26 nm, which is shifted about 560 pm to 1532.82 nm when the temperature is increased to 55 °C. The attenuation peak wavelength has shifted further from the reference wavelength by an approximate value of 1.72 nm to 1533.98 nm, when the temperature is raised to 85 °C. The spectral response observed above 65 °C seems little bit different compared to below 65 °C temperature. This can be explained as follows. The slight nonlinear wavelength shift against rising temperature is likely can be justified due to the bending deflection of the IMMZI structure

that may be induced during the heating process, since the fiber core and cladding materials are slightly inhomogeneous. In this experiment the temperature is increased gradually, which can induce a slight bending in the IMMZI at a certain temperature. Since the IMMZI has non-uniform profile due to the dual tapered region, this leads to additional change in the Δn_{eff}, excluding the normal increase caused by temperature increases (Xian *et al.*, 2016). At a temperature of ~65 °C and above the wavelength shift starts to drift higher when compared to the shift below 65 °C. This pattern was also observed with IMMZI after deposition with PNVC-PPy-GO. Though the linearity of wavelength was improved after deposition. In this study, besides wavelength shifting, output power is also considered as an additional parameter to observe the response of OMI-MZI sensor with respect to the temperature variations.

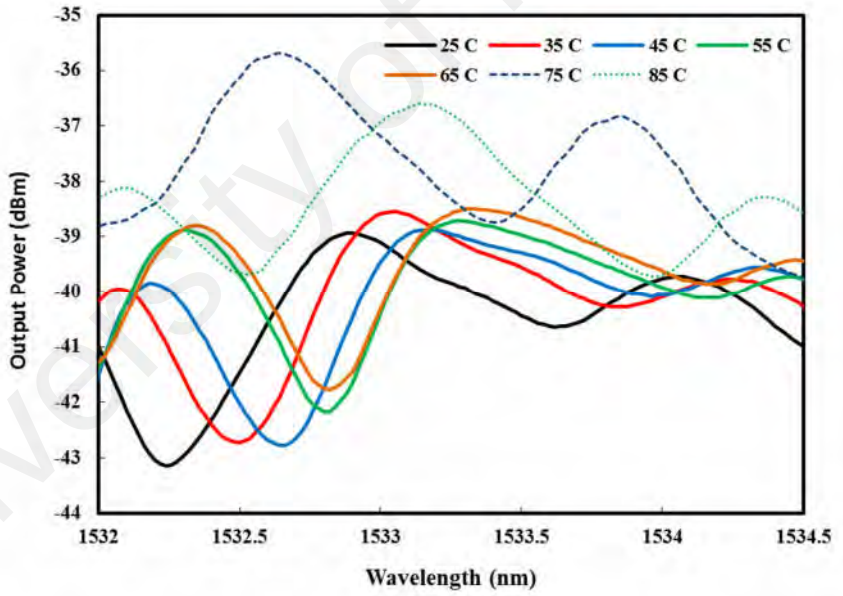

Figure 5.3: Transmitted interference spectra of the OMI-MZI at around 1532.26 nm with different temperatures applied (before deposition).

The plot of wavelength shifts against different temperature is illustrated in Figure 5.4. It is noteworthy to mention that the temperature readings plotted in Figure 5.4 is referring to OMI-MZI's surroundings temperature measured through the thermocouple. A

sensitivity of 30.4 pm/^{o}C is measured with a correlation coefficient of r >0.91 (r^2=0.84). The resolution of measurement is also calculated to be 0.986 ^{o}C. On the other hand, the output power of the peak wavelength is increased as a consequence of temperature increase. The output power at 90 ^{o}C temperature is recorded about 2.17 dB higher than the reference output power recorded at 25 ^{o}C temperature. The increment in the output power is a consequence of the reduced insertion loss of the OMI-MZI as a result of being exposed to heat. The enhancement of the output peak power with respect to temperature increment is also presented in Figure 5.4.

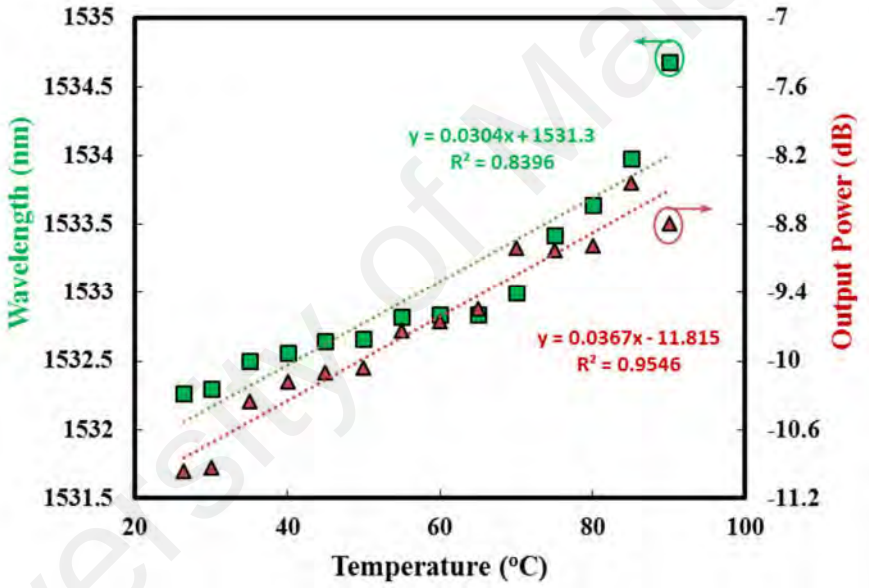

Figure 5.4: The shift of the dip wavelength and changes of the output power with respect to the temperature increment (before deposition).

Thereafter, the same OMI-MZI device is deposited with the PNVC-PPy/GO nanocomposite solution. The preparation of PNVC-PPy/GO solution has been described in Section 4.3.1.1(a). Similar deposition method described in Subsection 3.4.1.1 has been followed in the deposition process with the only exception that in this experiment PNVC-PPy-GO solution has been used instead of GO solution. The length of the OMI-MZI in which the PNVC-PPy/GO composite interacts with the incident light is estimated to be

20 mm as presented in Figure 5.5. The deposition loss was measured as 2.6 dB. The deposition processing time is recorded approximately 10 minutes. Figure 5.6 represents the schematic of PNVC-PPy/GO nanocomposite deposition process. The cross section of the PNVC-PPy/GO nanocomposite deposited OMI-MZI is represented in Figure 5.6(a), while the real microscope image of the PNVC-PPy-GO nanocomposite deposited microfiber is presented in Figure 5.6(b).

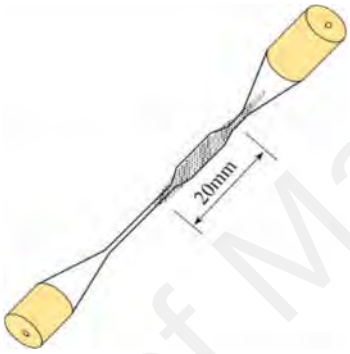

Figure 5.5: Deposition process of OMI-MZI with PNVC-PPy/GO nanocomposite.

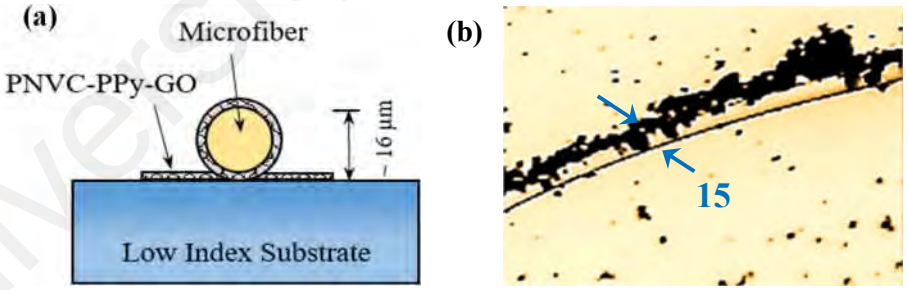

Figure 5.6: (a) Schematic diagram of the cross section, and (b) Optical microscope image; of the PNVC-PPy/GO deposited OMI-MZI.

The PNVC-PPy/GO coated OMI-MZI has been placed on the experimental set-up upon the completion of the deposition process, and the experiment is repeated. The temperature of the hot plate is increased sequentially, and the wavelength of the *k*-th order attenuation peak λ_v has exhibited blue-shifting trend with more stability. The blue shifts

occurred because of the decrease in Δn_{eff} resulting from the increment of the temperature of the OMI-MZI surroundings, assuming the changes of the interferometer length ΔL_{eff} remained the same before and after deposition. Because of deposition of PNVC-PPy/GO, the increase in the temperature creates a significant changes in the effective refractive index of the cladding modes $n_{clad}{}^{eff}$ compared to the effective refractive index of the core modes $n_c{}^{eff}$. The changes in the $n_{clad}{}^{eff}$ happened in higher degree compared to $n_c{}^{eff}$ which resulted a decreased value of Δn_{eff}. Therefore, the peak wavelength shifted to the shorter wavelength (blue shift).

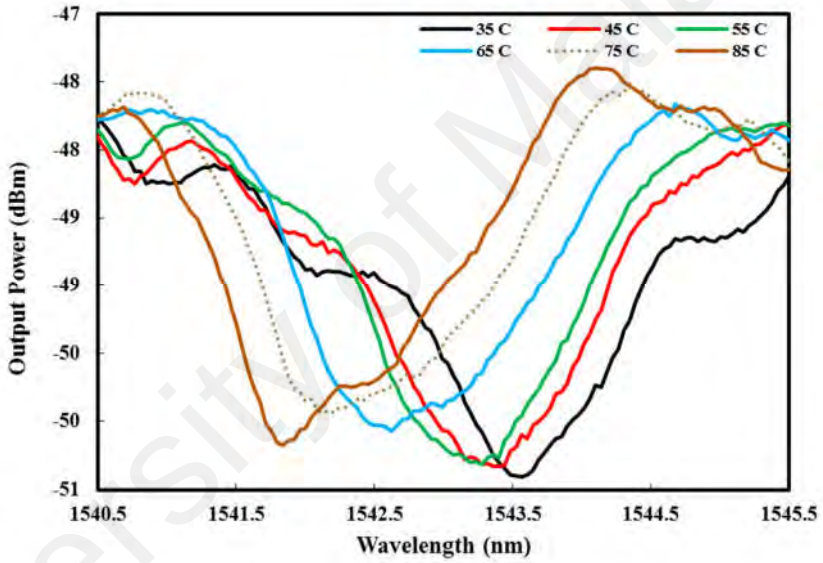

Figure 5.7: Transmitted interference spectra at around 1543.6 nm with different temperatures applied.

The shifts of the PNVC-PPy-GO nanocomposite deposited OMI-MZI's interference fringe against varying temperatures are illustrated in Figure 5.7. It can be observed from the spectrums that the interference fringes shift smoothly and more stably to the shorter wavelength (blue-shift), as a result of increase in the temperature. For instance, the reference attenuation peak is measured at 1543.56 nm at a temperature of 35 ^{o}C, which is shifted by approximately -290 pm to 1543.27 nm when the temperature is raised to 55 ^{o}C. The attenuation peak wavelength has shifted further to 1541.83 nm, approximately

- 1.73 nm from the reference wavelength, when the temperature is increased further to 85 °C. It is worth to mention that, both the uncoated and the PNVC-PPy/GO coated OMI-MZI temperature sensors exhibit almost the same wavelength shifts at 85 °C which is measured about ~ ± 1.7 nm. The only difference noted is that the PNVC-PPy/GO deposited OMI-MZI demonstrates high sensing stability in terms of temperature sensing.

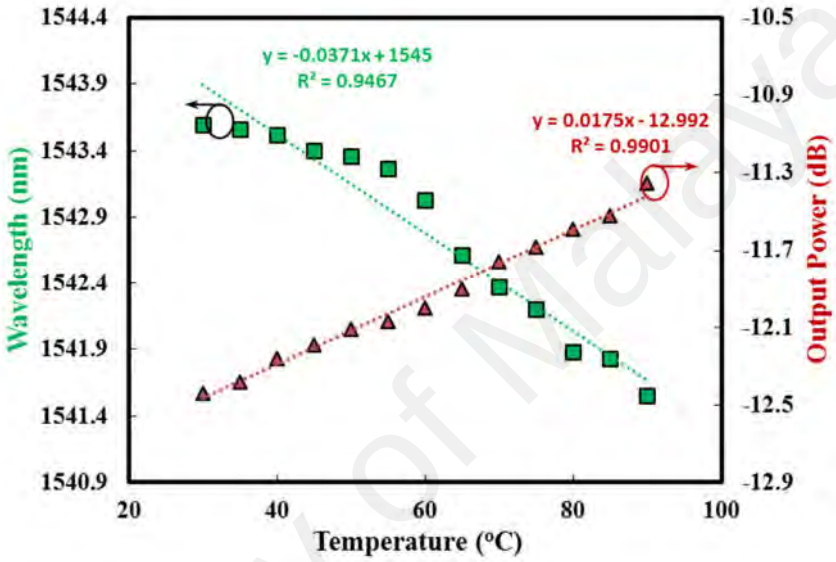

Figure 5.8: The shift of the dip wavelength and changes of the output power with respect to the temperature increment (after deposition).

The plot of the wavelength shifts of the PNVC-PPy/GO deposited OMI-MZI against temperature increment is described in Figure 5.8. A sensitivity of 37.1 pm/°C is measured with a correlation coefficient of r >0.97 (r^2=0.95). The resolution of measurement is recorded as 0.808 °C. By comparing the responses of the un-coated and PNVC-PPy/GO deposited OMI-MZI, it can be said that deposited OMI-MZI demonstrated better sensitivity of about 7 pm with 0.18 °C better resolution. Moreover, the output power of the sensor is improved slightly as a consequence of the temperature increase. For instance, the output power improved of about 1.09 dB at 90 °C, from the power reference

measurement at 30 ºC temperature. The enhancement of the output peak power is also displayed in Figure 5.8.

Differential scanning calorimetry (DSC) analysis is conducted in order to investigate the thermal properties of the PNVC-PPy/GO nanocomposite. A heating rate of 10 ºC/min is chosen and the behaviour of the nanocomposite is monitored during the heating. The attained results are displayed in Figure 5.9. The melting temperature of the PNVC-PPy-GO is measured as 149.87 ºC. It can be said that the nanocomposite has substantially good thermal stability under the present experimental condition, since the range of the temperature variation that is used for sensing experiment is below than the melting temperature.

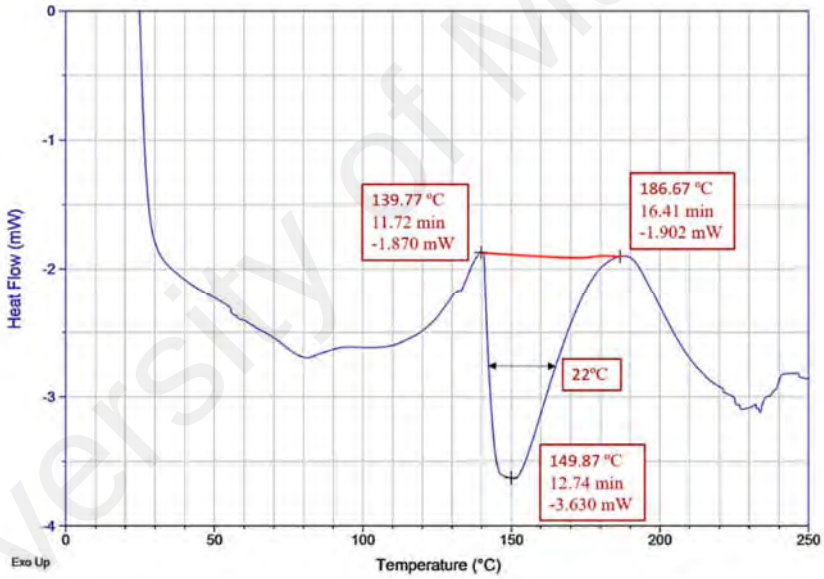

Figure 5.9: The DSC plot for the PNVC-PPy/GO nanocomposites.

The performance of the uncoated and PNVC-PPy/GO-coated OMI-MZI are summarized in Table 5.1. PNVC-PPy/GO-coated OMI-MZI performed better in terms of wavelength shifting sensitivity and stability. The sensing experiment demonstrates that by depositing PNVC-PPy/GO on OMI-MZI, the stability of temperature sensing can be modified which makes the effective refractive index very sensitive to temperature variation. The OMI-MZI device after the deposition shows high sensing stability that is

very important in environment based precise measurements. It is believed that the reported result of this experiment might serve as an important guideline towards advanced study of the effect of PNVC-PPy/GO nanocomposites on microfiber waveguide based sensors.

Table 5.1: comparison of the OMI-MZI response before and after the deposition.

Performance of the Sensor	**Type** / **Parameter**	**Uncoated OMI-MZI**	**PNVC-PPy/GO -coated OMI-MZI**
Wavelength Shifting	Sensitivity	30.4 pm/ ºC	37.1 pm/ ºC
	R^2	0.84	0.95
Output power	Sensitivity	0.0367 dB/ ºC	0.0175
	R^2	0.9546	0.9901

5.3 MKR based Humidity Sensor

The optical researchers have been found to be engaged in finding some humidity sensitive materials to increase the sensitivity of microfiber based humidity sensor. Microfiber based humidity sensors have been demonstrated by coating it with humidity sensitive materials, for instance graphene (Ahmad *et al.*, 2016a) and gelatin (Zhang *et al.*, 2008). In this current study, titanium dioxide (TiO_2) nanoparticle has been used to the coat the MKR. The TiO_2 has been selected since it is very sensitive to humidity, and it exhibits quick adsorption ability (Chen & Lu, 2005). TiO_2 nanoparticle owns a porous structure at room temperature, where water vapor molecules can be adsorbed easily (Chen & Lu, 2005). TiO_2 materials can exist in three phases, which are - anatase, rutile and brookite. Among these phases, the anatase phase exhibits higher water adsorption capability in comparison with both rutile and brookite (Chen & Lu, 2005). Two documented works have been found focusing on TiO_2 based fiber optic relative humidity sensor. To the best knowledge of the author, the first RH sensor based on optical fiber evanescent field of fiber coupled to porous TiO_2 waveguide was demonstrated in 2004 (Alvarez-Herrero *et al.*, 2004). In that work (Alvarez-Herrero *et al.*, 2004), a sensitivity

of 0.46 nm/%RH was measured in the range of 0% to 15% RH, and a sensitivity of 0.025 nm/%RH was observed in 30% to 80% RH range. In a different study, plastic clad silica fiber was de-cladded and TiO_2 nanoparticle sol-gel was deposited; and a sensitivity of 27.1 mV/%RH was attained in the 24% to 95% RH range (Aneesh & Khijwania, 2012). So far, no report has been found in the literature focusing on the response of TiO_2 nanoparticle-coated MKRs against humidity variations. In this study, the RH responses of the uncoated silica MKR and the TiO_2-coated MKR are demonstrated and compared. The sensitivities of both uncoated silica MKR and the TiO_2-coated MKR are compared in terms of two parameter changes - which are the resonance wavelength and transmitted output power level. In this study, a 2.5 mm diameter MKR is made using a 2.1 μm diameter microfiber which resulted a comb like output spectrum. The MKR is exposed to RH changes over a range of 40% to 95%. Subsequently, the MKR is coated with TiO_2 nanoparticles, and an increased sensitivity is measured over the same RH range. The details of this work are illustrated in a later part of this section.

5.3.1 Sensor Fabrication

A microfiber is fabricated using the flame brushing technique following the procedure described in Section 3.2.1, by means of the homemade fabrication stage. The microfiber is intentionally made long since it is used to fabricate the MKR later. The total length of the microfiber including the transition is measured as 12 cm which is sufficiently long to make the MKR. The diameter of the waist region microfiber is measured as 2.1 μm. The transmission spectrum and the output power spectrum of microfiber are characterized using an OSA and an OPM respectively, while an ASE is used as the feed during microfiber fabrication process. The transmission spectrums of the fabricated microfiber before and after the tapering process recorded through the OSA are displayed in

Figure 5.10. The OPM recorded average output power data before and after the fabrication process are compared, and the insertion loss due to tapering process is measured less than 2 dB. The image of the waist region of the microfiber captured through the microscope is displayed in Figure 5.11.

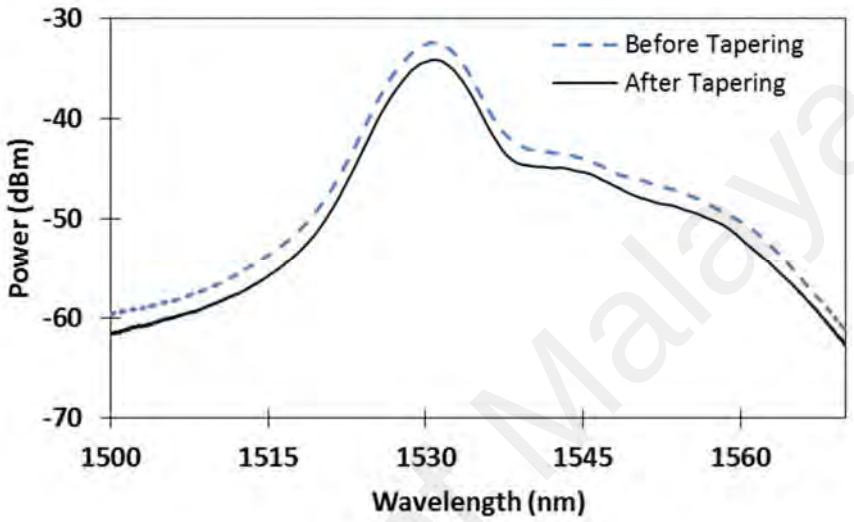

Figure 5.10: Transmission spectrum obtained both before and after the tapering process, measured using an OSA.

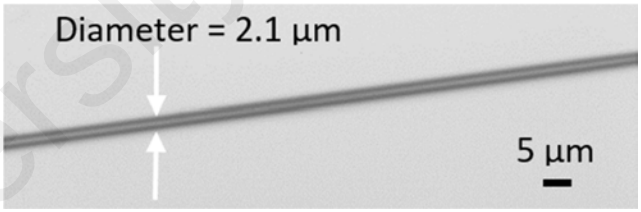

Figure 5.11: The waist region of the microfiber (waist diameter of 2.1 µm).

Consequently, an MKR with a diameter of 2.5 mm is formed (Figure 5.12(a)) following the procedure described in 3.4.3. The fabricated MKR has demonstrated a high quality factor (Q-factor) of 75,000 which is calculated from the sharp dips in the transmission spectrum. The FSR (free spectral range) value is observed within the range of 0.22 nm to 0.23 nm. The transmission spectrum of the MKR is illustrated in Figure 5.12(b), while a tunable laser source is used as the input to the MKR.

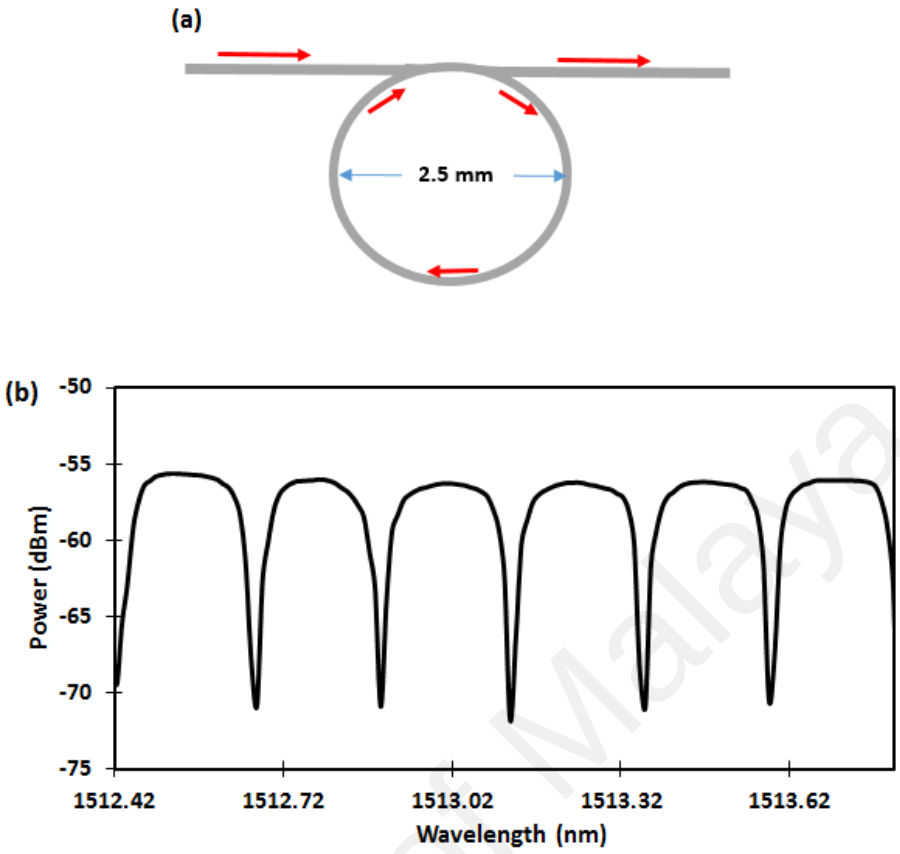

Figure 5.12: (a) Schematic Diagram of the MKR, and (b) Transmission spectrum of the MKR.

5.3.2 Result and Discussion

In the practical investigation, an airtight plastic box is used as a humidity chamber. Two adjustable valves are introduced in the chamber in order to control the humidity conditions inside the chamber (the surroundings of the MKR). One valve permits pure nitrogen (N_2) gas to enter into the humidity chamber to induce dry conditions. Another valve injects nitrogen gas into water which consequently produces wet air (water vapour), and the water vapour is inserted into the chamber to induce humid conditions. The system is designed in such a way that desired dry and humid conditions can be easily induced inside the chamber by controlling both of the valves. A stopcock is added in the chamber which allows the air to outflow from the chamber when opened.

A tunable laser source (TLS) (YOKOGAWA, model-AQ2200-136 TLS module) is used as a seed signal in the experiment. An OSA (YOKOGAWA, model-AQ6370B) is synchronized with the TLS where the output spectrums are monitored. The experimental set-up is presented in Figure 5.13. The MKR is positioned inside the humidity chamber, which has acted as a humidity sensor and responded against the humidity variations. The light from the TLS is inserted into the MKR and the light is allowed to circulate through the MKR. The output from the MKR (i.e. the sensor response) is divided into two equal portions using a 50:50 coupler (3 dB coupler). One of the ports of the 3 dB coupler is measured through the OSA, and the other port is measured using the OPM. Furthermore, the real humidity conditions of the chamber are measured for calibration purposes. A commercially available hygrometer is placed inside the chamber to provide a reference of the humid conditions.

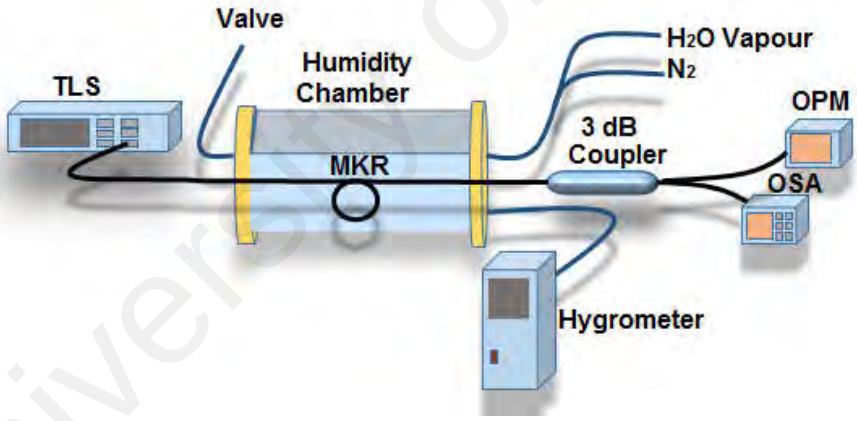

Figure 5.13: RH sensor measurement set-up.

In this study, the responses of the fabricated MKR against different humidity conditions are logged. The responses of the MKR as a function of the humidity are recorded before the coating (uncoated MKR) and after the coating with TiO_2 nanoparticles (Coated MKR). The temperature inside the laboratory is maintained at 25 ^{0}C (±0.4 ^{0}C) during the experimental period, with the intention of minimizing the unwanted effects of temperature change on the resonance wavelength shifting. The exact

RH conditions are monitored by placing the sensing probe of the commercial hygrometer inside the chamber, and the readings are recorded precisely throughout the measurement period.

(a)

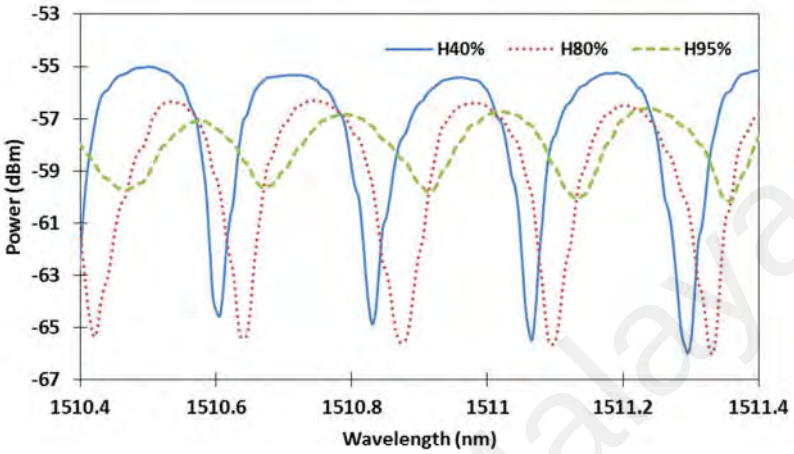

(b)

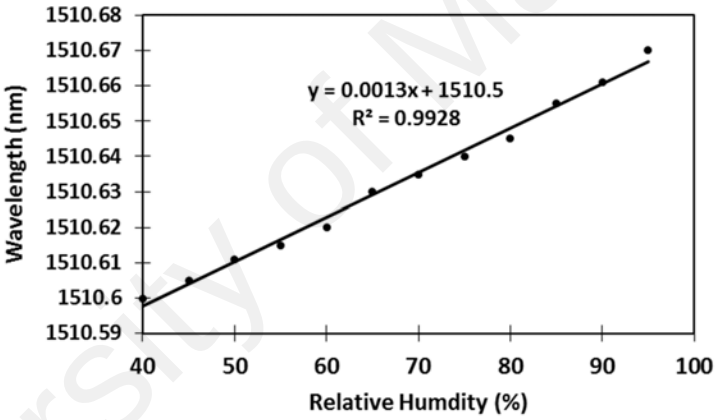

(c)

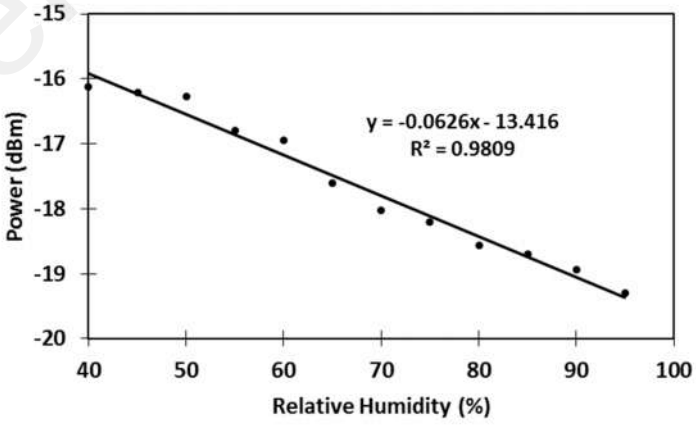

Figure 5.14: Behaviour of the MKR before TiO_2 deposition: (a) Transmitted power spectra for three different RH levels, (b) Resonance wavelength versus RH level, and (c) Output power variation with respect to RH level in the linear region.

The experiment is initiated by inducing humidity inside the chamber. The refractive index of the fiber is changed as a consequence of humidity increase inside the chamber, since the silica fiber adsorbs the molecules of the water vapour. The responses of an uncoated MKR against different humidity conditions are displayed in Figure 5.14. A positive resonance wavelength shift is observed. This behaviour of the shifting can be described as follows- when the RH conditions are increased, the density of the fiber increases owing to the trapped water molecules adsorption, and therefore, the refractive index increases which causes the shifts to the longer wavelength (red shifting) (Wu *et al.*, 2011).

The fabricated MKR has demonstrated a linear response over the 40% to 95% RH range. A sensitivity of 1.3 pm/%RH is recorded with a square regression coefficient (R^2) of 0.9928, as calculated by the resonance wavelength shift (Figure 5.14(b)). The attained sensitivity is in close agreement with a previously reported value of 1.2 pm/%RH (Wu *et al.*, 2011). On the other hand, the output power is decreased as the relative humidity is increased. The reduction in output power can be caused by - the adsorption and condensation of water vapour molecules in the MKR, the micro-bending occurred in the MKR due to the flow of humid air and nitrogen gas, and the variation of refractive index in microfiber-ambient medium or the combination of these factors. A sensitivity of 0.0626 dB/%RH with a square regression coefficient (R^2) of 0.9809 is recorded in terms of the average output power measured using the OPM as presented in Figure 5.14(c).

The MKR is subsequently coated using the ultrasonicated solution of TiO_2. The anatase phase TiO_2 is obtained commercially in the powder form, and the phase is confirmed by performing x-ray diffraction (XRD) analysis with Cu Kα radiation, using a Siemens D500 instrument. The XRD pattern obtained for the TiO_2 nanoparticles is shown in Figure 5.15(a). The observed sharp peaks correspond exactly with the published

diffraction pattern of anatase phase with reference number: 01-073-1764, which ensures that the prepared material is the anatase phase. The morphological and structural characteristics of the sample are investigated using field-emission scanning electron microscopy (FESEM), in a Hitachi SU8000 instrument. The FESEM image of the anatase-phase TiO_2 nanoparticles is shown in Figure 5.15(b).

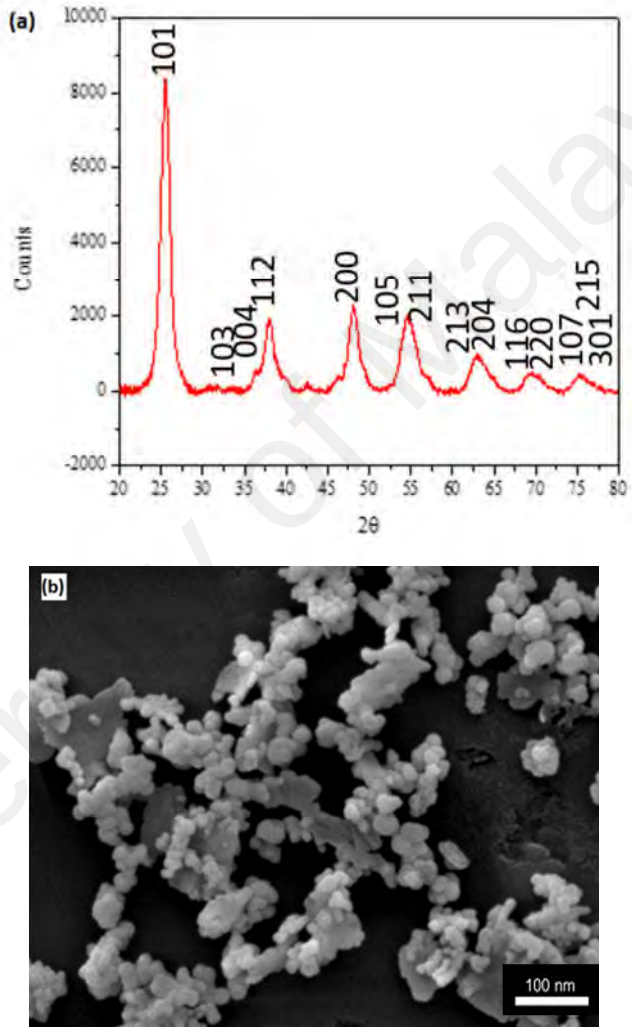

Figure 5.15: Anatase TiO_2 nanoparticles: (a) XRD pattern, and (b) FESEM image.

The TiO_2 powder is mixed with deionized (DI) water. 0.08 mg of TiO_2 powder is immersed in 100 ml of DI water in a glass bottle, giving a concentration of 0.08% w/v. The solution is stirred, using an ultrasonication process, for a period of 10 minutes, in

order to ensure that the solution is prepared as homogeneous. The solution is used for coating the MKR, immediately after carrying out the ultrasonication process.

During deposition, the TiO_2 solution is kept in a plastic vessel and the vessel is attached on top of a 3 dimensional (X-Y-Z) translational stage. The stage is mounted to the MKR height by adjusting the z axis and the MKR is immersed completely in the solution. It is ensured that no collision happened between the MKR and the vessel wall by taking extra precaution, and the loop length and shape of MKR are preserved constant. Once the deposition process is completed, the plastic vessel is taken down by adjusting the height of the z-axis of the translational stage. The deposition set-up is depicted in Figure 5.16. The light from the TLS is inserted into the MKR and the transmitted output power from the MKR is measured though the OPM. The output power readings with respect to the time are used to determine whether the TiO_2 nanoparticles are getting attached to the microfiber or not. Typically, when the nanoparticles get attached to the microfiber, it induces transmission loss which results a decrease in the output power. This behaviour can be used as an indication to understand the deposition progress. In this study, transmission loss has begun to rise instantly after the MKR is immersed in the TiO_2 solution (the output power decreased) giving a clear indication of the initiation of TiO_2 particle deposition in the MKR. The solvent of the coating solution is DI-water which can easily be evaporated and enabled the TiO_2 nanoparticles to become attached to the fiber knot. Besides, the intensity of the evanescent field surrounding the MKR has also attracted the TiO_2 nanoparticles to be deposited on the MKR. The possible mechanism behind the deposition can be explained by the swirl and convection caused by light injection and optical tweezer effect (Kashiwagi & Yamashita, 2009). The whole MKR is coated by the deposition and the length of the microfiber coated with TiO_2 is approximately equal to the circumference of the MKR. The behaviour of transmitted output power of the MKR during the deposition is presented in Figure 5.17. By comparing the output power

measured at the beginning (at $t = 0$) and at the end (at $t = 650s$) of the deposition process, an approximate power loss of 8 dB is measured due to the deposition process, as depicted in the Figure 5.17. It can be seen from Figure 5.17 that the transmission loss has increased monotonically after immersion of the MKR in the TiO_2 solution, and thus, the output power has decreased gradually, which clearly indicates that the TiO_2 nanoparticles are being attached to the MKR. After the deposition, the MKR is taken out of the solution and the output power is varied rapidly (as marked in the square shape). The refractive index of the solutions and the surroundings is different. When the MKR is taken out of the solution, it has experienced a sudden refractive index variation resulting a rapid change in the output power. However, the output power has been observed as stable after a few seconds.

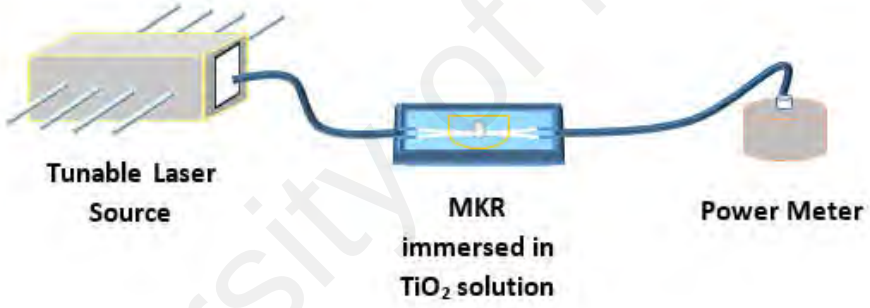

Figure 5.16: TiO_2 deposition process in MKR.

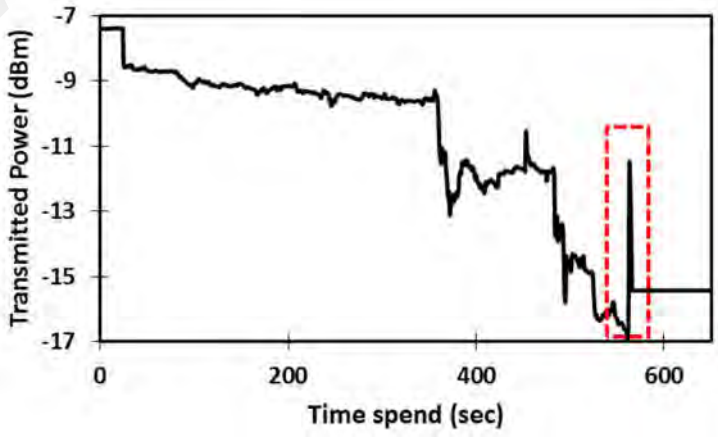

Figure 5.17: Transmission spectrum during deposition.

After the deposition of TiO_2 nanoparticle, the MKR is exposed to a range of different humidity levels. A higher sensitivity is expected from the coated MKR since, the TiO_2 coating is more sensitive to humidity. The structure of TiO_2 is porous – so adsorption and capillary condensation occurs in response to the increase in the RH (Alvarez-Herrero *et al.*, 2004). Owing to the water filling in the porous structure of the TiO_2, the refractive index increases. The responses of the TiO_2-coated MKR when exposed to different humidity conditions are summarized in Figure 5.18.

A linear response is recorded from the TiO_2-coated MKR over the range from 40% to 95% RH. An improved sensitivity of 2.5 pm/%RH is recorded in terms of the resonance wavelength shifts as described in Figure 5.18(b). The sensitivity of the TiO_2 coated MKR sensor is increased by 92.30%, compared to the uncoated MKR sensor. However, a little decrease in the linearity is noticed. The square regression-coefficient (R^2) is decreased to 0.9762, compared with 0.9928 for the response of the uncoated MKR. The reason behind the higher sensitivity exhibition can be illustrated as following: the nano-scale porous structure of the TiO_2 coating allows water molecules to be adsorbed more effectively than in the uncoated silica MKR sensor. The adsorption of the water vapour in the TiO_2 nanoparticle coating has happened in a higher rate compared to the uncoated one, when the RH is increased. Therefore, a more substantial resonance wavelength shift is exhibited by the coated MKR, compared to the uncoated one. On the other hand, the decrease in the output power has occurred at a slightly higher rate when the RH conditions are increased. The output power reduction is recorded about 5 dB over the range from 40% to 95%. A sensitivity of 0.0836 dB/%RH is measured which is higher than the uncoated-MKR (0.0626 dB/%RH), as presented in Figure 5.18(c). However, the linearity of the response in terms of output power is decreased a bit. The square regression coefficient (R^2) of the sensitivity of the output power is slightly decreased to 0.9778 - as compared with 0.9809 for the uncoated MKR.

(a)

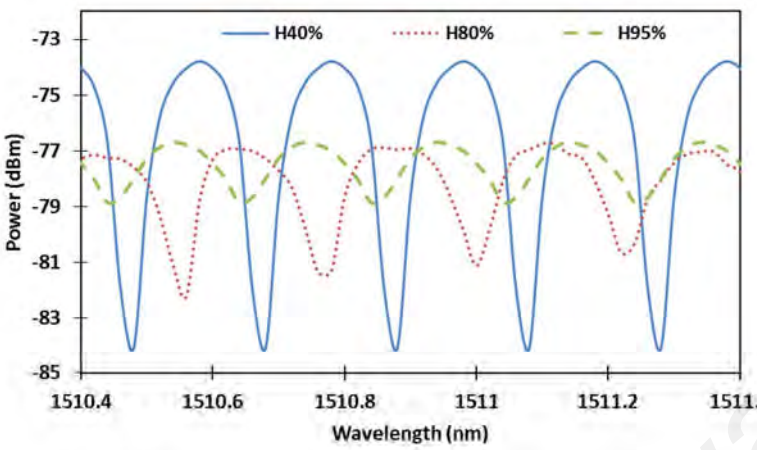

(b)

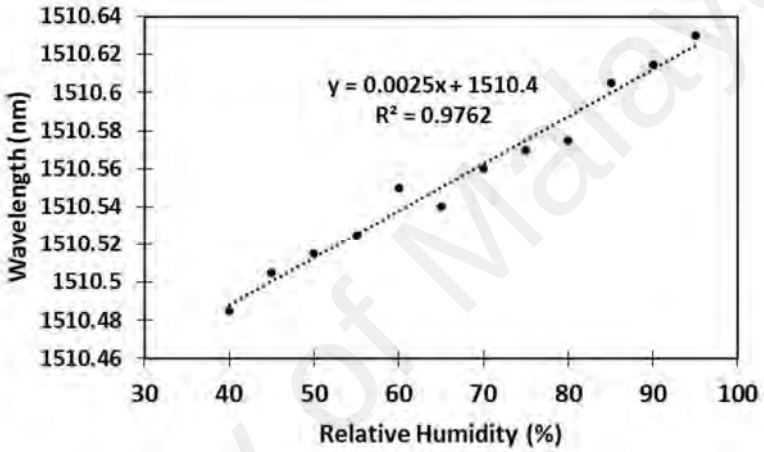

(c)

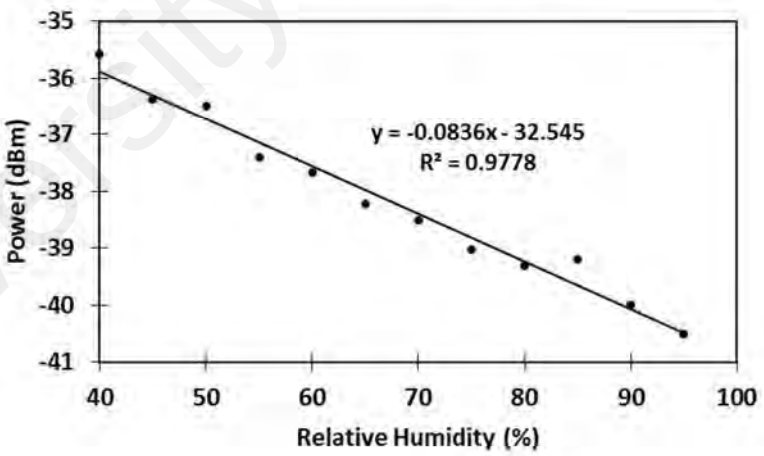

Figure 5.18: Behaviour of the MKR after TiO_2 deposition (a) Humidity response in various RH conditions, (b) Resonance wavelength shifting with respect to RH changes in the linear region, and (c) Output power variation with respect to RH changes.

Within 0-95% RH range, the fabricated MKR sensor didn't exhibit any saturation effect. No sign of saturation has been observed when the sensor is exposed to very high humidity levels. It is postulated that the saturation effect could occur at higher RH range

in the range of 96%-100% RH, possibly near to a humidity of 100%. However, the present experimental condition is capable of inducing up to 95% RH and therefore, the saturation cannot be validated in this current study.

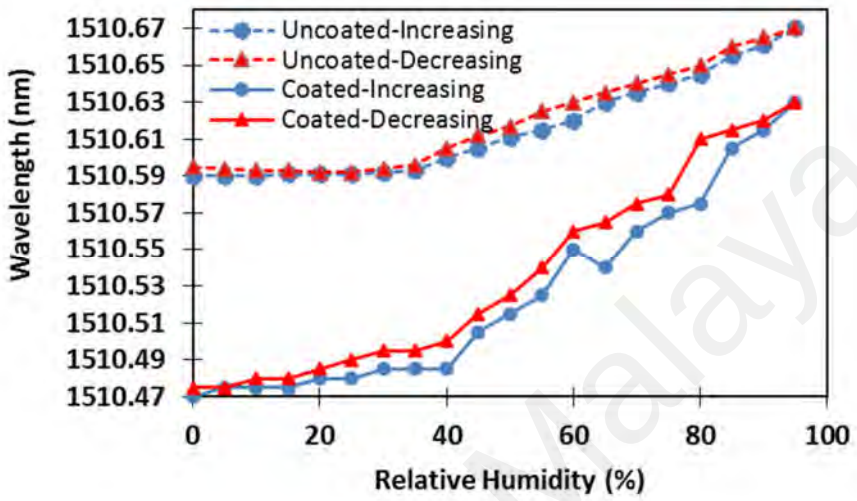

Figure 5.19: Response of the uncoated and TiO_2-coated MKR for increasing trend and decreasing trend of relative humidity.

This study has also considered the round trip response of the proposed MKR humidity sensor. The round trip measurement for the increasing and decreasing of RH cycle are recorded. Both the uncoated and TiO_2-coated MKR are exposed to the increasing trend of RH conditions (from 0% to 95% RH) and decreasing trend of RH conditions (from 95% to 0% RH). The round trip measurements of both the uncoated and TiO_2-coated MKR in terms of resonance wavelength are displayed in Figure 5.19. It can be observed from the Figure 5.19 that the resonance wavelength of the decreasing trend is slightly different from the increasing trend. The deviation between the two measurements is known as hysteresis error. This hysteresis error is originated from the slow dehumidification process. It is presumed that during the dehumidification process, some portion of adsorbed water is left on the MKR from the previous measurement, and therefore, the error is observed. For instance, when the chamber is dehumidified from 95% to 90% RH,

even the reference hygrometer has showed a reading of 90%; most likely the microfiber's humidity is not exactly 90%. The humidity condition of the MKR surroundings is a bit it higher than 90 % RH as hypothesized. It is worthy to mention that such hysteresis error can be minimized by elapsing (waiting) longer time between the measurements.

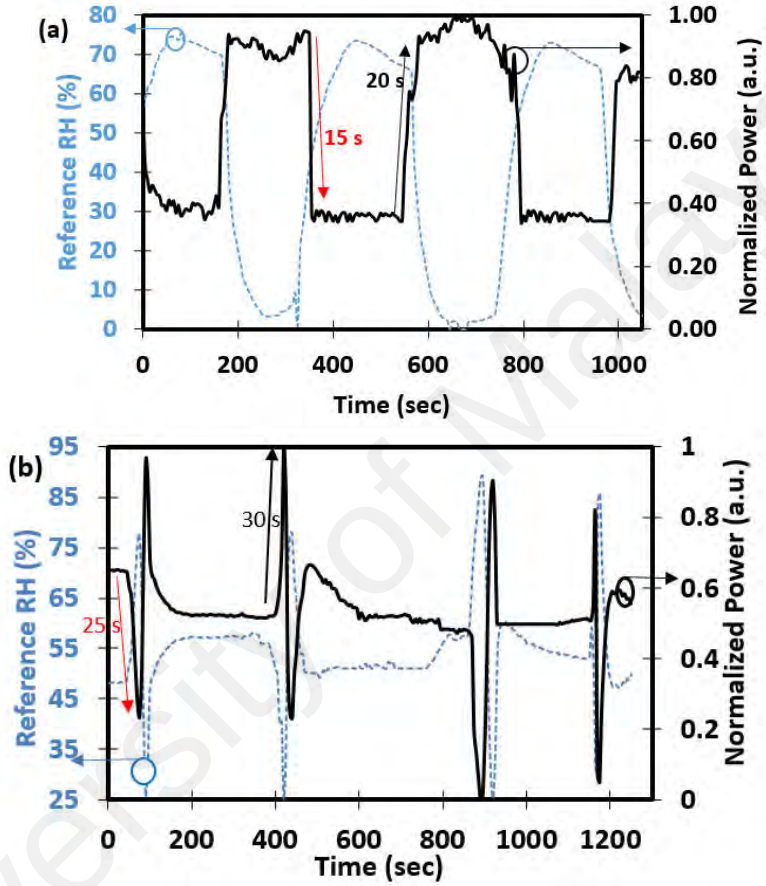

Figure 5.20: Response time measurement. (a) The response of the uncoated MKR against drastic humidity change, and (b) The response of the TiO_2- coated with respect to drastic humidity changes.

This study has also measured the response and recover time of both the uncoated and TiO_2-coated MKR. By inducing the humid and the dry air rapidly, the humidity conditions of the chamber are changed drastically, and both the uncoated and the coated MKR has experienced through an extreme RH variations. The response of the uncoated and the TiO_2-coated MKR response with respect to drastic humidity changes are displayed in Figure 5.20(a) and Figure 5.20(b), respectively. The reference relative humidity,

normalized output power and time spend are plotted on the primary y-axis, the secondary y-axis and the x-axis, respectively. The humidification and dehumidification pattern measured through reference hygrometer during the uncoated MKR response time measurement is recorded as follows: (70% RH (maintained for a while) → 0% RH (maintained for a while) →70% RH (maintained for a while) → 0% RH (maintained for a while) → 70% RH (maintained for a while) → 0% RH). The response time and recovery time are recorded approximately as 15 s and 20 s, respectively. For measuring the response time of TiO_2-coated MKR, the following pattern of humidification and dehumidification is recorded through reference hygrometer: (Room Humidity → 75% RH → 25% RH → Room Humidity (maintained for a while) → 25% RH → 75% RH → Room Humidity (maintained for a while) ->90% RH → 0% RH → Room Humidity (maintained for a while) → 85% RH → Room Humidity). It is wise to mention that, during the response time measurement, the humidity condition of the laboratory is measured about 50% RH. For the case of TiO_2-coated MKR, the response and the recovery time are measured as 25 s and 30 s respectively. A fast response time and a slow recovery time can be observed from the recorded responses of the sensor in both the uncoated and the coated cases. The fast response time and slow recovery time can be attributed to the fast diffusion process of the water molecule and slow desorption process.

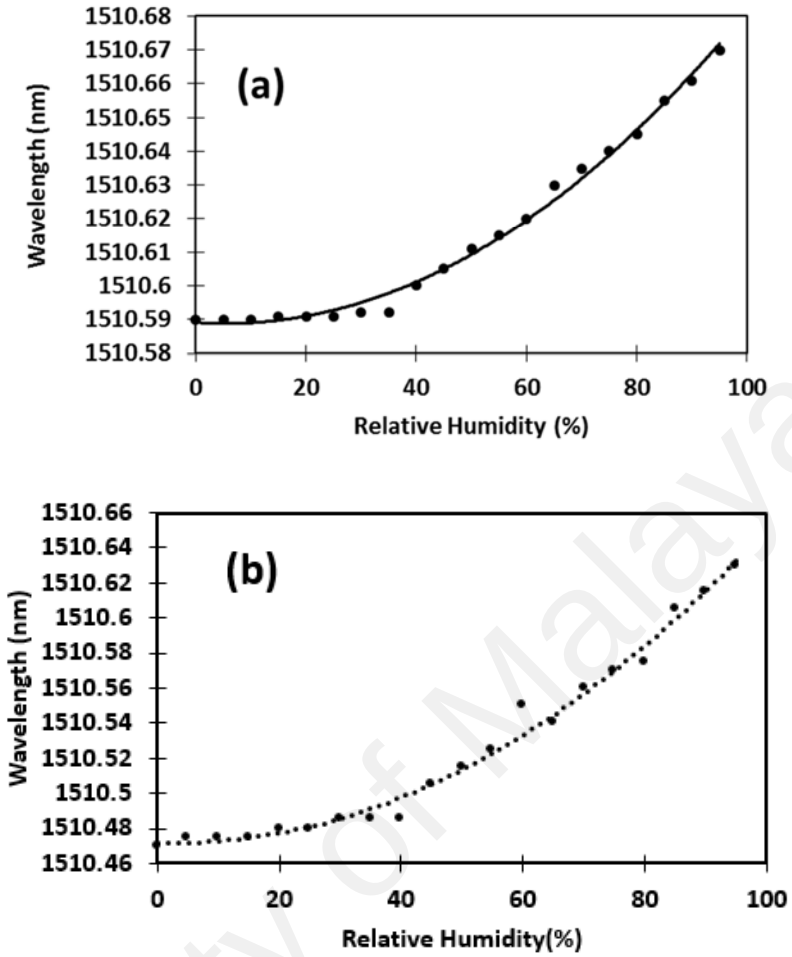

Figure 5.21: (a) The response of the uncoated MKR against relative humidity variation (0%-95% range), and (b) The response of the TiO_2-coated MKR against relative humidity variation (0%-95% range).

In the proposed sensor, the threshold of linear response is recorded as 40% RH. The sensor has linearly responded well in between the ranges of 40%-95% RH, and a much lesser sensitivity is observed in lower RH conditions (0%-35% RH), as depicted in Figure 5.21(a) and Figure 5.21(b). The sensitivities of the uncoated and TiO_2-coated MKR in terms of the resonance wavelength at lower humidity range (0%-35% RH) are recorded as 0.06 pm/%RH and 0.4 pm/%RH, respectively, which are much smaller than the sensitivity achieved at 40%-95% RH. Such response characteristic is attributed to the thickness of the microfiber. It is postulated that the fabricated microfiber (2.1 μm) is not sufficiently thin to perform precise sensing at lower RH conditions. Sub-micron diameter

microfiber could be a choice in order to detect humidity at lower RH range. In a study, Zhang *et al.* demonstrated a gelatine coated 680 nm diameter microfiber based humidity sensor which responded in much lower humidity range covering a wide measurement range comprising 9%-94% RH (Zhang *et al.*, 2008). However, material fragility could appear as a vital challenge in such case. Therefore, it is important to note into account that while this approach allows for measurement along a wide humidity range, the fragile nature of the materials and the very thin diameter of the microfiber can pose a substantial challenge to the fabrication and operation of the sensor.

Table 5.2: comparison of the MKR response before and after the deposition.

Performance of the Sensor	**MKR Type** / **Parameter**	**Uncoated MKR**	**TiO_2-coated MKR**
Resonance Wavelength Shifting	Sensitivity	1.3 pm/%RH	2.5 pm/%RH
	R^2	0.9928	0.9762
Output power	Sensitivity	0.0626 dB/%RH	0.0836 dB/%RH
	R^2	0.9809	0.9778

The responses of the uncoated MKR and TiO_2-coated MKR are compared in order to portrait the impact of TiO_2 coating on enhancing the humidity sensing performance. The comparison is presented in Table 5.2. It is obvious that the TiO_2-coated MKR has demonstrated higher sensitivity both in terms of the shift in the resonance wavelength and the rate of decrease of the transmitted output power. Due to higher humidity sensitivity of TiO_2 , the TiO_2 coated MKR observed more sensitive compared to the uncoated MKR. The sensing parameter can be selectively chosen based on the needs of the applications by balancing the required accuracy and budget. It is worthy to mention that relatively expensive equipment and experimental set-up are required to monitor the shift in the resonance wavelength, whereas the changes in the transmitted power can be measured

using cheaper equipment, such as an optical power meter. Therefore, output power based MKR humidity sensor can be employed in cost-effective humidity sensing applications. On the other hand, a resonance wavelength shifting (or a combination of resonance wavelength and transmitted power measurement) based MKR humidity sensor offers the benefit of being more precise and accurate, and therefore can be employed in more critical and accuracy-dependent sensing applications which require more cautious attentions.

It is believed that the reported result of this experiment might serve as an important guideline towards advanced study of the effect of TiO_2 nanocomposites on microfiber waveguide based sensors.

Table 5.3: Comparison of the fabricated MKR device with conventional sensors.

Types	**Sensing method**	**Reference**	**Sensitivity**	**Range (%RH)**	**Response time**
Conven-tional	Capacitive	(Kang *et al.*, 2006)	9 tF/%RH	3-98%	50 s (in adsorption) and 70 s in desorption
Conven-tional	Capacitive/Resistive. Thin-film surface micromachining technology (Substrate with resistor and interdigitated electrodes)	(Park *et al.*, 2001)	17tF/%RH	8-97%	40 s (in adsorption) and 70 s (in desorption)
Optical	MKR device	This work	1.3 pm/%RH	40-95%	15s(in adsorption) and 20s in desorption
	TiO_2 coated MKR device	This work	2.5 pm/ %RH	40-95%	25s (in adsorption) and 30s (in desorption)

The performance of the MKR device with conventional humidity sensors are described in Table 5.3. It can be seen that MKR based humidity sensor offers faster response than conventional sensors. This is one of reason of employing optical sensor in humidity measurement since it offers fast response compared to conventional one. Moreover,

optical sensor offers many other advantageous features such as small size, immunity to electromagnetic interference, multiplexing and remote sensing facility, making them a right choice for the circumstances where immunity to electromagnetic interference, multi sensor operation, in situ and remote monitoring are required.

5.4 Summary

In this chapter, microfiber based temperature sensor and microfiber based humidity sensor is presented. An OMI-MZI based temperature sensor is presented in Section 5.2, where the sensor fabrication, and the response of the OMI-MZI with respect to temperature increase have been depicted. The impact of the PNVC-PPy/GO coating in improving the sensing performance is also presented. In Section 5.3, a MKR based humidity sensor is portrayed. The sensor fabrication, and the response of the MKR device with respect to the humidity variation have been described. The effect of titanium dioxide (TiO_2) nanoparticle coating on the detection performance for relative humidity measurement has been investigated and presented too.

CHAPTER 6: CONCLUSION

6.1 Conclusion

Optical microfibers are considered one of the most adaptable and promising photonic components for future integrated photonic system. Optical microfibers have been studied intensively because of having many interesting versatile properties such as strong evanescent field, high nonlinearity, three dimensional assemble capability, high configurability and ease of integration with the fiber system, low fabrication cost, and low insertion loss. In this study, the microfiber has been fabricated using 'top-down' fabrication method known as flame brushing technique. Both the adiabatic and the non-adiabatic microfiber have been fabricated, and different types of microfiber based devices have been assembled and used in various laser and sensing applications. A non-adiabatic interferometric microfiber of a waist diameter of 2 μm and length of the 15 cm has been fabricated in which the abrupt change is made to obtain inter-modal interference. A significant interference pattern has been observed in the transmission spectrum of the fabricated non-adiabatic microfiber, and when the microfiber is inserted in the 1.5 μm laser cavity, stable dual wavelength has been achieved by taking the advantage of interference pattern which supresses the mode competition of the EDF gain medium. Six sets of dual wavelength operating in the C band region (particularly 1556.71 nm - 1562.13 nm) with different inter-spacing of 0.4 nm - 3.32 nm are attained by controlling the polarization state of the cavity with the assistance of a PC. This work demonstrates the promise and potential for the lasing technology in 1.5 μm wavelength region, especially for dual wavelength based laser application.

Moreover, microfiber based devices have been employed in the pulse laser applications. A microfiber of waist diameter of 8 μm and total length of 6.5 cm is

fabricated and subsequently coated with Poly (N-vinyl Carbazole) - Polypyrrole/Graphene Oxide (PNVC-PPy/GO) nanocomposite material to make microfiber based saturable absorber device. The SA device has been inserted in 1.5 μm laser cavity, and Q-switched pulses have been attained. The light which propagates through the microfiber interacts with the nanocomposite SA coating, and therefore, the saturable absorption occurs which generates the Q-switched pulses. Q-switched pulses are obtained with repetition rates of 25.2 kHz to 42.7 kHz and pulse widths of 5.74 μs to 2.48 μs over a pump power range of 12.8 mW to 40.0 mW. A maximum average power and pulse energy of 0.19 mW and 4.43 nJ are also observed respectively. The proposed cavity comes with a simple design and low fabrication cost, and it minimizes the drawbacks of conventional passive Q-switching technique of SA being burned due to high power laser operation. The demonstrated microfiber based Q-switched pulse laser can be used in various medical, industrial and material processing applications.

Furthermore, an adiabatic microfiber has also been employed in mode-locked pulse generation applications. Pulses with picosecond pulse width are highly desired for high precision laser applications. This study elucidates a technique to fabricate short pulse-width mode-locked pulses from a laser cavity. An adiabatic microfiber of waist diameter of 11 μm has been fabricated with special care by ensuring homogeneous and smooth conical transition region with minimal multimode interference and comb filter effect. Afterward, the graphene oxide is deposited on the waist region of the microfiber using the optical deposition technique to fabricate microfiber based GO SA device. A length of about 40 μm has been deposited and the fabricated SA device has been introduced into the laser cavity. Due to the saturable absorption, the proposed cavity fabricates the mode-locked pulse with a pulse width of 3.46 ps, a 3dB optical bandwidth of 11.82 nm and a repetition rate of 0.920 MHz. The demonstrated system has substantial potential for many crucial medical, communication, bio processing, military, and industrial applications. In

addition, a microfiber based novel tuning mechanism has been demonstrated in this study. A 3 dimensional pulling –losing mechanism made of two linear stages is demonstrated. By changing the interaction length and the refractive index due to the stretching-unstretching effects, the mode-locked pulse spectrum has been tuned. Tuning of the laser is done by stretching the microfiber from 0 to 100 μm in 10 μm increments through the use of the linear translation stage. The output from the fiber laser has been tuned over a span of 4.4 nm, from 1560.6 nm to 1556.2 nm, with a repetition rate of 14.3 MHz. The proposed tunable mode-locked laser covers the C21 to C26 channels of the ITU C-band optical communications spectrum, and maintains stable soliton operation as well as being repeatable and reversible, making it highly desired for various communications, medical and sensing applications.

On the other hand, microfiber based devices also have been employed in temperature and humidity sensing applications. An optical microfiber inline Microfiber Mach-Zehnder interferometer (OMI-MZI) has been fabricated with the following specifications- total length of 40 mm, and diameter of 9 μm and 15 μm for the dual tapered regions, and interferometer region between the two tapered regions of 106 μm. Significant interference has been attained among the various modes of the propagating light as a consequence of the microfiber structure. The OMI-MZI has been exposed to various temperature from 25 ^{o}C to 90 ^{o}C. A red shift trend is observed as a consequence of temperature increase, the measure peak wavelength spectrum has shifted from 1532.26 nm to 1534.68 nm, and a sensitivity of 30.4 pm/^{o}C is recorded. Subsequently, the OMMIZI is deposited with PNVC-PPy-GO solution and a length of 20 mm has been coated. The coated OMI-MZI has been exposed to various temperature ranged from 30 ^{o}C to 90 ^{o}C. The peak wavelength of the transmission fringe has been shifted from 1543.6 nm to 1541.55 nm, and sensitivity of 37.1 pm/^{o}C is measured. The wavelength shifts of the PNVC-PPy-GO deposited OMI-MZI is found more stable and uniform. The sensitivity and resolution of the sensor after

the deposition is improved about 7 pm/^{o}C and 0.18 ^{o}C respectively, compared to the sensor before deposition. Besides the wavelength shifting, the output power is measured as an additional parameter to measure the response of the OMI-MZI against the temperature variations. An increase in the output power is measured as a result of temperature increase. The output power of the uncoated OMI-MZI is increased about 2.17 dB, whereas the output power of PNVC-PPy-GO coated OMI-MZI is increased about 1.09 dB, when the temperature is increased from 30 ^{o}C to 90 ^{o}C. This study is believed to act as a guideline for future PNVC-PPy-GO nanocomposites based microfiber waveguide based sensors.

In the final experiment of this study, the responses of the microfiber knot resonator (MKR) have been investigated against humidity variations. A microfiber of a diameter of 2.1 μm is fabricated and a knot of diameter of 2.5 mm is produced subsequently with a high Q-factor of 75,000. The MKR has been exposed to various humidity conditions from 0% RH to 95% RH. Due to humidity changes, the refractive index of microfiber surroundings has been changed and therefore, the resonance wavelength of the MKR has been shifted. A linear response has been observed in the range of 40% RH to 95% RH, and the resonance wavelength has shifted from the 1510.6 nm to 1510.67 nm (referring to 40% RH and 95% RH respectively). A sensitivity of 1.3 pm/%RH is measured from the MKR sensor. Subsequently, the MKR has been coated with humidity sensitive titanium dioxide (TiO_2) nanoparticle coating using the proposed optical deposition technique and the lab-made deposition stage. The coated MKR has been exposed to similar humidity variations as the uncoated one. Since the coating is very sensitive to humidity, the resonance wavelength has shifted more substantially. A linear shifting has been observed in the range of 40%RH-95%RH, and the resonance wavelength has shifted from 1510.485 nm to 1510.63 nm (referring to 40% RH and 95% RH respectively). A sensitivity of 2.5 pm/%RH is measured from the TiO_2 coated MKR. The sensitivity has

increased greatly after the deposition of a porous TiO_2 nanoparticle coating on the MKR and in terms of percentage it is calculated as about 92.30% improvement. The responses of the uncoated and TiO_2 coated MKR have also been measured in terms of output power as an additional response parameter. In both cases, the output power has dropped. The output power of the uncoated MKR is dropped from -16.12 dBm to -19.3 dBm, when the RH conditions is increased from the 40% to 95% RH respectively, resulting a sensitivity of 0.0626 dB/%RH. On the other hand, the output power of the TiO_2 coated MKR has dropped from - 35.57 dBm to - 40.5 dBm, when the RH condition is increased from the 40% to 95% RH respectively, resulting a sensitivity of 0.0836 dB/%RH. It is obvious that the sensitivity of the TiO_2 coated MKR humidity sensor is much better compared to the uncoated MKR humidity sensor in terms of both measured parameters which are - the shift in the resonance wavelength and the rate of decrease of the transmitted output power. The increase in the sensitivity performance improvement is attributed to the porous structure of the coated TiO_2 nanoparticle. From the best of author knowledge, this study is the first demonstration of TiO_2 coated MKR based humidity sensor. The proposed sensor is potential to be employed in various humidity sensing applications, both in domestic and industrial use.

Based on the conducted study, it is clear that microfiber based devices have the immense potential to be used in various laser, sensing, communication, and bio-medical applications. Since, small dimension is a key edge for integrated photonics and micro-scale device, microfiber is highly prospective to be used small scaled laser and sensing integrated devices.

6.2 Future work

The future work should focus on developing new structure of microfiber, for instance new structures for interferometers and resonators which can be employed in various laser and sensing applications. On the other hand, coating the microfiber is found as a fruitful technique to improve the sensing characteristics of the microfiber. In the future study, the microfiber can be coated with various sensitive materials and employed in sensing applications. For instance, humidity sensitive materials can be coated in the microfiber if the microfiber is employed as humidity sensor, temperature sensitive materials can be coated in the microfiber if the microfiber is employed for temperature sensing. Moreover, microfiber based saturable absorber device is a very promising candidate for pulse fiber laser generation application. In the future study, many other SA materials can be coated in the microfiber to fabricate microfiber based SA device and utilized for saturable absorption and pulse generation. Furthermore, the tapering stage and the tapering program can be improved further to enable better quality microfiber fabrication with the desired specifications so that the success rate of good quality microfiber fabrication can be increased. In addition, the performance and properties of the microfiber degrades, when the microfiber is left open in the air. Therefore, the packaging of the microfiber should be considered for forthcoming study and real time implementation.

REFERENCES

Adachi, M., Hirasawa, M., Suguro, A., Karasawa, N., Kobayashi, S., Morita, R., & Yamashita, M. (2003). Spectral-phase characterization and adapted compensation of strongly chirped pulses from a tapered fiber. *Japanese Journal of Applied Physics, 42*(1A), L24.

Ahmad, H., Hamdan, K., Muhammad, F., Harun, S., & Zulkifli, M. (2015a). Switchable dual-wavelength CNT-based Q-switched using arrayed waveguide gratings (AWG). *Applied Physics B, 118*(2), 269-274.

Ahmad, H., Ismail, M. A., Suthaskumar, M., Tiu, Z. C., Harun, S. W., Zulkifli, M. Z., Samikannu, S., & Sivaraj, S. (2016). S-band Q-switched fiber laser using molybdenum disulfide (MoS2) saturable absorber. *Laser Physics Letters, 13*(3), 035103.

Ahmad, H., Latif, A., Talib, J., & Harun, S. (2013). Tunable, low frequency microwave generation from AWG based closely-spaced dual-wavelength single-longitudinal-mode fibre laser. *Journal of the European Optical Society-Rapid publications, 8*. doi:10.2971/jeos.2013.13038

Ahmad, H., Muhammad, F., Zulkifli, M., & Harun, S. (2012). Graphene-oxide-based saturable absorber for all-fiber Q-switching with a simple optical deposition technique. *IEEE Photonics Journal, 4*(6), 2205-2213.

Ahmad, H., Parvizi, R., Dimyati, K., Tamjis, M., & Harun, S. (2010). FWM-based multi-wavelength erbium-doped fiber laser using Bi-EDF. *Laser Physics, 20*(6), 1414-1417.

Ahmad, H., Rahman, M., Sakeh, S., Razak, M., & Zulkifli, M. (2016a). Humidity sensor based on microfiber resonator with reduced graphene oxide. *Optik-International Journal for Light and Electron Optics, 127*(5), 3158-3161.

Ahmad, H., Salim, M., Azzuhri, S., Zulkifli, M., & Harun, S. (2015b). Dual wavelength single longitudinal mode Ytterbium-doped fiber laser using a dual-tapered Mach-Zehnder interferometer. *Journal of the European Optical Society-Rapid publications, 10*. doi:10.2971/jeos.2015.15013

Ahmad, H., Salim, M., Azzuhri, S. R., Jaddoa, M., & Harun, S. (2016b). Tunable dual-wavelength ytterbium-doped fiber laser using a strain technique on microfiber Mach–Zehnder interferometer. *Applied Optics, 55*(4), 778-782.

Ahmad, H., Soltanian, M., Narimani, L., Amiri, I., Khodaei, A., & Harun, S. (2015c). Tunable S-Band Q-Switched Fiber Laser Using Bi 2 Se 3 as the Saturable Absorber. *IEEE Photonics Journal, 7*(3), 1-8.

Ahmad, H., Zulkifli, M., Latif, A., & Harun, S. (2009). Tunable dual wavelength fiber laser incorporating AWG and optical channel selector by controlling the cavity loss. *Optics Communications, 282*(24), 4771-4775.

Alavi, S., Soltanian, M., Amiri, I., Khalily, M., Supa'at, A., & Ahmad, H. (2016). Towards 5G: A Photonic Based Millimeter Wave Signal Generation for Applying in 5G Access Fronthaul. *Scientific Reports, 6*.

Allsop, T., Reeves, R., Webb, D. J., Bennion, I., & Neal, R. (2002). A high sensitivity refractometer based upon a long period grating Mach–Zehnder interferometer. *Review of Scientific Instruments, 73*(4), 1702-1705.

Alvarez-Herrero, A., Guerrero, H., & Levy, D. (2004). High-sensitivity sensor of low relative humidity based on overlay on side-polished fibers. *IEEE Sensors Journal, 4*(1), 52-56.

Aneesh, R., & Khijwania, S. K. (2012). Titanium dioxide nanoparticle based optical fiber humidity sensor with linear response and enhanced sensitivity. *Applied Optics, 51*(12), 2164-2171.

Arregui, F. J., Matías, I. R., & López-Amo, M. (2000). Optical fiber strain gauge based on a tapered single-mode fiber. *Sensors and Actuators A: Physical, 79*(2), 90-96.

Avouris, P., & Freitag, M. (2014). Graphene photonics, plasmonics, and optoelectronics. *Selected Topics in Quantum Electronics, IEEE Journal of, 20*(1), 72-83.

Bai, T., Li, C. Q., Sun, J., Song, Y., Wang, J., Blau, W. J., Zhang, B., & Chen, Y. (2015). Covalent Modification of Graphene Oxide with Carbazole Groups for Laser Protection. *Chemistry–A European Journal, 21*(12), 4622-4627.

Bao, Q., & Loh, K. P. (2012). Graphene photonics, plasmonics, and broadband optoelectronic devices. *ACS Nano, 6*(5), 3677-3694.

Bao, Q., Zhang, H., Ni, Z., Wang, Y., Polavarapu, L., Shen, Z., Xu, Q.-H., Tang, D., & Loh, K. P. (2011). Monolayer graphene as a saturable absorber in a mode-locked laser. *Nano Research, 4*(3), 297-307.

Bao, Q., Zhang, H., Wang, Y., Ni, Z., Yan, Y., Shen, Z. X., Loh, K. P., & Tang, D. Y. (2009). Atomic-layer graphene as a saturable absorber for ultrafast pulsed lasers. *Advanced Functional Materials, 19*(19), 3077-3083.

Bilodeau, F., Hill, K., Faucher, S., & Johnson, D. (1988). Low-loss highly overcoupled fused couplers: Fabrication and sensitivity to external pressure. *Journal of Lightwave Technology, , 6*(10), 1476-1482.

Birks, T. (1989). Twist-induced tuning in tapered fiber couplers. *Applied Optics, 28*(19), 4226-4233.

Birks, T., & Li, Y. W. (1992). The shape of fiber tapers. *Journal of Lightwave Technology, 10*(4), 432-438.

Bobb, L. C., Shankar, P., & Krumboltz, H. D. (1990). Bending effects in biconically tapered single-mode fibers. *Journal of Lightwave Technology, 8*(7), 1084-1090.

Boguslawski, J., Sobon, G., Zybala, R., & Sotor, J. (2015). Dissipative soliton generation in Er-doped fiber laser mode-locked by Sb 2 Te 3 topological insulator. *Optics Letters, 40*(12), 2786-2789.

Bonaccorso, F., Sun, Z., Hasan, T., & Ferrari, A. (2010). Graphene photonics and optoelectronics. *Nature Photonics, 4*(9), 611-622.

Bouyge, D., Crunteanu, A., Couderc, V., Sabourdy, D., & Blondy, P. (2008). Synchronized Tunable-Switched Fiber Lasers Using Deformable Achromatic Microelectromechanical Mirror. *IEEE Photonics Technology Letters, 20*(12), 991-993.

Brambilla, G. (2010). Optical fibre nanowires and microwires: a review. *Journal of Optics, 12*(4), 043001.

Brambilla, G., Koizumi, F., Feng, X., & Richardson, D. (2005). Compound-glass optical nanowires. *Electronics Letters, 41*(7), 1.

Brambilla, G., Xu, F., & Feng, X. (2006). Fabrication of optical fibre nanowires and their optical and mechanical characterisation. *Electronics Letters, 42*(9), 1.

Brambilla, G., Xu, F., Horak, P., Jung, Y., Koizumi, F., Sessions, N. P., Koukharenko, E., Feng, X., Murugan, G. S., & Wilkinson, J. S. (2009). Optical fiber nanowires and microwires: fabrication and applications. *Advances in Optics and Photonics, 1*(1), 107-161.

Buus, J., & Murphy, E. J. (2006). Tunable lasers in optical networks. *Journal of Lightwave Technology, 24*(1), 5.

Calizo, I., Balandin, A., Bao, W., Miao, F., & Lau, C. (2007). Temperature dependence of the Raman spectra of graphene and graphene multilayers. *Nano Letters, 7*(9), 2645-2649.

Cardenas-Sevilla, G., Monzon-Hernandez, D., Torres-Gomez, I., & Martínez-Ríos, A. (2012). Tapered Mach–Zehnder interferometer based on two mechanically induced long-period fiber gratings as refractive index sensor. *Optics & Laser Technology, 44*(5), 1516-1520.

Caspar, C., & Bachus, E.-J. (1989). Fibre-optic micro-ring-resonator with 2 mm diameter. *Electronics Letters, 25*(22), 1506-1508.

Chang, Y. M., Kim, H., Lee, J. H., & Song, Y.-W. (2010). Multilayered graphene efficiently formed by mechanical exfoliation for nonlinear saturable absorbers in fiber mode-locked lasers. *Applied Physics Letters, 97*(21), 211102.

Chen, G. Y., Ding, M., Newson, T., & Brambilla, G. (2013). A review of microfiber and nanofiber based optical sensors. *The Open Optics Journal, 7*(1).

Chen, J.-h., Deng, G.-q., Yan, S.-c., Li, C., Xi, K., Xu, F., & Lu, Y.-q. (2015). Microfiber-coupler-assisted control of wavelength tuning for Q-switched fiber laser with few-layer molybdenum disulfide nanoplates. *Optics Letters, 40*(15), 3576-3579.

Chen, N., Feng, Z., & Liaw, S. (2010). All-fiber pulsewidth tunable actively Q-switched erbium fiber laser using abrupt-tapered Mach-Zehnder block filter. *Laser Physics Letters, 7*(5), 363-366.

Chen, Y., Jiang, G., Chen, S., Guo, Z., Yu, X., Zhao, C., Zhang, H., Bao, Q., Wen, S., & Tang, D. (2015). Mechanically exfoliated black phosphorus as a new saturable absorber for both Q-switching and Mode-locking laser operation. *Optics Express, 23*(10), 12823-12833.

Chen, Y., Zhang, B., Liu, G., Zhuang, X., & Kang, E.-T. (2012). Graphene and its derivatives: switching ON and OFF. *Chemical Society Reviews, 41*(13), 4688-4707.

Chen, Z., & Lu, C. (2005). Humidity sensors: a review of materials and mechanisms. *Sensor Letters, 3*(4), 274-295.

Dalton, L. R., Harper, A. W., Ghosn, R., Steier, W. H., Ziari, M., Fetterman, H., Shi, Y., Mustacich, R., Jen, A.-Y., & Shea, K. J. (1995). Synthesis and processing of improved organic second-order nonlinear optical materials for applications in photonics. *Chemistry of Materials, 7*(6), 1060-1081.

Das, A., Chakraborty, B., & Sood, A. (2008). Raman spectroscopy of graphene on different substrates and influence of defects. *Bulletin of Materials Science, 31*(3), 579-584.

Desurvire, E., Zirngibl, M., Presby, H., & DiGiovanni, D. (1991). Dynamic gain compensation in saturated erbium-doped fiber amplifiers. *IEEE Photonics Technology Letters, 3*(5), 453-455.

Ding, J. F., Zhang, A. P., Shao, L.-Y., Yan, J.-H., & He, S. (2005). Fiber-taper seeded long-period grating pair as a highly sensitive refractive-index sensor. *IEEE Photonics Technology Letters, 17*(6), 1247-1249.

Ding, L., Belacel, C., Ducci, S., Leo, G., & Favero, I. (2010). Ultralow loss single-mode silica tapers manufactured by a microheater. *Applied Optics, 49*(13), 2441-2445.

Dong, B., Hao, J., Hu, J., & Liaw, C.-Y. (2010). Wide pulse-repetition-rate range tunable nanotube-switched low threshold erbium-doped fiber laser. *IEEE Photonics Technology Letters, 22*(24), 1853-1855.

Du, J., Wang, Q., Jiang, G., Xu, C., Zhao, C., Xiang, Y., Chen, Y., Wen, S., & Zhang, H. (2014). Ytterbium-doped fiber laser passively mode locked by few-layer Molybdenum Disulfide (MoS2) saturable absorber functioned with evanescent field interaction. *Scientific Reports, 4*. doi: 10.1038/srep06346

Essiambre, R.-J., & Tkach, R. W. (2012). Capacity trends and limits of optical communication networks. *Proceedings of the IEEE, 100*(5), 1035-1055.

Fan, D., Mou, C., Bai, X., Wang, S., Chen, N., & Zeng, X. (2014). Passively Q-switched erbium-doped fiber laser using evanescent field interaction with gold-nanosphere based saturable absorber. *Optics Express, 22*(15), 18537-18542.

Fang, Q., Kieu, K., & Peyghambarian, N. (2010). An All-Fiber 2-m Wavelength-Tunable Mode-Locked Laser. *IEEE Photonics Technology Letters, 22*(22), 1656-1658.

Ferrari, A., Meyer, J., Scardaci, V., Casiraghi, C., Lazzeri, M., Mauri, F., Piscanec, S., Jiang, D., Novoselov, K., & Roth, S. (2006). Raman spectrum of graphene and graphene layers. *Physical Review Letters, 97*(18), 187401.

Ferrari, A. C. (2007). Raman spectroscopy of graphene and graphite: disorder, electron–phonon coupling, doping and nonadiabatic effects. *Solid State Communications, 143*(1), 47-57.

Ferrari, A. C., & Robertson, J. (2000). Interpretation of Raman spectra of disordered and amorphous carbon. *Physical Review B, 61*(20), 14095.

Garmire, E. (2000). Resonant optical nonlinearities in semiconductors. *IEEE Journal of Selected Topics in Quantum Electronics, 6*(6), 1094-1110.

Gnauck, A. H., Tkach, R., Chraplyvy, A., & Li, T. (2008). High-capacity optical transmission systems. *Journal of Lightwave Technology, 26*(9), 1032-1045.

Graf, D., Molitor, F., Ensslin, K., Stampfer, C., Jungen, A., Hierold, C., & Wirtz, L. (2007). Raman imaging of graphene. *Solid State Communications, 143*(1), 44-46.

Grubsky, V., & Savchenko, A. (2005). Glass micro-fibers for efficient third harmonic generation. *Optics Express, 13*(18), 6798-6806.

Gu, Z., Li, C., Wang, G., Zhang, L., Li, X., Wang, W., & Jin, S. (2010). Synthesis and characterization of polypyrrole/graphite oxide composite by in situ emulsion polymerization. *Journal of Polymer Science Part B: Polymer Physics, 48*(12), 1329-1335.

Harun, S., Lim, K., Jasim, A., & Ahmad, H. (2010). Dual wavelength erbium-doped fiber laser using a tapered fiber. *Journal of Modern Optics, 57*(21), 2111-2113.

Hasan, T., Sun, Z., Wang, F., Bonaccorso, F., Tan, P. H., Rozhin, A. G., & Ferrari, A. C. (2009a). Nanotube-polymer composites for ultrafast photonics. *Adv. Mater, 21*(38-39), 3874-3899.

Hasan, T., Sun, Z., Wang, F., Bonaccorso, F., Tan, P. H., Rozhin, A. G., & Ferrari, A. C. (2009b). Nanotube–polymer composites for ultrafast photonics. *Advanced Materials, 21*(38-39), 3874-3899.

He, X., Liu, Z.-b., & Wang, D. (2012a). Wavelength-tunable, passively mode-locked fiber laser based on graphene and chirped fiber Bragg grating. *Optics Letters, 37*(12), 2394-2396.

He, X., Liu, Z.-B., Wang, D., Yang, M., Liao, C., & Zhao, X. (2012b). Passively mode-locked fiber laser based on reduced graphene oxide on microfiber for ultra-wide-band doublet pulse generation. *Journal of Lightwave Technology, 30*(7), 984-989.

Heisterkamp, A., Herman, P. R., Meunier, M., & Nolte, S. (2015). *Frontiers in Ultrafast Optics: Biomedical, Scientific, and Industrial Applications XV*. Paper presented at the Proc. of SPIE Vol.

Hendry, E., Hale, P. J., Moger, J., Savchenko, A., & Mikhailov, S. (2010). Coherent nonlinear optical response of graphene. *Physical Review Letters, 105*(9), 097401.

Huang, J., Huang, S., Chang, H., Su, K., Chen, Y., & Huang, K. (2008). Passive Q switching of Er-Yb fiber laser with semiconductor saturable absorber. *Optics Express, 16*(5), 3002-3007.

Huang, P. L., Lin, S.-C., Yeh, C.-Y., Kuo, H.-H., Huang, S.-H., Lin, G.-R., Li, L.-J., Su, C.-Y., & Cheng, W.-H. (2012). Stable mode-locked fiber laser based on CVD fabricated graphene saturable absorber. *Optics Express, 20*(3), 2460-2465.

Huang, Y., Luo, Z., Li, Y., Zhong, M., Xu, B., Che, K., Xu, H., Cai, Z., Peng, J., & Weng, J. (2014). Widely-tunable, passively Q-switched erbium-doped fiber laser with few-layer MoS 2 saturable absorber. *Optics Express, 22*(21), 25258-25266.

Humphrey, P. D., & Bowers, J. E. (1993). Fiber-birefringence tuning technique for an erbium-doped fiber ring laser. *IEEE Photonics Technology Letters, 5*(1), 32-34.

Jaddoa, M., Jasim, A., Razak, M., Harun, S., & Ahmad, H. (2016). Highly responsive NaCl detector based on inline microfiber Mach–Zehnder interferometer. *Sensors and Actuators A: Physical, 237*, 56-61.

Janisch, C., Mehta, N., Ma, D., Elías, A. L., Perea-López, N., Terrones, M., & Liu, Z. (2014). Ultrashort optical pulse characterization using WS 2 monolayers. *Optics Letters, 39*(2), 383-385.

Jasim, A., Harun, S., Lim, K., Rahman, B., & Ahmad, H. (2012). Microfibre Mach-Zehnder interferometer and its application as a current sensor. *IET Optoelectronics, 6*(6), 298-302.

Jasim, A., Harun, S., Muhammad, M., Arof, H., & Ahmad, H. (2013). Current sensor based on inline microfiber Mach–Zehnder interferometer. *Sensors and Actuators A: Physical, 192*, 9-12.

Jasim, A. A., Dernaika, M., Harun, S. W., & Ahmad, H. (2015). A Switchable Figure Eight Erbium-Doped Fiber Laser Based on Inter-Modal Beating By Means of Non-Adiabatic Microfiber. *Journal of Lightwave Technology, 33*(2), 528-534.

Jasim, A. A., Harun, S. W., Arof, H., & Ahmad, H. (2013). Inline microfiber Mach–Zehnder interferometer for high temperature sensing. *IEEE Sensors Journal, 13*(2), 626-628.

Jasim, A. A., Hayashi, N., Harun, S. W., Ahmad, H., Penny, R., Mizuno, Y., & Nakamura, K. (2014). Refractive index and strain sensing using inline Mach–Zehnder interferometer comprising perfluorinated graded-index plastic optical fiber. *Sensors and Actuators A: Physical, 219*, 94-99.

Jiang, X., Tong, L., Vienne, G., Guo, X., Tsao, A., Yang, Q., & Yang, D. (2006). Demonstration of optical microfiber knot resonators. *Applied Physics Letters, 88*(22), 223501.

Jung, Y., Brambilla, G., & Richardson, D. J. (2008). Broadband single-mode operation of standard optical fibers by using a sub-wavelength optical wire filter. *Optics Express, 16*(19), 14661-14667. doi:10.1364/oe.16.014661

Jung, Y., Brambilla, G., & Richardson, D. J. (2009a). Comparative study of the effective single mode operational bandwidth in sub-wavelength optical wires and conventional single-mode fibers. *Optics Express, 17*(19), 16619-16624.

Jung, Y., Jeong, Y., Brambilla, G., & Richardson, D. J. (2009b). Adiabatically tapered splice for selective excitation of the fundamental mode in a multimode fiber. *Optics Letters, 34*(15), 2369-2371.

Kang, J.-H., Lee, J.-Y., & Kim, W.-H. (2006). The Design and fabrication of Capacitive Humidity Sensor Having Interdigital Electrodes and Its Signal Processing Circuit. *The Transactions of the Korean Institute of Electrical Engineers P, 55*(1), 26-30.

Kashiwagi, K., & Yamashita, S. (2009). Deposition of carbon nanotubes around microfiber via evanascent light. *Optics Express, 17*(20), 18364-18370.

Keller, U. (2003). Recent developments in compact ultrafast lasers. *Nature, 424*(6950), 831-838.

Kieu, K., & Mansuripur, M. (2006a). Active Q switching of a fiber laser with a microsphere resonator. *Optics Letters, 31*(24), 3568-3570.

Kieu, K., & Mansuripur, M. (2006b). Tuning of fiber lasers by use of a single-mode biconic fiber taper. *Optics Letters, 31*(16), 2435-2437.

Kim, K. S., Zhao, Y., Jang, H., Lee, S. Y., Kim, J. M., Kim, K. S., Ahn, J.-H., Kim, P., Choi, J.-Y., & Hong, B. H. (2009). Large-scale pattern growth of graphene films for stretchable transparent electrodes. *Nature, 457*(7230), 706-710.

Kir'yanov, A. V., Barmenkov, Y. O., & Andres, M. V. (2013). An experimental analysis of self-Q-switching via stimulated Brillouin scattering in an ytterbium doped fiber laser. *Laser Physics Letters, 10*(5), 055112.

Klehr, A., Fricke, J., Knauer, A., Erbert, G., Walther, M., Wilk, R., Mikulics, M., & Koch, M. (2008). High-power monolithic two-mode DFB laser diodes for the generation of THz radiation. *Selected Topics in Quantum Electronics, IEEE Journal of, 14*(2), 289-294.

Kou, J.-l., Feng, J., Ye, L., Xu, F., & Lu, Y.-q. (2010). Miniaturized fiber taper reflective interferometer for high temperature measurement. *Optics Express, 18*(13), 14245-14250.

Kovalenko, A., Kurashov, V., & Kisil, A. (2008). Radiation losses in optical nanofibers with random rough surface. *Optics Express, 16*(8), 5797-5806.

Kulwicki, B. M. (1991). Humidity sensors. *Journal of the American Ceramic Society, 74*(4), 697-708.

Kuznetsov, A., & Babin, S. (2010). Q-switched fiber laser with spectral control for frequency doubling. *Laser Physics, 20*(5), 1266-1269.

Lacroix, S., Gonthier, F., Black, R. J., & Bures, J. (1988). Tapered-fiber interferometric wavelength response: The achromatic fringe. *Optics Letters, 13*(5), 395-397.

Laming, R. I., Poole, S. B., & Tarbox, E. (1988). Pump excited-state absorption in erbium-doped fibers. *Optics Letters, 13*(12), 1084-1086.

Lee, B. (2003). Review of the present status of optical fiber sensors. *Optical Fiber Technology, 9*(2), 57-79.

Lee, J., Jung, M., Koo, J., Chi, C., & Lee, J. H. (2015). Passively Q-Switched 1.89-μm fiber laser using a bulk-structured Bi 2 Te 3 topological insulator. *IEEE Journal of Selected Topics in Quantum Electronics, 21*(1), 31-36.

Lee, J., Koo, J., Chi, C., & Lee, J. H. (2014). All-fiberized, passively Q-switched 1.06 μm laser using a bulk-structured Bi2Te3 topological insulator. *Journal of Optics, 16*(8), 085203.

Letokhov, V. (1984). Laser biology and medicine. *Nature, 316*(6026), 325-330.

Li, B., Jiang, L., Wang, S., Zhou, L., Xiao, H., & Tsai, H.-L. (2011). Ultra-abrupt tapered fiber Mach-Zehnder interferometer sensors. *Sensors, 11*(6), 5729-5739.

Li, L., Xia, L., Xie, Z., & Liu, D. (2012). All-fiber Mach-Zehnder interferometers for sensing applications. *Optics Express, 20*(10), 11109-11120.

Li, X., & Ding, H. (2013). Investigation of the thermal properties of optical microfiber knot resonators. *Instrumentation Science & Technology, 41*(3), 224-235.

Li, X., Yang, C., Yang, S., & Li, G. (2012). Fiber-optical sensors: basics and applications in multiphase reactors. *Sensors, 12*(9), 12519-12544.

Li, Y., & Bao, X. (2008). The observation of comblike transmission spectrum from a tapered single mode fiber tip. *Applied Physics Letters, 93*(26), 261107.

Li, Y., & Tong, L. (2008). Mach-Zehnder interferometers assembled with optical microfibers or nanofibers. *Optics Letters, 33*(4), 303-305.

Liao, C., Wang, D., & Wang, Y. (2013). Microfiber in-line Mach–Zehnder interferometer for strain sensing. *Optics Letters, 38*(5), 757-759.

Lim, K., Ahmad, H., Arof, H., & Harun, S. (2012). *Fabrication and applications of microfiber*: INTECH Open Access Publisher.

Lim, K., Harun, S., Damanhuri, S., Jasim, A., Tio, C., & Ahmad, H. (2011). Current sensor based on microfiber knot resonator. *Sensors and Actuators A: Physical, 167*(1), 60-62.

Liu, M., Zheng, X.-W., Qi, Y.-L., Liu, H., Luo, A.-P., Luo, Z.-C., Xu, W.-C., Zhao, C.-J., & Zhang, H. (2014). Microfiber-based few-layer MoS 2 saturable absorber for 2.5 GHz passively harmonic mode-locked fiber laser. *Optics Express, 22*(19), 22841-22846.

Lorenz, L. (1880). The index of refraction. *Ann. d. Physik, 11*(3), 70.

Lu, P., Men, L., Sooley, K., & Chen, Q. (2009). Tapered fiber Mach–Zehnder interferometer for simultaneous measurement of refractive index and temperature. *Applied Physics Letters, 94*(13), 131110.

Luo, Z.-C., Liu, M., Liu, H., Zheng, X.-W., Luo, A.-P., Zhao, C.-J., Zhang, H., Wen, S.-C., & Xu, W.-C. (2013). 2 GHz passively harmonic mode-locked fiber laser by a microfiber-based topological insulator saturable absorber. *Optics Letters, 38*(24), 5212-5215.

Luo, Z., Huang, Y., Wang, J., Cheng, H., Cai, Z., & Ye, C. (2012). Multiwavelength dissipative-soliton generation in Yb-fiber laser using graphene-deposited fiber-taper. *IEEE Photonics Technology Letters, 24*(17), 1539-1542.

Luo, Z., Huang, Y., Zhong, M., Li, Y., Wu, J., Xu, B., Xu, H., Cai, Z., Peng, J., & Weng, J. (2014). 1-, 1.5-, and 2-μm fiber lasers Q-switched by a broadband few-layer MoS 2 saturable absorber. *Journal of Lightwave Technology, 32*(24), 4077-4084.

Luo, Z., Zhou, M., Weng, J., Huang, G., Xu, H., Ye, C., & Cai, Z. (2010). Graphene-based passively Q-switched dual-wavelength erbium-doped fiber laser. *Optics Letters, 35*(21), 3709-3711.

Ma, H., Jen, A. Y., & Dalton, L. R. (2002). Polymer-Based Optical Waveguides: Materials, Processing, and Devices. *Advanced Materials, 14*(19), 1339-1365.

Mahdi, M., Adikan, F. M., Poopalan, P., Selvakennedy, S., Chan, W., & Ahmad, H. (2000). Long-wavelength EDFA gain enhancement through 1550 nm band signal injection. *Optics Communications, 176*(1), 125-129.

Martinez, A., Fuse, K., Xu, B., & Yamashita, S. (2010). Optical deposition of graphene and carbon nanotubes in a fiber ferrule for passive mode-locked lasing. *Optics Express, 18*(22), 23054-23061.

Mary, R., Choudhury, D., & Kar, A. K. (2014). Applications of fiber lasers for the development of compact photonic devices. *IEEE Journal of Selected Topics in Quantum Electronics, 20*(5), 72-84.

McAtamney, C., Cronin, A., Sherlock, R., O'Connor, G., & Glynn, T. (2005). *Reproducible method for fabricating fused biconical tapered couplers using a CO2 laser based process*. Paper presented at the Proceedings of the Third International WLT-Conference on Lasers in Manufacturing.

Meng, L. L., Hao, Zheng, X.-W., Zhao, N., Luo, A.-P., Luo, Z.-C., & Xu, W.-C. (2014). Demonstration of multiwavelength erbium-doped fiber laser based on a microfiber knot resonator. *IEEE Photonics Technology Letters, 26*(14), 1387-1390.

Miao, Z., Xu, D., Ouyang, J., Guo, G., Zhao, X., & Tang, Y. (2002). Electrochemically induced sol-gel preparation of single-crystalline TiO2 nanowires. *Nano Letters, 2*(7), 717-720.

Mollenauer, L., Mamyshev, P., Gripp, J., Neubelt, M., Mamysheva, N., Grüner-Nielsen, L., & Veng, T. (2000). Demonstration of massive wavelength-division multiplexing over transoceanic distances by use of dispersion-managed solitons. *Optics Letters, 25*(10), 704-706.

Nguyen, L. V., Hwang, D., Moon, S., Moon, D. S., & Chung, Y. (2008). High temperature fiber sensor with high sensitivity based on core diameter mismatch. *Optics Express, 16*(15), 11369-11375.

Ortaç, B., Baumgart, M., Schmidt, O., Hideur, A., Sagnes, I., Granache, A., Limpert, J., & Tünnermann, A. (2009). *Fiber lasers VI: technology, systems, and applications.* Paper presented at the Proceedings of SPIE.

Park, N. H., Jeong, H., Choi, S. Y., Kim, M. H., Rotermund, F., & Yeom, D.-I. (2015). Monolayer graphene saturable absorbers with strongly enhanced evanescent-field interaction for ultrafast fiber laser mode-locking. *Optics Express, 23*(15), 19806-19812.

Park, S., Kang, J., Park, J., & Mun, S. (2001). One-bodied humidity and temperature sensor having advanced linearity at low and high relative humidity range. *Sensors and Actuators B: Chemical, 76*(1), 322-326.

Paschotta, R. article on 'group velocity dispersion' in the Encyclopedia of Laser Physics and Technology. www.rp-photonics.com/group_velocity_dispersion.html

Paschotta, R. (2008a). article on 'chromatic dispersion' in the Encyclopedia of laser physics and technology. (3527408282). Retrieved 2018-01-05, from Wiley-vch Berlin https://www.rp-photonics.com/chromatic_dispersion.html

Paschotta, R. (2008b). *article on 'group velocity dispersion' in the Encyclopedia of laser physics and technology* (Vol. 1): Wiley-vch Berlin.

Paschotta, R. (2008c). article on 'Q Switching' in the Encyclopedia of Laser Physics and Technology. Retrieved 2018-05-01 https://www.rp-photonics.com/q_switching.html

Paschotta, R. (2008d). *article on 'Q switching' in the Encyclopedia of laser physics and technology* (Vol. 1): Wiley-vch Berlin.

Paschotta, R. (2008e). *Field guide to laser pulse generation* (Vol. 14): SPIE Press Bellingham.

Pellandini, P., Stanley, R., Houdre, R., Oesterle, U., Ilegems, M., & Weisbuch, C. (1997). Dual-wavelength laser emission from a coupled semiconductor microcavity. *Applied Physics Letters, 71*(7), 864-866.

Pernites, R., Vergara, A., Yago, A., Cui, K., & Advincula, R. (2011). Facile approach to graphene oxide and poly (N-vinylcarbazole) electro-patterned films. *Chemical Communications, 47*(35), 9810-9812.

Pimenta, M., Dresselhaus, G., Dresselhaus, M. S., Cancado, L., Jorio, A., & Saito, R. (2007). Studying disorder in graphite-based systems by Raman spectroscopy. *Physical Chemistry Chemical Physics, 9*(11), 1276-1290.

Popa, D., Sun, Z., Hasan, T., Torrisi, F., Wang, F., & Ferrari, A. (2010a). Graphene Q-switched, tunable fiber laser. *arXiv preprint arXiv:1011.0115*.

Popa, D., Sun, Z., Torrisi, F., Hasan, T., Wang, F., & Ferrari, A. (2010b). Sub 200 fs pulse generation from a graphene mode-locked fiber laser. *Applied Physics Letters, 97*(20), 203106.

Ramaswami, R., Sivarajan, K., & Sasaki, G. (2009). *Optical networks: a practical perspective*: Morgan Kaufmann.

Razak Ab , M. Z., Reduan, S. A., Sharbirin, A. S., Jamaludin, N., Zulkifli, M. Z., & Ahmad, H. (2015). Noncontact Optical Displacement Sensor Using an Adiabatic U-Shaped Tapered Fiber. *IEEE Sensors Journal, 15*(10), 5388-5392.

Reekie, L., Mears, R. J., Poole, S. B., & Payne, D. N. (1986). Tunable single-mode fiber lasers. *Journal of Lightwave Technology, 4*(7), 956-960.

Ren, L., Xu, Y., Ma, C., Wang, Y., Kong, X., Liang, J., Ju, H., Ren, K., & Lin, X. (2016). *Optical microfiber knot resonator (MKR) and its slow-light performance.* Paper presented at the Journal of Physics Conference Series.

Rodenburg, C., Liu, X., Jepson, M. A., Boden, S. A., & Brambilla, G. (2011). Surface morphology of silica nanowires at the nanometer scale. *Journal of Non-Crystalline Solids, 357*(15), 3042-3045.

Schwelb, O. (2004). Transmission, group delay, and dispersion in single-ring optical resonators and add/drop filters-a tutorial overview. *Journal of Lightwave Technology, 22*(5), 1380-1394.

Shah, J. (2013). *Ultrafast spectroscopy of semiconductors and semiconductor nanostructures* (Vol. 115): Springer Science & Business Media.

Sharma, U., Kim, C.-S., Kang, J. U., & Fried, N. M. (2004). *Highly stable tunable dual-wavelength Q-switched fiber laser for DIAL applications.* Paper presented at the Laser Applications to Chemical and Environmental Analysis.

Smietana, M., Brabant, D., Bock, W. J., Mikulic, P., & Eftimov, T. (2012). Refractive-index sensing with inline core-cladding intermodal interferometer based on silicon nitride nano-coated photonic crystal fiber. *Journal of Lightwave Technology, 30*(8), 1185-1189.

Sobon, G. (2015). Mode-locking of fiber lasers using novel two-dimensional nanomaterials: graphene and topological insulators [Invited]. *Photonics Research, 3*(2), A56-A63.

Sobon, G., Sotor, J., Jagiello, J., Kozinski, R., Zdrojek, M., Holdynski, M., Paletko, P., Boguslawski, J., Lipinska, L., & Abramski, K. M. (2012a). Graphene oxide vs. reduced graphene oxide as saturable absorbers for Er-doped passively mode-locked fiber laser. *Optics Express, 20*(17), 19463-19473.

Sobon, G., Sotor, J., Pasternak, I., Grodecki, K., Paletko, P., Strupinski, W., Jankiewicz, Z., & Abramski, K. M. (2012b). Er-doped fiber laser mode-locked by CVD-graphene saturable absorber. *Journal of Lightwave Technology, 30*(17), 2770-2775.

Sobon, G., Sotor, J., Pasternak, I., Krajewska, A., Strupinski, W., & Abramski, K. M. (2013). Thulium-doped all-fiber laser mode-locked by CVD-graphene/PMMA saturable absorber. *Optics Express, 21*(10), 12797-12802.

Song, Y.-W., Jang, S.-Y., Han, W.-S., & Bae, M.-K. (2010). Graphene mode-lockers for fiber lasers functioned with evanescent field interaction. *Applied Physics Letters, 96*(5), 051122.

Sotor, J., Sobon, G., Kowalczyk, M., Macherzynski, W., Paletko, P., & Abramski, K. M. (2015). Ultrafast thulium-doped fiber laser mode locked with black phosphorus. *Optics Letters, 40*(16), 3885-3888.

Stokes, L. F., Chodorow, M., & Shaw, H. J. (1982). All-single-mode fiber resonator. *Optics Letters, 7*(6), 288-290.

Sulaiman, A., Muhammad, M., Harun, S., Arof, H., & Ahmad, H. (2013). Demonstration of acoustic vibration sensor based on microfiber knot resonator. *Microwave and Optical Technology Letters, 55*(5), 1138-1141.

Sumetsky, M. (2008). Basic elements for microfiber photonics: Micro/nanofibers and microfiber coil resonators. *Journal of Lightwave Technology, 26*(1), 21-27.

Sumetsky, M., Dulashko, Y., & Windeler, R. (2010). Optical microbubble resonator. *Optics Letters, 35*(7), 898-900.

Sun, Z., Hasan, T., Torrisi, F., Popa, D., Privitera, G., Wang, F., Bonaccorso, F., Basko, D. M., & Ferrari, A. C. (2010a). Graphene mode-locked ultrafast laser. *ACS Nano, 4*(2), 803-810.

Sun, Z., Popa, D., Hasan, T., Torrisi, F., Wang, F., Kelleher, E. J., Travers, J. C., Nicolosi, V., & Ferrari, A. C. (2010b). A stable, wideband tunable, near transform-limited, graphene-mode-locked, ultrafast laser. *Nano Research, 3*(9), 653-660.

Svelto, O., & Hanna, D. C. (1976). *Principles of Lasers*: Springer.

Szipocs, R., Krolopp, Á., Csákányi, A., Haluszka, D., Vass, L., & Wikonkál, N. (2016). *FiberScope: an Optical Fiber Laser Based, Handheld 3D Nonlinear Microscope System for in vivo Diagnostic Applications in Dermatology and Nanomedicine.* Paper presented at the Optical Tomography and Spectroscopy.

Taccheo, S., Schuster, K., Ferrari, M., Seddon, A., Marciniak, M., Taudt, C., Troles, J., Valentini, G., Dorosz, D., & Prudenzano, F. (2016). *Challenges and future trends*

in fiber lasers. Paper presented at the Transparent Optical Networks (ICTON), 2016 18th International Conference on.

Tan, S., Tiu, Z., Harun, S., & Ahmad, H. (2015). Sideband-controllable soliton pulse with bismuth-based erbium-doped fiber. *Chinese Optics Letters, 13*(11), 111406.

Tan, S., Yan, F., Li, Q., Peng, W., Liu, S., Feng, T., & Chang, F. (2013). A stable single-longitudinal-mode dual-wavelength erbium-doped fiber ring laser with superimposed FBG and an in-line two-taper MZI filter. *Laser Physics, 23*(7), 075112.

Taudt, C., Baselt, T., Nelsen, B., Assmann, H., Greiner, A., Koch, E., & Hartmann, P. (2016). *Two-dimensional low-coherence interferometry for the characterization of nanometer wafer topographies.* Paper presented at the SPIE Photonics Europe.

Terrones, M., Martín, O., González, M., Pozuelo, J., Serrano, B., Cabanelas, J. C., Vega-Díaz, S. M., & Baselga, J. (2011). Interphases in Graphene Polymer-based Nanocomposites: Achievements and Challenges. *Advanced Materials, 23*(44), 5302-5310.

Tian, Z., Yam, S. S.-H., Barnes, J., Bock, W., Greig, P., Fraser, J. M., Loock, H.-P., & Oleschuk, R. D. (2008a). Refractive index sensing with Mach–Zehnder interferometer based on concatenating two single-mode fiber tapers. *IEEE Photonics Technology Letters, 20*(8), 626-628.

Tian, Z., Yam, S. S., & Loock, H.-P. (2008b). Refractive index sensor based on an abrupt taper Michelson interferometer in a single-mode fiber. *Optics Letters, 33*(10), 1105-1107.

Tiu, Z. C., Tan, S. J., Zarei, A., Ahmad, H., & Harun, S. W. (2014). Nonlinear Polarization Rotation-Based Mode-Locked Erbium-Doped Fiber Laser with Three Switchable Operation States. *Chinese Physics Letters, 31*(9), 094206.

Tong, L., Gattass, R. R., Ashcom, J. B., He, S., Lou, J., Shen, M., Maxwell, I., & Mazur, E. (2003). Subwavelength-diameter silica wires for low-loss optical wave guiding. *Nature, 426*(6968), 816-819.

Tong, L., Hu, L., Zhang, J., Qiu, J., Yang, Q., Lou, J., Shen, Y., He, J., & Ye, Z. (2006). Photonic nanowires directly drawn from bulk glasses. *Optics Express, 14*(1), 82-87.

Tong, L., Lou, J., & Mazur, E. (2004). Single-mode guiding properties of subwavelength-diameter silica and silicon wire waveguides. *Optics Express, 12*(6), 1025-1035.

Tong, L., Lou, J., Ye, Z., Svacha, G. T., & Mazur, E. (2005). Self-modulated taper drawing of silica nanowires. *Nanotechnology, 16*(9), 1445.

Traversa, E. (1995). Ceramic sensors for humidity detection: the state-of-the-art and future developments. *Sensors and Actuators B: Chemical, 23*(2), 135-156.

Türke, D., Wohlleben, W., Teipel, J., Motzkus, M., Kibler, B., Dudley, J., & Giessen, H. (2006). Chirp-controlled soliton fission in tapered optical fibers. *Applied Physics B, 83*(1), 37-42.

Vienne, G., Li, Y., & Tong, L. (2007). Effect of host polymer on microfiber resonator. *IEEE Photonics Technology Letters, 19*(18), 1386-1388.

Villegas, I., Cuadrado-Laborde, C., Díez, A., Cruz, J., Martínez-Gámez, M., & Andrés, M. (2011). Yb-doped strictly all-fiber laser actively Q-switched by intermodal acousto-optic modulation. *Laser Physics, 21*(9), 1650-1655.

Walsh, B. (2010). Dual wavelength lasers. *Laser Physics, 20*(3), 622-634.

Wang, C.-L., Chuang, Y.-H., & Pan, C.-L. (1995). Two-wavelength interferometer based on a two-color laser-diode array and the second-order correlation technique. *Optics Letters, 20*(9), 1071-1073.

Wang, C.-L., & Pan, C.-L. (1995). Tunable multiterahertz beat signal generation from a two-wavelength laser-diode array. *Optics Letters, 20*(11), 1292-1294.

Wang, F., Rozhin, A., Scardaci, V., Sun, Z., Hennrich, F., White, I., Milne, W. I., & Ferrari, A. C. (2008). Wideband-tuneable, nanotube mode-locked, fibre laser. *Nature Nanotechnology, 3*(12), 738-742.

Wang, F., Xu, E.-M., Dong, J.-J., & Zhang, X.-L. (2011). A tunable and switchable single-longitudinal-mode dual-wavelength fiber laser incorporating a reconfigurable dual-pass Mach–Zehnder interferometer and its application in microwave generation. *Optics Communications, 284*(9), 2337-2340.

Wang, J., Luo, Z., Zhou, M., Ye, C., Fu, H., Cai, Z., Cheng, H., Xu, H., & Qi, W. (2012). Evanescent-light deposition of graphene onto tapered fibers for passive Q-switch and mode-locker. *IEEE Photonics Journal, 4*(5), 1295-1305.

Wang, P., Gu, F., Zhang, L., & Tong, L. (2011). Polymer microfiber rings for high-sensitivity optical humidity sensing. *Applied Optics, 50*(31), G7-G10.

Wang, Y., Yang, M., Wang, D., Liu, S., & Lu, P. (2010). Fiber in-line Mach-Zehnder interferometer fabricated by femtosecond laser micromachining for refractive index measurement with high sensitivity. *JOSA B, 27*(3), 370-374.

Wei, T., Lan, X., & Xiao, H. (2009). Fiber Inline Core–Cladding-Mode Mach–Zehnder Interferometer Fabricated by Two-Point CO Laser Irradiations. *IEEE Photonics Technology Letters, 21*(10), 669-671.

Westwater, J., Gosain, D., Tomiya, S., Usui, S., & Ruda, H. (1997). Growth of silicon nanowires via gold/silane vapor–liquid–solid reaction. *Journal of Vacuum Science & Technology B, 15*(3), 554-557.

Woodward, R., Kelleher, E., Howe, R., Hu, G., Torrisi, F., Hasan, T., Popov, S., & Taylor, J. (2014). Tunable Q-switched fiber laser based on saturable edge-state absorption in few-layer molybdenum disulfide (MoS 2). *Optics Express, 22*(25), 31113-31122.

Wu, X., & Tong, L. (2013). Optical microfibers and nanofibers. *Nanophotonics, 2*(5-6), 407-428.

Wu, Y., Rao, Y.-J., Chen, Y.-h., & Gong, Y. (2009). Miniature fiber-optic temperature sensors based on silica/polymer microfiber knot resonators. *Optics Express, 17*(20), 18142-18147.

Wu, Y., Zhang, T., Rao, Y., & Gong, Y. (2011). Miniature interferometric humidity sensors based on silica/polymer microfiber knot resonators. *Sensors and Actuators B: Chemical, 155*(1), 258-263.

Xian, P., Feng, G., & Zhou, S. (2016). A compact and stable temperature sensor based on a gourd-shaped microfiber. *IEEE Photonics Technology Letters, 28*(1), 95-98.

Xu, F., & Brambilla, G. (2007). Embedding optical microfiber coil resonators in Teflon. *Optics Letters, 32*(15), 2164-2166.

Xu, Y., Chen, X., & Zhu, Y. (2008). Modeling of micro-diameter-scale liquid core optical fiber filled with various liquids. *Optics Express, 16*(12), 9205-9212.

Yang, R., Yu, Y.-S., Xue, Y., Chen, C., Chen, Q.-D., & Sun, H.-B. (2011). Single S-tapered fiber Mach–Zehnder interferometers. *Optics Letters, 36*(23), 4482-4484.

Yao, Y., Chen, X., Dai, Y., & Xie, S. (2006). Dual-wavelength erbium-doped fiber laser with a simple linear cavity and its application in microwave generation. *Photonics Technology Letters, IEEE, 18*(1), 187-189.

Yu, C.-B., Wu, Y., Liu, X.-L., Yao, B.-C., Fu, F., Gong, Y., Rao, Y.-J., & Chen, Y.-F. (2016). Graphene oxide deposited microfiber knot resonator for gas sensing. *Optical Materials Express, 6*(3), 727-733.

Yu, H., Xiong, L., Chen, Z., Li, Q., Yi, X., Ding, Y., Wang, F., Lv, H., & Ding, Y. (2014). Solution concentration and refractive index sensing based on polymer microfiber knot resonator. *Applied Physics Express, 7*(2), 022501.

Zeng, X., Wu, Y., Hou, C., Bai, J., & Yang, G. (2009). A temperature sensor based on optical microfiber knot resonator. *Optics Communications, 282*(18), 3817-3819.

Zhai, G., & Tong, L. (2007). Roughness-induced radiation losses in optical micro or nanofibers. *Optics Express, 15*(21), 13805-13816.

Zhang, H., Bao, Q., Tang, D., Zhao, L., & Loh, K. (2009a). Large energy soliton erbium-doped fiber laser with a graphene-polymer composite mode locker. *Applied Physics Letters, 95*(14), 141103.

Zhang, H., Lu, S., Zheng, J., Du, J., Wen, S., Tang, D., & Loh, K. (2014). Molybdenum disulfide (MoS 2) as a broadband saturable absorber for ultra-fast photonics. *Optics Express, 22*(6), 7249-7260.

Zhang, H., Tang, D., Zhao, L., Bao, Q., & Loh, K. (2009b). Large energy mode locking of an erbium-doped fiber laser with atomic layer graphene. *Optics Express, 17*(20), 17630-17635.

Zhang, H., Tang, D., Zhao, L., Bao, Q., Loh, K., Lin, B., & Tjin, S. (2010). Compact graphene mode-locked wavelength-tunable erbium-doped fiber lasers: from all anomalous dispersion to all normal dispersion. *Laser Physics Letters, 7*(8), 591.

Zhang, L., Gu, F., Lou, J., Yin, X., & Tong, L. (2008). Fast detection of humidity with a subwavelength-diameter fiber taper coated with gelatin film. *Optics Express, 16*(17), 13349-13353.

Zhang, L., Zhuo, Z., Wang, J., & Wang, Y. (2012). Passively Q-switched fiber laser based on graphene saturable absorber. *Laser Physics, 22*(2), 433-436.

Zhang, Y., Zhang, Q., Li, Y., Wang, N., & Zhu, J. (2000). Coating of carbon nanotubes with tungsten by physical vapor deposition. *Solid State Communications, 115*(1), 51-55.

Zhao, C., Zhang, H., Qi, X., Chen, Y., Wang, Z., Wen, S., & Tang, D. (2012a). Ultra-short pulse generation by a topological insulator based saturable absorber. *Applied Physics Letters, 101*(21), 211106.

Zhao, C., Zou, Y., Chen, Y., Wang, Z., Lu, S., Zhang, H., Wen, S., & Tang, D. (2012b). Wavelength-tunable picosecond soliton fiber laser with topological insulator: Bi 2 Se 3 as a mode locker. *Optics Express, 20*(25), 27888-27895.

Zhao, L., Tang, D., Zhang, H., Wu, X., Bao, Q., & Loh, K. P. (2010). Dissipative soliton operation of an ytterbium-doped fiber laser mode locked with atomic multilayer graphene. *Optics Letters, 35*(21), 3622-3624.

Zheng, Y., Dong, X., Zhao, C., Li, Y., Shao, L., & Jin, S. (2013). Relative humidity sensor based on microfiber loop resonator. *Advances in Materials Science and Engineering, 2013*.

Zhou, D.-P., Wei, L., Dong, B., & Liu, W.-K. (2010). Tunable passively-switched erbium-doped fiber laser with carbon nanotubes as a saturable absorber. *IEEE Photonics Technology Letters, 22*(1), 9-11.

Zhu, P.-F., Lin, Z.-B., Ning, Q.-Y., Cai, Z.-R., Xing, X.-B., Liu, J., Chen, W.-C., Luo, Z.-C., Luo, A.-P., & Xu, W.-C. (2013). Passive harmonic mode-locking in a fiber laser by using a microfiber-based graphene saturable absorber. *Laser Physics Letters, 10*(10), 105107.

Zhu, Y., Chen, X., & Wang, A. (2009). Observation of interference in a fiber taper interferometer with a subwavelength tip and its sensing applications. *Optics Letters, 34*(18), 2808-2810.

LIST OF PUBLICATIONS AND PAPERS PRESENTED

1. Ahmad, H., **Faruki, M. J.**, Razak, M. Z. A., Tiu, Z. C., & Ismail, M. F. (2017). Evanescent field interaction of tapered fiber with graphene oxide in generation of wide-bandwidth mode-locked pulses. Optics & Laser Technology, 88, 166-171.

2. **Faruki, M. J.**, Ab Razak, M. Z., Azzuhri, S. R., Rahman, M. T., Soltanian, M. R. K., Brambilla, G., ... & Ahmad, H. (2016). Effect of titanium dioxide (TiO2) nanoparticle coating on the detection performance of microfiber knot resonator sensors for relative humidity measurement. Materials Express, 6(6), 501-508.

3. Ahmad, H., **Faruki, M. J**., Tiu, Z. C., & Thambiratnam, K. (2017). Sub-nanometer tuning of mode-locked pulse by mechanical strain on tapered fiber. Optics Communications, 387, 84-88.

4. Ahmad, H., **Faruki, M. J.**, Razak, M. Z. A., Jaddoa, M. F., Azzuhri, S. R., Rahman, M. T., & Ismail, M. F. (2017). A combination of tapered fibre and polarization controller in generating highly stable and tunable dual-wavelength C-band laser. Journal of Modern Optics, 64(7), 709-715.

5. Ahmad, H., **Faruki, M. J.**, Jasim, A. A., Ooi, S. I., & Thambiratnam, K. (2018). Poly (N-vinyl Carbazole)–Polypyrrole/graphene oxide nanocomposite material on tapered fiber for Q-switched pulse generation. Optics & Laser Technology, 99, 184-190.

6. Ahmad, H., Jasim, A. A., **Faruki, M. J.**, Rahman, M. S., & Thambiratnam, K. (2017). Poly (N-vinylcarbazole)-Polypyrrole/Graphene Oxide Nanocomposites based Microfiber Interferometer for High Stability Temperature Sensor. Sensors and Actuators A: Physical. https://doi.org/10.1016/j.sna.2017.05.038

7. **Faruki M.J.**, & Ahmad H. (2016). An Experimental Approach for Relative Humidity Measurement using Microfiber Knot Resonator, Photonics Conference & Meeting: Photonics and its application, University of Malaya.

Optics & Laser Technology 88 (2017) 166–171

Contents lists available at ScienceDirect

Optics & Laser Technology

journal homepage: www.elsevier.com/locate/optlastec

Full length article

Evanescent field interaction of tapered fiber with graphene oxide in generation of wide-bandwidth mode-locked pulses

H. Ahmad*, M.J. Faruki, M.Z.A. Razak, Z.C. Tiu, M.F. Ismail

Photonics Research Center, University of Malaya, 50603 Kuala Lumpur, Malaysia

ARTICLE INFO

Keywords:
Mode-locked lasers
Micro-optics
Ultrafast lasers
Oxide material

ABSTRACT

Pulses with picosecond pulse widths are highly desired for high precision laser applications. A mode-locked pulse laser utilizing evanescent field interaction of a tapered fiber with graphene oxide (GO) is demonstrated. A homemade fabrication stage was used to fabricate the tapered fiber using systematic flame brushing and a GO solution was used to coat the microfiber using optical deposition technique. Pulse trains with a pulse width of 3.46 ps, a 3 dB optical bandwidth of 11.82 nm and a repetition rate of 920 kHz were obtained. The system has substantial potential for many crucial medical, communication, bio processing, military, and industrial applications.

1. Introduction

Ultrafast and ultrashort pulses are crucial elements in many applications such as micromachining, surgery, terahertz wave generation, optical imaging and supercontinuum generation [1], in particular for communications applications in the S-band [2], C-band [3] and L-band [4]. For efficient pulse generation, the longitudinal modes in the resonator must be synchronized to generate the desired ultrafast pulses [1]. Passively ultrafast pulsed laser can be achieved using two methods: i) by integrating a saturable absorber (SA) in the cavity, or ii) by taking the advantages of nonlinear effects occurring in the fiber [1] such as the nonlinear polarization rotation technique or by using a nonlinear amplification loop mirror [5]. Since fine-tuning of the polarization state is not required, using the SA inside the cavity is seen as the most effective technique to generate the pulse train [6]. Various nano materials can be used to create the SAs, and the most common approach is to deposit the SA on the fiber ferrules on the connector, allowing light to penetrate the SA directly. Another viable approach is to deposit the SA on the tapered waist of the microfiber or side polish fiber as a coating, allowing the interaction between the evanescent field and the SA to generate a pulse. Direct depositing of the SA material onto the fiber ferrule has its limitations, including thermal damage probability, weak optical absorption and parasitic reflection [7–9]. Thermal damage in particular would occur when light passes directly through the SA layers, possibly hindering safe and robust SA application. On the other hand, the evanescent field based SAs such as SA coated tapered fibers and side polish fibers require only a small portion of light to interact with thin layer of SA in the waist diameter, thus allowing for a faster cooldown and reducing the probability of thermal damage in high optical power applications [7]. Unfortunately, there are some drawbacks to the use of side polished fiber based SAs, such as difficulties in obtaining a perfect smooth surface structure and high unavoidable sensitivity because of the asymmetric structure [7]. Thus, a tapered fiber based SA seemed a better choice which can generate pulse employing evanescent field interaction.

Many types of SA have been tested for ultrafast generation such as graphene [10–19], MoS_2 [20], WS_2 [21], CNT [15], topological insulator [22] and black phosphorus [23]. Among these SAs, graphene has become the focus of interest of many researchers because of its exceptional electrical and electronics properties [1,24–26] including outstanding nonlinear optical response. There are many features of graphene such as large Kerr nonlinearity, ultrafast carrier dynamics, easy integration with optical system, ultrafast recovery time (200 fs), very low saturable absorption threshold, and a wide operating range covering even the telecom band [9,27] that make it highly desirable for wavelength dependent nonlinear signal generation [28] and broadband nonlinear saturable absorption for mode locking [9]. Bao et. al [29] first demonstrated the mode locked fiber laser using multilayer graphene, and this was quickly followed by various similarly designed systems [10–19]. Most of the SAs in these works were fabricated using the direct deposition technique either by putting layered graphene [10–14,29] or graphene flake-polymer composites [1,15–19] onto a fiber ferrule that is then joined using connectors. The very first mode locked fiber laser exploiting evanescent field interactions with a based graphene SA [27] managed to generate a pulse train output with a repetition rate of 6.99 MHz and a cavity length of 28 m. In this case,

* Corresponding author.
E-mail address: harith@um.edu.my (H. Ahmad).

http://dx.doi.org/10.1016/j.optlastec.2016.09.005
Received 23 May 2016; Received in revised form 6 August 2016; Accepted 8 September 2016

Optics Communications 387 (2017) 84–88

Contents lists available at ScienceDirect

Optics Communications

journal homepage: www.elsevier.com/locate/optcom

Sub-nanometer tuning of mode-locked pulse by mechanical strain on tapered fiber

Harith Ahmad*, Md Jahid Faruki, Zian Cheak Tiu, K. Thambiratnam

Photonics Research Center, University of Malaya, 50603 Kuala Lumpur, Malaysia

ARTICLE INFO

Keywords:
Mode-locked pulse laser
Tapered fiber
Tunable mode-locked pulse laser

ABSTRACT

A tunable mode-locked fiber laser based on the non-linear polarization rotation (NPR) technique is proposed and demonstrated. A passively generated mode-locked output is obtained with a repetition rate of about 70 ns and an average output power of 0.7 mW, as well as a laser efficiency of 0.53%. The mode-locked pulses can be tuned over a span of 4.4 nm, from 1560.6 nm to 1556.2, corresponding to a stretching of the tapered fiber from 0 to 100 μm in 10 μm increments. The pulses have an average signal-to-noise ratio of about 41 dB in the frequency domain, indicating a highly stable mode-locked output. The system can repeat and reverse the generation of these pulses, a crucial criterion of many communications and sensing applications.

1. Introduction

The generation of ultrafast pulses in fiber lasers has become the key focus of substantial research efforts due to their potential applications in spectroscopy [1], biomedical research [2], telecommunications [3–5] and other avenues of scientific research [6]. These pulses, also known as mode-locked pulses, can be generated through various means both active and passive. Initial works on ultrafast pulses focused on the use of active mode-locking techniques, and while these techniques were able to generate the desired pulse output, various inherent factors limited their performance, including modulator bandwidth constraints as well as their general bulky size and high manufacturing cost [6,7].

In an effort to develop ultrafast laser sources that would be more suitable to the needs and requirements of the industry, research efforts have now turned towards passive mode-locking techniques to generate ultrafast pulses in fiber lasers. Passively mode-locked lasers are capable of generating the same output as their active counterparts, albeit with slightly less control over certain parameters. Nevertheless, passively mode-locked fiber lasers are able to provide the desired pulses in a compact, cost-effective and easy to operate package [6]. Mode-locking in fiber lasers can be accomplished by using saturable absorbers, such as graphene [8], transition metal dichalcogenides [9,10] and black phosphorus [11], or by exploiting certain optical phenomena such as nonlinear polarization rotation (NPR), nonlinear optical loop mirrors (NOLMs) and nonlinear amplifying loop mirrors (NALMs). Both approaches have their advantages and disadvantages; saturable absorbers are easy to fabricate and incorporate into laser cavities, while using the NPR, NOLM and NALM techniques allows for the generation of high power pulses and robust operation [8,12–15].

In this work, a mode-locked fiber laser based on the NPR technique is proposed and demonstrated. The laser also incorporates a novel tuning mechanism based on a tapered fiber, which allows for the mode-locked pulses to be tuned in the sub-nanometer scale, below 1.0 nm. The proposed method is simple to fabricate and operate, and thus highly cost effective in comparison to other tuning methods such as the use of gratings [16], exploiting fiber birefringence [17] or through the use of tunable filters [18–21]. In this regard, tapered fibers have already seen widespread use in multiple applications such as tunable fiber lasers [7,22,23], displacement sensors [24], refractive index sensors, strain sensors [25], supercontinuum generators [26] and microsphere resonator couplers [27]. Kieu et al. had already demonstrated that spectral response of the tapered fiber can be tuned by stretching the tapered fiber [22], while Fang et al. demonstrated a wavelength tunable thulium-doped mode locked pulse laser operating at around 2 μm with a tapered fiber was stretched for spectral tuning [7]. However in both cases, key issues arise, including the use of saturable absorbers that might be damaged during high power operation as well as tuning resolutions higher than 1.0 nm, making them undesirable for use in ITU optical channels.

2. Experimental set-up

The proposed mode-locked laser is built around an erbium doped fiber (EDF) as the primary gain medium and utilizes the NPR effect to generate the desired mode-locked output pulse. The setup of the proposed laser is shown in Fig. 1.

* Corresponding author.
E-mail address: harith@um.edu.my (H. Ahmad).

http://dx.doi.org/10.1016/j.optcom.2016.11.039
Received 9 September 2016; Received in revised form 16 November 2016; Accepted 17 November 2016

JOURNAL OF MODERN OPTICS, 2016
http://dx.doi.org/10.1080/09500340.2016.1260172

Taylor & Francis
Taylor & Francis Group

A combination of tapered fibre and polarization controller in generating highly stable and tunable dual-wavelength C-band laser

H. Ahmad, M. J. Faruki, M. Z. A. Razak, M. F. Jaddoa, S. R. Azzuhri, M. T. Rahman and M. F. Ismail

Photonics Research Center, University of Malaya, Kuala Lumpur, Malaysia

ABSTRACT

This paper demonstrates the use of a tapered fibre in generating a highly stable and tunable dual-wavelength fibre laser. By unique arrangement of polarization controller, adjustable spacing range between 0.94 and 3.32 nm and side mode suppression ratio (SMSR) up to 50 dB were recorded. The results were achieved at laser pump power of 94.7 mW. The inter-modal interference is achieved through the use of a non-adiabatic tapered fibre, made by a systematic flame brushing technique. The tapered fibre suppresses the mode competition in the 3-m erbium-doped fibre (EDF) gain medium. Over 60 min, the laser exhibited very high stability with acceptable peak power and SMSR. The proposed EDF laser operates from 1556.71 to 1562.13 nm range.

ARTICLE HISTORY
Received 26 July 2016
Accepted 31 October 2016

KEYWORDS
Dual-wavelength fibre laser; erbium-doped fibre laser; tapered fibre

Introduction

Laser devices have reshaped the world's technological landscape in last 20 years and have been used in many practical applications such as CD players, laser pointers, computer chip etching, remote sensing and many more (*1*). Currently, dual-wavelength fibre lasers (DWFLs) and multiple wavelength fibre laser (*2–4*) have garnered much research attention since it is useful for many applications such as wavelength division multiplexing (WDM) (*5*), microwave generation, high-resolution spectroscopy, fibre sensing, distance measurements (*6*), terahertz difference signal generation (*7*), frequency mixing (*8*), differential absorption lidars (DIALs) (*9*) and radio over fibre (ROF) (*10*). DWFL can produce perfectly synchronized two wavelength pulses using one laser (*9*) and this is the reason why DWFLs are very favourable. Meanwhile, DIALs are used mainly to monitor trace gas (*9*) and in this case the DWFL can be used to produce DIALs system with low cost, rugged, light and compact, alignment free hassle, polarization independent, sustainable, highly efficient and broadly tunable. It is believed that Terahertz radiation could also be generated using a reaction of DWFL output with external crystal that can be further used in new industrial process quality control and security monitoring (*11*, *12*).

Optical microfibres, which are also known as tapered fibres, have attracted significant research interest because of their interesting and useful optical properties such as large evanescent fields, nonlinearity, configurability and robustness (*13*). Microfibres can be integrated easily using a conventional single-mode fibre (SMF). Using the transition region of the tapered fibre and by controlling the adiabatic angle, many useful things can be designed such as broadband single-mode filters and couplers (*13–16*), selective excitation of the fundamental mode in multimode fibres (*17*), comb-like filters for tunable lasers.

To date, only a few works have been found on the generation of dual wavelength using tapered fibre (*18–20*). An SLM-based erbium doped fibre (EDF) ring laser with one superimposed FBG and dual-tapered Mach–Zehnder interferometer (MZI) was demonstrated (*18*). In another work, a dual-wavelength EDF laser has been developed using a tapered fibre (*20*) as a comb filter with a spacing of 1.6 nm, SNR > 40 dB, operated at 1557.0 and 1558.6 nm. So far no report has been found about the tunability of DWFL on 1.5 μm region. A dual-wavelength SLM Ytterbium-doped fibre laser using dual-tapered MZI for 1 μm region was reported in (*19*) where tunability of DWFL was done by utilizing the dual-tapered MZI and adjustment of cavity polarization state using a polarization controller (PC).

The focus of this work was to produce tunable DWFL and the work was motivated by designing a simple yet effective set-up using tapered fibre. In this paper, a highly stable and tunable dual wavelength with various spacing of 0.4, 0.94, 1.1, 2.02, 3.12 and 3.32 nm that operates of wavelength between 1556.71 and 1562.13 nm is presented.

CONTACT H. Ahmad harith@um.edu.my

Materials Express

2158-5849/2016/6/501/008
doi:10.1166/mex.2016.1342
www.aspbs.com/mex

Effect of titanium dioxide (TiO_2) nanoparticle coating on the detection performance of microfiber knot resonator sensors for relative humidity measurement

Md Jahid Faruki[1], Mohd Zulhakimi Ab Razak[1], Saaidal R. Azzuhri[1], Muhammad Towfiqur Rahman[1], Mohammad Reza Khalifeh Soltanian[1], Gilberto Brambilla[2], B. M. Azizur Rahman[3], Kenneth T. V. Grattan[3], Richard De La Rue[4], and Harith Ahmad[1,*]

[1]*Photonic Research Center, University of Malaya, 50603 Kuala Lumpur, Malaysia*
[2]*Optoelectronics Research Center, University of Southampton, Southampton, SO17 1TW, UK*
[3]*School of Mathematics, Computer Science and Engineering, City University London, Northampton Square, London, EC1V 0HB, UK*
[4]*Optoelectronics Research Group, School of Engineering, University of Glasgow, Rankine Building, Oakfield Avenue, Glasgow, G12 8LT, UK*

Article

ABSTRACT

In this study, the sensitivity and the linearity of the un-coated and TiO_2-coated microfiber knot resonator (MKR) have been analyzed. The MKR is very sensitive to humidity changes since its refractive index is strongly humidity dependent. As a result, shifts occur in the resonance wavelength and there are also changes in output power. The un-coated MKR showed a sensitivity of 1.3 pm/%RH, in terms of the resonance wavelength, and a sensitivity of 0.0626 dB/%RH for the transmitted output power. The sensitivity increased greatly after the deposition of a porous TiO_2 nanoparticle coating on the MKR. The TiO_2-coated MKR showed an improved sensitivity of 2.5 pm/%RH, with respect to the resonance wavelength, and 0.0836 dB/%RH for the transmitted output power. This MKR sensor has the potential for use in a variety of humidity sensing applications.

Keywords: Fiber Sensor, Tapered Fiber, Microfiber Knot Resonator, Humidity Sensor, Titanium Dioxide (TiO_2).

1. INTRODUCTION

The microfiber knot resonator (MKR) has a wide range of possible sensing applications, such as humidity,[1] temperature,[2,3] acoustic wave vibration,[4] current,[5] and solution-concentration sensings.[6] Light travelling inside the loop of the knot resonator (in an approximately circular shape) creates an evanescent field at the outer surface that can be used for very effective sensing purposes. It offers many advantages[1]-such as high resonance quality-factor (Q-factor), low-loss and a faster and more reliable response, in terms of resonance wavelength shifting and transmitted output power variation. The MKR is very sensitive to changes in the refractive index of the fiber.[1] When the refractive index in the sensing region (the tapered region of the knot) varies, it changes the resonance wavelength[1] and the transmitted intensity of the light.[7,8]

This paper focuses on the specific area of humidity sensing, since humidity is an important parameter in many industrial and environmental control processing

*Author to whom correspondence should be addressed.
Email: harith@um.edu.my

Optics and Laser Technology 98 (2018) 184–190

Contents lists available at ScienceDirect

Optics and Laser Technology

journal homepage: www.elsevier.com/locate/optlastec

Full length article

Poly (N-vinyl Carbazole) – Polypyrrole/graphene oxide nanocomposite material on tapered fiber for Q-switched pulse generation

H. Ahmad, M.J. Faruki, A.A. Jasim, S.I. Ooi, K. Thambiratnam *

Photonics Research Centre, University of Malaya, 50603 Kuala Lumpur, Malaysia

ARTICLE INFO

Article history:
Received 19 November 2016
Received in revised form 2 March 2017
Accepted 7 September 2017
Available online 28 September 2017

Keywords:
Q-switched pulses
Graphene oxide
Poly (N-vinyl Carbazole) – Polypyrrole
Fiber laser
Optical tapered fiber

ABSTRACT

A passively Q-switched fiber laser using a Saturable Absorber (SA) fabricated from a new Poly (N-vinyl Carbazole) – Polypyrrole/Graphene Oxide (PNVC-PPy/GO) nanocomposite material deposited on a tapered fiber is proposed and demonstrated. The PNVC-PPy/GO composition is deposited along a 3 mm length of the 6.5 cm tapered fiber which has a tapered waist of 8 μm. Q-switched pulses are obtained with repetition rates of 25.15–42.7 kHz and pulse widths of 5.74–2.48 μs over a pump power range of 12.8–40.0 mW. A maximum average power of 0.19 mW and pulse energy of 4.43 nJ are also observed. The proposed Q-switched maintains advantages of a simple design and low fabrication cost while at the same time generating high quality Q-switched pulses.

1. Introduction

Over recent years, the ability to obtain Q-switched pulses from fiber lasers has become the focus of efforts amongst researchers globally due to the crucial role that such a system would play in a wide range of applications encompassing communications, manufacturing, sensing and material processing [1–6]. The ability to generate Q-switched pulses in the 1.5 micron region is of particular interest, as this region falls within the main telecommunications bandwidth, thus providing a multitude of applications in which Q-switched pulses are required. Furthermore, most Q-switched pulses generated at this wavelength region employ erbium doped fibers (EDFs) as the gain medium to generate the desired pulses. This is highly advantageous, as the repetition rate of the pulses generated from the EDF are in the kHz range with a pulse width in the microsecond range [6,7]. In generating the desired Q-switched pulses, both active and passive techniques can be employed. Initially, these pulses were typically actively generated through the use of acousto- or electro-optic modulators (AOMs or EOMs) [8–10]. Such direct approaches were common and in one case even resorting to physically oscillating a microsphere in front of the propagating beam to generate the desired pulse output [11]. While this approach provides substantial control over many of the output pulse's characteristics, they impose significant limitations, including increased size, complexity and cost. Regardless, passive Q-switching has become the preferred technique for obtaining pulses in fiber lasers. Although passive Q-switching provides less control over the characteristics of the output pulse, this drawback is outweighed by the advantages of passive Q-switching techniques, primarily its compact geometry and simple set-up, as well as its typically lower cost [6]. Passive Q-switching can be achieved through various means, most commonly through the use of semiconductor saturable absorber mirrors (SESAMs) [12,13]. However, the discovery of graphene and its highly desirable optical characteristics quickly saw the rapid development of saturable absorbers (SAs), mostly because of the compact size, low fabrication and operation cost as well as easy integration into current optical technologies [5,6,14,15]. Since graphene, many other 2-dimensional (2D) and 3-dimensional (3D) materials have been analysed and their potential for use as SAs explored, including carbon nanotubes (CNTs) [16,17], transition metal dichalcogenides and topological insulators such as MoS_2 [18], $MoSe_2$ [19], Bi_2Se_3 [20,21] and Bi_2Te_3 [22,23] as well as other new materials such as gold nanospheres [24] and black phosphorus [25]. However, graphene still remains the choice candidate for SA applications as it is still considered the thinnest material in the world. The first graphene based SA was demonstrated by Bao et al. [26] and has since shown significant promise for the development of pulse lasers [14–16,18,24,27,28]. Graphene also has the added advantage of a broadband absorption spectrum which allows frequency independent optical inter-band transitions and large absorption of incident

* Corresponding author.
E-mail address: [redacted] (K. Thambiratnam).

Sensors and Actuators A 263 (2017) 44–51

Contents lists available at ScienceDirect

Sensors and Actuators A: Physical

journal homepage: www.elsevier.com/locate/sna

Poly (*N*-vinylcarbazole)-polypyrrole/graphene oxide nanocomposites based microfiber interferometer for high stability temperature sensor

H. Ahmad [a,*], A.A. Jasim [a], M.J. Faruki [a], M.S. Rahman [b], K. Thambiratnam [a]

[a] Photonics Research Centre (PRC), University of Malaya, Kuala Lumpur, 50603 Malaysia
[b] Faculty of Science, Department of Chemistry, University of Malaya, Kuala Lumpur, 50603 Malaysia

ARTICLE INFO

Article history:
Received 17 October 2016
Received in revised form 19 May 2017
Accepted 25 May 2017
Available online 26 May 2017

Keywords:
N-vinylcarbazole
Polypyrrole
Graphene oxide
Inline microfiber mach-Zehnder interferometer
Temperature sensor

ABSTRACT

An all-optical, highly stable temperature sensor based built around Poly (N-vinylcarbazole)-polypyrrole/graphene oxide nanocomposites (PNVC-PPy-GO) deposited on an inline Microfiber Mach-Zehnder interferometer (IMMZI) is investigated and demonstrated. Depositing the PNVC-PPy-GO solution on the IMMZI is seen to enhance the temperature sensing stability, and the resulting wavelength shift as a result of heating the IMMZI with a heating element was linearly proportional to temperature variations, and observed to be stable and uniform. The sensitivity and resolution of the sensor after deposition improves by about 7 pm/°C and 0.18 °C respectively, as compared to the sensor before deposition. The IMMZI with PNVC-PPy-GO coating will be a highly viable candidate for sensing applications requiring highly stable and precise measurements.

1. Introduction

Sensors utilizing optical signals as a means of detecting and measuring a variety of measurands have recently become the emphasis of research efforts around the globe. Optical sensors provide users with the ability to cost-effectively monitor a variety of physical, chemical and biological parameters in real-time [1–3]. Furthermore, optical based sensors also possess significant advantages over their conventional counterparts, including compact form factors and robustness, as well as their relatively simple design and ease of fabrication. Most significantly however is the ability of optical sensors to be multiplexed, providing significant cost-savings for applications requiring multiple sensors.

Optical sensors can be realized in many configurations, taking advantage of the different characteristics of light. Simple optical sensors can be realized through the use of Fresnel reflection [4,5], while more sensitive and accurate sensors can be obtained by exploiting the high phase sensitivity of light to perturbations in an external media [6–9]. However, both approaches have their disadvantages; Fresnel based sensors, more-often than not require direct contact with the measurand, while interferometer based sensors typically require high-cost specialty fibers or large dimensions to operate in. In this regard, the tapered fiber has become the current choice for optical sensors, as they enjoy the benefits of a small form-factor, low manufacturing cost, immunity to electromagnetic interference, small and durability [10,11], as well as the high sensitivity of an interferometer. Of particular interest is the in-line microfiber Mach-Zehnder Interferometer (IMMZI), which is highly sensitive to perturbations in the refractive indices of external media as the small waist diameter of the microfiber allows the travelling beam's evanescent field to interact more with the surrounding media [12–17].

The IMMZI functions by inducing a phase difference in the beams of light travelling along two microfibers with different path lengths due to the core-cladding coupling modes in the interferometer region which is located between dual tapered regions [18]. Consequently, light interference occurs at the output side of the microfiber. As these fibers allow the evanescent wave of the travelling beam to interact with its surrounding media, thus coating the microfiber with highly sensitive materials would in turn increase the sensitivity and performance of the IMMZI itself, especially for sensing applications. Carbon nanotubes (CNTs) and graphene have already been demonstrated as coatings for microfibers, allow for the generation of Q-switched pulse and mode-locking [19–22], as well as stabilizing single-longitudinal mode outputs [23] and inducing four-wave-mixing [24]. Gold nanoparticles have also been applied to microfibers in the effort to create highly sensitive surface plasmon resonance (SPR) based sensors [25]. Graphene, and

* Corresponding author.
E-mail address: kamil@um.edu.my (H. Ahmad).

http://dx.doi.org/10.1016/j.sna.2017.05.038
0924-4247/